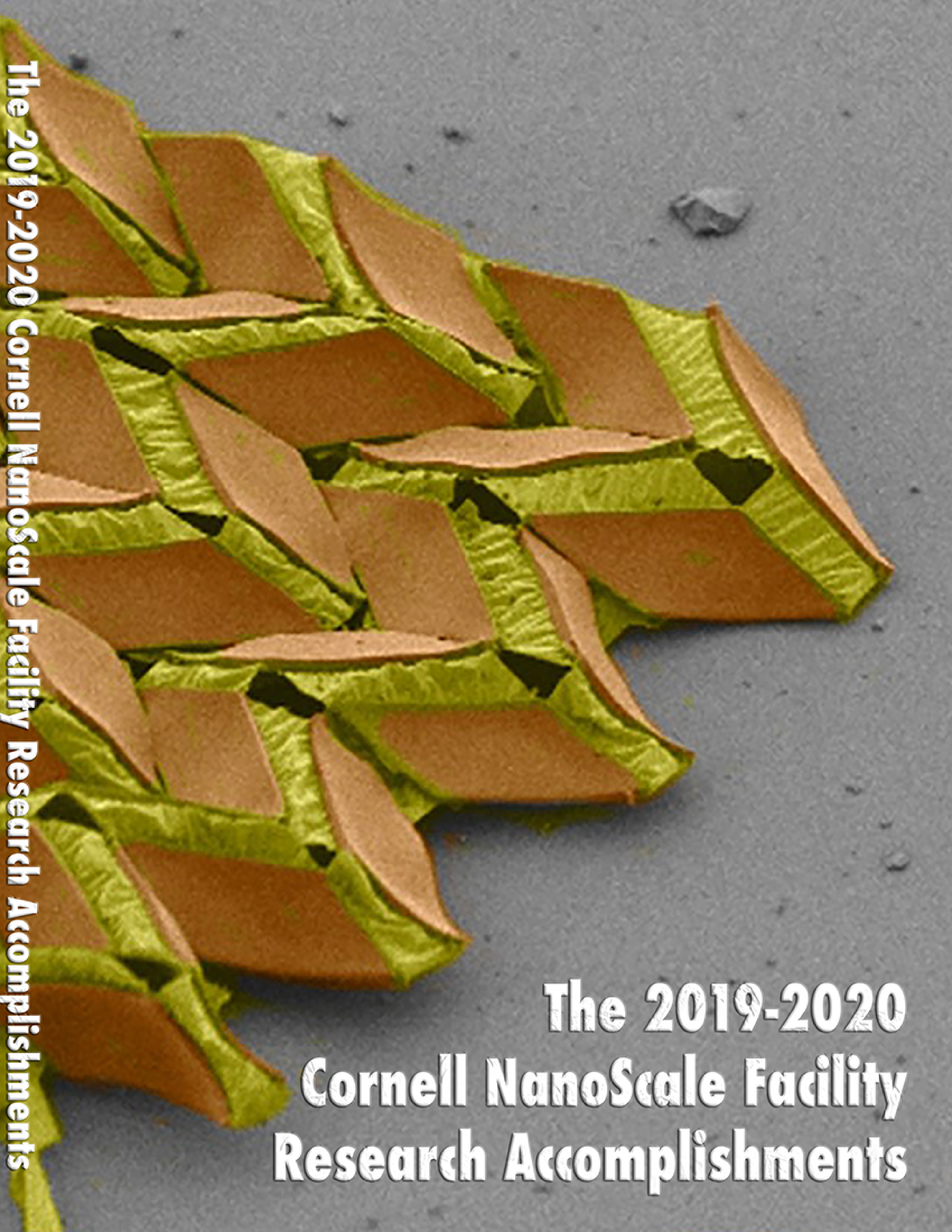

The 2019-2020
Cornell NanoScale Facility
Research Accomplishments

CNF Cornell NanoScale
Science and Technology Facility

250 Duffield Hall • 343 Campus Road • Ithaca NY 14853-2700
Phone: 607.255.2329 • Fax: 607.255.8601 •
Email: information@cnf.cornell.edu • Website: www.cnf.cornell.edu

Cornell NanoScale Facility
2019-2020
Research Accomplishments

CNF Lester B. Knight Director:
Christopher Kemper Ober

Director of Operations:
Ronald Olson

Cornell NanoScale Facility (CNF) is a member of the
National Nanotechnology Coordinated Infrastructure *(www.nnci.net)*
and is supported by the National Science Foundation under Grant No. NNCI-1542081,
the New York State Office of Science, Technology and Academic Research,
Cornell University, Industry, and our Users.

The 2019-2020 CNF Research Accomplishments are also available on the web:
http://cnf.cornell.edu/publications/research_accomplishments

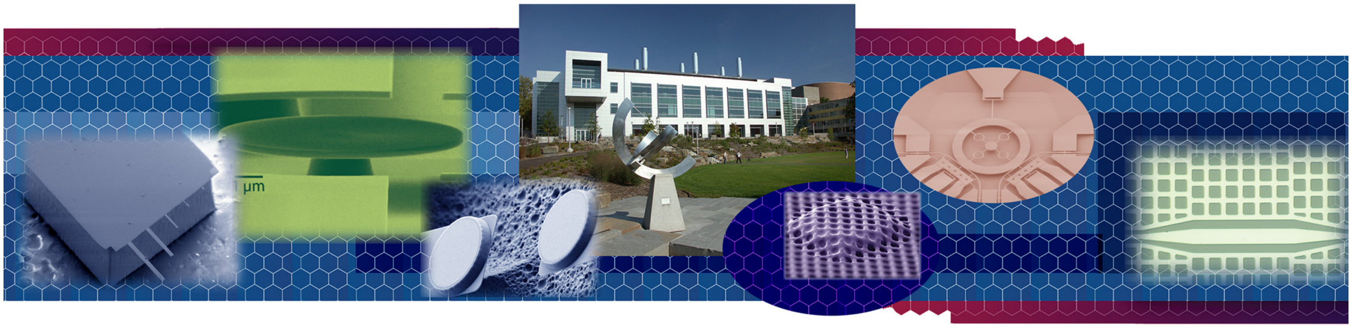

CNF 2019-2020 Research Accomplishments • Table of Contents

Mechanical Devices, 80-91

Optics & Opto-Electronics, 92-125

Physics & Nanostructure Physics, 126-169

Process & Characterization, 170-181

Index, 182-184

2019-2020 Research Accomplishments • Directors' Welcome

Cornell NanoScale Facility (CNF) is proud to present the 2019-2020 CNF Research Accomplishments! We are pleased to showcase the research excellence demonstrated by the users and research groups who are making use of CNF. Users continue to benefit from interaction and collaboration with expert staff, an expansive tool set, and nanofabrication capabilities enabling realization of unique, diverse state-of-the-art results. In addition to the 90 featured research reports contained in this book, a section on CNF-research-related patents, presentations, and publications (close to 400 in 2019) has been included.

CNF's "2020 vision" was disrupted by the COVID-19 pandemic; however, even with University directives to close the cleanroom, office, second floor labs and CAD room on March 17th, focus was never lost for the user community.

After 2.5 months of closure (the longest in CNF history) a reactivation plan was authorized in June for the gradual reopening of the CNF. This plan allowed for the return of local, internal academic users in accordance with State and University guidelines intended to preserve the safety and well-being of CNF users, employees, and the Campus Community. During these initial stages of reopening, the CNF staff and users worked on assigned teams with limited hours. Beginning in mid-August the CNF offered expanded hours of access to users.

We are pleased to let you know that CNF is currently back to 24/7 operational status for users who have been approved and retrained. While some things have changed, one thing remains paramount — the CNF's firm commitment to protecting its community. Anyone seeking to re-gain access to the CNF is required to complete re-training aimed at providing continued education on new COVID safety and social distancing protocols. CNF continues to follow Cornell University and New York State travel guidelines for users seeking approval for cleanroom access. New user orientation and user equipment training protocols have been updated and include remote Zoom training, pre-recorded on-line training videos, and one on one training with social distancing. The CNF will start equipment training and accepting new users in September.

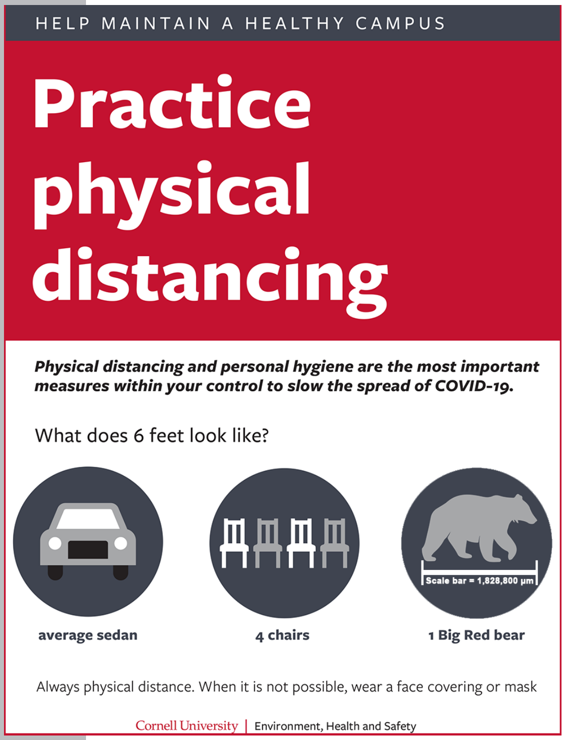

Cornell puts its own unique spin on physical distancing! We added the scale bar to the bear.....

A sincere thank you is extended to our users for their continued patience and understanding. The community efforts to follow newly established protocols for social distancing, surface cleaning, face mask wearing, and hand sanitizing is testimony to their dedication to keeping our facility safe. The CNF staff continues to show resilience and tenacity when presented with challenges. Their enthusiasm as they work together to discover creative ways to teach new users while working to solve difficult and interesting problems is impressive and much appreciated.

Despite the uncertainty the future may present, opportunities for positive change exist. As we continue to collaborate and improve, there is no doubt we will emerge stronger on the other side.

> ***"The difference between STUMBLING BLOCKS and STEPPING STONES, is how you use them."***
> ***~ Unknown***

Staffing News

WELCOME

This year we are pleased to announce the addition of a new Associate Director, ***Prof. Claudia Fischbach-Teschl***, presently Director of Cornell's Physical Sciences Oncology Center (PSOC). Dr. Fischbach-Teschl's charge is multi-faceted. She will work to drive strategies, lead CNF efforts to better understand, serve, and communicate with the life science community, integrate the new Multiscale 3D Fabrication Facility (M3FF) and the 3D Visualization Facility (3VF) while fostering new convergent and life science activities.

In January, ***George "Mac" McMurdy*** joined the CNF family after graduating from the Rochester Institute of Technology with a master's degree in Microelectronic Engineering.

We look forward to George establishing himself as a key staff member dedicated to the support of our user programs.

THANK YOU FOR YOUR SERVICE

The CNF continues to thrive due to the efforts of its staff members. We are grateful for the service and dedication of the following members of the CNF family and we extend best wishes as they enter retirement. Thank you, you will be missed!

- ***Denise Budinger***, with 26 years of service at CNF, retired on August 7th. *(Left)*
- ***Jerry Drumheller***, with 26 years of service at CNF, retired on January 31st. *(See Jerry below at one of our short courses showing off the sputtering system he managed for years!)*
- ***Kathy Springer***, with 17 years of service at CNF, will retire on September 15th. *(Left)*

With your support, we look forward to continued membership in the 16-site National Nanotechnology Coordinated Infrastructure (NNCI) and ongoing support from the National Science Foundation (NSF) as well as maintaining our strong reputation as one of the major academic, nanofabrication facilities in the United States. In the words of Walton Peyton,

> ***"We are stronger together than we are alone."***

We wish all of you continued health and wellbeing and look forward to seeing you back on campus.

Christopher Ober
Lester B. Knight Director, Cornell NanoScale Facility (CNF)
director@cnf.cornell.edu

Claudia Fischbach-Teschl
Associate Director, Cornell NanoScale Facility (CNF)
cf99@cornell.edu

Ron Olson
Director of Operations, Cornell NanoScale Facility (CNF)
olson@cnf.cornell.edu

Comments, feedback, and suggestions about CNF are always welcome. Feel free to use our online User Comment Form at https://www.cnfusers.cornell.edu/user_feedback

Full Color Versions of Some Research Images

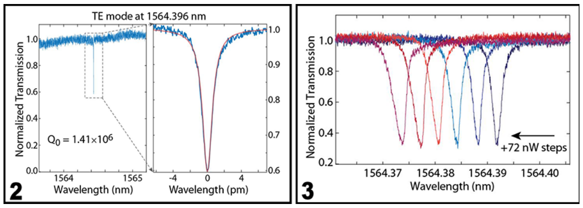

CNF Project 1997-11, Page 96

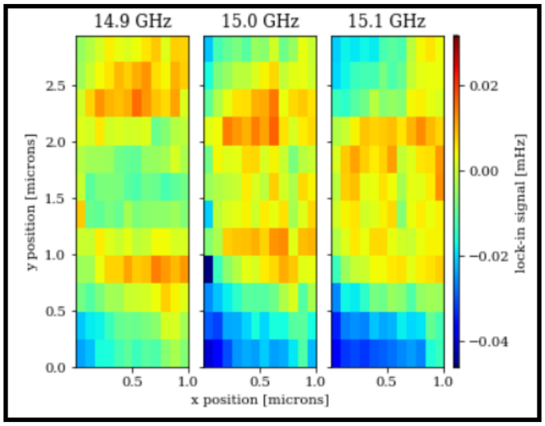

CNF Project 2125-12, Page 148

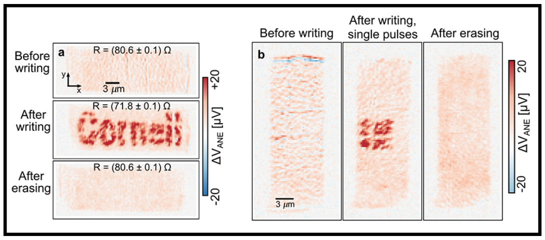

CNF Project 2091-11, Page 138

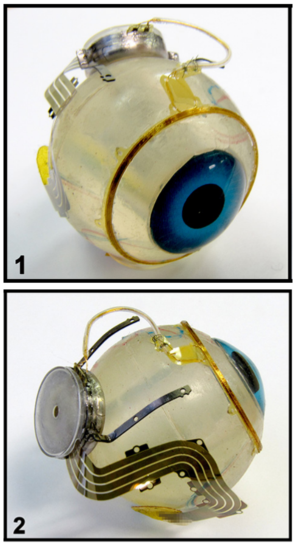

CNF Project 2504-16, Page 18

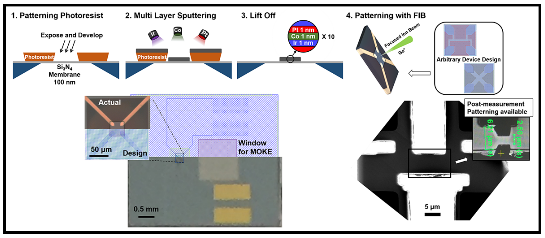

CNF Project 2091-11, Page 142

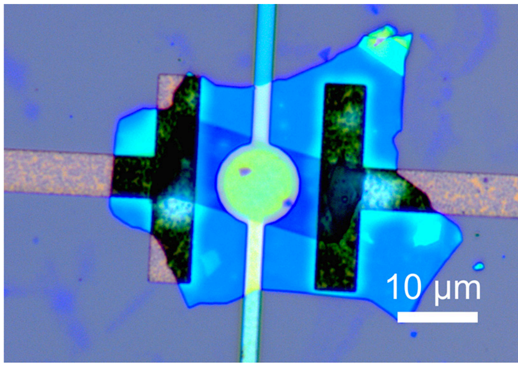

CNF Project 2126-12, Page 84

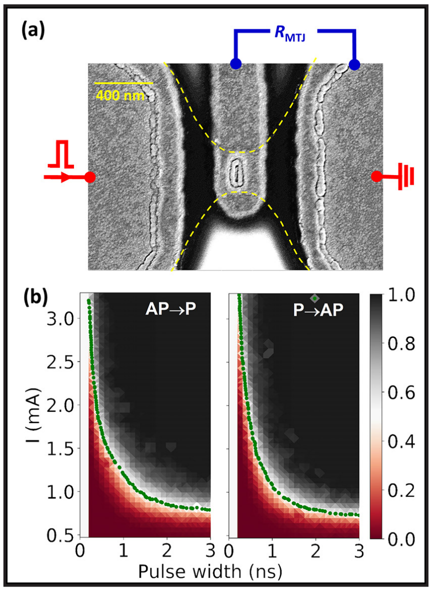

CNF Project 2444-16, Page 158

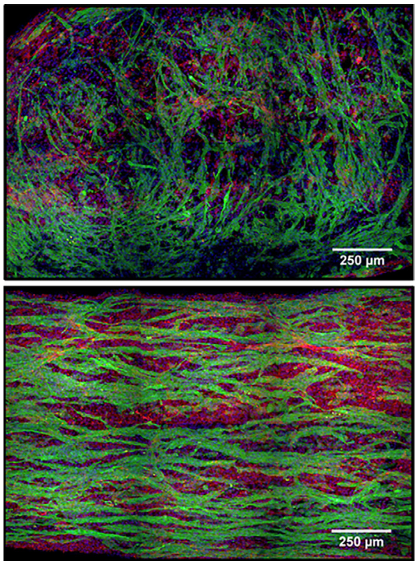

CNF Project 2619-17, Page 22

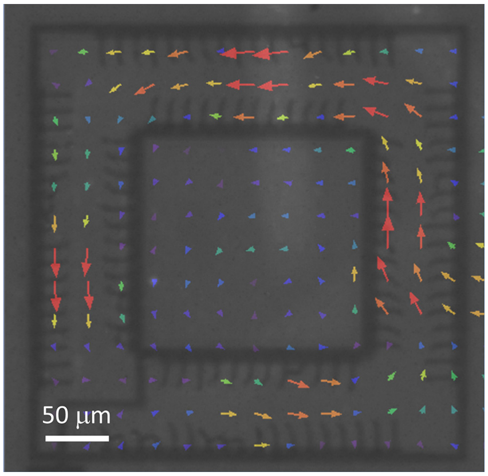

CNF Project 2416-16, Page 90

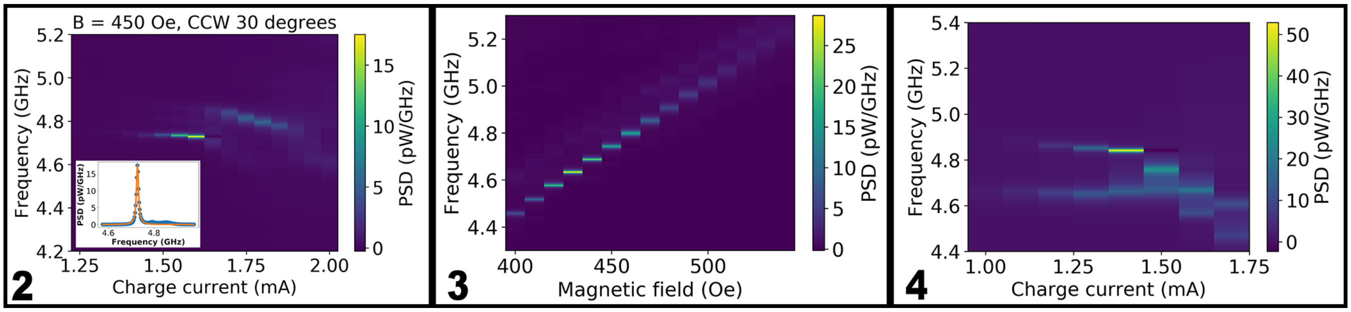

CNF Project 2091-11, Page 144

CNF Project 2525-17, Page 116

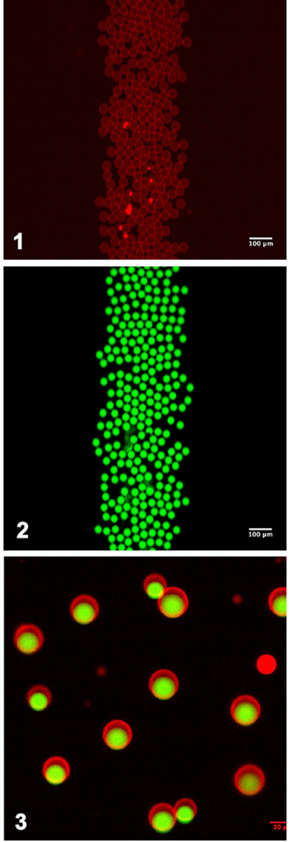

CNF Project 2754-18, Page 28

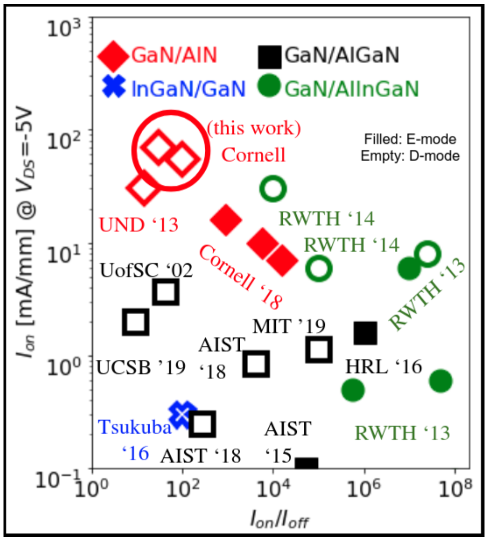

CNF Project 2800-19, Page 48

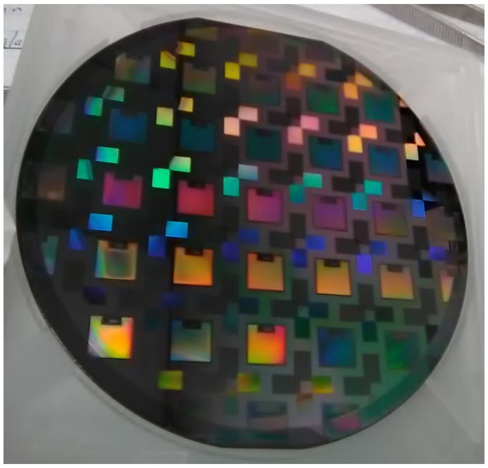

CNF Project 2661-18, Page 120

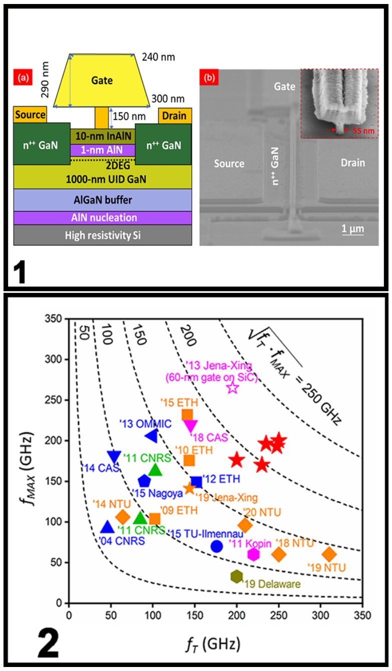

CNF Project 2800-19, Page 54

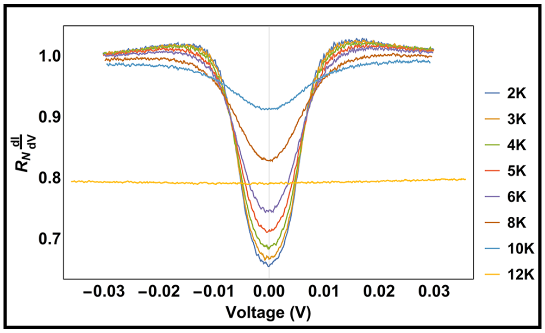

CNF Project 2803-19, Page 56

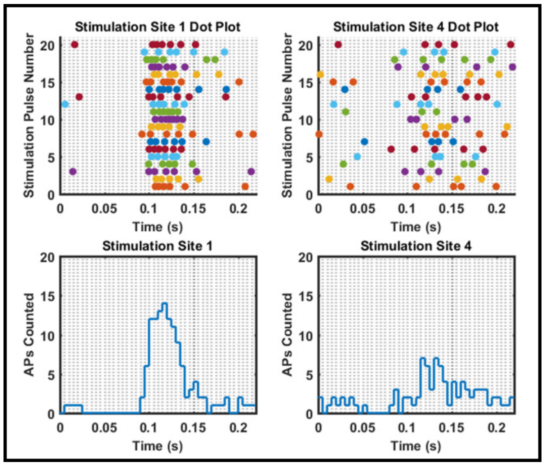

CNF Project 2847-19, Page 58

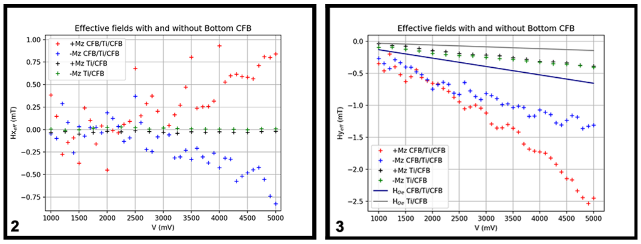

CNF Project 598-96, Page 130

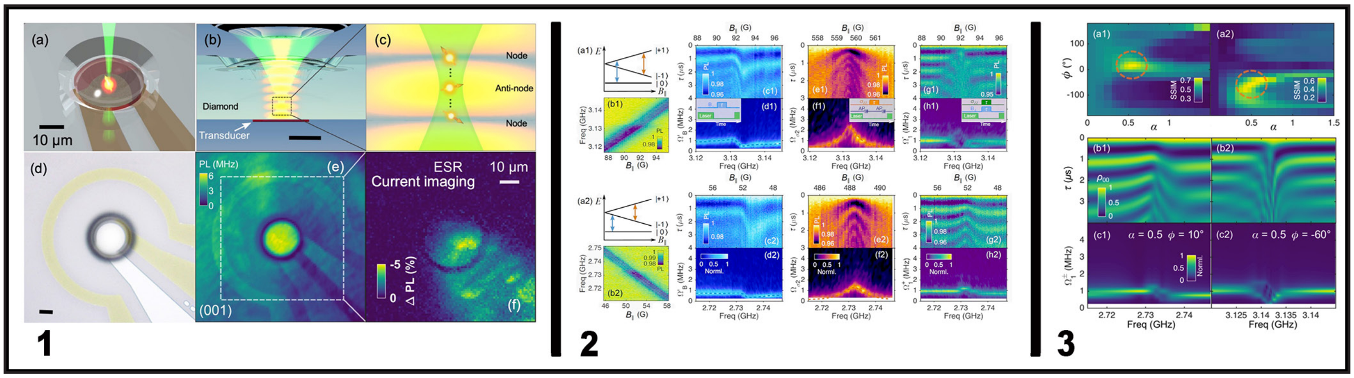

CNF Project 2126-12, Page 150

A Selection of 2019 Cornell NanoScale Facility Research-Related Patents, Presentations, and Publications

“1.6 kV vertical Ga2O3 FinFETs with source-connected field plates and normally-off operation”; Hu, Zongyang, Nomoto, Kazuki, Li, Wenshen, Jinno, Riena, Nakamura, Tohru, Jena, Debdeep, Xing, Huili, 2019 31st International Symposium on Power Semiconductor Devices and ICs (ISPSD), IEEE, page(s) 483-486 (Cornell University).

“3D ElectroStatic Comb Actuators (3D-ESCA) for Micro Robotics”; Amit Lal, Robert Shepherd, 8578, Filed by Cornell, 3/22/19, Invention (Cornell University).

“A high-voltage p-channel FET based on III-Nitride heterostructures”; Samuel Bader, Reet Chaudhuri, Debdeep Jena, Huili Grace Xing, 8358-02-US, United States, US from PRV, Filed, 11/6/19, 16/676, 083 (Cornell University).

“A Highly Selective, Tunable High-Pass X-Ray Filter System and the Method of Fabrication”; David Agyeman-Budu, Arthur Woll, 8827-01-US, United States, MPR-Manuscript Provisional, Filed, 8/2/19, 62/882, 259 (Cornell University).

“A max activity filter for regulatory DNA elements”; Nathaniel Tippens, Haiyuan Yu, 8796, Unfiled, 6/4/19, Invention (Cornell University).

“A mechanically tunable GHz passive voltage element using microstrip resonator”; Di Ni, Adarsh Ravi, K B Vinaya Kumar and Amit Lal, Journal of Physics: Conf. Ser.1407 012051 (2019) (Cornell University).

“A micro-synthetic jet in a microchannel using bubble growth and collapse”; Ehsan Sourtiji, Yoav Peles, Applied Thermal Engineering, Volume 160, September 2019, 114084, https://doi.org/10.1016/j.applthermaleng.2019.114084 (University of Central Florida).

“A New Kind of Magnetic Microscope: Using Ultrafast Heat Pulses to Image Spin-Orbit Torques and Dynamics in Ferromagnetic and Antiferromagnetic Devices”; Fuchs, G., Condensed Matter Physics Seminar, Texas A&M University, College Station, TX 2019 INVITED (Cornell University).

“A polarization-induced 2D hole gas in undoped gallium nitride quantum wells”; Chaudhuri, Reet, Bader, Samuel James, Chen, Zhen, Muller, David A., Xing, Huili Grace, Jena, Debdeep, Science, Vol. 365, Issue # 6460, page(s) 1454-1457 (Cornell University).

“A Polymer Brush Approach to Controlling Biological Binding to Surfaces”; Christopher K. Ober, CDT Summer School, invited talk, University of Sheffield, Sheffield, UK, July 24, 2019 (Cornell University).

“A Polymer Brush Approach to Controlling Biological Binding to Surfaces”; Christopher K. Ober, MSE Seminar, invited talk, University of Pennsylvania, Philadelphia, PA, Oct. 3, 2019 (Cornell University).

“A practical and efficient method for filtering x-ray radiation”; David Agyeman-Budu, Arthur Woll, 8827, Filed by Cornell, 6/26/19, Invention (Cornell University).

“A review of giant correlation-length effects via proximity and weak-links coupling in a critical system: 4He near the superfluid transition”; J K Perron, M O Kimball and F M Gasparini, Reports on Progress in Physics, Volume 82, Number 11, Published 2 October 2019 • © 2019 IOP Publishing Ltd (University at Buffalo).

“A Tool to Improve Reproductive Management and Performance of Ruminant Females through Determination of their Reproductive Physiological Status”; D Erickson, J Giordano, M Masello, 9089, Unfiled Invention, 8/20/19, (Cornell).

“Absorption coefficient estimation of thin MoS2 film using attenuation of silicon substrate Raman signal”; Joon Young Kwak, Results in Physics, Volume 13, June 2019, 102202, Elsevier, https://doi.org/10.1016/j.rinp.2019.102202 (Morgan State University).

“Acoustic Sensing Systems, Devices and Methods”; M Abdelmejeed, J Kuo, A Lal, 7683-02-PC, Patent Cooperation Treaty, Filed, 2/4/19, PCT/US2019/016564 (Cornell).

“Acousto Electro Optic Modulator”; Amit Lal, 9105, Filed by Cornell, 8/22/19, Invention (Cornell).

“Acousto-Optic Modulation of Water in a Microfluidic Channel Using Planar Fresnel Type GHz Ultrasonic Transducer”; Adarsh Ravi, Mamdouh Abdelmejeed, Justin Kuo, Amit Lal, 2019 IEEE International Ultrasonics Symposium (IUS), 6-9 Oct. 2019, Glasgow, United Kingdom, United Kingdom, DOI: 10.1109/ULTSYM.2019.8925614 (Cornell University).

“Adaptive Illumination Apparatus, Method, and Applications”; Michael Buttolph, Kriti Charan, Bo Li, Chunhui (Chris) Xu, 7610-03-US, United States, US from PCT, Filed, 4/23/19, 16/344, 157 (Cornell University).

“Adaptive Illumination Apparatus, Method, and Applications”; Michael Buttolph, Kriti Charan, Bo Li, Chunhui (Chris) Xu, 7610-04-EP, Europe, EPC-European Patent Convention, Filed, 5/9/19, 17871203 (Cornell University).

“Adsorption-controlled growth and properties of epitaxial SnO films”; Mei, Antonio B., Miao, Ludi, Wahila, Matthew J., Khalsa, Guru, Wang, Zhe, Barone, Matthew, Schreiber, Nathaniel J., Noskin, Lindsey E., Paik, Hanjong, Tiwald, Thomas E., [PDF] diva-portal.org, Vol. 3, Issue # 10, page(s) 105202 (Cornell University).

“Adsorption, Desorption, and Crystallization of Aqueous Solutions in Nanopores”; Piyush Jain, Olivier Vincent, Abraham D. Stroock, Langmuir 2019, 35, 11, 3949-3962, February 20, 2019, https://doi.org/10.1021/acs.langmuir.8b04307 (Cornell University).

“Advancements in Design and Application of Microfluidic Devices to Study Cell Migration in Confined Environments”; Windsor, Aaron Joseph, Cornell Theses and Dissertations, Date Issued 2019-05-30, https://doi.org/10.7298/4ht2-t728 (Cornell University).

“All-glass, large metalens at visible wavelength using deep-ultraviolet projection lithography”; Park, Joon-Suh, Zhang, Shuyan, She, Alan, Chen, Wei Ting, Lin, Peng, Yousef, Kerolos MA, Cheng, Ji-Xin, Capasso, Federico, Nano letters, 2019, 19, 12, 8673-8682, November 14, 2019, https://doi.org/10.1021/acs.nanolett.9b03333 (Harvard University).

“Aluminum Nitride-based High Electron Mobility Transistor”; Samuel Bader, Reet Chaudhuri, Austin Hickman, SM Islam, Debdeep Jena, Huili Grace Xing, 8773-01-US, United States, MPR-Manuscript Provisional, Filed, 6/7/19, 62/858, 531 (Cornell University).

“An Atmosphere-breathing Refillable Biphasic Device for Cell Replacement Therapy”; Duo An, Alexander Ernst, James Flanders, Minglin Ma, Longhai Wang, 9204-01-US, United States, EPR-Enhanced Provisional, Filed, 12/5/19, 62/944, 169 (Cornell University).

“An Atmosphere-breathing Refillable Biphasic Device for Cell Replacement Therapy”; Duo An, Alexander Ernst, James Flanders, Minglin Ma, Longhai Wang, 9204, Filed-Attorney Instructed to File, 10/28/19, Invention (Cornell).

“An Integrated Microfluid Device for Capture and Spectroscopic Characterization of Live Cells Under Various Treatment Conditions”; H Huang, G Kelp, G Shvets, 8311-02-PC, Not Applicable (PCT App), PCT-Patent Cooperation Treaty, Filed, 7/25/19, PCT/US1943439 (Cornell University).

“Anomalous Charge Noise in Superconducting Qubits”; B. G. Christensen, C. D. Wilen, A. Opremcak, J. Nelson, F. Schlenker, C. H. Zimonick, L. Faoro, L. B. Ioffe, Y. J. Rosen, J. L. DuBois, B. L. T. Plourde, and R. McDermott, Physical Review B 100, 140503(R) - 24 October 2019 (University of Wisconsin).

“Antibiotic Susceptibility of Escherichia coli Cells during Early-Stage Biofilm Formation”; Huan Gu, Sang Won Lee, Joseph Carnicelli, Zhaowei Jiang, Dacheng Ren, George O’Toole, Editor, Journalof Bacteriology, September 2019 Volume 201 Issue 18 e00034-19 (Syracuse University).

“Apparatus for Improved Energy Resolution in Electron Microscopy”; Cameron Duncan, Jared Maxson, David Muller, 9107-01-US, United States, MPR-Manuscript Provisional, Filed, 9/3/19, 62/895, 300 (Cornell University).

“Apparatus for Improved Energy Resolution in Electron Microscopy”; C Duncan, J Maxson, D Muller, 9107, Filed by Cornell, 8/26/19, Invention (Cornell University).

“Application of metasurface-enhanced infra-red spectroscopy to distinguish between normal and cancerous cell types”; Kelp, G., Arju, N., Lee, A., Esquivel, E., Delgado, R., Yu, Y., Dutta-Gupta, S., Sokolov, K., Shvets, G., Analyst, Vol. 144, Issue # 4, page(s) 1115-1127 (Cornell University).

“Aqueous one-pot synthesis of epoxy-functional diblock copolymer worms from a single monomer: new anisotropic scaffolds for potential charge storage applications”; Hatton, Park, Zhang, Fuchs, Ober, and Armes, Polym. Chem. 10, 194-200 (2019). https://doi.org/10.1039/C8PY01427B (Cornell).

“Atomic Force Microscopy Apparatus, Methods and Applications”; R Dwyer, J Marohn, S Nathan, 7633-03-US, United States, US from PCT, Filed, 11/11/19, 16/612, 473 (Cornell University).

“Atomic layer deposition for membranes, metamaterials, and machines”; K Dorsey, T Pearson, E Esposito, B Bircan, Y Han, S Russell, D Muller, I Cohen, P McEuen, Paul, APS Meeting, https://doi.org/10.1002/adma.201901944 (Cornell).

“Atomic Layer Deposition for Membranes, Metamaterials, and Mechanisms”; Kyle J. Dorsey, Tanner G. Pearson, Edward Esposito, Sierra Russell, Baris Bircan, Yimo Han, Marc Z. Miskin, David A. Muller, Itai Cohen, Paul L. McEuen, Advanced Materials, Volume 31, Issue 29, First published: 30 May 2019, https://doi.org/10.1002/adma.201901944 (Cornell).

“Bandgap narrowing and Mott transition in Si-doped Al0.7Ga0.3N”; Shyam Bharadwaj, S. M. Islam, Kazuki Nomoto, Vladimir Protasenko, Alexander Chaney, Huili (Grace) Xing, Debdeep Jena, Applied Physics Letters 114, 113501 (2019); https://doi.org/10.1063/1.5086052 (Cornell University).

“Bidirectional Folding with Atomic Layer Deposition Bimorphs for Autonomous Micro-Origami”; I Cohen, B Bircan, M Miskin, R Lang, K Dorsey, P McEuen, APS March Meeting 2019, abstract id.X57.001 (Cornell University).

“Biometric Thin Card Reader With Energy Harvesting”; Amit Lal, US20190278953A1 United States, 2019-09-12 Publication of US20190278953A1 (Cornell University).

“Block Copolymer Self-Assembly Directed Hierarchically Structured Materials from Nonequilibrium Transient Laser Heating”; Tan, K. W., and Wiesner, U., Macromolecules 52, 395-409 (2019) (Cornell University).

“Block copolymers containing stable radical and fluorinated blocks with long-range ordered morphologies prepared by anionic polymerization”; Alicia Cintora, Hiroki Takano, Mohit Khurana, Teruaki Hayakawa, Christopher K. Ober, Polymer Chemistry, 2019, DOI: 10.1039/C9PY00416E (Cornell).

“Blue (In, Ga) N light-emitting diodes with buried n+-p+ tunnel junctions by plasma-assisted molecular beam epitaxy”; Cho, Y., Bharadwaj, S., Hu, Z., Nomoto, K., Jahn, U., Xing, H.G., Jena, D., Japanese Journal of Applied Physics, Vol. 58, Issue # 6, page(s) 60914 (Cornell University).

“Blue (In, Ga)N Light-Emitting Diodes with Buried n+−p+ Tunnel Junctions by Plasma-Assisted Molecular Beam Epitaxy”; Y Cho, S Bharadwaj, Z Hu, K Nomoto, U Jahn, HG Xing, D Jena, 2019 Compound Semiconductor Week, 19-23 May 2019, DOI: 10.1109/ICIPRM.2019.8819130 (Cornell).

“Breakdown Walkout in Polarization-Doped Vertical GaN Diodes”; Fabris, E., De Santi, C., Caria, A., Nomoto, K., Hu, Z., Li, W., Gao, X., Jena, D., Xing, H.G., Meneghesso, G., IEEE Transactions on Electron Devices, Vol. 66, Issue # 11, page(s) 4597-4603 (Cornell University).

“Broadband enhancement of thermal radiation”; Gaurang R. Bhatt, Avik Dutt, Steven A. Miller, Raphael St-Gelais, Felippe A. S. Barbosa, Paulo A. Nussenzveig, and Michal Lipson, Optics Express Vol. 27, Issue 12, pp. A818-A828 (2019) https://doi.org/10.1364/OE.27.00A818 (Columbia University).

“Broken Symmetry Effects due to Polarization on Resonant Tunneling Transport in Double-Barrier Nitride Heterostructures”; J Encomendero, V Protasenko, B Sensale-Rodriguez, P Fay, F Rana, D Jena, HG Xing, Physical Review Applied, Vol. 11, Issue # 3, page(s) 34032 (Cornell University).

"Capillary Origami with Atomically Thin Membranes"; Reynolds, Michael F., McGill, Kathryn L., Wang, Maritha A., Gao, Hui, Mujid, Fauzia, Kang, Kibum, Park, Jiwoong, Miskin, Marc Z., Cohen, Itai, McEuen, Paul L., Nano letters, Vol. 19, Issue # 9, page(s) 6221-6226 (Cornell University).

"Capillary Origami with Atomically Thin Sheets"; Reynolds, Michael, McGill, Kathryn, Wang, Maritha, Miskin, Marc, Gao, Hui, Mujid, Fauzia, Kang, Kibum, Park, Jiwoong, Cohen, Itai, McEuen, Paul, APS Meeting Abstracts (Cornell University).

"Capillary-based system for accelerated antimicrobial susceptibility testing"; David Erickson, Sasank Vemulapati, Ruisheng Wang, 9274-01-US, United States, EPR-Enhanced Provisional, Filed, 12/23/19, 62/952, 985 (Cornell).

"Capillary-based system for accelerated antimicrobial susceptibility testing"; David Erickson, Sasank Vemulapati, Ruisheng Wang, 9274, Filed by Cornell, 12/11/19, Invention (Cornell University).

"Carbon Supported RuCo, RuNi and RuFe Alloy Nanoparticles as Hydrogen Oxidation and Evolution Electrocatalysts in Alkaline Media"; Hector Abruna, Hongsen Wang, 8550, Filed by Cornell, 3/4/19, Invention (Cornell University).

"Carrier confinement effects observed in the normal-state electrical transport of electron-doped cuprate trilayers"; Sacco, Chiara, Galdi, Alice, Romeo, Francesco, Coppola, Nunzia, Orgiani, Pasquale, Wei, Haofei I., Goodge, Berit H., Kourkoutis, Lena F., Shen, Kyle, Schlom, Darrell G., Maritato, Luigi, Journal of Physics D: Applied Physics, Volume 52, Issue 13, article id. 135303 (2019) (Cornell University).

"Cavity-enhanced optical parametric generation in a modal-phase-matched lithium niobate microring"; Luo, Rui, He, Yang, Liang, Hanxiao, Li, Mingxiao, Ling, Jingwei, Lin, Qiang, CLEO: Science and Innovations, Optical Society of America, STh1J-2 (University of Rochester).

"Cell migration through three-dimensional confining pores: speed accelerations by deformation and recoil of the nucleus"; M Krause, FW Yang, M te Lindert, P Isermann, J Schepens, RJA Maas, C Venkataraman, J Lammerding, A Madzvamuse, W Hendriks, Philosophical Transactions of the Royal Society B, Vol. 374, Issue # 1779, page(s) 20180225 (Cornell).

"Characterization and Modeling of Co/BaTiO3/SrRuO3 Ferroelectric Tunnel Junction Memory by Capacitance-Voltage (C-V), Current-Voltage (I-V), and High-Frequency Measurements"; M Abuwasib, H Lee, J Lee, C Eom, A Gruverman, U Singisetti, IEEE Transactions on Electron Devices, Volume: 66 Issue: 5, May 2019, DOI: 10.1109/TED.2019.2904019 (University at Buffalo).

"Chemical reaction and diffusion kinetics during laser-induced submillisecond heating for lithographic applications"; J Jiang, B Jung, M Thompson, C Ober, Journal of Vacuum Science & Technology B 37, 041601 (2019); https://doi.org/10.1116/1.5086871 (Cornell).

"Chip-based frequency comb sources for optical coherence tomography"; Ji, Xingchen, Yao, Xinwen, Klenner, Alexander, Gan, Yu, Gaeta, Alexander L., Hendon, Christine P., Lipson, Michal, Optics express, Vol. 27, Issue # 14, page(s) 19896-19905 (Columbia University).

"Chiral Gyroidal Thin Films from Block Copolymer Self-Assembly as Structural Directing Templates for Fabrication of Mesostructured Crytalline Inorganic Materials"; Zhang, Qi, Yu, Fei, Wiesner, Ulrich, APS March Meeting, 2019, Boston, MA, abstract id.F50.002 (Cornell University).

"Chlorine evolution reaction electrocatalysis on RuO2(110) and IrO2(110) grown using molecular-beam epitaxy"; D Kuo, H Paik, J Nelson, K Shen, D Schlom, and J Suntivich, J. Chem. Phys. 150, 041726 (2019); https://doi.org/10.1063/1.5051429 (Cornell).

"Clog and Release, and Reverse Motions of DNA in a Nanopore"; T Kubota, K Lloyd, N Sakashita, S Minato, K Ishida, and T Mitsui, Polymers 2019, 11(1), 84; https://doi.org/10.3390/polym11010084, 7 January 2019 (Aoyama Gakuin University).

"CMOS Controlled Ghz Ultrasonic Impedance Imager"; M Abdelmejeed, J Kuo, A Ravi, A Lal, 20th International Conference on Solid-State Sensors, Actuators and Microsystems & Eurosensors XXXIII, 23-27 June 2019, DOI: 10.1109/transducers.2019.8808493 (Cornell University).

"Coherent quantum dynamics of systems with coupling-induced creation pathways"; Rogers, Steven D., Graf, Austin, Javid, Usman A., Lin, Qiang, Communications Physics, Vol. 2, Issue # 1, page(s) 1-9 (University of Rochester).

"Collaborative RFID Reader Using Code Divisional Multiple Access (CDMA) and Methods for Same"; X Hui, E Kan, 8145-02-PC, Not Applicable (PCT App), Patent Cooperation Treaty, Filed, 5/14/19, PCT/US19/32255 (Cornell University).

"Computation Devices and Artificial Neurons Based on Nanoelectromechanical Systems"; S Ardanuc, J Hoople, J Kuo, A Lal, 5966-03-US, United States, Issued, 5/8/14, 14/273, 540, 2/26/19, 10, 217, 045, US20140355381A1 United States, 2019-02-26 Publication of US10217045B2 (Cornell).

"Controlling spin current polarization through non-collinear antiferromagnetism"; Nan, T., C. Quintela, J. Irwin, G. Gurung, D. Shao, J. Gibbons, N. Campbell, K. Song, S. Choi, L. Guo, R. Johnson, P. Manuel, R. Chopdekar, I. Hallsteinsen, T. Tybell, P. Ryan, J. Kim, Y. Choi, P. Radaelli, D. Ralph, E. Tsymba, M. Rzchowski, C. Eom, arXiv:1912.12586 [cond-mat.mtrl-sci] (Cornell University).

"Correlation Between Optical Fluorescence and Microwave Transmission During Single-Cell Electroporation"; Li, Hang, Ma, Xiao, Du, Xiaotian, Li, Lei, Cheng, Xuanhong, Hwang, James C. M., IEEE Transactions on Biomedical Engineering, Volume: 66, Issue: 8, Aug. 2019, Page(s): 2223-2230, DOI: 10.1109/TBME.2018.2885781 (Lehigh University).

"Cross-resonance interactions between superconducting qubits with variable detuning"; M Ware, B Johnson, J Gambetta, T Ohki, J Chow, B Plourde, arXiv:1905.11480 [quant-ph] (Submitted 27 May 2019) (Syracuse University).

"Cryogenic Memory Architecture Integrating Spin Hall Effect based Magnetic Memory and Superconductive Cryotron Devices"; M.Nguyen, et al., arXiv preprint arXiv:1907.00942 (Submitted on 1 Jul 2019) (Cornell University).

"Current-Induced Torques with Dresselhaus Symmetry Due to Resistance Anisotropy in 2D Materials"; G Stiehl, D MacNeill, N Sivadas, I El Baggari, M Guimaraes, N Reynolds, L Kourkoutis, C Fennie, R Buhrman, D Ralph, ACS nano, Vol. 13, Issue # 2, page(s) 2599-2605 (Cornell University).

"Defect Center Hybrid Quantum Systems for Transduction and Sensing: Challenges and Opportunities"; Fuchs, G., AFOSR Workshop on Quantum Materials, University of Chicago, Chicago, IL 2019 (Cornell University).

"Defect Qubits"; Fuchs, G., Materials Research Society/Kavli Future of Materials Workshop on Solid-State Materials and Quantum Information, Phoenix, AZ 2019 (Cornell University).

"Demonstration of waferscale voltage amplifier and electrostatic quadrupole focusing array for compact linear accelerators"; K. B. Vinayakumar, S. Ardanuc, Q. Ji, A. Persaud, P. Seidl, T. Schenkel, A. Lal, J of Applied Physics 125, 194901 (2019); https://doi.org/10.1063/1.5091979 (Cornell).

"Densely functionalized lubricin scaffolds and uses thereof"; L Bonassar, M Colville, M Paszek, H Reesink, S Schmidt, 8851, Unfiled, 7/19/19, Invention (Cornell University).

"Design, fabrication, and analysis of 1 cm diameter metalens in the visible"; J Park, S Zhang, A She, W Chen, K Yousef, Y Ibrahim, and F Capasso, SPIE Optics+Photonics 2019, San Diego, CA. Aug 11-15, 2019. (Harvard University).

"Development of isoporous microslit silicon nitride membranes for sterile filtration applications"; E Wright, J Miller, M Csordas, A Gosselin, J Carter, J McGrath, D Latulippe, J Roussie, Biotechnology & Bioengineering, 30 November 2019, https://doi.org/10.1002/bit.27240 (SiMPore Inc).

"Development of metal organic cluster EUV photoresists"; Christopher K. Ober, SPIE Advanced Lithography, invited talk, San Jose, CA, Feb. 24-28, 2019 (Cornell University).

"Development of metal organic cluster EUV photoresists"; K Sakai, S Jung, W Pan, E Giannelis, C Ober, Proceedings V.10960, Advances in Patterning Materials and Processes XXXVI; 1096015; https://doi.org/10.1117/12.2516133; SPIE Advanced Lithography, 2019, San Jose, CA (Cornell).

"Device and Method for Point-of-Care Diagnostics and Antibiotic Resistance Identification, and Applications Thereof"; David Erickson, Seoho Lee, Saurabh Mehta, 7108-03-US, United States, Issued, 1/19/18, 15/875, 686, 7/9/19, 10, 345, 295 (Cornell University).

"Device and System for Repairing Intervertebral Disc herniation and Methods of Use"; L Bonassar, S Chen, A Cunha-Gavidia, R Hartl, M McCarter, M Messina, G Shibu, 7837-03-US, United States from PCT, 11/15/19, 16/614, 072 (Cornell).

"Device for Collecting or Extruding a Cell-Containing Biological Material"; L Bonassar, J Matthews, 9131-01-US, Enhanced Provisional, Filed, 9/30/19, 62/908, 329 (Cornell).

"Digital Coherent Control of a Superconducting Qubit"; E. Leonard Jr, M. Beck, J. Nelson, B. Christensen, T. Thorbeck, C. Howington, A. Opremcak, I. Pechenezhskiy, K. Dodge, N. Dupuis, J. Ku, F. Schlenker, J. Suttle, C. Wilen, S. Zhu, M. Vavilov, B. Plourde, R. McDermott, Physical Review Applied 11, 014009 (2019) arXiv:1806.07930 (Syracuse).

"Dirac nodal lines protected against spin-orbit interaction in IrO2"; Nelson, J., Ruf, J., Lee, Y., Zeledon, C., Kawasaki, J., Moser, S., Jozwiak, C., Rotenberg, E., Bostwick, A., Schlom, D., Physical Review Materials, Vol. 3, Issue # 6, page(s) 64205 (Cornell).

"Direct addition of sulfur and nitrogen functional groups to graphite felt electrodes for improving all-vanadium redox flow battery performance"; A Shah, Y Wu, Y Joo, Electrochimica Acta, V.297, 20 February 2019, Pages 905-915, https://doi.org/10.1016/j.electacta.2018.12.052 (Cornell).

"Drug testing complementary metal-oxide-semiconductor chip reveals drug modulation of transmitter release for potential therapeutic applications"; Huang, Meng, Rathore, Shailendra S., Lindau, Manfred, Journal of Neurochemistry, Vol. 151, Issue # 1, page(s) 38-49 (Cornell University).

"Dual-frequency spin resonance spectroscopy of diamond nitrogen-vacancy centers in zero magnetic field"; A. K. Dmitriev, H. Y. Chen, G. D. Fuchs, A. K. Vershovskii, Physical Review A 100, 011801(R) (2019). https://doi.org/10.1103/PhysRevA.100.011801 (Cornell University).

"Dynamic DNA material with emergent locomotion behavior powered by artificial metabolism"; Hamada, S., K.Yancey, Y.Pardo, M.Gan, M.Vanatta, D.An, Y.Hu, T.Derrien, R.Ruiz, P.Liu, J.Sabin, and D.Luo, Science Robotics, 10 Apr 2019, Vol. 4, Issue 29, eaaw3512, DOI: 10.1126/scirobotics.aaw3512 (Cornell).

"Dynamic response of a tunable MEMS accelerometer based on repulsive force"; M Daeichin, M Ozdogan, S Towfighian, R Miles, Sensors and Actuators A: Phys, 289, 15-04-2019, 34-43, https://doi.org/10.1016/j.sna.2019.02.007 (Binghamton).

"Effective Spin-Mixing Conductance of Heavy-Metal-Ferromagnet Interfaces"; L Zhu, D Ralph, R Buhrman, Physical Review Letters 123, 057203, (2019), https://doi.org/10.1103/PhysRevLett.123.057203 (Cornell University).

"Effects of Forming Gas Anneal on the Structure of Al2O3/GaN Interface"; B. McEwen, I. Mahaboob, K. Hogan, E. Rocco, V. Meyers, S. Tozier, A. Lelis, R. Green, F. Nouketcha, and F. Shahedipour-Sandvik, 61st Electronic Materials Conf, June 2019, University of Michigan (SUNY Polytechnic Institute).

"Effects of millisecond scale laser spike anneals on amorphous barium titanate thin films"; Haber, Lewis Rosevere, Cornell Theses and Dissertations, Date Issued 2019-05-30, https://doi.org/10.7298/sqd0-vc42 (Cornell).

"Effects of Semiconductor Surface Treatments and Dielectric Anneal on the Electrical Characteristics of GaN-Based Metal-Insulator-Semiconductor Devices"; B. McEwen, I. Mahaboob, K. Hogan, E. Rocco, V. Meyers, S. Tozier, A. Lelis, R. Green, F. Nouketcha, and F. Shahedipour-Sandvik, 13th International Conference on Nitride Semiconductors, Bellevue, WA, July 7-12, 2019 (SUNY Polytechnic Institute).

"Electric force microscopy of sample having appreciable sample impedance"; R. P. Dwyer and J. A. Marohn, NanoScientific, 2019, 16, 6 -9, URL https://www.parksystems.com/index.php/medias/resources/nanoscientific (Cornell).

"Electrical manipulation of the fine-structure splitting of WSe2 quantum emitters"; C Chakraborty, N Jungwirth, G Fuchs, and A Vamivakas, PRB 045308 (2019). https://doi.org/10.1103/PhysRevB.99.045308 (Cornell University).

“Electroplating of Sn Film on Nb Substrate for Generating Nb3sn Thin Films and Post Laser Annealing”; Sun, Z., Liepe, M., Oseroff, T., Porter, R. D., Arias, T., Sitaraman, N., Connolly, A., Scholtz, J., Thompson, M. O., 19th Int. Conf. on RF Superconductivity, Germany; JACoW, ISBN:978-3-95450-211-0, doi:10.18429/JACoW-SRF2019-MOP014 (Cornell).

“ElectroStatic Comb Actuators for Micro Robotics”; A Lal, R Shepherd, 8578-01-US, United States, MPR-Manuscript Provisional, Filed, 3/26/19, 62/824, 234 (Cornell).

“Energetic costs regulated by cell mechanics and confinement are predictive of migration path during decision-making”; M Zanotelli, A Rahman-Zaman, J VanderBurgh, P Taufalele, A Jain, D Erickson, F Bordeleau, and C Reinhart-King, Nature Communications V10, # 4185 (2019), https://www.nature.com/articles/s41467-019-12155-z (Cornell University).

“Energy-efficient ultrafast SOT-MRAMs based on low-resistivity spin Hall metal Au0. 25Pt0. 75”; Zhu, Lijun, Zhu, Lujun, Shi, Shengjie, Ralph, D. C., Buhrman, R. A., arXiv preprint arXiv:1910.11896 (Cornell University).

“Engineering Electron-Phonon Coupling of Quantum Defects to a Semiconfocal Acoustic Resonator”; H Chen, N Opondo, B Jiang, E MacQuarrie, R Daveau, S Bhave, and G Fuchs, Nano Letters 19, 7021-7027 (2019). https://doi.org/10.1021/acs.nanolett.9b02430 (Cornell University).

“Engineering transferrable microvascular meshes for subcutaneous islet transplantation”; Song, W., A.Chiu, L.-H. Wang, R.E. Schwartz, B.Li, N.Bouklas, D.T. Bowers, D.An, S.H. Cheong, J.A. Flanders, Y.Pardo, Q.Liu, X.Wang, V.K. Lee, G.Dai, and M.Ma, Nature Communications, V.10, #4602, 10 October 2019, doi:10.1038/s41467-019-12373-5 (Cornell University).

“Enhanced injection efficiency and light output in bottom tunnel-junction light-emitting diodes using UID GaN spacers”; S Bharadwaj, J Miller, K Lee, J Lederman, M Siekacz, H Xing, D Jena, C Skierbiszewski, H Turski, arXiv preprint arXiv:1911.03532 [physics.app-ph] (8 Nov 2019) (Cornell).

“Enhanced Thermal Stability of Low-k Ethyl-Bridged Organosilicas Using Laser Spike Annealing”; Sun, Zeming, Bell, Robert T., Thompson, Michael O., ACS Applied Electronic Materials (Cornell University).

“Enhancement of spin transparency by interfacial alloying”; Zhu, Lijun, Ralph, Daniel C., Buhrman, Robert A., Physical Review B 9, 180404, (2019), https://doi.org/10.1103/PhysRevB.99.180404 (Cornell University).

“Enhancing Spin-Orbit Torque by Strong Interfacial Scattering From Ultrathin Insertion Layers”; Zhu, Lijun, Zhu, Lujun, Shi, Shengjie, Sui, Manling, Ralph, D. C., Buhrman, R. A., Physical Review Applied, Vol. 11, Issue # 6, page(s) 61004 (Cornell).

“Enhancing Wall-Plug Efficiency for Deep-UV Light-Emitting Diodes: From Crystal Growth to Devices”; SM Islam, V Protasenko, S Bharadwaj, J Verma, K Lee, HG Xing, D Jena, Light-Emitting Diodes pp 337-395, Solid State Lighting Technology and App Series, (SSLTA, V.4, 2019) (Cornell).

“Entropic death of nonpatterned and nanopatterned polyelectrolyte brushes”; M Menzel, W Chen, K Simancas, H Xu, O Prucker, C Ober, J Rühe, Journal of Polymer Science Part A: Polymer Chemistry, 2019 57(12) 1283-1295 (Cornell).

“Epitaxial Conducting Coatings for Reversible Metal Anodes”; L Archer, T Tang, Q Zhao, J Zheng, 8571-01-US, United States, Enhanced Provisional, Filed, 4/26/19, 62/839, 485 (Cornell).

“Epitaxial integration of high-mobility La-doped BaSnO3 thin films with silicon”; Wang, Zhe, Paik, Hanjong, Chen, Zhen, Muller, David A., Schlom, Darrell G., APL Materials, Vol. 7, Issue # 2, page(s) 22520 (Cornell University).

“Epitaxial SrTiO3 film on silicon with narrow rocking curve despite huge defect density”; Z. Wang, B. H. Goodge, D. J. Baek, M. J. Zachman, X. Huang, X. Bai, C. M. Brooks, H. Paik, A. B. Mei, J. D. Brock, J-P. Maria, L. F. Kourkoutis, and D. G. Schlom, Physical Review Materials 3, 073403 - Published 29 July 2019 (Cornell University).

“EUV photolithography: resist progress in metal-organic complex photoresists”; H Xu, V Kosma, K Sakai, E Giannelis, C Ober, Journal of Micro/Nanolithography, MEMS, and MOEMS (2019), 18(1), 11007 (Cornell University).

“Ex Situ and In Situ Measurement of Water Activity with a MEMS Tensiometer”; W Black II, M Santiago, S Zhu, A Stroock, Anal. Chem. 2020, 92, 1, 716-723, Nov 25, 2019, https://doi.org/10.1021/acs.analchem.9b02647 (Cornell University).

“Exceptionally High, Strongly Temperature Dependent, Spin Hall Conductivity of SrRuO3”; Ou, Y., Z. Wang, C.S. Chang, H.P. Nair, H. Paik, N. Reynolds, D.C. Ralph, D.A. Muller, D.G. Schlom, R.A. Buhrman, Nano Lett. 2019, 19, 6, 3663-3670, May 2, 2019, https://doi.org/10.1021/acs.nanolett.9b00729, 2019 American Chemical Society (Cornell University).

“Experimental and Numerical Study of Wicking in Porous Structure of Micro/Nano Channels”; S Poudel, A Zou, S Raut, S Maroo, ASME 2019 Summer Heat Transfer Conference, Bellevue, WA. (2019/7/16) (Syracuse University).

“Expitaxial Semiconductor/Superconductor Heterostructures”; B Downey, D Jena, D Katzer, G Khalsa, D Meyer, N Nepal, J Wright, HG Xing, R Yan, 8152-02-PC, Patent Cooperation Treaty, Filed 3/6/19 PCT/US19/20911 (Cornell).

“Extent of Cell Confinement in Microtracks Affects Speed and Results in Differential Matrix Strains”; J Mosier, A Rahman-Zaman, M Zanotelli, J VanderBurgh, F Bordeleau, B Hoffman, C Reinhart-King, Biophysical Journal, V 117, Issue 9, 5 November 2019, Pages 1692-1701, https://doi.org/10.1016/j.bpj.2019.09.024 (Cornell University).

“Fabricating Autonomous Machines for the Cellular Scale”; Miskin, Marc, Cortese, Alejandro, Cohen, Itai, McEuen, Paul, APS March Meeting 2019, abstract id.V64.005 (Cornell).

“Fabrication and Experimental Characterization of a MEMS Microphone Using Electrostatic Levitation”; M Ozdogan, S Towfighian and R Miles, 2019 IEEE Sensors, 27-30 Oct. 2019, DOI: 10.1109/sensors43011.2019.895687 (Binghamton).

“Fabrication of Resistive Thermo-Optic Heaters on Silicon Photonice Integreated Circuits”; V Deenadayalan, RIT Thesis (2019) (Rochester Institute of Technology).

“Fast Sn-ion transport on Nb surface for generating NbxSn thin films and XPS depth profiling”; Z. Sun, M. Liepe, J. T. Maniscalco, T. Oseroff, R. D. Porter, D. Zhang, X. Deng, Proceedings of North American Particle Accelerator Conference, 2019. (In press) (Cornell University).

“Ferroelectric properties of ion-irradiated bismuth ferrite layers grown via molecular-beam epitaxy”; A Mei, S Saremi, L Miao, M Barone, Y Tang, C Zeledon, J Schubert, D Ralph, L Martin, D Schlom, APL Materials, Vol. 7, Issue # 11, page(s) 111101 (Cornell University).

“Ferromagnetism and Conductivity in Atomically Thin SrRuO3”; Boschker, H., T. Harada, T. Asaba, R. Ashoori, A. V. Boris, H. Hilgenkamp, C. R. Hughes, M. E. Holtz, L. Li, D. A. Muller, H. Nair, P. Reith, X. Renshaw Wang, D. G. Schlom, A. Soukiassian, and J. Mannhart, Physical Review X 9, 011027, 8 Feb 2019 (Cornell University).

“Fiber-to-chip fusion splicing for low-loss photonic packaging”; J Nauriyal, M Song, R Yu, J Cardenas, Optica, Vol. 6, Issue # 5, page(s) 549-552 (University of Rochester).

“Field-Plated Ga2O3 Trench Schottky Barrier Diodes With a BV2/ Ron, sp of up to 0.95 GW/cm2”; W Li, K Nomoto, Z Hu, D Jena, HG Xing, IEEE Electron Device Letts, V: 41, Issue: 1, P 107-110, DOI: 10.1109/LED.2019.2953559 (Cornell).

“Field-plated Ga2O3 trench Schottky barrier diodes with a figure-of-merit of up to 0.95 GW/cm2”; W Li, K Nomoto, Z Hu, D Jena, and HG Xing, IEEE Electron Dev. Lett., 2019 (Cornell).

“Fin-channel orientation dependence of forward conduction in kV-class Ga2O3 trench Schottky barrier diodes”; Li, Wenshen, Nomoto, Kazuki, Hu, Zongyang, Jena, Debdeep, Xing, Huili Grace, Applied Physics Express, Vol. 12, Issue # 6, page(s) 61007 (Cornell University).

“Floating Gate Based Sensor Apparatus and Related Floating Gate Based Sensor Applications”; Krishna Jayant, Edwin Kan, 6365-03-US, United States, Issued, 12/4/15, 14/896, 010, 6/4/19, 10/309, 924 (Cornell University).

“From Spin Transfer Torque to Spin-Orbit Torques: Discoveries, Advances and Possibilities for Memory Technology”; Buhrman, R, Seminar, Korean Institute for Science & Technology, Seoul, Korea, Nov 2019 (Cornell).

“Fully Integrated Active Quenching Circuit Driving Custom-Technology SPADs With 6.2-ns Dead Time”; Ceccarelli, Francesco, Acconcia, Giulia, Gulinatti, Angelo, Ghioni, Massimo, Rech, Ivan, IEEE Photonics Technology Letters, Volume: 31, Issue: 1, Jan.1, 1 2019, Page(s): 102-105, DOI: 10.1109/LPT.2018.2884740 (Politecnico di Milano).

“Ga2O3 Power Schottky Barrier Diodes and Transistors: Design Principles and Experimental Validation”; HG Xing, W Li, Z Hu, N Tanen, R Jinno, K Nomoto, De Jena, 2019 Compound Semiconductor Week, 19-23 May 2019, Nara, Japan, DOI: 10.1109/ICIPRM.2019.8819233 (Cornell).

“GaN-Based FETs with Laterally-Gated Multi-2DEG Channels for High Power and Linearity”; K Shinohara, C King, E Regan, J Bergman, A Carter, A Arias, M Urteaga, B Brar, R Page, R Chaudhuri, Teledyne Scientific and Imaging Thousand Oaks United States., 25 Mar 2019, Full Text : https://apps.dtic.mil/dtic/tr/fulltext/u2/1075401.pdf (Cornell University).

“GaN-Based Multiple 2DEG Channel BRIDGE (Buried Dual Gate) HEMT Technology for High Power and Linearity”; K Shinohara, C King, E Regan, M Gomez, J Bergman, A Carter, A, Arias, M Urteaga, B Brar, Berinder, R Ryan, ECS Transactions, pgs 103-108, Issue 4, Vol 92 (2019) (Cornell University).

“GaN-on-AlN as a Superior Platform for Integrated Wide-bandgap Electronics”; SJ Bader, A Hickman, R Chaudhuri, K Nomoto, HG Xing, D Jena, 2019-apps.dtic.mil (unsafe website tho….) (Cornell University).

“Gate-Tunable Graphene Hall Sensors with High Magnetic Field Sensitivity”; B Schaefer, L Wang, A Jarjour, K Watanabe, T Taniguchi, P McEuen, and K Nowack, arXiv:1912.12678 [cond-mat.mes-hall] (Cornell University).

“GHz-THz Ultrasonics and Optics for Neurotechnology Devices, Methods and Apllications”; A Lal, A Singh, C Xu, 8282-02-PC, PCT-Patent Cooperation Treaty, Filed, 5/23/19, PCT/US19/33688 (Cornell University).

“Giant Enhancement of Spin-Orbit Torque by Interface Scattering from Ultra-thin Insertion Layers”; Robert Buhrman, Lijun Zhu, 8546-01-US, United States, MPR-Manuscript Provisional, Filed, 3/15/19, 62/819, 419 (Cornell University).

“Giant enhancement of spin-orbit torque by interface scattering from ultra-thin insertion layers”; R Buhrman, L Zhu, 8546, Filed by Cornell, 3/1/19, Invention (Cornell).

“Glycation of collagen matrices promotes breast tumor cell invasion”; Y Suh, M Hall, Y Huang, S Moon, W Song, M Ma, L Bonassar, J Segall, M Wu, Integrative Biology, V.11, Issue 3, March 2019, Pages 109-117, https://doi.org/10.1093/intbio/zyz011 (Cornell University).

“Graphene-based Hall sensors for scanning magnetic microscopy”; Schaefer, Brian, Wang, Lei, Jarjour, Alexander, Watanabe, Kenji, Taniguchi, Takashi, McEuen, Paul, Nowack, Katja, APS March Meeting 2019, abstract id.A12.008 (Cornell).

“Growth of PdCoO2 by ozone-assisted molecular-beam epitaxy”; J Sun, M Barone, C Chang, M Holtz, H Paik, J Schubert, D Muller, and D Schlom, APL Materials 7, 121112 (2019); https://doi.org/10.1063/1.5130627 (Cornell).

“Heterodyne-detected sum frequency generation of water at surfaces with varying hydrophobicity”; Stephanie E. Sanders and Poul B. Petersen, J. Chem. Phys. 150, 204708 (2019); https://doi.org/10.1063/1.5078587 (Cornell University).

“High Aspect Ratio Nanoneedles Hybrids for Intracellular Delivery”; Sungwoong Kim, Brian Rudd, Ankur Singh, 8769-01-US, United States, MPR-Manuscript Provisional, Filed, 5/10/19, 62/846, 219 (Cornell University).

“High Aspect Ratio Nanoneedles Hybrids for Intracellular Delivery”; Sungwoong Kim, Brian Rudd, Ankur Singh, 8769, Filed by Cornell, 5/10/19, Invention (Cornell University).

“High Breakdown Voltage in RF AlN/GaN/AlN Quantum Well HEMTs”; Hickman, Austin, Chaudhuri, Reet, Bader, Samuel James, Nomoto, Kazuki, Lee, Kevin, Xing, Huili Grace, Jena, Debdeep, IEEE Electron Device Letters, Vol. 40, Issue # 8, page(s) 1293-1296 (Cornell University).

“High index contrast photonic platforms for on-chip Raman spectroscopy”; Raza, Ali, Clemmen, Stéphane, Wuytens, Pieter, De Goede, Michiel, Tong, Amy SK, Le Thomas, Nicolas, Liu, Chengyu, Suntivich, Jin, Skirtach, Andre G., Garcia-Blanco, Sonia M., Optics express, Vol. 27, Issue # 16, page(s) 23067-23079 (Cornell University).

"High surface-area carbon microcantilevers"; Steven G. Noyce, Richard R. Vanfleet, Harold G. Craighead, and Robert C. Davis, Nanoscale Adv., 2019, 1, 1148-1154 DOI: 10.1039/C8NA00101D (Paper) (Brigham Young University).

"High Trap Stiffness Microcylinders for Nanophotonic Trapping"; Ryan P. Badman, Fan Ye, Wagma Caravan, Michelle D. Wang, ACS Appl. Mater. Interfaces 2019, 11, 28, 25074-25080; June 21, 2019; https://doi.org/10.1021/acsami.9b10041 (Cornell University).

"High Voltage Group III Trioxide Trench MOS Barrier Schottky and Methods of Fabricating Same"; Z Hu, D Jena, W Li, K Nomoto, HG Xing, 8418-02-PC, PCT-Patent Cooperation Treaty, Filed, 10/30/19, PCT/US19/58864 (Cornell).

"High-Frequency GaN Electronic Devices"; Patrick Fay, Debdeep Jena, Paul Maki, Editors, 2019-Springer (Cornell).

"High-Loading Composition-Tolerant Co-Mn Spinel Oxides with Performance beyond 1 W/cm2 in Alkaline Polymer Electrolyte Fuel Cells"; H Abruna, H Peng, L Xiao, Y Yang, L Zhuang, 8548, Filed by Cornell, 3/4/19, Invention (Cornell).

"High-mobility two-dimensional electron gas at (Al, Ga)GaN/GaN heterostructures grown on GaN bulk wafers and GaN template substrates"; Y Cho, Y Ren, HG Xing and D Jena, Appl. Phys. Express 12, 121003 (2019) (Cornell University).

"High-Overtone Bulk Diffraction Wave Gyroscope"; B Davaji, A Lal, V Pinrod, 8383-02-US, United States, MPR-Manuscript Provisional, Filed, 10/3/19, 62/909, 912 (Cornell University).

"High-overtone bulk diffraction wave gyroscope"; Pinrod, Visarute, Davaji, Benyamin, Lal, Amit, 2019 IEEE 32nd International Conference on Micro Electro Mechanical Systems (MEMS), IEEE, page(s) 202-205 (Cornell University).

"High-Q 2D Lithium Niobate Photonic Crystal Slab Nanoresonators"; M Li, H Liang, R Luo, Y He, Q Lin, Laser & Photonics Reviews, V.13, Issue 5, 07 April 2019, https://doi.org/10.1002/lpor.201800228 (University of Rochester).

"High-speed device synchronization in optical microscopy with an open-source hardware control platform"; Colville, Marshall J., Park, Sangwoo, Zipfel, Warren R., Paszek, Matthew J., BioRxiv, page(s) 533349 (Cornell University).

"High-throughput microfluidic micropipette aspiration device to probe time-scale dependent nuclear mechanics in intact cells"; P Davidson, G Fedorchak, S Mondésert-Deveraux, E Bell, P Isermann, D Aubry, R Allena, J Lammerding, BioRxiv, page(s) 641084 (Cornell University).

"High-Voltage β-Ga2O3 vertical Power Diodes and Transistors with Fin Channels"; W Li, Z Hu, K Nomoto, R Jinno, T Nakamura, D Jena, and HG Xing, ECS Meeting, Abstract MA2019-01 1267, Ultra-Wide Bandgap Materials and Devices-May 27 2019 (Cornell University).

"High-voltage, high-frequency aluminum nitride-based high-electron-mobility transistor"; S Bader, R Chaudhuri, A Hickman, SM Islam, D Jena, HG Xing, 8773, Filed by Cornell, 5/15/19, Invention (Cornell University).

"Highly Multiplexed Phylogenetic Imaging of Microbial Communities"; I De Vlaminck, H Shi, 8158-02-PC, Filed, 3/7/19, PCT/US2019/021088 (Cornell University).

"How Solutes Modify the Thermodynamics and Dynamics of Filling and Emptying in Extreme Ink-Bottle Pores"; O Vincent, J Zhang, E Choi, S Zhu, and A Stroock, Langmuir 2019, 35, 8, 2934-2947, January 25, 2019, https://doi.org/10.1021/acs.langmuir.8b03494 (Cornell University).

"Hybrid Quantum Systems and Qubit Correlation Spectroscopy for Quantum Sensing"; G Fuchs, Quantum Exchange Workshop, Quantum Sensing, Chicago, IL 2019 (Cornell University).

"Image-based Measurements of Biological Forces in a Dual Optical Trap"; J Inman, J Killian, M Wang, 8136-02-PC, Not Applicable (PCT App), PCT-Patent Cooperation Treaty, Filed, 4/5/19, PCT/US2019/26150 (Cornell University).

"Imaging uncompensated moments and exchange-biased emergent ferromagnetism in FeRh thin films"; Gray, Isaiah, Stiehl, Gregory M., Heron, John T., Mei, Antonio B., Schlom, Darrell G., Ramesh, Ramamoorthy, Ralph, Daniel C., Fuchs, Gregory D., arXiv preprint arXiv:1906.07243 (Cornell).

"Implantable Therapeutic Delivery System and Methods Thereof"; Duo An, James Flanders, Minglin Ma, 6480-03-US, United States, Issued, 12/9/16, 15/317, 657, 12/3/19, 10, 493, 107 (Cornell University).

"Implantable Therapeutic Delivery System and Methods Thereof"; Duo An, James Flanders, Minglin Ma, 6480-06-US, United States, CON-Continuation, Filed, 10/29/19, 16/666, 987 (Cornell University).

"Improving Hole Mobility in Electronic Devices"; Feliciano Giustino, Debdeep Jena, Samuel Ponce, 8816-01-GB, United Kingdom, FOR-Foreign, Filed, 7/29/19, 1910788.7 (Cornell).

"In Situ Stimulated Raman Spectroscopy Reveals the Phosphate Network in the Amorphous Cobalt Oxide Catalyst and Its Role in the Catalyst Formation"; Eom, C. J., J. Suntivich, The Journal of Physical Chemistry C 2019, 123, 48, 29284-29290, November 10, 2019, https://doi.org/10.1021/acs.jpcc.9b10308, 2019 American Chemical Society (Cornell).

"Integrated near-field thermo-photovoltaics for on-demand heat recycling"; G Bhatt, B Zhao, S Roberts, I Datta, A Mohanty, T Lin, J Hartmann, R St-Gelais, S Fan, M Lipson, arXiv:1911.11137 [physics.app-ph] (Columbia University).

"Interactions between single defect centers and phonons"; Fuchs, G., International Conference on Defects in Semiconductors, Seattle, WA 2019 (Cornell University).

"Intermittent Acoustic Perturbations to Maintain the Dethickened State of a Shear Thickening Suspension"; Itai Cohen, Brian Kirby, Meera Ramaswamy, Prateek Sehgal, 8497, Filed by Cornell, 1/21/19, Invention (Cornell University).

"Internal ion-gated organic electrochemical transistor: A building block for integrated bioelectronics"; George D. Spyropoulos, Jennifer N. Gelinas, and Dion Khodagholy, Science Advances 27 Feb 2019, Vol. 5, no. 2, eaau7378, DOI: 10.1126/sciadv.aau7378 (Columbia University).

"Intrinsic Conductance of Domain Walls in BiFeO3"; Y Zhang, H Lu, X Yan, X Cheng, L Xie, T Aoki, L Li, C Heikes, S Lau, D Schlom, L Chen, A Gruverman, X Pan, Advanced Materials, V.31, Issue 36, Sept 6, 2019, 1902099, 28 July 2019, https://doi.org/10.1002/adma.201902099 (Cornell University).

"Investigation of Scale Factor versus Frequency for a Bulk Wave Diffraction Gyroscope"; V Pinrod, B Davaji, A Lal, 2019 IEEE International Symposium on Inertial Sensors and Systems (INERTIAL), IEEE, page(s) 1-2 (Cornell University).

"Iridium Electrodes for Hexagonal Ferroelectrics"; Megan Holtz, Darrell Schlom, Rachel Steinhardt, 9189, Filed by Cornell, 9/19/19, Invention (Cornell University).

"Lagrangian and Impedance-Spectroscopy Treatments of Electric Force Microscopy"; R. P. Dwyer, L. E. Harrell, and J. A. Marohn, Physical Review Appl., 2019, 11, 064020, URL http://dx.doi.org/10.1103/PhysRevApplied.11.064020, available at https://arxiv.org/abs/1807.01219 (Cornell University).

"Large-area, single material metalens in the visible: An approach for mass-production using conventional semiconductor manufacturing techniques"; J Park, S Zhang, A She, W Chen, K Yousef, and F Capasso, CLEO 2019, San Jose, CA. May 5-10, 2019. (Harvard University).

"Large-scale fabrication of submicron-gate-length MOSFETs with a trilayer PtSe2 channel grown by molecular beam epitaxy"; K. Xiong, M. Hilse, L. Li, A. Göritz, M. Lisker, M. Wietstruck, M. Kaynak, R. Engel-Herbert, A. Madjar, and J. C. M. Hwang, IEEE Trans. Electron Devices. (Lehigh University).

"Lattice Matched Substrate with Perovskite Structure for Epitaxial Growth of BaSnO3 and related Materials for Electronics"; M Bratzam, C Guguschev, H Paik, D Schlom, 8544, Filed by Joint Owner, 2/22/19, Invention (Cornell).

"Layer-dependent spin-orbit torques generated by the centrosymmetric transition metal dichalcogenide B-MoTe2"; G Stiehl, R Li, V Gupta, I El Baggari, S Jiang, H Xie, L Kourkoutis, K Mak, J Shan, R Buhrman, Physical Review B 100, 184402 (2019) https://doi.org/10.1103/PhysRevB.100.184402 (Cornell University).

"Light and Substrate Dependent Electron and Ion Motion in Lead Halide Perovskite"; A. M. Tirmzi, J. A. Christians, R. P. Dwyer, D. T. Moore, and J. A. Marohn, American Chemical Society Northeast Regional Meeting; Saratoga, NY; June 23-26, 2019, URL https://www.acsnerm.org/ (Cornell University).

"Light emitting diodes using ultra-thin quantum heterostructures"; SM Islam, V Protasenko, HG Xing, D Jena, J Verma, US20190148584A1 United States, 2019-02-04 Assigned to Cornell University, 2019-05-16 Publication of US20190148584A1 (Cornell University).

"Light Patternable Mesoporous Material"; T Hanrath, J Huang, H Liu, 8638, Filed by Cornell, 4/9/19, Invention (Cornell).

"Light Patternable of Inorganic Materials"; T Hanrath, J Huang, H Liu, 8638-01-US, United States, Enhanced Provisional, Filed, 6/25/19, 62/865, 722 (Cornell University).

"Light Patterning of Silica Nanocage Materials"; T Aubert, T Hanrath, J Huang, U Wiesner, 9174-01-US, United States, Manuscript Provisional Filed 11/1/19, 62/929, 470 (Cornell).

"Light-Induced Currents at Domain Walls in Multiferroic BiFeO3"; B. Guzelturk, A.B. Mei, L. Zhang, L.Z. Tan, P. Donahue, A.G. Singh, D.G. Schlom, L.W. Martin, and A. M. Lindenberg, Nano Lett. 2020, 20, 1, 145-151, November 20, 2019, https://doi.org/10.1021/acs.nanolett.9b03484 (Cornell University).

"Local Photothermal Control of Phase Transitions for On-demand Room-temperature Rewritable Magnetic Patterning"; Mei, A.B., Gray, I., Tang, Y., Schubert, J., Werder, D., Bartell, J., Ralph, D.C., Fuchs, G.D., Schlom, D.G., arXiv preprint arXiv:1906.07239 (Cornell University).

"Local, transient heat transfer measurements for flow boiling in a microchannel with a pin fin"; Y Wang, J Shin, C Woodcock, X Yu, Y Peles, International J of Heat & Mass Transfer, V.134, May 2019, p 377-387, https://doi.org/10.1016/j.ijheatmasstransfer.2019.01.048 (University of Central FL).

"Long valley lifetime of dark excitons in single-layer WSe2"; Yanhao Tang, Kin Fai Mak, and Jie Shan, Nature Communications, 2019; 10: 4047, Published online 2019 Sep 6. doi: 10.1038/s41467-019-12129-1 (Cornell University).

"Loss of sirtuin 1 alters the secretome of breast cancer cells by impairing lysosomal integrity"; A Latifkar, L Ling, A Hingorani, E Johansen, A Clement, X Zhang, J Hartman, C Fischbach, H Lin, R Cerione, Developmental cell, Vol. 49, Issue # 3, page(s) 393-408 (Cornell University).

"Low energy photoemission from (100) Ba 1- x La x SnO 3 thin films for photocathode applications"; A Galdi, C Pierce, L Cultrera, G Adhikari, W Schroeder, H Paik, D Schlom, J Nangoi, T Arias, E Lochocki, The European Physical Journal Special Topics, Vol. 228, Issue # 3, page(s) 713-718 (Cornell).

"Low-loss composite photonic platform based on 2D semiconductor monolayers"; I Datta, S Chae, G Bhatt, M Tadayon, B Li, Y Yu, C Park, J Park, L Cao, D Basov, J Hone, M Lipson, arXiv:1906.00459 (2 Jun 2019) (Columbia).

"Magnetic Manipulation Using Spin-Orbit Torque"; Ralph, D. C., Semiconductor Research Corporation e-Webinar, May 13, 2019 (Cornell University).

"Magnetic Separation of Biological Entities from Fluid Sample Using Sleeve Device"; D Erickson, S Vemulapati, 8323-03-USA, Provisional Filed 7/22/19, 62/877, 293 (Cornell University).

"Magnetic Separation of Biological Entities from Fluid Sample"; D Erickson, S Vemulapati, 8323-02-PC, Patent Cooperation Treaty 7/22/19, PCT/US2019/42887 (Cornell).

"Materials and Computing at Cornell"; Christopher K. Ober, Tokyo Tech, Tokyo, Japan, Feb. 14, 2019 (Cornell University).

"Materials Relevant to Realizing a Field-Effect Transistor based on Spin-Orbit Torques"; P Dang, Z Zhang, J Casamento, X Li, J Singhal, D Schlom, D Ralph, H Xing, D Jena, arXiv:1912.11715 (25 Dec 2019) (Cornell).

"Materials Systems for 2-Photon Lithography"; Christopher K. Ober, 3D microfabrication using two-photon polymerization - 2nd ed., Tomasso Baldachini, ed., Elsevier, 2019 (Cornell).

"Maximizing Spin-Orbit-Torque Efficiency of Pt/Ti Multilayers: Trade-Off Between Intrinsic Spin Hall Conductivity and Carrier Lifetime"; Zhu, Lijun, Buhrman, R. A., Physical Review Applied, V. 12, # 5, page(s) 51002 (Cornell).

"Maximizing the spin-orbit torque efficiency of Pt/Ti multilayers by optimization of the tradeoff between the intrinsic spin Hall conductivity and carrier lifetime"; L Zhu, R Buhrman, arXiv preprint arXiv:1908.06528 (Cornell).

“Mechanical Stress Compromises Bacterial Toxin Efflux”; Genova, L.A., Roberts, M.F., Wong, Y-C, Harper, C.E., Santiago, A.G., Fu, B., Srivastava, A., Jung, W., Kreminski, L., Mao, X., Sun, X., Yang, F., Hui, C-Y, Chen, P, Hernandez, C.J., PNAS December 17, 2019 116 (51) 25462-25467; first published Nov 26, 2019 https://doi.org/10.1073/pnas.1909562116 (Cornell).

“Mechanical stress compromises multicomponent efflux complexes in bacteria”; Genova, L., M.Roberts, Y.Wong, C.Harper, A.Santiago, B.Fu, A.Srivastava, W.Jung, L.Wang, Ł.Krzemiński, X.Mao, X.Sun, C.Hui, P.Chen, and C.Hernandez, PNAS December 17, 2019 116 (51) 25462-25467; first published November 26, 2019 https://doi.org/10.1073/pnas.1909562116 (Cornell University).

“Mechanical stress compromises multicomponent efflux complexes in bacteria”; Genova, Lauren A., Roberts, Melanie F., Wong, Yu-Chern, Harper, Christine E., Santiago, Ace George, Fu, Bing, Srivastava, Abhishek, Jung, Won, Wang, Lucy M., Krzemiński, Lukasz, bioRxiv, page(s) 571398 (Cornell).

“MEMS-in-the-lens 3D beam scanner for in vivo microscopy”; Dickensheets, David L., Liu, Tianbo, Rajadhyaksha, Milind, MOEMS and Miniaturized Systems XVIII, International Society for Optics and Photonics, Vol. 10931, page(s) 1093110 (Montana State University).

“MEMS-in-the-lens architecture for a miniature high-NA laser scanning microscope”; Tianbo Liu, Milind Rajadhyaksha, and David L. Dickensheets, Light: Science & Applications volume 8, Article number: 59 (2019), https://www.nature.com/articles/s41377-019-0167-5 (Montana State University).

“Metal Organic Cluster Photoresists for EUV Lithography in Cornell’s CNF, the original NSF supported nanofabrication facility”; Christopher K. Ober, IBM Almaden, invited talk, Almaden, CA, Jan. 22, 2019 (Cornell University).

“Metal Organic Cluster Photoresists for EUV Lithography”; Sakai, K, Jung, SH, Pan, WY, Giannelis, EP, Ober, CK, Journal of Photopolymer Science and Technology, 2019, 32(5), 711-714; DOI: 10.2494/photopolymer.32.711 (Cornell University).

“Metal organic cluster photoresists for next generation EUV lithography”; Christopher K. Ober, Bayreuth Polymer Symposium, invited talk, Universität Bayreuth, Bayreuth, Germany, September 21-24, 2019 (Cornell University).

“Metal organic cluster photoresists: new metal oxide systems”; Sakai, K, Jung, SH, Pan, W, Giannelis, EP, Ober, CK, Advanced Etch Technology For Nanopatterning VIII, Wise, RS; Labelle, CB, eds. Proceedings of SPIE, 2019, 10963, 1096306, DOI: 10.1117/12.2515148 (Cornell University).

“Metal organic cluster resists: new metal oxide systems for microlithography”; Christopher K. Ober, Facebook, invited talk, Redmond, WA, August 27, 2019 (Cornell University).

“Metal oxide nanoparticles and MOF-inspired clusters for microlithography”; Christopher K. Ober, 258th ACS National Meeting, invited talk, San Diego, CA, August 25 to 29, 2019 (Cornell University).

“Method for improving the hole mobility of electronic devices based on GaN”; Feliciano Giustino, Debdeep Jena, Samuel Ponce, 8816, Filed by Cornell, 6/14/19, Invention (Cornell).

“Microfluidic Device, System, and Method for Tracking Single Cells and Single Cell Lineages”; David Erickson, Michael Mak, 5947-03-US, United States, Issued, 12/8/14, 14/406, 310, 1/1/19, US10168317B2 United States, 2019-01-01 Publication of US10168317B2, 2019-01-01 Application granted (Cornell University).

“Microfluidic Platform for the Concentration and Detection of Bacterial Populations in Liquid”; L Alonzo, S Garing, A Le Ny, K Nichols, S Nugen, J Williford, 8095-02-PC, Patent Cooperation Treaty, Filed, 1/10/19, PCT/US19/12979 (Cornell University).

“Mobile device enabled point-of-care quantification of cancer biomarkers”; David Erickson, Saurabh Mehta, Balaji Ventkatesh, 9286, Unfiled, 12/17/19, Invention (Cornell).

“Mobile device enabled point-of-care quantification of nutrition and inflammation biomarkers using saliva or urine”; David Erickson, Julia Finkelstein, Bryan Gannon, Marshall Glesby, Saurabh Mehta, Balaji Ventkatesh, 9285, Unfiled, 12/17/19, Invention (Cornell University).

“Mobile device enabled point-of-care test for screening birth defects”; David Erickson, Saurabh Mehta, Balaji Ventkatesh, 9287, Unfiled, 12/17/19, Invention (Cornell University).

“Mode Structure in Superconducting Metamaterial Transmission-Line Resonators”; H Wang, A Zhuravel, S Indrajeet, B Taketani, M Hutchings, Y Hao, F Rouxinol, F Wilhelm, M LaHaye, A Ustinov, B Plourde, Phys Rev Applied 11, 054062, 22 May 2019, DOI: https://doi.org/10.1103/PhysRevApplied.11.054062 (Syracuse University).

“Modeling and Circuit Design of Associative Memories with Spin Orbit Torque FETs”; Afuye, Olalekan, Li, Xiang, Guo, Felicia, Jena, Debdeep, Ralph, Daniel C., Molnar, Alyosha, Xing, Huili Grace, Apsel, Alyssa, IEEE Journal on Exploratory Solid-State Computational Devices and Circuits, 08 November 2019, Page(s): 1-1, DOI: 10.1109/JXCDC.2019.2952394 (Cornell).

“Modular Fabrication Systems and Methods”; Lawrence Bonassar, Daniel Cohen, Hod Lipson, Evan Malone, 3527-10-US, United States, Issued, 6/29/18, 16/023, 153, 9/10/19, 10/406, 262 (Cornell University).

“Modular Fabrication Systems and Methods”; L Bonassar, D Cohen, H Lipson, E Malone, 3527-11-USA, CON-Continuation, Prosecution, 7/31/19, 16/528, 593 (Cornell University).

“Molecular beam epitaxial growth of scandium nitride on hexagonal SiC, GaN, and AlN”; Joseph Casamento, John Wright, Reet Chaudhuri, Huili (Grace) Xing, and Debdeep Jena, Appl. Phys. Lett. 115, 172101 (2019); https://doi.org/10.1063/1.5121329 (Cornell University).

“Molecular Beam Epitaxy of Transition Metal Nitrides for Superconducting Device Applications”; D.Katzer, N.Nepal, M.Hardy, B.Downey, D.Storm, E.Jin, R.Yan, G.Khalsa, J.Wright, A.Lang, T.Growden, V.Gokhale, V.Wheeler, A.Kramer, J.Yater, H.Xing, D.Jena, D.Meyer, Physica status solidi (a), 12 October 2019 https://doi.org/10.1002/pssa.201900675 (Cornell).

“Monolithic pzt actuator, stage, and method for making”; A Lal, S Nadig, S Ardanuc, US20190214543A1 United States, 2019-07-11 Publication of US20190214543A1 (Cornell).

"MoS2 pixel arrays for real-time photoluminescence imaging of redox molecules"; M Reynolds, M Guimarães, H Gao, K Kang, A Cortese, D Ralph, J Park, P McEuen, Science Advances, 08 Nov 2019, V. 5, #11, eaat9476, DOI: 10.1126/sciadv.aat9476 (Cornell University).

"Motion sensor integrated nano-probe n/mems apparatus, method, and applications"; A Lal, K Amponsah, 2019-01-17 Publication of US20190018039A1 (Cornell University).

"Multi Kilovolt Lithium Niobate Pyroelectric Cantilever Switched Power Supply"; D Ni, K Vinayakumar, V Pinrod, A Lal, IEEE 32nd International Conf on MEMs, Jan. 2019, pgs 970-973, DOI: 10.1109/MEMSYS.2019.8870799 (Cornell).

"Multi-phase, non-isothermal transfer of water in a simple geometry"; Lidon, Pierre, Perrot, Etienne, Stroock, Abraham D., arXiv preprint arXiv:1902.04468 (Cornell University).

"Multi-Photon Wavefront Sensor, Methods and Applications"; D Sinefeld, F Xia, C Xu, 7709-03-US, United States, US from PCT, Filed, 8/6/19, 16/483, 971 (Cornell University).

"Multi-Photon Wavefront Sensor, Methods and Applications"; D Sinefeld, F Xia, C Xu, 7709-04-EP, Europe, European Patent Convention, Filed, 9/6/19, 18753686.7 (Cornell University).

"Multiomic Analysis of cell Analytes using Microfluidic Systems"; A Bisogni, H Craighead, D Lin, H Tian, 8443-02-PC, Not Applicable (PCT App), PCT-Patent Cooperation Treaty, Filed, 11/29/19, PCT/US2019/063866 (Cornell University).

"Multiorgan microfluidic platform with breathable lung chamber for inhalation or intravenous drug screening and development"; Miller, PG, Chen, CY, Wang, Y, Gao, E, Shuler, ML, Biotechnology and Bioengineering, V: 117, #: 2, P 486-497, DOI: 10.1002/bit.27188, Early Access: NOV 2019 (Cornell).

"Mutant lamins cause nuclear envelope rupture and DNA damage in skeletal muscle cells"; A Earle, T Kirby, G Fedorchak, P Isermann, J Patel, S Iruvanti, S Moore, G Bonne, L Wallrath, J Lammerding, Nature Materials doi: 10.1038/s41563-019-0563-5, Posted March 23, 2019 (Cornell).

"Myosin IIA suppresses glioblastoma development in a mechanically sensitive manner"; H.Picariello, R.Kenchappa, V.Rai, J.Crish, A.Dovas, K.Pogoda, M.McMahon, E.Bell, U.Chandrasekharan, A.Luu, R.West, J.Lammerding, P.Canoll, D.Odde, P.Janmey, T.Egelhoff, and S.Rosenfeld, Proceedings of the National Academy of Sciences, p 201902847 (Cornell).

"Nano-scale Photoemission Based Electron Sources for Electron Microscopy"; S Karkare, J Maxson, H Padmore, 9289, Unfiled, 12/19/19, Invention (Cornell University).

"Nanosecond Reversal of Three-Terminal Spin Hall Effect Memories Sustained at Cryogenic Temperatures"; G Rowlands, M Nguyen, S Aradhya, S Shi, C Ryan, R Buhrman, T Ohki, arXiv:1909.10613 (23 Sep 2019) (Cornell).

"Nanosecond- Timescale Low- Error Switching of 3-Terminal Magnetic Tunnel Junction Circuits through Dynamic In-Plane- Field Assisted Spin-Hall Effect"; S Aradhya, R Buhrman, D Ralph, G Rowlands, 7376-02-US, United States, Issued, 3/17/17, 15/462, 760, 6/25/19, US Patent 10333058B2, 2019-06-25 Publication of US10333058B2 (Cornell).

"Nanostructured Stable Radical Polymer Thin Films: A Battery Electrode Material"; Khurana, Mohit Ravi, Cornell University, ProQuest Dissertations, 2019. 22592073. (Cornell).

"Narrow-linewidth, tunable external cavity dual-band diode lasers through InP/GaAs-Si 3 N 4 hybrid integration"; Zhu, Yeyu, Zhu, Lin, Optics express, Vol. 27, Issue # 3, page(s) 2354-2362 (Clemson University).

"NEMS Electrostatic Resonant Near-Zero Power Resistive Contact RF Wake-Up Switch with PT FIB Contact"; A Ruyack, B Davaji, L Pancoast, N Shalabi, A Molnar, A Lal, 2019 IEEE 32nd International Conf on MEMS, IEEE, page(s) 129-132 (Cornell).

"NEMS Electrostatic RF Wakeup Switch with Pt FIB Contact"; A Ruyack, L Pancoast, N Shalabi, A Molnar and A Lal, J. Phys.: Conf. Ser.1407 012077 (Cornell University).

"Neuromorphic Event-driven Neural Computing Architecture in a Scalable Neural Network"; F Akopyan, J Arthur, R Manohar, P Merolla, D Modha, A Molnar, W Risk, 5586-03-US, Issued 1/6/16, 14/989,579, 12/10/19, 10,504,021 (Cornell).

"New Physics in GaN Resonant Tunneling Diodes"; HG Xing, J Encomendero, D Jena, Gallium Nitride Materials and Devices XIV, International Society for Optics and Photonics, Vol. 10918, page(s) 109180Z (Cornell University).

"Nitride LEDs and Lasers with Buried Tunnel Junctions"; Turski, H, Siekacz, M, Muziol, G, Hajdel, M, Stanczyk, S, Zak, M, Chlipala, M, Skierbiszewski, C, Bharadwaj, S, Xing, HG, Jena, D, ECS Journal of Solid State Science and Technology, V.9, Issue: 1, # 015018, DOI: 10.1149/2.0412001JSS, DEC 5 2019 (Cornell University).

"Non-Planar Electrodes, Method of Making Same, and Uses Thereof"; L Archer, Q Zhao, J Zheng, 8470-01-US, Enhanced Provisional, Filed, 4/19/19, 62/836, 486 (Cornell University).

"Non-reversible tissue fixation retains extracellular vesicles for in situ imaging"; Gupta, Mrinali P., Tandalam, Sangeetha, Ostrager, Shariss, Lever, Alexander S., Fung, Angus R., Hurley, David D., Alegre, Gemstonn B., Espinal, Jasmin E., Remmel, H. Lawrence, Mukherjee, Sushmita, Nature methods, page(s) 1-5 (Cornell University).

"Non-thermal fluence threshold for femtosecond pulsed x-ray radiation damage in perovskite complex oxide epitaxial heterostructures"; H.J. Lee, Y. Ahn, S.D. Marks, E.C. Landahl, J.Y. Lee, T.Y. Kim, S. Unithrattil, J.Y. Jo, S.H. Chun, S. Kim, S.-Y. Park, I. Eom, C. Adamo, D.G. Schlom, H. Wen, and P.G. Evans, Applied Physics Letters, DOI: 10.1063/1.5128509 (Cornell).

"Nonlinear anomalous Hall effect in few-layer WTe2"; K. Kang, T. Li, E. Sohn, J. Shan, and K. F. Mak, Nature Mater. 18, 324-328 (2019) http://dx.doi.org/10.1038/s41563-019-0294-7 (Cornell University).

"Nonlinear Ultrafast Fiber Amplifiers"; W Fu, P Sidorenko, F Wise, 8528-01-US, United States, MPR-Manuscript Provisional, Filed, 7/9/19, 62/872, 178 (Cornell University).

"Novel sample preparation method for single-electron magnetic resonance detection and imaging"; M. C. Boucher, 2019 American Chemical Society Northeast Regional Meeting, Saratoga, NY; June 26, 2019 (Cornell University).

“Observation of live cells’ attachment, spreading, and drug interactions using metasurface-enhanced infrared reflection spectroscopy”; Huang, Steven H., Gupta, Shourya Dutta, Delgado, Robert, Kelp, Glen, Hume, Kelly, Shvets, Gennady, Optical Biopsy XVII: Toward Real-Time Spectroscopic Imaging and Diagnosis, International Society for Optics and Photonics, Vol. 10873, page(s) 108730V (Cornell University).

“Observation of Strong Polarization Enhancement in Ferroelectric Tunnel Junctions”; Li L., X. Cheng, T. Blum, H. Huyan, Y. Zhang, C. Heikes, X. Yan, C. Gadre, T. Aoki, M. Xu, L. Xie, Z. Hong, C. Adamo, D.G. Schlom, L.-Q. Chen, X. Pan, Nano Lett. 2019, 19, 10, 6812-6818, September 11, 2019, https://doi.org/10.1021/acs.nanolett.9b01878, 2019 American Chemical Society (Cornell University).

“Omnidirectional low frequency energy harvester for wearable applications”; C Ou, V Pinrod, B Davaji and A Lal, Journal of Physics: Conference Series, Volume 1407, conference 1, 1407 012122 (Cornell University).

“On-chip tunable photonic delay line”; Ji, Xingchen, Yao, Xinwen, Gan, Yu, Mohanty, Aseema, Tadayon, Mohammad A., Hendon, Christine P., Lipson, Michal, APL Photonics, Vol. 4, Issue # 9, page(s) 90803 (Columbia University).

“Optical lace for synthetic afferent neural networks”; Xu, Patricia A., Mishra, A. K., Bai, H., Aubin, C. A., Zullo, L., Shepherd, R. F., Science robotics, eaaw6304, Vol. 4, Issue # 34 (Cornell University).

“Optical Parametric Generation in a Lithium Niobate Microring with Modal Phase Matching”; Luo, Rui, He, Yang, Liang, Hanxiao, Li, Mingxiao, Ling, Jingwei, Lin, Qiang, Physical Review Applied, Published 11 March 2019, Vol. 11, Issue # 3, page(s) 34026 (University of Rochester).

“Optofluidic Photobioreactor Apparatus, Method, and Applications”; David Erickson, David Sinton, 5200-04-EP, Europe, Issued, 7/12/13, 11841822.7, 9/11/19, 2640826 (Cornell University).

“Optofluidic Photobioreactor Apparatus, Method, and Applications”; David Erickson, David Sinton, 5200-07-FR, France, Issued, 7/12/13, EP11841822.7, 9/11/19, EP2640826 (Cornell University).

“Optofluidic Photobioreactor Apparatus, Method, and Applications”; David Erickson, David Sinton, 5200-08-DE, Germany, Issued, 7/12/13, EP11841822.7, 9/11/19, EP2640826 (Cornell University).

“Optofluidic Photobioreactor Apparatus, Method, and Applications”; David Erickson, David Sinton, 5200-09-GB, United Kingdom, Issued, 7/12/13, EP11841822.7, 9/11/19, EP2640826 (Cornell University).

“Ordered Si Micropillar Arrays via Carbon-Nanotube-Assisted Chemical Etching for Applications Requiring Nonreflective Embedded Contacts”; T Wilhelm, I Kecskes, M Baboli, A Abrand, M Pierce, B Landi, I Puchades, and P Mohseni, ACS Appl. Nano Mater. 2019, 2, 12, 7819-7826, Nov 6, 2019, https://doi.org/10.1021/acsanm.9b01838 (RIT).

“Origin and Evolution of Microlayer in Pool Boiling”; A Zou, M Gupta, S Maroo, ASME 2019 Summer Heat Transfer Conference, Bellevue, WA. (2019/7/15) (Syracuse University).

“Oxygen Incorporation in the Molecular Beam Epitaxy Growth of ScxGa1-xN and ScxAl1-xN”; Joseph Casamento, Huili Grace Xing, Debdeep Jena, Phys. Status Solidi B2020, 1900612 DOI: 10.1002/pssb.201900612 (Cornell University).

“Pathogenic Bacteria Detection Using RNA-Based Loop-Mediated Isothermal-Amplification-Assisted Nucleic Acid Amplification via Droplet Microfluidics”; M Azizi, M Zaferani, S Cheong, and A Abbaspourrad, American Chemical Society Sens. 2019, 4, 4, 841-848, March 25, 2019, https://doi.org/10.1021/acssensors.8b01206 (Cornell University).

“Perfect soliton crystals on demand”; He, Yang, Ling, Jingwei, Li, Mingxiao, Lin, Qiang, arXiv preprint arXiv:1910.00114 (University of Rochester).

“Performance of CVD diamond single crystals as side-bounce monochromators in the Laue geometry at high photon energies”; S. Stoupin, T. Krawczyk, J.P.C. Ruff, K.D. Finkelstein, H.H. Lee, and R.Huang (acknowledges Chris Alpha, CNF Staff), AIP Conference Proceedings, V.2054, Issue 1, id.060019, Jan 2019, DOI: 10.1063/1.5084650 (Cornell University).

“Photon acceleration and tunable broadband harmonics generation in nonlinear time-dependent metasurfaces”; Shcherbakov, M, Werner, K, Fan, Z, Talisa, N, Chowdhury, E, Shvets, G, Nature communications, Vol. 10, Issue # 1, page(s) 1345 (Cornell University).

“Physical Principles of Membrane Shape Regulation by the Glycocalyx”; C.Shurer, J.Kuo, L.Roberts, J.Gandhi, M.Colville, T.Enoki, H.Pan, J.Su, J.Noble, M.Hollander, J.O’Donnell, R.Yin, K.Pedram, L.Möck, L.Kourkoutis, W.Moerner, C.Bertozzi, G.Feigenson, H.Reesink, M.Paszek, Cell, Volume 177, Issue 7, 13 June 2019, Pages 1672-1674, https://doi.org/10.1016/j.cell.2019.04.017 (Cornell University).

“Piezoelectric bioMEMS cantilever for measurement of muscle contraction and for actuation of mechanosensitive cells”; E Coln, A Colon, C Long, N Srira, M Esch, J Prot, D Elbrecht, Y Wang, M Jackson, M Shuler, and J Hickman, Materials Research Society 2019, DOI: https://doi.org/10.1557/mrc.2019.129 Cambridge University Press: 27 Sept 2019 (Cornell).

“Planar GHz Ultrasonic Lens for Fourier Ultrasonics”; Juneho Hwang, Justin Kuo, Amit Lal, 2019 IEEE International Ultrasonics Symposium (IUS), 6-9 Oct. 2019, Glasgow, United Kingdom, United Kingdom; DOI: 10.1109/ULTSYM.2019.8925662 (Cornell University).

“Plasmonic metasurfaces with 42.3% transmission efficiency in the visible”; Zhang, J, ElKabbash, M, Wei, R, Singh, S, Lam, B, Guo, C, Light: Science & Applications, Vol. 8, Issue # 1, page(s) 53 (University of Rochester).

“Platforms Enabled by Buried Tunnel Junction for Integrated Photonic and Electronic Systems”; Shyam Bharadwaj, Alexander Chaney, Debdeep Jena, Kazuki Nomoto, Henryk Turski, Huili Grace Xing, 8026-02-PC, Not Applicable (PCT App), PCT-Patent Cooperation Treaty, Filed, 1/31/19, PCT/2019/015991 (Cornell University).

“Polarization control in nitride quantum well light emitters enabled by bottom tunnel-junctions”; Turski, H, Bharadwaj, S, Xing, H, Jena, D, Journal of Applied Physics, Vol. 125, Issue # 20, page(s) 203104 (Cornell University).

“Polarization field assisted heterostructure design for efficient deep ultra-violet light emitting diodes”; SM Islam, V Protasenko, H Xing, D Jena, US20190148593A1 United States, 2019-05-16 Publication of US20190148593A1 (Cornell).

“Polarization sensitive black phosphorus nanomechanical resonators”; Arnob Islam, Anno van den Akker, and Philip X.-L. Feng, Optical Materials Express Vol. 9, Issue 2, pp. 526-535 (2019) https://doi.org/10.1364/OME.9.000526 (Case Western Reserve University).

“Polarization states synthesizer based on a thermo-optic dielectric metasurface”; Bosch, M., Shcherbakov, M. R., Fan, Z., Shvets, G., Journal of Applied Physics, Vol. 126, Issue # 7, page(s) 73102 (Cornell University).

“Polarization-induced 2d Hole Gases for High-Voltage p-channel Transistors”; Samuel Bader, Reet Chaudhuri, Debdeep Jena, Huili Grace Xing, 8340-02-PC, Not Applicable (PCT App), PCT-Patent Cooperation Treaty, Filed, 7/19/19, PCT/US19/42584 (Cornell University).

“Polymer Brushes on Hexagonal Boron Nitride”; W.Sheng, I.Amin, C.Neumann, R.Dong, T.Zhang, E.Wegener, W.Chen, P.Förster, H.Tran, M.Löffler, A.Winter, R.Rodriguez, E.Zschech, C.Ober, X.Feng, A.Turchanin, R.Jordan, Small, Vol. 15, Issue # 19, page(s) 1805228 (Cornell University).

“Pool Boiling Coupled with Nanoscale Evaporation Using Buried Nanochannels”; Zou, An, Poudel, Sajag, Raut, Sidharth P., Maroo, Shalabh C., Langmuir, Vol. 35, Issue # 39, page(s) 12689-12693 (Syracuse University).

“Porous Zero-Mode Waveguides for Picogram-Level DNA Capture”; Jadhav, V; Hoogerheide, D; Korlach, J; Wanunu, M; Nano Lett. 2019, 19, 2, 921-929, https://doi.org/10.1021/acs.nanolett.8b04170 (Northeastern University).

“PP2A inhibitor PME-1 suppresses anoikis, and is associated with therapy relapse of PTEN-deficient prostate cancers”; C.Rupp, A.Aakula, A.Isomursu, A.Erickson, O.Kauko, P.Shah, A.Padzik, A.Kaur, S.Li, Y.Pokharel, L.Trotman, A.Rannikko, P.Taimen, J.Lammerding, I.Paatero, T.Mirtti, J.Ivaska, J.Westermarck, bioRxiv, page(s) 581660 (Cornell University).

“Programmable self-assembly of magnetic handshake materials”; Niu, Ran, Esposito, Edward, Du, Chrisy, Wang, Wei, Ng, Jakin, Brenner, Michael, McEuen, Paul, Cohen, Itai, APS March Meeting 2019, abstract id.S61.002 (Cornell University).

“Puzzling Perovskite Photoconductivity Dynamics Revealed by Scanned Probe Measurements of Electric Force Gradients, Dissipation, and Impedance Spectra”; J. A. Marohn, A. M. Tirmzi, R. P. Dwyer, L. E. Harrell, R. Cohn, J. A. Christians, D. T. Moore, F. Jiang, J. Precht, R. Giridharagopal, and D. Ginger, Materials Research Society Fall Meeting; Boston, Massachusetts; December 1-6, 2019, URL https://www.mrs.org/fall2019/symposium-sessions/symposium-sessions-detail?code=EN09 (Cornell University).

“Quantum Transport in 2DEGs in Epitaxial GaN Quantum Wells on Superconducting NbN”; Dang, Phillip, Khalsa, Guru, Katzer, D., Nepal, Neeraj, Downey, Brian, Suslov, Alexey, Xing, Huili, Meyer, David, Jena, Debdeep, APS March Meeting 2019, abstract id.Y08.015 (Cornell University).

“Rabi oscillations and resonance fluorescence from a single hexagonal boron nitride quantum emitter”; Kumarasiri Konthasinghe, Chitraleema Chakraborty, Nikhil Mathur, Liangyu Qiu, Arunabh Mukherjee, Gregory D. Fuchs, and A. Nick Vamivakas, Optica 6, 542 (2019). https://doi.org/10.1364/OPTICA.6.000542 (Cornell University).

“Radical sensitive zinc-based nanoparticle EUV photoresists”; Yang, K, Xu, H, Sakai, K, Kosma, V, Giannelis, EP, Ober, CK, Advances In Patterning Materials And Processes XXXVI, Gronheid, R; Sanders, DP, eds. Proceedings of SPIE, 2019, 10960, 109601R, DOI: 10.1117/12.2514982 (Cornell).

“Real-time Monitoring of Live Cells for Drug Screening Using Metasurface-enhanced IR Spectroscopy (Combined into 8311)”; He (Steven) Huang, Gennady Shvets, 8539, Closed-Combined, 2/25/19, Invention (Cornell University).

“Real-time vibrations of a carbon nanotube”; Barnard, A, Zhang, M, Wiederhecker, G, Lipson, M, McEuen, P, Nature, Vol. 566, Issue # 7742, page(s) 89 (Cornell University).

“Realization of Epitaxial Thin Films of the Topological Crystalline Insulator Sr3SnO”; Y Ma, A Edgeton, H Paik, B Faeth, C Parzyck, B Pamuk, S Shang, Z Liu, K Shen, D Schlom, C Eom, arXiv:1912.13431 [cond-mat.mtrl-sci] (Cornell).

“Realization of GaN PolarMOS using selective-area regrowth by MBE and its breakdown mechanisms”; W.Li, K.Nomoto, A.Sundar, K.Lee, M.Zhu, Z.Hu, E.Beam, J.Xie, M.Pilla, X.Gao, S.Rouvimov, D.Jena, and H.Xing, Japanese Journal of Applied Physics, SCCD15, Vol. 58 (Cornell University).

“Recent Progress of GaN-Based Vertical Devices”; K Nomoto, Z Hu, W Li, M Zhu, K Lee, D Jena, and H Xing, ECS Meeting, Abstract MA2019-02 1348, H03-GaN Technologies-Oct 16 2019 (Cornell University).

“Room-Temperature Graphene-Nanoribbon Tunneling Field-Effect Transistors”; W Hwang, P Zhao, S Kim, R Yan, G Klimeck, A Seabaugh, S Fullerton-Shirey, H Xing, and D Jena, npj 2D Materials and Applications V3, #43 (2019) (Cornell).

“Rotationally aligned hexagonal boron nitride on sapphire by high-temperature molecular beam epitaxy”; Page, Ryan, Casamento, Joseph, Cho, Yongjin, Rouvimov, Sergei, Xing, Huili Grace, Jena, Debdeep, Physical Review Materials, Vol. 3, Issue # 6, page(s) 64001 (Cornell University).

“Scalable Synthesis of Switchable Assemblies of Gold Nanorod Lyotropic Liquid Crystal Nanocomposites”; X Liu, G Qi, A Park, A Rodriguez-Gonzalez, A Enotiadis, W Pan, V Kosma, G Fuchs, B Kirby, E Giannelis, Small, V 15, # 22, May 29, 2019, 1901666 https://doi.org/10.1002/smll.201901666 (Cornell).

“Scaling of a compact multi-beam ion accelerator to higher beam power for plasma heating”; Ji, Q; Persaud, A; Seidl, P; Garske, M; Giesbercht, G; Schenkel, T; Ni, D; Sinha, S; Afridi, K; Lal, A; 61st Annual Mtg of the APS Division of Plasma Physics, October 21-25, 2019; Fort Lauderdale, Florida, Volume 64, Number 11, Abstract: TO6.00015 (Cornell University).

“Science and Culture: Why seeing some scientific phenomena entails a touch of artistry and a dash of interpretation”; Amy McDermott, Science Writer, PNAS | October 29, 2019 | vol. 116 | no. 44 | 21953-21956 (Quotes Amrita Banerjee) (PNAS).

“Seat Integration of RF Vital-Sign Monitoring”; Xiaonan Hui, Edwin Kan, 8480-01-US, United States, EPR-Enhanced Provisional, Filed, 3/26/19, 62/824, 268 (Cornell University).

“Seat Integration of RF Vital-Sign Monitoring”; Xiaonan Hui, Edwin Kan, 8480, Filed by Cornell, 1/10/19, Invention (Cornell University).

“Self-assembly and properties of domain walls in BiFeO3 layers grown via molecular-beam epitaxy”; Mei, Antonio B., Tang, Yongjian, Schubert, Jürgen, Jena, Debdeep, Xing, Huili, Ralph, Daniel C., Schlom, Darrell G., APL materials, Vol. 7, Issue # 7, page(s) 71101 (Cornell University).

“Self-Assembly Behavior of an Oligothiophene-Based Conjugated Liquid Crystal and Its Implication for Ionic Conductivity Characteristics”; Liu, Ziwei, Dong, Ban Xuan, Misra, Mayank, Sun, Yangyang, Strzalka, Joseph, Patel, Shrayesh N., Escobedo, Fernando A., Nealey, Paul F., Ober, Christopher K., Advanced Functional Materials 29(2), 1805220 (2019) (Cornell University).

“Self-starting bi-chromatic LiNbO3 soliton microcomb”; Y He, Q Yang, J Ling, R Luo, H Liang, M Li, B Shen, H Wang, K Vahala, and Q Lin, Optica V6, #9, pp. 1138-1144 (2019) https://doi.org/10.1364/OPTICA.6.001138 (University of Rochester).

“Semi-Nonlinear Nanophotonic Waveguides for Highly Efficient Second-Harmonic Generation”; Luo, R; He, Y; Liang, H; Li, M; Lin, Q; Laser & Photonics Reviews, Vol. 13, Issue # 3, page(s) 1800288 (University of Rochester).

“Semiconductor Tweezers and Instrumentation for Tissue Detection and Characterization”; P Chen, A Lal, F Michelassi, C Wu, 6424-03-US, United States, Issued, 2/5/16, 14/910, 660, 12/31/19, 10, 517, 626 (Cornell University).

“Semiconductor Tweezers and Instrumentation for Tissue Detection and Characterization”; P Chen, A Lal, F Michelassi, C Wu, 6424-04-US, United States, CON-Continuation, Filed, 12/26/19, 16/727, 775 (Cornell University).

“Separation devices and sensors including two dimensional materials that change properties when exposed to components separated from a sample”; Halpern, Joshua, US10481135B1 United States 2019-11-19 Publication of US10481135B1 (Howard University).

“Significantly Reduced Thermal Conductivity in Beta-(Al0.1Ga0.9)2O3/Ga2O3 Superlattices”; Z Cheng, N Tanen, C Chang, J Shi, J McCandless, D Muller, D Jena, H Xing, S Graham, Applied Physics Letter 115, 092105 (2019) arXiv:1905.00139 [physics.app-ph] (30 Apr 2019) (Cornell University).

“Silicon carbide double-microdisk resonator”; Lu, Xiyuan, Lee, Jonathan Y., Rogers, Steven D., Lin, Qiang, Optics letters, Vol. 44, Issue # 17, page(s) 4295-4298 (University of Rochester).

“Single crystal growth and characterization of Ba2ScNbO6-A novel substrate for BaSnO3 films”; Guguschev, C., Klimm, D., Brützam, M., Gesing, T. M., Gogolin, M., Paik, H., Dittmar, A., Fratello, V. J., Schlom, D. G., Journal of Crystal Growth, Vol. 528, page(s) 125263 (Cornell University).

“Smartphone-Based Apparatus and Method for Obtaining Repeatable, Quantitative Colorimetric Measurement”; D Erickson, D O’Dell, V Oncescu, 6152-05-EP, Europe, Issued, 8/20/15, 14740730.8, 11/11/19, 2946198 (Cornell).

“Smartphone-Based Apparatus and Method for Obtaining Repeatable, Quantitative Colorimetric Measurement”; David Erickson, Dakota O’Dell, Vlad-Victor Oncescu, 6152-08-FR, France, Issued, 8/20/15, EP14740730.8, 11/11/19, EP2946198 (Cornell University).

“Smartphone-Based Apparatus and Method for Obtaining Repeatable, Quantitative Colorimetric Measurement”; David Erickson, Dakota O’Dell, Vlad-Victor Oncescu, 6152-09-DE, Germany, Issued, 8/20/15, 60201055933, 11/11/19, EP2946198 (Cornell University).

“Smartphone-Based Apparatus and Method for Obtaining Repeatable, Quantitative Colorimetric Measurement”; David Erickson, Dakota O’Dell, Vlad-Victor Oncescu, 6152-10-GB, United Kingdom, Issued, 8/20/15, EP14740730.8, 11/11/19, EP2946198 (Cornell University).

“Soil Integrated Gigahertz Ultrasonic Imager Devices, Systems and Methods”; Mamdouh Abdelmejeed, Justin Kuo, Amit Lal, 7683-03-US, United States, MPR-Manuscript Provisional, Not Converted, 1/11/19, 62/791, 716 (Cornell University).

“Spatially Controlled Cell-Free Protein Synthesis and Glycosylation on Chip”; Manzer, Z., Cell-Free Systems Conference in Boston, MA; December 5, 2019; Won the Synthetic and Systems Biotechnology 3rd Prize Poster Award (Cornell University).

“Spatially Controlled Transience of Graphene-Polymer Electronics with Silicon Singulation”; V Gund, A Ruyack, A Leonardi, K Vinayakumar, C Ober and A Lal, Advanced Functional Materials, 29(20), 1900592; DOI: 10.1002/adfm.20190059 (Cornell University).

“Spatially Resolved Headspace Extractions of Trace-Level Volatiles from Planar Surfaces for High-Throughput Quantitation and Mass Spectral Imaging”; Rafson, J; Bee, M; Sacks, G; Journal of agricultural and food chemistry, 2019, 67, 50, 13840-13847, April 4, 2019, https://doi.org/10.1021/acs.jafc.9b01091 (Cornell University).

“Spin and Orbital Resonance Driven by a Mechanical Resonator”; G Fuchs, CLEO, San Jose, CA 2019 (Cornell).

“Spin and Orbital Resonance Driven by a Mechanical Resonator”; Fuchs, G., Compact Free Electron Laser Quantum Materials Workshop, Arizona State University, Phoenix, AZ 2019 INVITED (Cornell University).

“Spin and Orbital Resonance Driven by a Mechanical Resonator”; Fuchs, G., March Meeting of the APS, Boston, MA 2019 INVITED (Cornell University).

“Spin Seebeck Imaging of Spin-Torque Switching in Antiferromagnetic Pt/NiO Heterostructures”; I. Gray, T. Moriyama, N. Sivadas, G.M. Stiehl, J.T. Heron, R. Need, B.J. Kirby, D.H. Low, K.C. Nowack, D.G. Schlom, D.C. Ralph, T. Ono, and G.D. Fuchs, Physical Review X 9, 041016 - Published 22 October 2019 (Cornell University).

“Spin tunnel field-effect transistors based on two-dimensional van der Waals heterostructures”; S. Jiang, L. Li, Z. Wang, J. Shan, and K.F. Mak, Nature Electronics 2, 159-163 (2019) https://doi.org/10.1038/s41928-019-0232-3 (Cornell).

"Spin-Orbit Coupling, Spin Hall Conductivity and Spin Currents"; Buhrman, R, Invited talk presented at Samsung Research Foundation Global Research Symposium, Seoul, Korea, Nov. 22-23, 2019 (Cornell University).

"Spin-orbit torques from low-symmetry materials"; Ralph, D. C., 2019 Magnetism and Magnetic Materials Conference, Nov. 4-8, 2019, Las Vegas, NV (Cornell University).

"Spin-Orbit Torques in Heavy-Metal-Ferromagnet Bilayers with Varying Strengths of Interfacial Spin-Orbit Coupling"; Zhu, Lijun, Ralph, D. C., Buhrman, R. A., Physical review letters, Vol. 122, Issue # 7, page(s) 77201 (Cornell University).

"Spin-Orbit Torques: Discoveries, Advances and Possibilities for Memory Technology"; Buhrman, R, Applied Materials, San Jose CA, 2/12/2019 INVITED SEMINAR (Cornell University).

"Spin-Orbit-Torque Field-Effect Transistor (SOTFET): A New Magnetoelectric Memory"; X Li, P Dang, J Casamento, Z Zhang, O Afuye, A Mei, A Apsel, D Schlom, D Jena, D Ralph, H Xing, arXiv:1909.08133 [physics.app-ph] (17 Sep 2019 (v1), last revised 20 Sep 2019) (Cornell University).

"Spin-orbit-torque magnetic manipulation with 2D materials"; Ralph, D. C., 2019 Experimental Condensed Matter Physics Principal Investigators' Meeting (DOE), Sept. 16-18, 2019, Gaithersburg, MD (Cornell University).

"Spin-orbit-torque magnetic manipulation with 2D materials"; Ralph, D. C., 2019 March Meeting of the American Physical Society, March 4-8, 2019, Boston, MA (Cornell University).

"Stability and microbial toxicity of HfO2 and ZrO2 nanoresists for photolithography"; J Gonzalez-Estrella, J Field, C Ober, R Sierra-Alvarez, Green Materials, https://doi.org/10.1680/jgrma.18.00056 (Cornell University).

"Stethoscope using Near-Field Coherent Sensing"; Xiaonan Hui, Edwin Kan, 8481-01-US, United States, EPR-Enhanced Provisional, Filed, 3/26/19, 62/824, 261 (Cornell University).

"Stiffness of hip adductor myofibrils is decreased in children with spastic cerebral palsy"; Leonard, Timothy R., Howard, Jason J., Larkin-Kaiser, Kelly, Joumaa, Venus, Logan, Karl, Orlik, Benjamin, El-Hawary, Ron, Gauthier, Luke, Herzog, Walter, Journal of Biomechanics, Volume 87, 18 April 2019, Pages 100-106, https://doi.org/10.1016/j.jbiomech.2019.02.023 (University of Calgary).

"Strictures of a microchannel impose fierce competition to select for highly motile sperm"; Zaferani, Meisam, Palermo, Gianpiero D., Abbaspourrad, Alireza, Science advances, eaav2111, Vol. 5, Issue # 2 (Cornell University).

"Strong Damping-Like Spin-Orbit Torque and Tunable Dzyaloshinskii-Moriya Interaction Generated by Low-Resistivity Pd1-xPtx Alloys"; L Zhu, K Sobotkiewich, X Ma, X Li, D Ralph, R Buhrman, Adv Functional Materials, V29, Issue 16, 1805822, First published: 27 February 2019, https://doi.org/10.1002/adfm.201805822 (Cornell University).

"Structure Control of a π-Conjugated Oligothiophene-Based Liquid Crystal for Enhanced Mixed Ion/Electron Transport Characteristics"; B Dong, Z Liu, M Misra, J Strzalka, J Niklas, O Poluektov, F Escobedo, C Ober, P Nealey, S Patel, ACS Nano, (2019), 13(7), 7665-767; doi: 10.1021/acsnano.9b01055 (Cornell University).

"Super-Resolution Optical Imaging of Non-Fluorescent Species"; P Chen, X Mao, 8385-02-US, United States, US from PRV, Filed, 9/26/19, 16/584, 219 (Cornell University).

"Supercapillary Architecture-Activated Two-Phase Boundary Layer Structures for Highly Stable and Efficient Flow Boiling Heat Transfer"; W Li, Z Wang, F ang, T Alam, M Jiang, X Qu, F Kong, A Khan, M Liu, M Alwazzan, Y Tong, C Li, Adv Materials, V 32, # 2, Jan 16, 2020, 1905117, https://doi.org/10.1002/adma.201905117 (University of South Carolina).

"Superlattice Structure including Two-Dimensional Material and Device including the Superlattice Structure"; Natalie Dawley, Craig Fennie, Gerhard Olsen, Darrell Schlom, Zhe Wang, 8493-02-US, United States, UTM-Utility, Filed, 5/31/19, 16/428, 006 (Cornell University).

"Supported Plant Plasma Lipid Bilayer on-a-Chip"; Susan Daniel, Han-Yuan Liu, Martin Stuebler, 8321-02-PC, Not Applicable (PCT App), PCT-Patent Cooperation Treaty, Filed, 7/11/19, PCT/US2019/041402 (Cornell University).

"Synergistic Coordination of Chromatin Torsional Mechanics and Topoisomerase Activity"; Michelle Wang, 9173-01-US, United States, EPR-Enhanced Provisional, Filed, 10/9/19, 62/913, 036 (Cornell University).

"Synergistic Coordination of Chromatin Torsional Mechanics and Topoisomerase Activity"; Xiang Gao, James Inman, Tung Le, Jaeyoon Lee, Seong Park, Michelle Wang, 9173, Filed by Cornell, 10/9/19, Invention (Cornell University).

"Synergistic Coordination of Chromatin Torsional Mechanics and Topoisomerase Activity"; Le, T; Gao, X; ha Park, S; Lee, J; Inman, J; Lee, J; Killian, J;, Badman, R; Berger, J; Wang, M; Cell, Vol. 179, Issue # 3, page(s) 619-631 (Cornell University).

"Synthesis of organic-inorganic hybrid nanoparticles and their application in additive manufacturing"; Wu, Dung-Yi, Cornell Ph.D. Thesis (Cornell University).

"Syringe-based Impedance Analyzer"; L Bonassar, J Matthews, 9131, Filed by Cornell, 9/11/19, Invention (Cornell).

"System and Method for Reflective Spectroscopy of a Cell Membrane Using a Fiber with a Plasmonic Metasurface"; S Gupta, G Shvets, 7743-03-US, United States, US from PCT, Filed, 11/8/19, 16/611, 912 (Cornell University).

"Tailored Nonlinear Anisotropy in Mie-Resonant Dielectric Oligomers"; Kroychuk, Maria K., Yagudin, Damir F., Shorokhov, Alexander S., Smirnova, Daria A., Volkovskaya, Irina I., Shcherbakov, Maxim R., Shvets, Gennady, Kivshar, Yuri S., Fedyanin, Andrey A., Advanced Optical Materials, Vol. 7, Issue # 20, page(s) 1900447 (Cornell University).

"Targeted chemical pressure yields tuneable millimetre-wave dielectric"; N Dawley, E Marksz, A Hagerstrom, G Olsen, M Holtz, V Goian, C Kadlec, J Zhang, X Lu, J Drisko, R Uecker, S Ganschow, C Long, J Booth, S Kamba, C Fennie, D Muller, N Orloff, and D Schlom, Nature Materials (2019) doi:10.1038/s41563-019-0564-4 (Cornell University).

"Temporally Asymmetric Bi-photon States in Cavity Enhanced Optical Parametric Processes"; Javid, Usman A., Rogers, Steven D., Graf, Austin, Lin, Qiang, arXiv preprint arXiv:1904.09686 (University of Rochester).

“Temporally Asymmetric Biphoton States in Cavity-Enhanced Optical Parametric Processes”; Javid, UA, Rogers, SD, Graf, A, Lin, Q, Physical Review Applied, Volume: 12, Issue: 5, Article Number: 054019, DOI: 10.1103/PhysRevApplied.12.054019, Published: NOV 8 2019 (University of Rochester).

“The Design of The CCAT-prime Epoch of Reionization Spectrometer Instrument”; N Cothard, S Choi, C Duell, T Herter, J Hubmayr, J McMahon, M Niemack, T Nikola, C Sierra, G Stacey, E Vavagiakis, E Wollack, B Zou, arXiv:1911.11687 [astro-ph.IM] (Cornell University).

“The Evolution of the Cornell NanoScale Facility and Synergies with the Semiconductor Industry”; Tennant, D., Novel Patterning Technologies for Semiconductors, MEMS/NEMS, and MOEMS 2019 (Keynote Presentation) Paper 10958-1, International Society for Optics and Photonics, Vol. 10958, page(s) 1095802 (Cornell University).

“The New Nitrides: Layered, ferroelectric, magnetic, metallic and superconducting nitrides to boost the GaN photonics and electronics eco-system”; D Jena, R Page, J Casamento, P Dang, J Singhal, Z Zhang, J Wright, G Khalsa, Y Cho, and H Xing, Japanese Journal of Applied Physics, Volume 58, Number SC, Published 17 May 2019 (Cornell University).

“Thermal conductivity of AlN single crystal and the influence of atomic-scale defects”; R Xu, M Rojo, S Islam, A Sood, B Vareskic, A Katre, N Mingo, K Goodson, H Xing, D Jena and E Pop, J. Appl. Phys.126, 185105 (2019); https://doi.org/10.1063/1.5097172 (Cornell University).

“Thermal Dependence of Al2O3 Passivated RF WSe2 MOSFETs”; K. Xiong, 2019 CNF Annual Meeting, poster presentation, Ithaca, NY, USA, Sep 2019 (Lehigh University).

“Thermal Dependence of Al2O3 Passivated RF WSe2 MOSFETs”; K. Xiong, 2019 Graphene & Beyond, poster, State College, PA, USA, May 2019 (Lehigh University).

“Thermal transport of helium-3 in a strongly confining channel”; D. Lotnyk, A. Eyal, N. Zhelev, T.S. Abhilash, E.N. Smith, M. Terilli, J. Wilson, E. Mueller, D. Einzel, J. Saunders, J.M. Parpia, arXiv preprint arXiv:1910.08414 (Submitted on 18 Oct 2019) (Cornell University).

“Thickness dependence of superconductivity in ultrathin NbS2”; Rusen Yan, Guru Khalsa, Brian T Schaefer, Alexander Jarjour, Sergei Rouvimov, Katja C Nowack, Huili G Xing, and Debdeep Jena, Applied Physics Express, Volume 12, Number 2, Published 1 February 2019 (Cornell University).

“Thin Film Iridium Electrodes for Hexagonal Ferroelectrics”; Megan Holtz, Darrell Schlom, Rachel Steinhardt, 9189-01-US, United States, MPR-Manuscript Provisional, Filed, 10/21/19, 62/924, 127 (Cornell University).

“Three-Dimensional Numerical Modeling of Surface-Acoustic-Wave Devices: Acoustophoresis of Micro-and Nanoparticles Including Streaming”; Skov, Nils R., Sehgal, Prateek, Kirby, Brian J., Bruus, Henrik, Physical Review Applied, Vol. 12, Issue # 4, page(s) 44028 (Cornell University).

“Three-Dimensional Printing of Hierarchical Porous Architectures”; Jen-Yu Huang, Hong Xu, Eliad Peretz, Dung-Yi Wu, Christopher Kemper Ober, Tobias Hanrath, Chemistry of Materials, 2019, 31, 24, 10017-10022 (Cornell University).

“Time-resolved magneto-thermal microscopy: high-resolution dynamic imaging of magnetic materials using picosecond heat pulses”; Fuchs, G., Spring Meeting of the MRS, Phoenix, AZ 2019 INVITED (Cornell University).

“Time-variant metasurfaces enable tunable spectral bands of negative extinction”; Shcherbakov, Maxim R., Lemasters, Robert, Fan, Zhiyuan, Song, Jia, Lian, Tianquan, Harutyunyan, Hayk, Shvets, Gennady, Optica, Vol. 6, Issue # 11, page(s) 1441-1442 (Cornell University).

“Tissue Scaffold Materials for Tissue Regeneration and Methods of Making”; John Morgan, Jason Spector, Abraham Stroock, 6458-13-JP, Japan, FOR-Foreign DIV, Filed, 7/29/19, 2019-133223 (Cornell University).

“Towards a CMOS Integrated Optically Controlled AlN Transducer”; Y Liu, J Kuo, M Abdelmejeed, A Lal, 2019 IEEE International Ultrasonics Symposium (IUS), 6-9 Oct. 2019, Glasgow, United Kingdom, United Kingdom, DOI: 10.1109/ULTSYM.2019.8926050 (Cornell University).

“Towards Digitally Controlled Ultrasonic IQ Modulator”; Mamdouh Abdelmejeed, Benyamin Davaji, Amit Lal, 2019 IEEE International Ultrasonics Symposium (IUS), 6-9 Oct. 2019, Glasgow, United Kingdom, United Kingdom; DOI: 10.1109/ULTSYM.2019.8925880 (Cornell University).

“Transmit-receive delay element apparatus, method, and applications”; Lal, Amit, Abdelmejeed, Mamdouh, Kuo, Justin, US20190074818A1 United States, 2019-03-07 Publication of US20190074818A1 (Cornell University).

“Tuning pair-breaking at the surface of topological superfluid 3He”; Heikkinen, P. J., Casey, A., Levitin, L. V., Rojas, X., Vorontsov, A., Sharma, P., Zhelev, N., Parpia, J. M., Saunders, J., arXiv preprint arXiv:1909.04210 (Cornell University).

“Turn-key, high-efficiency Kerr comb source”; B Kim, Y Okawachi, J Jang, M Yu, X Ji, Y Zhao, C Joshi, M Lipson, and A Gaeta, Optics Letts V44, #18, pp. 4475-4478 (2019) https://doi.org/10.1364/OL.44.004475 (Columbia University).

“Ultra-high Q microring resonators using a single-crystal aluminum-nitride-on-sapphire platform”; Sun, Y; Shin, W; Laleyan, D; Wang, P; Pandey, A; Liu, X; Wu, Y; Soltani, M; Mi, Z; Optics Letters, Vol. 44, Issue # 23, page(s) 5679-5682 (University of Michigan).

“Ultra-high Temperature Growth of Layered Hexagonal Boron Nitride on Sapphire by Molecular Beam Epitaxy”; R Page, Y Cho, J Casamento, S Rouvimov, H Xing, D Jena, Compound Semiconductor Week (CSW), 19-23 May 2019, Nara, Japan, INSPEC Accession Number: 19010201 (Cornell University).

“Ultrasonic Devices and Techniques for Sono-Mechanics”; Lal, Amit, 9105-01-US, United States, MPR-Manuscript Provisional, Filed, 8/22/19, 62/890, 548 (Cornell University).

“Ultrasonic Fourier Computation Hardware for Convolutional Neural Network Computing”; Lal, Amit, 9138-01-US, United States, MPR-Manuscript Provisional, Filed, 9/19/19, 62/902, 690 (Cornell University).

“Ultrasonic Fourier Computtation Hardware for Convolutional Neural Netwrok Computing”; Lal, Amit, 9138, Filed by Cornell, 9/12/19, Invention (Cornell University).

"Ultrasonic Fourier Transform Analog Computing Apparatus, Method and Applications"; Lal, Amit, 7368-04-PC, Not Applicable (PCT App), PCT-Patent Cooperation Treaty, Filed, 5/23/19, PCT/US19/33724 (Cornell University).

"Ultrasonic Fourier Transforms with Isotropic Propagation Medium"; Mamdouh Abdelmejeed, Justin Kuo, Amit Lal, 8859, Unfiled, 8/1/19, Invention (Cornell University).

"Using Acoustic Perturbations to Dynamically Tune Shear Thickening in Colloidal Suspensions"; Sehgal, Prateek, Ramaswamy, Meera, Cohen, Itai, Kirby, Brian J., arXiv preprint arXiv:1905.06445 (Cornell University).

"Valveless Microfluidic Flow Control Using Planar Fresnel Type GHz Ultrasonic Transducers"; Lal, Amit, 9170-01-US, United States, MPR-Manuscript Provisional, Filed, 10/7/19, 62/911, 938 (Cornell University).

"Valveless Microfluidic Flow Control Using Planar Fresnel Type GHz Ultrasonic Transducers"; Lal, Amit, 9170, Filed by Cornell, 10/7/19, Invention (Cornell University).

"Valveless Microfluidic Flow Control Using Planar Fresnel Type GHz Ultrasonic Transducers"; A Ravi, J Kuo, A Lal, 2019 IEEE International Ultrasonics Symposium (IUS), 6-9 Oct. 2019, Glasgow, United Kingdom, DOI: 10.1109/ULTSYM.2019.8925727 (Cornell University).

"Variation of the giant intrinsic spin Hall conductivity of Pt with carrier lifetime"; Zhu, Lijun, Zhu, Lujun, Sui, Manling, Ralph, Daniel C., Buhrman, Robert A., Science Advances 5, eaav8025 (2019), https://doi.org/10.1126/sciadv.aav8025 (Cornell University).

"Vertical Gallium Oxide (Ga203) Power FETs"; Z Hu, D Jena, W Li, K Nomoto, H Xing, 8178-02-PC, Not Applicable (PCT App), PCT-Patent Cooperation Treaty, Filed, 3/28/19, PCT/US19/24634 (Cornell University).

"Vibronic coupling and optical coherence of single photon emitters in hexagonal boron nitride"; Fuchs, G., 11th Conference on Coherence and Quantum Optics, Rochester, NY 2019 (Cornell University).

"Wafer-Based Charged Particle Accelerator, Wafer Components, Methods and Applications"; Serhan Ardanuc, Vinaya Kumar Kadayra Basavarajappa, Qing Ji, Amit Lal, Arun Persaud, Thomas Schenkel, Peter Seidl, Will Waldron, 7390-03-US, United States, Issued, 11/2/18, 16/098, 537, 8/13/19, 10, 383, 205 (Cornell University).

"Wafer-Based Charged Particle Accelerator, Wafer Components, Methods and Applications"; Serhan Ardanuc, Vinaya Kumar Kadayra Basavarajappa, Qing Ji, Amit Lal, Arun Persaud, Thomas Schenkel, Peter Seidl, Will Waldron, 7390-04-US, United States, CON-Continuation, Filed, 8/12/19, 16/538, 653 (Cornell University).

"Wafer-based charged particle accelerator, wafer components, methods, and applications"; Amit Lal, Thomas Schenkel, Arun Persaud, Qing Ji, Peter Seidl, Will Waldron, Serhan Ardanuc, Vinaya Kumar Kadayra Basavarajappa, US10383205B2 United States, 2019-08-13 application granted (Cornell University).

"Wearable sensor to monitor respiratory depression in people with opioid addiction"; J Imperato-McGinley, E Kan, A Krieger, 8812, Unfiled, 5/22/19, Invention (Cornell University).

"Wet Etching of P-Gan for Crystallographically Smooth Vertical Sidewalls"; Hsu, Jui-Yuan, Cornell Ph.D. Thesis https://doi.org/10.7298/z48a-sg68 (Cornell University).

"Wicking in Cross-Connected Buried Nanochannels"; Poudel, S;, Zou, A; Maroo, S;, The Journal of Physical Chemistry C, Vol. 123, Issue # 38, page(s) 23529-23534 (Syracuse University).

"Wicking vs. Contact Line Extension for Boiling Enhancement in Porous Structures"; An Zou, Sajag Poudel, Shalabh Maroo, ASME 2019 Summer Heat Transfer Conference, Bellevue, WA. (2019/7/15) (Syracuse University).

"Wireless, Optically-Powered Optoelectonics Sensors"; A Cortese, S Lee, P McEuen, A Molnar, 8107-03-PC, Not Applicable (PCT App), PCT-Patent Cooperation Treaty, Filed, 2/8/19, PCT/US2019/017377 (Cornell University).

"Wurtzite phonons and the mobility of a GaN/AlN 2D hole gas editors-pick"; S Bader, R Chaudhuri, M Schubert, H Then, H Xing, and D Jena, Appl. Phys. Lett. 114, 253501 (2019); https://doi.org/10.1063/1.5099957 (Cornell University).

"Zero-power sensor apparatus, method, and applications"; A Lal, A Molnar, US20190078913A1 United States, 2019-03-14 Publication of US20190078913A1 (Cornell University).

"Zinc-Based Photoresist for High-Resolution EUV (Extreme Ultraviolet) Lithography"; Yang, Kou, Cornell Theses and Dissertations, Date Issued 2019-08-30, https://doi.org/10.7298/adrq-np68 (Cornell University).

The 2019-2020 Cornell NanoScale Facility Research Accomplishments are online in PDF,

http://cnf.cornell.edu/publications/research_accomplishments

Common Abbreviations & Meanings

µl	microliter
µm	micron, micrometer
µN	micro-Newtons
µs	microsecond
Ω	Ohm
<	is less than
>	is greater than
~	approximately
1D	one-dimensional
2D	two-dimensional
2DEG	two-dimensional electron gas
3D	three-dimensional
^3He	helium-3
α-Al_2O_3	sapphire
α-Si	amorphous silicon
AC	alternating current
AFM	atomic force microscopy/microscope
AFOSR	Air Force Office of Scientific Research
Ag	silver
Al	aluminum
Al_2O_3	aluminum oxide
ALD	atomic layer deposition
AlGaAs	aluminum gallium arsenide
AlGaN	aluminum gallium nitride
Ar	argon
ARC	anti-reflective coating
ArF	argon fluoride
As	arsenic
atm	standard atmosphere (as a unit of pressure)
Au	gold
AuNPs	gold nanoparticles
B	boron
B. subtilis	*Bacillus subtilis*
Bi	bismuth
BOE	buffered oxide etch
Br	bromine
C	carbon
C	centigrade
C-V	capacitance-voltage
C_3N_4	carbon nitride
$CaCl_2$	calcium chloride
$CaCO_3$	calcium carbonate
CAD	computer-aided design
CaF_2	calcium fluoride
CCMR	Cornell Center for Materials Research
Cd	cadmium
CdS	cadmium sulfide
CdSe	cadmium selenide
CDW	charge-density-wave
Ce	cerium
CF_4	carbon tetrafluoride or tetrafluoromethane
CFD	computational fluid dynamics
CH_4	methane
CHESS	Cornell High Energy Synchrotron Source
CHF_3	trifluoromethane
Cl	chlorine
Cl_2	chlorine gas
Cl_2/SF_6	chlorine sulfur hexafluoride
cm	centimeter
CMOS	complementary metal oxide semiconductor
CMP	chemical mechanical polishing
CNF	Cornell NanoScale Science & Technology Facility
Co	cobalt
CO_2	carbon dioxide
Co_3O_4	cobalt oxide
CoFeAl	cobalt iron aluminum
CoFeB	cobalt iron boron
CoP	cobalt porphyrin
CPC	colloidal photonic crystal
CPD	contact potential difference
CpG	cytosine-phosphate-guanine
Cr	chromium
CRDS	cavity ring-down spectrometer
cryoSAXS	cryogenic small angle x-ray scattering
CTE	coefficients of thermal expansion
CTL	confinement tuning layer
Cu	copper
CVD	cardiovascular disease
CVD	chemical vapor deposition
CW	continuous wave
CXRF	confocal x-ray fluorescence microscopy
DARPA	Defense Advanced Research Projects Agency
DC	direct current
DCB	double cantilever beam
DCE	1,2-dichloroethane
DCM	dichloromethane
DEP	dielectrophoresis
DFT	density functional theory
DFT	discrete Fourier transform
DI	de-ionized
DMF	dimethyl formamide
DNA	deoxyribonucleic acid
DNP	dynamic nuclear polarization
DOE	United States Department of Energy
DPPC	1,2-dipalmatoyl-sn-glycero-3-phosphocholine
DRAM	dynamic random access memory
DRIE	deep reactive ion etch
DSA	directed self assembly
dsDNA	double-stranded DNA
DUV	deep ultraviolet
e-beam	electron beam lithography
E. coli	*Escherichia coli*
EBL	electron-beam lithography
EDS	energy dispersive spectroscopy

EELS	electron energy loss spectroscopy
EG	ethylene glycol
EIS	electrochemical impedance spectroscopy
ELISA	enzyme-linked immunosorbent assays
EO	electro-optic
EOT	equivalent oxide thickness
EPICs	electronic photonic integrated circuits
Er	erbium
ErAs	erbium arsenide
ESM	effective screening medium
EUV	extreme ultraviolet
ex situ	Latin phrase which translated literally as 'off-site' -- to examine the phenomenon in another setting than where it naturally occurs
ex vivo	Latin for "out of the living" -- that which takes place outside an organism
F	fluorine
FDA	United States Food & Drug Administration
FDMA	fluorinated perfluorodecyl methacrylate
Fe	iron
Fe_2O_3	iron oxide
$FeCl_3$	iron(III) chloride, aka ferric chloride
FeGe	iron germanium
FEM	finite element method
FET	field-effect transistor
FFTs	fast Fourier transforms
fg	femto gram
FIB	focused ion beam
FIR	far infrared
fJ	femto Joules
FM	frequency modulation
FMR	ferromagnetic resonance
FOTS	fluorosilane, tridecafluoro-1,1,2,2-tetrahydrooctyltrichlorosilane
FTIR	Fourier transform infrared spectroscopy
Ga	gallium
Ga_2O_3	gallium(III) trioxide
GaAs	gallium arsenide
GaAsN	gallium arsenide nitride
GaInNAs	gallium indium nitride arsenide
GaN	gallium nitride
GaP	gallium phosphide
GaSb	gallium antimonide
Gd	gadolinium
Ge	germanium
GFET	graphene field effect transistor
GHz	gigahertz
GI	gastrointestinal
GMR	giant magnetoresistance
GPa	gigapascal
GPS	global positioning system
h	hours
H	hydrogen
H_2O_2	hydrogen peroxide
HBAR	high-overtone bulk acoustic resonator
hBN	hexagonal boron nitride
HBr	hydrogen bromide
hcp	hexagonal close packing
He	helium
HEMTs	high electron mobility transistors
Hf	hafnium
HF	hydrofluoric acid
HfB_2	hafnium diboride
HFEs	hydrofluoroethers
HfO_2	hafnium dioxide
Hg	mercury
high-κ	high dielectric constant
HMDS	hexamethyldisilazane
HRS	high resistance state
HSQ	hydrogen silsesquioxane
HSQ/FOx	negative electron beam resist hydrogen silsesquioxane
Hz	Hertz
I-V	current-voltage
I/O	input/output
IARPA	Intelligence Advanced Research Projects Activity
IC	integrated circuit
ICP	inductively coupled plasma
ICP-MS	inductively coupled plasma mass spectroscopy
ICP-RIE	inductively coupled plasma reactive ion etcher
IFVD	impurity free vacancy diffusion
IID	impurity induced disordering
IIEI	ion implant enhanced interdiffusion
In	indium
in situ	Latin phrase which translated literally as 'in position' -- to examine the phenomenon exactly in place where it occurs
in vitro	Latin for "within glass" -- refers to studies in experimental biology that are conducted using components of an organism that have been isolated from their usual biological context in order to permit a more detailed or more convenient analysis than can be done with whole organisms
in vivo	Latin for "within the living" -- experimentation using a whole, living organism
InAlN	indium aluminum nitride
InAs	indium arsenide
InAs NWs	indium arsenide nanowires
INDEX	Institute for Nanoelectronics Discovery and Exploration
InGaAsN	indium gallium arsenide nitride
$InGaZnO_4$	indium gallium zinc oxide
InP	indium phosphide
IPA	isopropyl alcohol
IR	infrared
IrO_2 or IrO_x	iridium oxide
ITO	indium tin oxide
JP-8	Jet Propellant 8
κ	dielectric constant
K	Kelvin (a unit of measurement for temperature)
K	potassium
KFM	Kelvin force microscopy
kg	kilogram
kHz	kilohertz
KOH	potassium hydroxide
La	lanthanum

LED	light-emitting diode
LER	line edge roughness
Li	lithium
low-κ	low dielectric constant
LPCVD	low pressure chemical vapor deposition
lpm	liter per minute
LRS	low resistance state
Lu	lutetium
LWR	line width roughness
MBE	molecular beam epitaxy
MEMs	microelectromechanical systems
MFMR	microfabricated micro-reactors
MgO	magnesium oxide
MGs	molecular glasses
MHz	megahertz
micron	micrometer, aka µm
min	minutes
ml	milliliter
mm	millimeter
mM	millimolar
Mo	molybdenum
MOCVD	metal oxide chemical vapor deposition
MOS	metal oxide semiconductor
MoS$_2$	molybdenum disulfide
MoSe$_2$	molybdenum diselenide
MOSFET	metal oxide semiconductor field effect transistor
MRAM	magnetic random access memory
MRFM	magnetic resonance force microscopy
MRI	magnetic resonance imaging
ms	millisecond
MSM	metal-semiconductor-metal
mTorr	millitorr
mV	millivolt
MVD	molecular vapor deposition
MΩ	megaohms
N	nitrogen
N$_2$	nitrous oxide
nA	nanoAmperes
NaCl	sodium chloride
NASA	National Aeronautics & Space Administration
Nb	niobium
Nb$_3$Sn	triniobium-tin
NCs	nanocrystals
Nd	neodymium
NEMs	nanoelectromechanical systems
NH$_4$F	ammonium fluoride
Ni	nickel
NIH	National Institutes of Health
NIR	near-infrared
nL	nanoliter
nm	nanometer
NMP	n-methyl-2-pyrrolidone
NNCI	National Nanotechnology Coordinated Infrastructure
NPs	nanoparticles
NPs	nanopores
ns	nanosecond
NSF	National Science Foundation
NV	nitrogen-vacancy
NVM	non-volatile memory
NW FETs	nanowire field-effect transistors
O	oxygen
O$_3$	trioxygen
OFET	organic field effect transistor
OLED	organic light-emitting diode
ONO	oxide/nitride/oxide
ONR-MURI	Office of Naval Research Multidisciplinary University Research Initiative
OPV	organic photovoltaic cells
OTFT	organic thin-film transistor
Pa	Pascals
PAB	post-apply bake
PaC	Parylene-C
PAG	photoacid generator
Pb	lead
PBG	photonic bandgap
PbS	lead sulfide
PBS	phosphate-buffered saline
PbSe	lead selenide
PC	persistent current
PC	photocurrent
PCN	photonic crystal nanocavity
Pd	palladium
PD	photodetector
PDMS	polydimethylsiloxane
PEB	post-exposure bake
PEC	photoelectrochemical
PECVD	plasma enhanced chemical vapor deposition
PEDOT:PSS	poly(3,4-ethylenedioxythiophene): poly(styrenesulfonate)
PEG	polyethylene glycol
PEI	polyethyleneimine
pFET	p-channel field-effect transistor
PFM	piezo-response force microscopy
PGMA	poly(glycidyl methacrylate)
pH	a measure of the activity of hydrogen ions (H+) in a solution and, therefore, its acidity
Ph.D.	doctorate of philosophy
PhC	photonic crystal
PL	photoluminescence
pL	picoliter
PLD	pulsed laser deposition
PMMA	poly(methyl methacrylate)
poly-Si	polycrystalline silicon
PS	polystyrene
PS-*b*-PMMA	polystyrene-*block*-poly(methyl methacrylate)
Pt	platinum
Pt/Ir	platinum/iridium
PtSe$_2$	platinum diselenide
PV	photovoltaic
PVD	physical vapor deposition
Py	permalloy, Ni$_{81}$Fe$_{19}$
Q	quality factor

QD	quantum dots
QW	quantum well
RA	resistance-area
REU	Research Experience for Undergraduates Program
RF	radio frequency
RF MEMS	radio frequency microelectromechanical systems
RIE	reactive ion etch
RMS or rms	root mean square
RNA	ribonucleic acid
RTA	rapid thermal anneal
RTD	resistance temperature device
RTD	resonant tunneling diodes
Ru	ruthenium
s	seconds
S	sulfur
SAMs	self-assembled monolayers
SAXS	small angle x-ray scattering
Sb	antimony
Sc	scandium
sccm	standard cubic centimeters per minute
$scCO_2$	supercritical carbon dioxide
SDS	sodium dodecyl sulfate
Se	selenium
sec	seconds
SEM	scanning electron microscopy/microscope
SERS	surface enhanced Raman spectroscopy
SF_6	sulfur hexafluoride
Si	silicon
Si_3N_4	silicon nitride
SiC	silicon carbide
SiH_4	silane
SiN	silicon nitride
SiO_2	silicon dioxide, silica
Sn	tin
SnO_2	tin oxide
$SnSe_2$	tin selenide or stannous selenide
SOI	silicon-on-insulator
SPR	surface plasmon resonance
SQUID	superconducting quantum interference device
Sr_2RuO_4	strontium ruthenate
SRC	Semiconductor Research Corporation
$SrTiO_3$	strontium titanate
STEM	scanning transmission electron microscopy/microscope
t-BOC	*tert*-butoxycarbonyl
Ta	tantalum
Ta_2O_5	tantalum pentoxide
TaN	tantalum nitride
TAO_x	tantalum oxide
Te	tellurium
TEM	transmission electron microscopy/microscope
TFET	tunnel field effect transistor
TFT	thin-film transistor
Tg	glass transition temperature
THz	terahertz
Ti	titanium
TiN	titanium nitride
TiO_2	titanium dioxide
TM	transverse magnetic
TXM	transmission x-ray microscopy
UHV	ultra-high vacuum
USDA	United States Department of Agriculture
UV	ultraviolet
UV-Vis	ultraviolet-visible
V	vanadium
V	voltage
vdW	van der Waals
VLS	vapor-liquid-solid
VRMs	voltage regulator modules
VSM	vibrating sample magnetometry
W	tungsten
WDM	wavelength-division multiplexing
WSe_2	tungsten diselenide
XeF_2	xenon difluoride
XPM	cross-phase modulation
XPS	x-ray photoelectron spectroscopy
XRD	x-ray diffraction
XRR	x-ray reflectivity
ZMW	zero-mode waveguide
Zn	zinc
$ZnCl_2$	zinc chloride
ZnO	zinc oxide
ZnO:Al	zinc aluminum oxide
ZnS	zinc sulfide or zinc-blende
Zr	zirconium
ZrO_2	zirconium dioxide
ZTO	zinc tin oxide

Photography Credits

The cover image is from CNF Project Number: 2416-16, "Atomically Thin Actuator-Enabled Micro-Machines and Micro-Structures"; Principal Investigators Itai Cohen and Paul L. McEuen; CNF Users: Qingkun Liu, Wei Wang, Baris Bircan, and Michael F. Reynolds. Used with the permission of the research group. The full report starts on page 90. The staff photographs on pages iv-v were taken by University Photo or CNF staff. The color images on pages vi-vii were provided by the research groups noted under each image.

• • •

Reminder to Use the CNF Wiki!

The goal of the wiki is to maintain up-to-date manuals, user-submitted recipes, and other information that may be helpful to other CNF users.

https://confluence.cornell.edu/display/CNFUserWiki

Cornell NanoScale Science & Technology Facility (CNF)

2019-2020 Research Accomplishments

Large-Scale Microfluidic Device Fabrication for Non-Equilibrium RNA Kinetic Experiments

CNF Project Number: 692-98

Principal Investigator(s): Lois Pollack

User(s): Alex Plumridge

Affiliation(s): Applied and Engineering Physics, Cornell University

Primary Source(s) of Research Funding: National Institutes of Health

Contact: lp26@cornell.edu, ap866@cornell.edu

Website: https://pollack.research.engineering.cornell.edu/

Primary CNF Tools Used: Plasma-Therm deep silicon etcher, substrate bonder, dicing saw, ABM contract aligner, Heidelberg mask writer

Abstract:

Here we report the design and implementation of a large-scale fabrication protocol to produce ~ 100 microfluidic mixing devices per wafer. These devices enable non-equilibrium single-molecule fluorescence measurements. This upgraded protocol improves on our previous work by increasing the yield, number and robustness of devices while decreasing the fluorescence background. Such improvements allow kinetic measurements on RNA to be made more routinely, easily and with higher data quality.

Summary of Research:

Non-equilibrium measurements are powerful tools that can be applied to study biological interactions [1]. The rapid initiation of biological reactions and examination of their time evolution, exposes information that is hidden in simple equilibrium experiments. This technique provides details on short lived intermediates, folding pathways and transition states.

While the benefits of non-equilibrium measurements are numerous, such techniques are rarely applied when compared to their equilibrium counterparts. The major bottle-neck is the lack of commercially available systems to perform these experiments. Only the stopped-flow technique is widely used, but requires high sample volumes, limiting the number of kinetic measurements that have been made. Additionally, in cases where kinetic measurements are applied, the experiments report bulk averages. Therefore, sparse or short-lived intermediates are challenging to identify, and careful analysis is required to resolve the presence of other intermediate states along reaction pathways [2].

Coupling microfluidic mixing to single-molecule fluorescence circumvents the above challenges. Examination of single molecules allows resolution of individual subpopulations within a sample, nanomolar concentrations are used, and ~ms timescales are accessible using microfluidics, with sparse sample consumption [3]. We previously designed and fabricated microfluidic mixing devices using SU-8 and glass, however this protocol had some disadvantages. The number of devices per wafer was limited by the use of standard sized glass coverslips, and device robustness and fluorescence background were compromised due to the use of an SU-8 sealing layer.

To bypass these limitations, we developed a fabrication protocol where channels are etched into silicon. Full wafers are subsequently anodically bonded to full sized glass wafers to seal devices. The protocol is schematically shown in Figure 1.

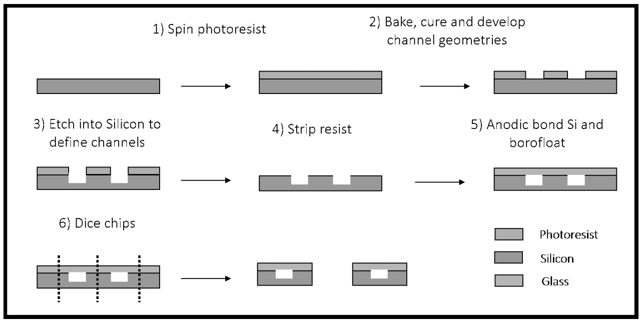

Figure 1: Fabrication process utilized to obtain a large number of robust microfluidic mixing devices.

In brief, a 4 µm thick layer of Shipley resist is spun, baked, and cured on a standard sized silicon wafer. Channel patterns are exposed, and the resist developed. The microfluidic channels are then etched into the silicon using the Plasma-Therm deep silicon etcher — we aim for channel depths of 105 µm. After etching, the resist is removed. The etched silicon piece and a 170 µm thick, full wafer sized borofloat wafer are Piranha cleaned before anodic bonding using the substrate bonder. As a final step, the dicing saw separates individual devices, and liberates channel cross-sections at the edges of each device. Interfacing to the devices is complete by gluing 105 µm outer diameter glass capillary lines into the revealed sockets with UV curable epoxy.

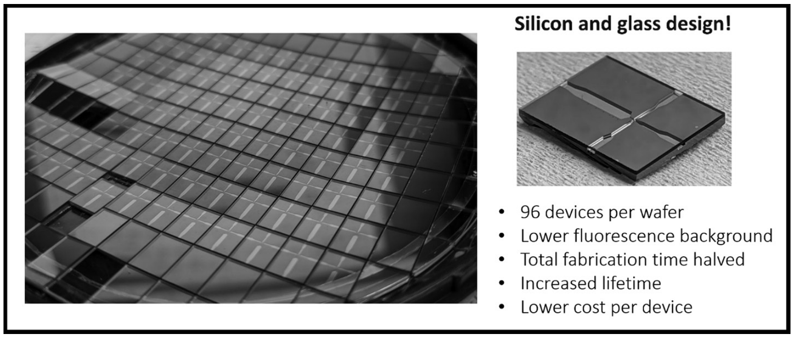

Silicon and glass design!

- 96 devices per wafer
- Lower fluorescence background
- Total fabrication time halved
- Increased lifetime
- Lower cost per device

Figure 2: The left shows a wafer of microfluidic devices after the final dicing step. On the right is a stereoscope image of a single device. The thin glass layer can be seen covering the base silicon wafer. Sockets liberated during dicing process are present at the end of the channel and facilitate the connection of fluid lines using UV curable epoxy.

A full wafer of separated devices is shown in Figure 2. Ninety-six devices are made in the same process. On the right, a stereoscope image of a single device from this wafer is shown.

In the stereoscope image, the sockets that interface with external lines are clearly visible. The thin glass layer on top of the silicon base layer is also resolved. Fabrication of devices without an extra adhesive layer in between glass and channel geometries grants higher pressure resilience (as we limit crack propagation at the sealing layer) and reduces the intrinsic fluorescence background from SU-8 and similar epoxies.

Conclusions and Future Steps:

Here we describe an improved fabrication protocol that yields silicon microfluidic mixers as opposed to recent past efforts using glass and SU-8. This new protocol creates many more devices per wafer, at lower cost and reduced fabrication time per piece. We are now positioned to pursue non-equilibrium RNA folding experiments without concern for device robustness, lifetime or inventory.

References:

[1] Al-Hashimi, H. M.; Walter, N. G. Curr. Opin. Struct. Biol. 2008, 18 (3), 321.

[2] Daniels, K. G.; Suo, Y.; Oas, T. G. Proc. Natl. Acad. Sci. 2015, 112 (30), 9352.

[3] Wunderlich, B.; Nettels, D.; Benke, S.; Clark, J.; Weidner, S.; Hofmann, H.; Pfeil, S. H.; Schuler, B. Nat. Protoc. 2013, 8 (8).

Body-on-a-Chip Systems for Studying Liver Metastasis

CNF Project Number: 731-98

Principal Investigator(s): Michael L. Shuler, Harold G. Craighead

User(s): Ying Wang, Paula Miller, Vivek Sitaram Jadhav

Affiliation(s): Nancy E. and Peter C. Meinig School of Biomedical Engineering, Robert Frederick Smith School of Chemical and Biomolecular Engineering; Cornell University

Primary Source(s) of Research Funding: National Center for Advancing Translational Sciences, National Science Foundation, National Institutes of Health

Contact: mls50@cornell.edu, hgc1@cornell.edu, ying.wang@cornell.edu, pgm6@cornell.edu, vj76@cornell.edu

Primary CNF Tools Used: VersaLaser engraver/cutter tool, ABM contact aligner, SU-8 hot plates, SUEX/ADEX laminator, PDMS casting station, hot press, ObJet30 Pro 3D printer

Abstract:

Our organ-on-a-chip devices are physiological tissue-engineered microsystems that mimic human organs, structurally and functionally [1]. Human cell-based multi-organ on-a-chip systems, could be used for drug development [2], simulate human physiology and disease progression. The organ-organ interactions offer more accurate predictions of human responses to therapeutics and provide mechanistic insights into human diseases, while significantly reduce drug development cost and animal usage. Currently, we are developing several microphysiological systems, which are fabricated with tools at CNF, and will be used to study chemotherapeutic toxicity, model cancer cell metastasis, and simulate immune responses.

Summary of Research:

Here, we describe two unidirectional metastatic devices to study colon cancer metastasis and the human liver sinusoidal vasculature for colon cancer extravasation. The both devices have unidirectional flow; colon-liver chip is "pumpless" using a rocker platform for fluid (blood surrogate) unidirectional recirculation and the liver sinusoidal vascular chip is a gravity-driven single pass microfluidic platform.

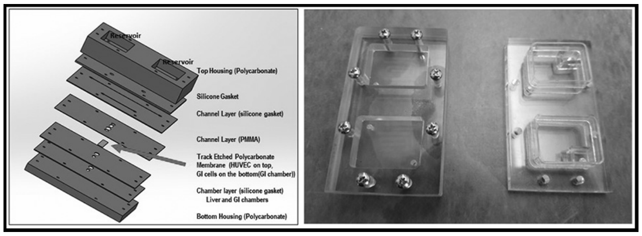

Figure 1: Design of the two-chamber unidirectional device for liver metastasis. Schematic view and actual photographs of the assembled frames.

Colon-Liver Chip:

We have modified our original dual-organ-on-a-chip system to model colorectal cancer (CRC) liver metastasis. This microphysiological system is based on a pumpless platform [3,4]. Two organ chambers representing colon and liver are interconnected and perfused with gravity-driven flow at physiological perfusion rates [5]. The frame was milled out of a polycarbonate sheet with silicone gaskets to help seal the device. Microfluidic channels, chambers and medium reservoirs were patterned with laser ablation into a poly(methyl methacrylate) (PMMA) sheet and/or silicone sheets using the VersaLaser VLS3.60 Cutting and Engraving CO_2 Laser (Universal Laser Systems, Scottsdale, Arizona) at CNF. The flow dynamics were characterized computationally and experimentally. Flow rates were measured to be within 15% of the designed values. The prototype devices tested with colon and liver cells maintained greater than 85% cell viability.

Using this colon-liver platform, we will incorporate organotypic CRC model and 3D liver constructs to investigate the metabolic stress due to CRC liver metastasis. We will investigate the cellular interaction, differentiation, migration and invasion of primary tumor and metastatic fibroblast tumor microenvironment to evaluate contributing factors in CRC metastasis [Fig.1].

Liver Sinusoidal Vascular Chip:

We have designed and constructed a gravity-driven microfluidic platform for modeling the human liver sinusoidal microenvironment and investigating the extravasation of liver metastatic colorectal cancer (CRC) cells. The frame was fabricated in poly(methyl methacrylate) (PMMA). PMMA layers of desired thickness were patterned using a CO_2 laser (VersaLaser VLS3.50), and were bond together using a hot press at CNF after a 15 min UV/Ozone (Samco UV and Ozone stripper) exposure. Also, flow-through microfluidic channels and chambers were patterned with laser ablation into silicone sheets using the VersaLaser. A propeller stirring device was designed in Inventor to overcome the issue of settling, attachment and aggregation of CRC cells in the feed reservoirs. The propeller stirring device was fabricated using the ObJet30 Pro 3D printer at CNF.

The stirring device was driven by a small stir bar on a magnetic stirrer. We have tested different propeller designs, the positioning in the reservoir, and the stirring speed, to optimize stirring scheme that produced minimal cell aggregation while preserving maximal cell viability. We are currently focusing on characterizing the phenotype of liver sinusoidal endothelial cells in our microfluidic model and comparing CRC cell interactions with human liver sinusoidal endothelial cells versus human umbilical vascular endothelial cells [Figure 2].

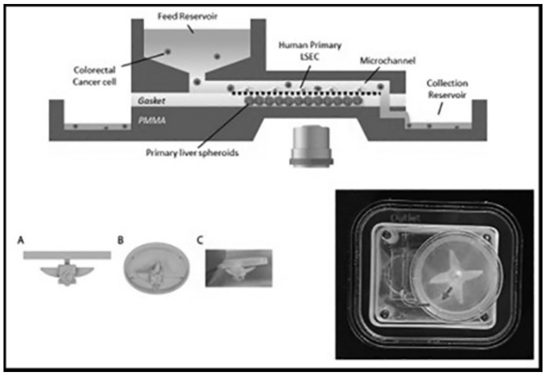

Figure 2: Design of the human liver sinusoidal vasculature for colon cancer extravasation. Schematic views of the device and the propeller stirring device with actual photographs.

References:

[1] Wang YI, Carmona C, Hickman JJ, Shuler ML. Multiorgan Microphysiological Systems for Drug Development: Strategies, Advances, and Challenges. Adv Healthc Mater;7:1701000. doi.org/10.1002/adhm.201701000.2 (2018).

[2] Sung JH, Wang YI, Narasimhan Sriram N, Jackson M, Long C, Hickman JJ, et al.Recent Advances in Body-on-a-Chip Systems. Anal Chem;91:330-51. doi.org/10.1021/acs.analchem.8b05293.3 (2019).

[3] Price PS, Conolly RB, Chaisson CF, Gross E a, Young JS, Mathis ET, Tedder DR. Modeling interindividual variation in physiological factors used in PBPK models of humans. Crit Rev Toxicol.;33(5):469-503. doi:10.1080/713608360 (2003).

[4] Brown RP, Delp MD, Lindstedt SL, Rhomberg LR, Beliles RP. Physiological Parameter Values for Physiologically Based Pharmacokinetic Models. Toxicol Ind Health.;13(4):407-484. doi:10.1177/074823379701300401 (1997).

[5] Forrester DW, Spence VA, Walker WF. The measurement of colonic mucosal.submucosal blood flow in man. J Physiol.;299(1):1-11. doi:10.1113/jphysiol.1980.sp013106 (1980).

Mechanical Unzipping of DNA Molecules in Parallel Using Nanophotonic Tweezers

CNF Project Number: 1738-08

Principal Investigator(s): Michelle D. Wang

User(s): Fan Ye, Yifeng Hong

Affiliation(s): a) Department of Physics, Cornell University; b) Howard Hughes Medical Institute

Primary Source(s) of Research Funding: Howard Hughes Medical Institute

Contact: mdw17@cornell.edu, fy72@cornell.edu, yh874@cornell.edu

Website: http://wanglab.lassp.cornell.edu/

Primary CNF Tools Used: ASML deep ultraviolet stepper, Oxford 100 plasma etcher, Unaxis 770 deep Si etcher, Heidelberg mask writer DWL2000, SÜSS MA6-BA6 contact aligner, Gamma automatic coat-develop tool, LPCVD nitride - B4 furnace, wet/dry oxide - B2 furnace, N2 annealing - B1 furnace, AJA sputter deposition, CVC sputter deposition, GSI PECVD, Oxford PECVD, SC4500 odd-hour evaporator, Zeiss Supra SEM, Zeiss Ultra SEM

Abstract:

Optical trapping has become a major technique widely used in biological and materials sciences, on size scales ranging from the single molecule to the cellular level, and force scales ranging from sub piconewton (pN) to tens of pN [1]. The rapid development of nanofabrication techniques in the past few decades has bolstered the emergence of nanophotonic evanescent-field traps. The ability of nanostructures to direct and confine light beyond the diffraction limit enables miniaturized, on-chip devices with abilities beyond traditional microscope-based optical tweezers [2,3]. The Wang lab has developed and implemented such an on-chip device based on Si or Si_3N_4 waveguides, coined a nanophotonic standing-wave array trap (nSWAT), that allows for controlled and precise manipulation of trapped single biomolecule (such as DNA) arrays via microparticle handles [4-7]. We present here the latest development of the nSWAT platform based on a resonator design that achieves large enough manipulation forces for mechanical unzipping an array of DNA molecules. This benchmark achievement is one step closer to the full realization of nanophotonic tweezers' capabilities, promising increased accessibility and expansion of these platforms to a wide range of biological and biomedical research topics.

Summary of Research:

Over the past decade, the Wang lab has demonstrated a high-throughput, near-field nanophotonic trapping platform that achieves stable trapping and precision manipulation of microparticles [4-7]. The kernel of this platform is the formation of standing waves along a nanophotonic waveguide: by counter propagating two coherent laser beams along a single mode nanophotonic waveguide. The antinodes of the standing wave form an array of stable optical traps. We call this type of trap a nanophotonic standing-wave array trap (nSWAT). By tuning the phase difference between the two counter-propagating laser beams via thermo-optic effect, the antinode locations can be precisely repositioned, and consequently, the optical trap positions can be precisely manipulated. The nSWAT platform holds the capability for high throughput precision measurements for single biomolecules.

Since 2018, we have implemented major upgrades of the nSWAT platform, including the following three aspects.

(1) We have implemented a resonator-based design for ultimate local intensity enhancement into the nSWAT devices. Compared to previous designs, this resonator design gives the highest force enhancement factor, limited only by the total scattering loss of the trapped beads onto the waveguide. We have measured around four times force enhancement, reaching > 30 pN, significantly larger than our previous force-double design [6].

(2) We have implemented a balanced layout and differential operation mode for the micro heaters. This greatly reduced the response time of the micro heaters (from ~ 30 μs to ~ 1 μs). This is shown to be crucial

for maintaining high trapping forces for a trapped bead under strong biased forces under single molecule manipulations.

(3) We have also designed a special sample holder for the nSWAT chip that can greatly reduce (by two orders of magnitude) the thermal drift of the sample caused by the micro heaters. This greatly enhanced the thermal stability of the nSWAT devices. Thanks to the above described improvements, we have achieved mechanical DNA unzipping on the nSWAT devices for the first time.

In the past year, we have continued optimizing the nSWAT platform to achieve our final goal of unzipping an array of DNA molecules. We have further optimized the flow chamber design of the nSWAT devices to achieve better DNA molecule trapping efficiency. We have also implemented SU-8 layer as the anti-corrosion protection layer for the nSWAT device which works significantly better than the Si_3N_4 protection layer we used before [5]. With all these improvements, we are looking forward to the achievement of trapping and unzipping an array of DNA molecules in the near future. Our development and improvement of the nSWAT platform has led to seven publications in the past few years [2-7], and more to come later this year.

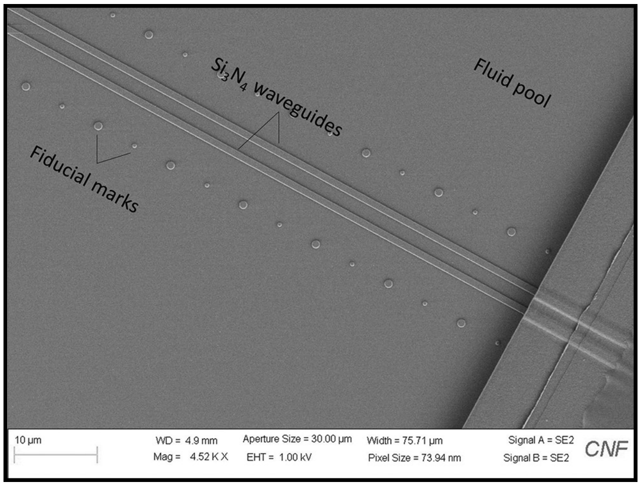

Figure 1: An SEM image of the step boundary of the fluid pool region. Inside the fluid pool region, the two parallel Si_3N_4 waveguides trap two arrays of polystyrene microbeads (380 nm diameter) with DNA molecules tethered in between. The dot arrays near the parallel waveguides are fiducial marks for local position tracking.

References:

[1] J. L. Killian, F. Ye, M. D. Wang, "Optical Tweezers: A Force to Be Reckoned With" Cell 175 (6), 1445-1448 (2018).

[2] J. E. Baker, R. P. Badman, and M. D. Wang, "Nanophotonic trapping: precise manipulation and measurement of biomolecular arrays" WIREs Nanomed Nanobiotechnol. e1477 (2017).

[3] R. Badman, F. Ye, M.D. Wang, "Towards biological applications of nanophotonic tweezers" Current Opinion in Chemical Biology 53, 158-166 (2019).

[4] M. Soltani, J. Lin, R. A. Forties, J. T. Inman, S. N. Saraf, R. M. Fulbright, M. Lipson, and M. D. Wang, "Nanophotonic trapping for precise manipulation of biomolecular arrays" Nature Nanotechnology 9(6), 448-452 (2014).

[5] F. Ye, R. P. Badman, J. T. Inman, M. Soltani, J. L. Killian, and M. D. Wang, "Biocompatible and high stiffness nanophotonic trap array for precise and versatile manipulation" Nano Letters 16(10), 6661-6667 (2016).

[6] F. Ye, M. Soltani, J. T. Inman, and M. D. Wang, "Tunable nanophotonic array traps with enhanced force and stability" Optics Express 25 (7) 7907-7918 (2017).

[7] R. Badman, F. Ye, W. Caravan, and M. D. Wang, "High Trap Stiffness Microcylinders for Nanophotonic Trapping" ACS Appl. Mater. Interfaces 11 (28), 25074-25080 (2019).

Bacterial Mechanics and Mechanobiology

CNF Project Number: 1970-10

Principal Investigator(s): Christopher J. Hernandez

User(s): Christine E. Harper, Melanie F. Roberts, Junsung Lee

Affiliation(s): Sibley School of Mechanical and Aerospace Engineering,
Meinig School of Biomedical Engineering, Cornell University

Primary Source(s) of Research Funding: Army Research Office Grant Number W911NF-19-1-0121

Contact: cjh275@cornell.edu, ceh272@cornell.edu, mfr75@cornell.edu, jl3939@cornell.edu

Website: hernandezresearch.com

Primary CNF Tools Used: ASML, Oxford 100, AJA sputter deposition, VersaLaser, MOS clean anneal

Abstract:

Bacteria naturally experience mechanical forces in the environment. Mechanical stresses and strains are generated as bacteria swim in fluids, attach to surfaces, grow in biofilms, and even during normal internal pressure homeostasis. Recent studies have shown that bacteria can sense and respond to mechanical forces, and mechanical stress and strain can influence cell division, cell shape, virulence, biofilm initiation, motility, and toxin resistance. However, because of the small scale of bacteria, it is a challenge to apply controlled mechanical stimuli on a single cell level. We developed a microfluidic platform to apply mechanical loads to single bacteria cells *in vivo*. We used this microfluidic platform as a method of applying mechanical stimuli to *Escherichia coli* (*E. coli*) and determining how mechanical stress affects a group bacterial cell envelope proteins used for toxin and antibiotic resistance. In addition, we are using this microfluidic device in the first step toward determining the mechanical properties of the bacterial cell envelope.

Summary of Research:

Our work involves the use of microfluidic devices as tools for mechanical testing of live bacteria. Within our devices, individual bacteria are flowed into tapered channels and trapped (Figure 1). The bacteria experience mechanical loading from the hydrostatic fluid pressure as well as contact with the tapered channels walls (Figure 2). Key advantages of this microfluidic platform include minimal sample preparation, no chemical immobilization or labeling, the ability to analyze hundreds of cells at once, and the ability to apply different magnitudes of mechanical loading to different bacteria simultaneously [1]. We manufactured devices on silica glass wafers using deep UV photolithography to achieve nanoscale features (250 nm smallest dimension). These glass-on-glass devices were manufactured using the ASML, Oxford 100, AJA sputter deposition, VersaLaser, and MOS clean anneal tools at the Cornell NanoScale Science and Technology Facility.

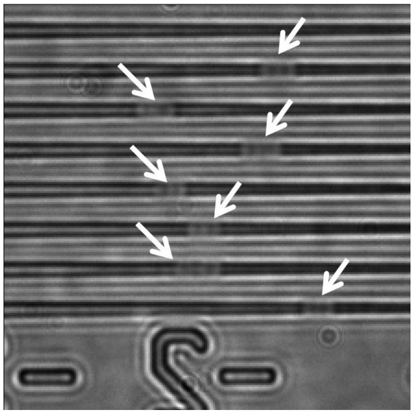

Figure 1: E. coli *cells trapped within the tapered channels of the microfluidic device. Fluid pressure is used to flow the bacteria into the tapered channels.*

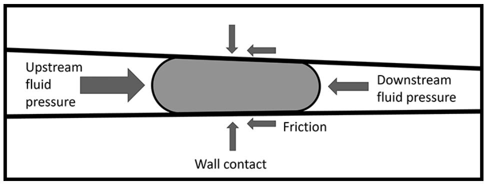

Figure 2: The bacteria cells experiences mechanical loading in the tapered channels due to the hydrostatic pressure, which varies from the upstream end to the downstream end, and due to contact with the walls of the tapered channel.

Recently we have investigated the effects of mechanical stress and strain on the functionality of multicomponent efflux complexes in bacteria. Multicomponent efflux complexes create channels that cross the cell envelope of bacteria and are used to remove toxins including metal ions and antibiotics. Since multicomponent efflux complexes form a rigid link across the cell envelope, we targeted them as being sensitive to changes in cell envelope stress caused by mechanical loading in our microfluidic device. Our data suggests that the assembly and function of the multicomponent efflux

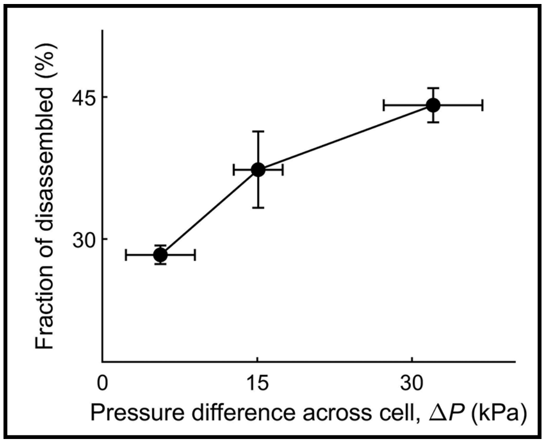

Figure 3: Increased pressure difference across the cell, which correlates with increased applied mechanical load, was shown to increase disassembly of the multicomponent efflux complex CusCBA in E. coli*.*

complex CusCBA in *E. coli* is impaired by increased mechanical stress. Increased applied mechanical stress due to increased pressure in our microfluidic device was shown to promote disassembly of the CusCBA efflux complex (Figure 3). Disassembled CusCBA complexes are nonfunctional and incapable exporting copper ion toxins, suggesting copper ion resistance of mechanically stressed cells is reduced [2]. We are currently investigating if mechanical stress in the cell envelope affects other trans-envelope multicomponent complexes. Preliminary evidence shows that assembly of the multicomponent efflux complex MacABTolC, a multicomponent efflux complex that contributes to macrolide antibiotic resistance, is also sensitive to mechanical stress [3].

Conclusions and Future Steps:

So far, we have seen that in *E. coli* mechanical stress and strain impairs the proper assembly and function of some of the cellular machinery needed for toxin and antibiotic resistance. In the future we will focus on using our microfluidic device to quantify the mechanical properties of the bacterial cell envelope. Establishing a reliable method of measuring the mechanical properties of the bacterial cell envelope will help us identify subcellular components that contribute to bacterial mechanics as well as how different environmental factors such as antibiotic treatment can change bacterial mechanical properties. Measuring bacterial mechanical properties has historically been quite challenging and has mostly been limited to atomic force microscopy measurements using fixed bacteria, which has limitations due to uncertain boundary conditions and difficulties separating internal pressure from membrane elasticity [4]. We are working to better understand bacterial mechanical properties by combining experimental data from the microfluidic devices with finite element modelling to calculate numerical estimates for the Young's Modulus of the bacterial cell envelope.

References:

[1] X. Sun, W.H. Weinlandt. H. Patel, M. Wu, C.J. Hernandez. (2014) "A Microfluidic Platform for Profiling Biomechanical Properties of Bacteria." Lab Chip. 14 (14), 2491-2498. NIHMS600175.

[2] L.A. Genova, M.F. Roberts, Y.C. Wong, C.E. Harper, A.G. Santiago, B. Fu, A. Srivastava, W. Jung, L.M Wang, Krzemiski, X. Mao, X. Sun, C.Y. Hui, P. Chen, C.J. Hernandez. (2019) "Mechanical stress compromises multicomponent efflux complexes in bacteria". Proceedings of the National Academy of Sciences U. S. A. 116 (51) 25462-25467.

[3] C.E. Harper, W. Zhang, P. Chen, C.J. Hernandez. (2020) "Mechanical stress promotes disassembly of the antibiotic efflux complex MacAB-TolC". Biophysical Society Annual Meeting. San Diego, CA, USA.

[4] C.E. Harper, C.J. Hernandez. (2020) "Cell biomechanics and mechanobiology in bacteria: Challenges and opportunities". Applied Physics Letters Bioengineering. 4 (2) 201501.ß

Robotic Microswimmers Powered by Ultrasound for Biomedical Applications

CNF Project Number: 2068-11
Principal Investigator(s): Mingming Wu
User(s): Tao Luo

Affiliation(s): Department of Biological and Environmental Engineering, Cornell University
Primary Source(s) of Research Funding: National Cancer Institute
Contact: MW272@cornell.edu, TL565@cornell.edu
Primary CNF Tools Used: Heidelberg mask writer-DWL2000, ABM contact aligner, scanning electron microscope (SEM)

Abstract:

Microrobotics, an interdisciplinary field that combines robotics, micro/nanotechnology, biomedical engineering, and materials science, paves a novel way for biomedical applications, such as targeted drug and/or cell delivery for cancer therapy. However, the technology itself is still at an infant stage before reaching the full potential for various biomedical applications. In this project, we are aiming to develop an untethered microrobotic swimmer that can be propelled and navigated in liquids using an external ultrasound. A challenging aspect of the project is to develop the nano-size flagellum that can be used to propel the robotic swimmers in fluids. As a first step of this project, we engineered a microcantilever that will be used as the micropropeller for the microswimmer. This SU-8 microcantilever was fabricated using a two-layer photolithography along with a sacrificial layer for releasing.

Summary of Research:

Robotic microswimmers, which have the capability to be propelled and navigated wirelessly in biological fluid, can open new doors for addressing very challenging issues in biomedical fields, such as targeted drug delivery. However, the size of microswimmers, which is usually smaller than one millimeter, made it difficult for on-board integration of components, such as batteries and motors. Hence, novel powering and propulsion mechanisms are demanded. Studies on using various untethered external power sources showed that magnetic and ultrasonic waves were the most promising candidates for *in vivo* applications. In contrast to magnetic actuation, ultrasonic wave has the advantages of low cost and long distance control. Here, we designed a simple microcantilever for the studies of cantilever fluid interaction, in particular, the fluid streaming behavior when the cantilever is under resonance. This study will lay a foundation for the micro-propeller design in future work.

To fabricate the microcantilever structure, we have developed a modified two-layer SU-8 process along with a sacrificial layer (PVA) release method. First, a two-layer SU-8 structure was fabricated on a PVA coated 4-inch silicon wafer by using the standardized alignment photolithography (Figure 1A). Here, the pattern of the bottom layer consists of the cantilevers and that of the top layer supporting structures for the cantilever. (See Figure 1A).

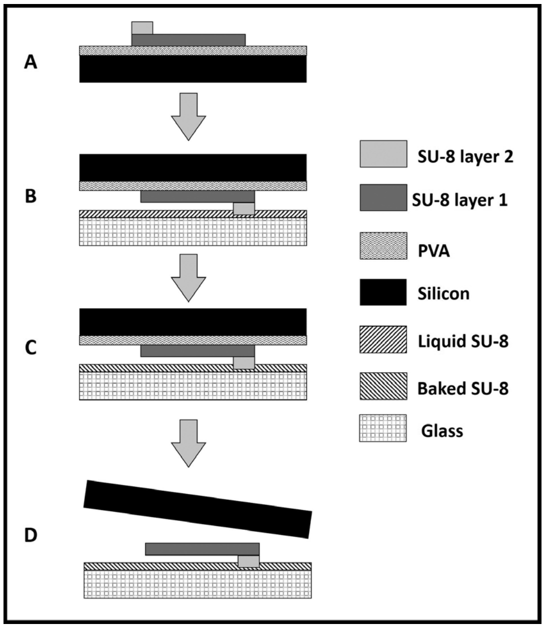

Figure 1: Fabrication process of the SU-8 microcantilever. (A) A two-layer SU-8 structure is fabricated on the PVA coated Si wafer by using alignment photolithography of two SU-8 layers. (B) PVA coated Si wafer with two-layer SU-8 structures is flipped and put on glass slide with a thin layer of liquid SU-8. (C) The sandwiched device is baked to solidify the liquid SU-8 layer on the glass slide. (D) The sandwiched device is immersed into water for 30 min to dissolve the PVA layer and release the Si wafer.

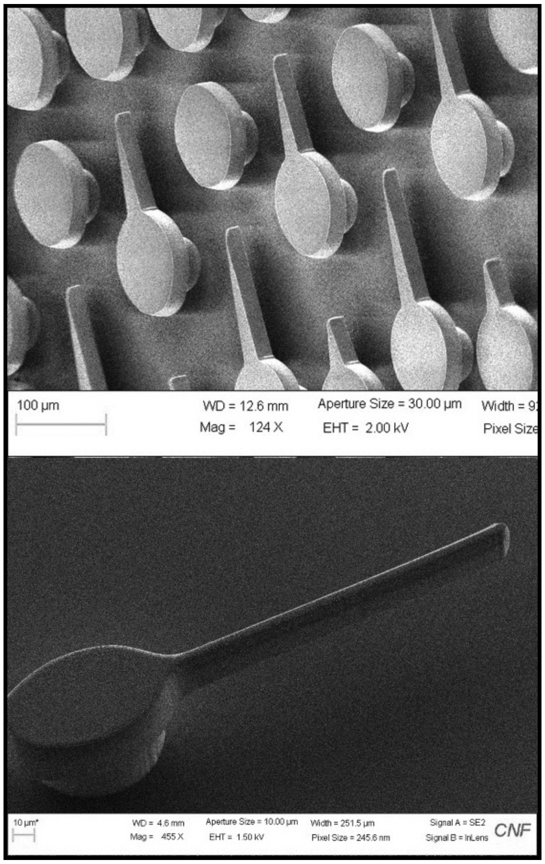

Figure 2: SEMs of SU-8 microcantilevers on glass slides.

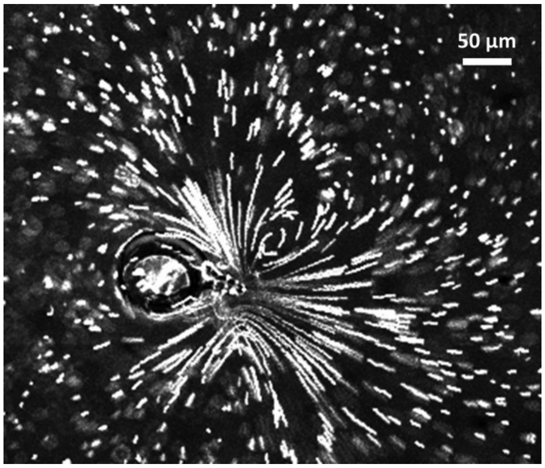

Figure 3: Acoustic streaming of a microcantilever in water revealed by fluorescent microsized beads when the cantilever is excited by the 1.35 MHz ultrasound.

Second, the silicon wafer with the two-layer SU-8 structures was flipped and put on a glass slide, which has been coated with a liquid SU-8 layer (Figure 1B). Then, the sandwiched structure was placed on the hot plate and baked under 95°C for 15 min to solidify the liquid SU-8 layer (Figure 1C). In this way, the second SU-8 layer from the silicon wafer was glued on the glass slide. After cooling down with the hot plate, the sandwiched structure was immersed into water for 30 min to dissolve the PVA layer, and the two-layer SU-8 structure was transferred from the silicon wafer to the glass slide (Figure 1D). In this way, the first and second layer of SU-8 on the silicon wafer has been flipped on the glass slide, which formed a cantilever structure.

The quality of the fabricated microcantilevers can be very good, even for structures with high aspect ratios (Figure 2).

The fabricated microcantilevers were immersed into the water, and an ultrasonic transducer was used to transmit ultrasound waves in the water to excite the microcantilevers. We have tuned the frequency of the ultrasound waves to detect the resonance frequency of the microcantilever based on the magnitude and pattern of the streaming flow around the microcantilever. A dual vortex like flow pattern was visualized by putting 0.83 µm fluorescent polystyrene microbeads when the microcantilever was excited under its first resonance (Figure 3).

Conclusions and Future Steps:

In this work, we fabricated SU-8 microcantilevers by integrating a two-layer SU-8 photolithography method with a PVA sacrificial releasing method. The microcantilever was used as the simplest model for understanding the fluid-structure interaction under ultrasonic excitation. We had successfully excited the fabricated microcantilever remotely by using ultrasound and observed the streaming flow for the first vibration mode of the microcantilever. Future study will be quantitatively characterizing the propulsion force generated by streaming flows under different excitation conditions.

Microfabrication of Fixed Length Sample Holders for Cryogenic Small Angle X-Ray Scattering

CNF Project Number: 2157-12

Principal Investigator(s): Robert Thorne

User(s): David Moreau

Affiliation(s): Cornell Laboratory of Atomic and Solid State Physics, Cornell University

Primary Source(s) of Research Funding: National Institutes of Health

Contact: ret6@cornell.edu, dwm265@cornell.edu

Primary CNF Tools Used: Heidelberg mask writer - DWL2000, SÜSS MA6-BA6 contact aligner, Oxford 80, Objet30 Pro 3D printer, VersaLaser engraver/cutter tool, YES polyimide curing oven, potassium hydroxide wet etch station

Abstract:

Small-angle X-ray scattering (SAXS) is a key tool for probing the structure and function of proteins, nucleic acids, and macromolecular complexes. Most synchrotron sources have dedicated BioSAXS beam lines, but efforts to improve their throughput have not kept pace with user demand. Large sample volumes and low duty cycles are critical bottlenecks in the expansion of BioSAXS. Cryogenic sample freezing overcame these bottlenecks in an analogous X-ray technique, macromolecular crystallography. Cryocooling significantly reduces the effects of X-ray radiation damage, reducing the necessary sample volume to collect adequate amounts of data, and eases the sample handling of sensitive or unstable samples. Likewise, CryoSAXS should require much smaller sample volumes per measurement, allow sample preparation in the home lab immediately after purification, easy sample storage and shipping, and automated high-throughput data collection. This will enable dramatically more efficient use of both biomolecules and synchrotron beam time, and significantly expand the potential scope of BioSAXS studies.

Summary of Research:

We envision CryoSAXS as a routine method analogous to cryocooling in macromolecular crystallography (MX). The reduction in radiation damage at T = 100 K significantly reduces the amount of protein required per measurement and sample holders compatible with standard macromolecular cryocrystallography (MX) infrastructure could be transformative step in increasing the throughput and potential of BioSAXS. CryoSAXS could be especially useful for high-throughput parameter and ligand interaction screening and for study of difficult to produce proteins or complexes, applications in which BioSAXS may have the greatest impact on human health.

Despite the demonstrations of its potential [1,2], the lack of a robust experimental platform has prevented CryoSAXS from becoming a routine experimental technique. The need to subtract a highly matched background scattering pattern from the macromolecule's scatter and the difficulty in vitrifying bulk-like solutions have posed serious technical challenges for the development of sample holders adequate for routine use. Shown in Figure 1 is a new generation of CryoSAXS devices we recently developed using microfabrication techniques at the Cornell NanoScale Science and Technology Facility (CNF).

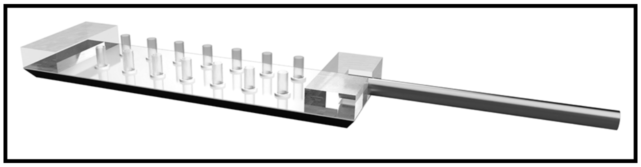

Figure 1: Computer generated image of CryoSAXS sample devices. The sample is held in place between two silicon nitride X-ray windows by Kapton tube. The X-ray passes axially through the tubing. Multiple sample cells are present in a single device in two rows. One row contains solutions with a macromolecule and the other is analogous solutions without the macromolecule to be used for background subtraction.

These devices constrain the sample held between two silicon nitride windows at a 1 mm fixed pathlength. Double-sided polished wafers coated in 500 nm of low-pressure chemical vapor deposited silicon nitride were procured from Silicon Valley Microelectronics. One side of the wafer was patterned with photoresist then dry etched to remove the nitride for a later potassium hydroxide (KOH) wet etch. SU-8 was deposited and patterned on the other side to serve as a hydrophobic layer to aid in the pinning of the sample to the X-ray windows. A KOH wet etch then formed the X-ray windows and diced the wafer. Spacers were laser cut from 1 mm thick quartz glass sheets then glued to one portion of the wafer pieces. Using laser cut jigs, 1 mm long Kapton tubing was cut and glued to the devices. The devices are filled from the open end of the tube, then a second wafer piece is affixed to the top of the device to seal the sample. The samples are then cryogenically frozen by plunging into liquid nitrogen (LN_2), stored in LN_2 and later mounted in an X-ray beam while being kept at T = 100 K by a cold gas stream.

X-ray data collection was performed at Cornell High Energy Synchrotron Source (CHESS) beamline ID7A1 for the protein apoferritin using 45% w/w propylene glycol as a cryoprotectant. Figure 2 shows results from apoferritin at three different protein concentrations. Figure 2a shows the background subtracted X-ray diffraction intensity. The inset shows this data in a Gunier plot. Deviations from linearity at low scattering angles are indicative poor data quality, including incorrect background subtraction at low scattering angles. The normalized Kratky plot in Figure 2b. This should go to zero at higher scattering angles for globular proteins such as apoferritin. Deviations indicate incorrect background subtraction at high scattering angles.

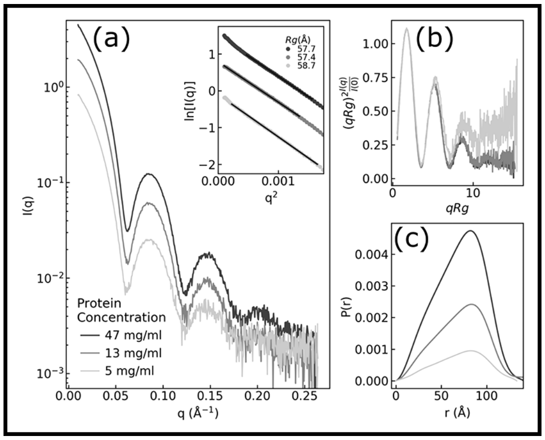

Figure 2: Background subtracted X-ray diffraction intensity from apoferritin at three different concentrations.

Conclusions and Future Steps:

The development and subsequent adoption of cryogenic methods for BioSAXS could significantly increase sample throughput and reduce sample consumption, enabling SAXS to extend to a larger user base. It could open up the possibility of new science through high-throughput screening of ligands or other therapeutics. CryoSAXS's potential has been known for a while, but critical technical challenges have prevented the widespread adoption of the method. A well-matched background for subtraction is necessary for SAXS and the cryocooling step tends to introduce significant variability to the background. X-ray scatter from ice present in the sample quickly overwhelms the scatter from the protein, as does parasitic scatter from a sample that has cracked under the stress induced by cryocooling. This new generation of devices is designed to maximize the sample's cooling rates and minimize internal stress. Future steps involve the refinement of this technique through iterative design.

References:

[1] Meisburger, S. P., et al., (2013) Biophys. J., 104, 227-236.

[2] Hopkins, J. B., et al., (2015) J. Appl. Cryst. 48, 227-237.

Dual-Gradient Microhabitat Platform for Microalgae Growth

CNF Project Number: 2262-13
Principal Investigator(s): Dr. Mingming Wu
User(s): Fangchen Liu

Affiliation(s): Department of Biological and Environmental Engineering, Cornell University

Primary Source(s) of Research Funding: United State Department of Agriculture - National Institute of Food and Agriculture

Contact: MM272@cornell.edu, FL373@cornell.edu
Website: biofluidics.bee.cornell.edu

Primary CNF Tools Used: Heidelberg mask writer - DWL2000, ABM contact aligner, P10 profilometer, MVD 100

Abstract:

The occurrence of harmful algal blooms (HABs) is increasing at an alarming rate worldwide, threatening water resources and aquatic ecosystems. Nutrients are known to trigger the onset of HABs and systematic investigation at a cellular level is lacking. To study the combination effects of multiple nutrients on microalgae growth in a high throughput way, a dual-gradient microhabitat platform was designed, fabricated, and characterized. Using the platform, the synergistic effect of nitrogen and phosphorous on the growth of model microalgal *Chlamydomonas reinhardtii* was revealed.

Summary of Research:

Harmful algal blooms, or HABs, are serious environmental problems, where a sudden growth of algae or cyanobacteria poses a threat to freshwater and marine ecosystems. HABs deteriorate drinking water quality and have huge environmental and economical costs. Nutrient enrichment is believed to be the fundamental cause of HABs, and climate change may further intensity the problem [1]. However, there lacks a quantitative/mechanistic understanding of the roles of environmental factors in the onset of HABs at a cellular level. The goal of this project is to investigate the synergistic roles of multiple environmental factors in the growth of cyanobacteria.

Environmental conditions known to affect algae growth include nutrients, mainly nitrogen (N) and phosphorous (P), light intensity and temperature. These conditions are hard to control in nature, and also cannot be quantified in a high throughput way in flasks and chemostats. Previously, a high throughput array microhabitat platform has been developed in our lab that is suitable for monitoring growth of photosynthetic microbes [2], which is capable of generating a stable single nutrient gradient. Using this platform, we discovered that the growth rates of *Chlamydomonas reinhardtii* (*C. reinhardtii*) in the presence of NH_4Cl gradient fit into a modified Monod kinetics model with the half saturation constant of NH_4Cl to be 1.2 ± 0.3 µM.

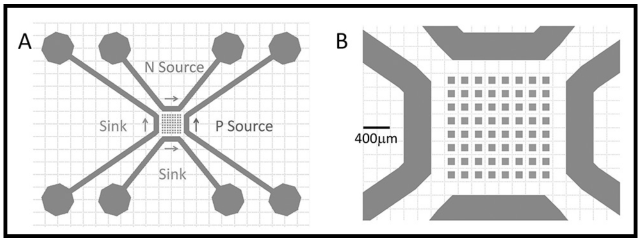

Figure 1: Dual-gradient microfluidic platform design. A. Top view of a device. B. A zoomed-in view of microhabitats and channel. The 8 × 8 array of 100 µm cubic habitats are separated by 100 µm from each other. These habitats are surrounded by four channels with width of 400 µm and height of 200 µm. N source and P source runs through the top and right channel respectively, and the other channels are sink channels. A gradient is generated for each chemical species in the microhabitat array region through molecular diffusion.

In this project, we developed a microhabitat platform that can provide dual nutrient gradients to facilitate a more realistic condition found in nature. The design of our device is shown in Figure 1, which consists of 64 microhabitats in the form of an 8 × 8 array and each habitat is 100 µm × 100 µm × 100 µm. The microhabitat array is surrounded by two sets of side channels each with the width of 400 µm and height of 200 µm. In each set of side channels, we can run source media (with N, or P) and blank media respectively, and a stable gradient can be simultaneously generated along vertical and horizontal directions.

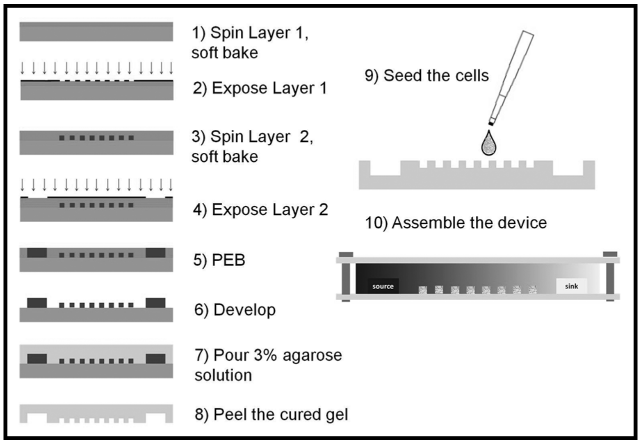

Figure 2: Schematics of a two-layer SU-8 photolithography procedure and the final microfluidic device assembly. First, a 100 µm resist layer was spun on a wafer, soft baked and exposed. Then, another 100 µm layer was spun on top and baked together overnight, followed by the second exposure and post exposure bake (PEB) for the 200 µm structures. The unexposed resist was then developed and the structures went through hard bake. For device assembly, the pattern was imprinted on an agarose gel, and cells were seeded in the microhabitats. The gel was then sandwiched between glass slide and manifolds and tightened by screws.

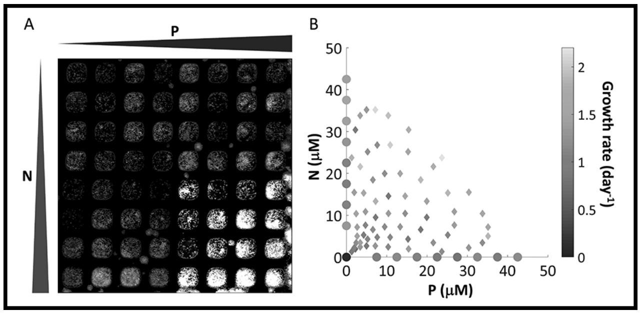

Figure 3: Growth of C. reinhardtii *under nutrients (N, P) gradient. A. Fluorescence images of nutrients co-limited cells growing under N and P dual gradients at day 4. B. The growth rate of* C. reinhardtii *under: control condition, no N or P (dot at the origin), single P gradient (dots on x axis), single N gradient (dots on y axis), and dual-gradient (all the diamonds). Shade is coded for the value of the growth rate.*

Soft lithography was used to make this dual-gradient microhabitat platform, which involves fabricating the silicon master mold and molding the pattern onto agarose gel for device assembly. Schematics of the step by step procedure are shown in Figure 2. The silicon master mold was fabricated using two-layer SU-8 negative resist photolithography, since the channels are 200 µm high and the microhabitats are 100 µm high. The post exposure bake (PEB) of the first layer of photo resist was combined with the soft bake of the second layer of the photo resist. Also, it was found that slow temperature ramping and relaxation time after each bake is critical to minimize internal stress in order to prevent resist detachment problem. After developing, the height of the feature was measured using the P10 profilometer, and a layer of FOTS was deposited using molecular vapor deposition (MVD 100) to increase the surface hydrophobicity for easier demolding of agarose gel. To transfer the pattern, boiled 3% agarose solution was poured on the silicon master and peeled once it cured. The gradient behavior of this dual-gradient platform was characterized using fluorescent dyes (for details see reference [3]).

The platform was used to study the growth of *C. reinhardtii* under nitrogen (N) and phosphorous (P) gradients. Experiments with N, P co-limited cells showed that N and P synergistically promoted cell growth (Figure 3A), while no discernible response was observed when single N or P gradient was imposed [3]. Growth rates under single gradient, dual-gradients, and control conditions were obtained and organized in Figure 3B, which could benefit the quantitative study of microalgal growth. These results proved the enabling power of the dual-gradient microhabitat platform in screening effects of multiple environmental factors in photosynthetic cell growth [3].

References:

[1] Paerl, Hans W., et al. Environmental Science and Technology (2018): 5519-5529.

[2] Kim, Beum Jun, et al. Lab on a Chip 15.18 (2015): 3687-3694.

[3] Liu, Fangchen, et al. Lab on a Chip 20.4 (2020): 798-805.

Metasurface-Enhanced Infrared Spectroscopy for Real-Time Measurement of Live Cells

CNF Project Number: 2472-16

Principal Investigator(s): Gennady Shvets

User(s): Steven He Huang, Po-Ting Shen, Jiaruo Li

Affiliation(s): Applied and Engineering Physics, Cornell University

Primary Source(s) of Research Funding: Cornell University internal funding

Contact: gs656@cornell.edu, hh623@cornell.edu, ps944@cornell.edu, jl2596@cornell.edu

Website: http://shvets.aep.cornell.edu

Primary CNF Tools Used: JEOL 9500, SC4500 evaporator, Zeiss Supra SEM, PDMS casting station, Anatech resist strip

Abstract:

Infrared (IR) spectroscopy for the label-free, nondestructive analysis of biological samples is a rapidly expanding area of research. When combined with multivariate statistical analysis and machine learning techniques, IR spectroscopy has been shown to be a powerful tool that can distinguish different types of tissues and cells. However, current applications of IR spectroscopy for live cells are limited due to the strong attenuation of IR light in water. In our lab, we have developed Metasurface-Enhanced Infrared Spectroscopy (MEIRS) as a novel tool to perform spectral analysis of live cells in standard cell culture conditions. The cells are cultured on plasmonic nanoantennas (metasurface), and the plasmonic hotspots are used to enhance the IR signal. We have used MEIRS to track the changes in the cells *in situ* as they are introduced to different stimuli. We are also investigating the combination of MEIRS with electrical-impedance sensing to create a multi-modal cellular assay.

Summary of Research:

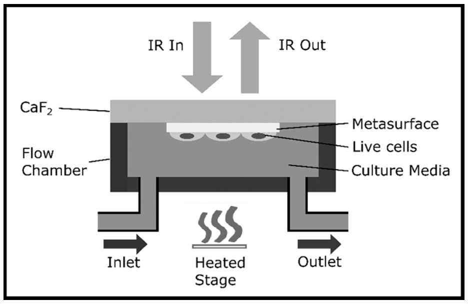

Figure 1: Schematic drawing of the flow-chamber setup for in situ *IR spectroscopy of live cells.*

Infrared (IR) spectroscopy is widely used to identify chemical compounds through their molecular vibration fingerprints.

Recently, IR spectroscopy has found applications in biological analysis as a tool for histology and cytopathology, identifying tumor tissues from normal tissues and monitoring the effect of chemotherapeutics on cancer cells. However, IR light is strongly attenuated in water, and thus traditional IR spectroscopy often involves fixing and drying the biological sample, limiting its utility as a cellular assay. We have developed a novel technique that we named metasurface-enhanced infrared spectroscopy (MEIRS) to measure live cells in physiological conditions.

In MEIRS, cells are seeded on a planar array of gold plasmonic nanoantennas called metasurfaces. These resonant nano-antennas support plasmonic hot spots in their vicinity, enhancing the light-matter interaction. The IR absorption signal from cells interacting with these plasmonic hot spots can be measured through the reflected light, overcoming the attenuation in water.

In the past, we have used this metasurface for the IR spectroscopy of protein monolayers [1] as well as fixed and dried cells [2]. Our current work focus on further extending this technique to the measurement of live cells on the metasurface, monitoring their changes in response to different compounds.

The plasmonic metasurfaces are fabricated in the CNF cleanroom. Metasurfaces are fabricated on IR-transparent CaF_2 substrates. First, patterns are defined on poly(methyl methacrylate) (PMMA) using electron beam lithography with the JEOL 9500 system. This is followed by gold evaporation and lift-off in acetone to create the gold nanoantennas.

Once the fabrication is done, Anatech resist strip is used to clean the metasurface and remove any resist residues. To perform *in situ* spectroscopy with live cells, we use a polydimethylsiloxane (PDMS) based flow chamber to maintain physiological conditions, which is also fabricated at the CNF. A schematic drawing of our measurement setup is shown in Figure 1.

Human squamous carcinoma cell line A431 cells were seeded on metasurfaces coated with fibronectin. Scanning electron microscope (SEM) images of the cells on the metasurface (Figure 2) shows that the cells preferentially attach to the gold nanostructures rather than the CaF_2 substrate. The interaction between the cells and the metasurface is still under investigation, but cellular attachment on gold nanoantennas implies that there is a significant spatial overlap between the plasmonic hotspot and the cells, which can lead to a strong enhancement in the detected signal.

We have monitored the response of A431 cells to 10 mM methyl-beta-cyclodextrin (MBCD), a compound known to extract cholesterol from the cellular membrane. The result was analyzed by principal component analysis (PCA) followed by promax rotation (Figure 3). Two different cellular processes, with different spectral features as well as temporal dynamics, can be seen. We attribute component 1 to the detachment of adhesion sites from the metasurface, while component 2 is thought to reflect changes in IR light scattered by the cells due to changes in cell morphology. We also found significant changes in the IR absorption from lipids right after MBCD was added to the flow chamber, which is attributed to the cholesterol extraction from the cellular membrane.

We are also investigating the combination of electrical impedance-based measurement with our metasurface-enhanced spectroscopy. The cell electrical impedance sensing (ECIS) is a proven technique to monitor *in situ* cell behaviors. The technique involves growing the cells on a surface with patterned microelectrodes and monitoring the changes in electrical impedance as the cells undergo certain changes.

Figure 4 shows A431 cells on the microelectrodes in our prototype device. The electrodes are connected to an impedance analyzer (we use an oscilloscope for preliminary tests) that uses AC voltage to measure the voltage and current across the attached cells. The electrodes of ECIS must be patterned in a specific way such that the attached cells block the current between electrodes. Different phases of cell attachment, spreading, migration, and proliferation can be distinguished through the change in impedance. We believe that although both ECIS and MEIRS detect phenotypical changes in the cells, there is a subtle difference in their signal, and this could provide more insight into the biological processes occurring in the cells.

References:

[1] Wu, C., et al. Fano-resonant asymmetric metamaterials for ultrasensitive spectroscopy and identification of molecular monolayers. Nat. Mater. 11, 69-75 (2011).

[2] Kelp, G., et al. Application of metasurface-enhanced infra-red spectroscopy to distinguish between normal and cancerous cell types. Analyst 144, 1115-1127 (2019).

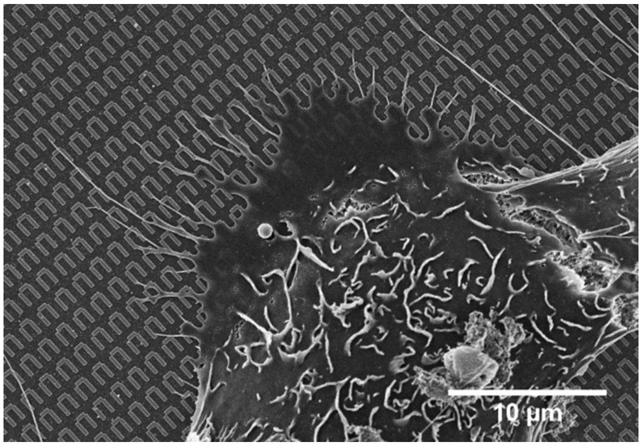

Figure 2: SEM image of A431 cells grown on the plasmonic metasurface.

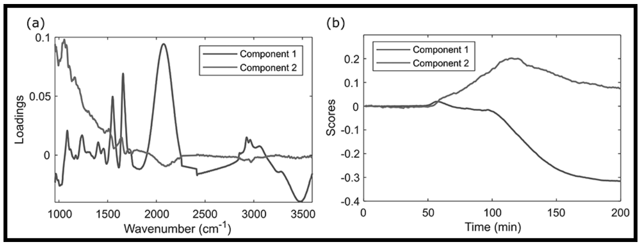

Figure 3: The spectral changes of A431 cell in response to MBCD. The results were analyzed using PCA, followed by promax rotation. (a) Component loadings and (b) the associated component scores. MBCD arrives at the flow chamber at approximately t = 45 min.

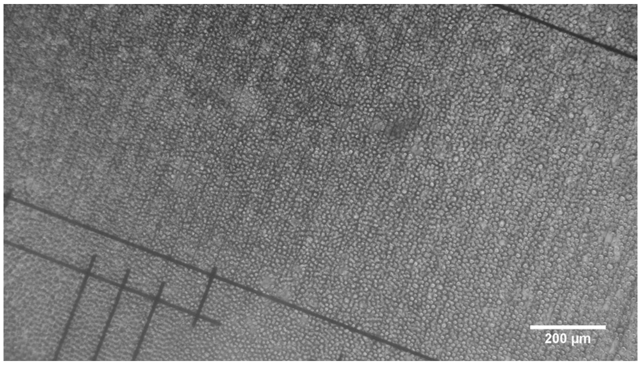

Figure 4: A431 cells on a microelectrode-patterned surface for electrical impedance measurement.

Retinal Implant Project

CNF Project Number: 2504-16

Principal Investigator(s): Douglas Shire, Ph.D.[1,3,4]

User(s): Marcus Gingerich, Ph.D.[1,4], Patricia Wong[2,4]

Affiliation(s): 1. Dept. of Electrical Engineering, Cornell University; 2. Dept. of Neuro-Ophthalmology, Massachusetts Eye and Ear Infirmary; 3. VA Cleveland Healthcare System; 4. Bionic Eye Technologies, Inc.

Primary Source(s) of Research Funding: NIH/NIBIB U01EB018873; NIH/NIBIB R01EB022013, NIH R43 NS113708-01 Massachusetts Lions Eye Research Fund, DoD W81XWH-16-2-0015

Contact: dbs6@cornell.edu, mdg37@cornell.edu, pwong@bionicvisiontechnologies.com

Website: http://www.bostonretinalimplant.org

Primary CNF Tools Used: PT-72, Lithography toolset/MA6, DWL2000, evaporators, AJA sputter, Gamma spray coater, SEMs, gold electro-plating, Class 2 lithography toolset, Oxford PECVD, Oxford 100 etcher, Oxford Cobra etcher, Glenn 1000, YES polyimide oven, Parylene-C coater, VersaLaser, numerous metrology tools

Abstract:

The purpose of the Retinal Implant Project is to restore useful vision to patients who are blind with degenerative retinal diseases. The primary illnesses we hope to treat are retinitis pigmentosa (a primary cause of inherited blindness) and age-related macular degeneration (the leading cause of blindness in the developed world). Both these diseases cause the eventual destruction of the photoreceptor cells — rods and cones — in the retina, leaving intact the ganglion cells, which transmit electrical impulses (and hence visual information) to the brain. The ganglion cells may be stimulated, however, with biphasic current pulses from a microfabricated electrode array. Blind surgical volunteers have consistently described visual percepts that resulted from such stimuli, and this has led our team to develop a wireless, implantable retinal prosthesis.

Summary of Research:

The implanted portion of our device consists of power and data secondary receiving coils, and — in a sealed Ti can — a small number of discrete components, and a custom designed application specific integrated circuit (ASIC), which consists of circuitry for clock and data recovery, current drivers for electrodes in a stimulating electrode array, and a programmable function generator capable of stimulating with a wide range of pulse widths and amplitudes. The current outputs drive high-charge capacity sputtered iridium oxide film (SIROF) stimulating electrodes, which in turn give rise to the visual percepts mentioned above.

CNF-fabricated components of this system have included various proof-of-concept test structures and tools used in the research effort and an integrated combination flexible circuit and stimulating electrode array. Si wafers serve as carriers for these freestanding films during processing. The electrode leads are fabricated inside of 'sandwiches' of polyimide and amorphous silicon carbide (SiC), while the SIROF electrodes are reactively sputter-deposited.

Assembly of the intraocular components of the prosthesis is accomplished by flip chip solder ball bonding of the IC and solder attachment of discrete components onto an internal flexible circuit board which is hermetically sealed into an ultraminiature Ti can. The RF coils are soldered and glued to the integrated external flex-array which is in turn thermosonically bonded to the hermetic feedthrough of the Ti can. Finally, the thermosonic bonds are protected and insulated with an over-mold. An external patient interface unit, will consist of a video camera for capturing images, a digital signal processor, and a radio frequency (RF) transmitter and coil to relay power and data to the implanted device.

Scientific challenges still remain in realizing a chronically implantable retinal prosthesis. While our first-generation device was primarily encapsulated in polymers for short term proof-of-concept implant studies, our second-generation system focused on a system which would last many years *in vivo*. Our more recent efforts have focused on developing a device with 256+ stimulation channels which is still small enough and of a configuration to be easily implanted in the ocular orbit and continue to function for many years *in vivo*. Thus, a major effort has been the development of a technological platform to build a robust, hermetically packaged, high-density subretinal visual prosthesis with a lifetime of > ten years in biological saline that is scalable to hundreds of I/O channels.

Recent efforts have focused on improvements in assembly techniques, under-filling, overmolding and final Parylene-C protection, using the Parylene coater, have yielded a passive retinal implant system which has been successfully implanted in an animal model for several months with no significant adverse effects. Figures 1 and 2 show an example of the implant mounted on a model eyeball.

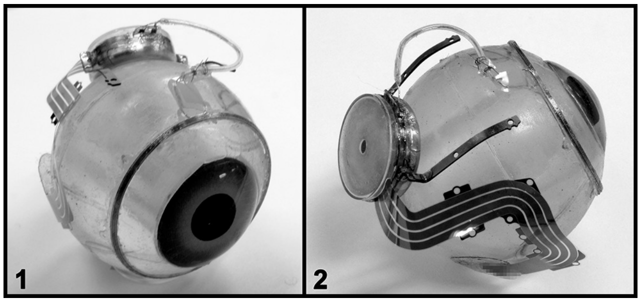

Figure 1, left: A side-frontal view of a passive retinal implant assembly is shown on an eyeball demonstrating the location of the power and data coil around the front of the eye. Figure 2, right: A side-rear view of a retinal implant assembly mounted is shown on an eyeball demonstrating the location of the hermetic titanium case and the stimulating electrode array at the back of the eye. (See pages vi-vii for full color versions of both images.)

Other efforts at the CNF have included developing a microfabrication process for penetrating electrodes for long-term implantation in brain tissue. The goal is to extend the existing retinal stimulator platform to include electrodes which can be placed at different points in the visual tract to enable the restoration of sight due to other causes of blindness. These electrodes can be placed into structures such as the lateral geniculate nucleus (LGN) to produce visual signals at that location. The LGN is a structure located deeper within the brain thus a system of implanting the electrode array into the target location has had to be developed as well. A prototype insertion device, shown in Figure 3, includes a protective split-sheath inserter, the actual electrode array/signal cable and the insertion rod. The resulting system has the potential to be utilized in other applications such as those requiring deep brain stimulation including Parkinson's disease, severe depression, morbid obesity, and obsessive-compulsive disorder, to name a few.

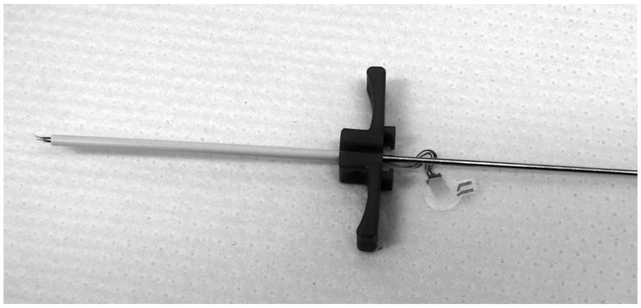

Figure 3: A prototype deep brain insertion sub-assembly is shown which includes a protective split-sheath inserter, the actual electrode array/ signal cable and the tungsten insertion rod.

References:

[1] J. F. Rizzo, J. Wyatt, J. Loewenstein, S. Kelly, and D. Shire, "Methods and Perceptual Thresholds for Short-Term Electrical Stimulation of Human Retina with Microelectrode Arrays," Investigative Ophthalmology and Visual Science, vol. 44, no. 12, Dec. 2003, pp. 5355-5361.

Circulating Extracellular Vesicles and Physical Stress in ME/CFS

CNF Project Number: 2590-17
Principal Investigator(s): Maureen R. Hanson, Ludovic Giloteaux
User(s): Ludovic Giloteaux

Affiliation(s): Department of Molecular Biology and Genetics, Cornell University, Ithaca NY
Primary Source(s) of Research Funding: NIH U54
Contact: mrh5@cornell.edu, lg349@cornell.edu
Website: https://neuroimmune.cornell.edu/research/vesicles-and-signaling/
Primary CNF Tools Used: Malvern NS300 NanoSight

Abstract:

Myalgic Encephalomyelitis/Chronic Fatigue Syndrome (ME/CFS) is a disabling illness affecting approximately two million Americans, with symptoms including extreme fatigue, pain, unrefreshing sleep, orthostatic intolerance, and cognitive difficulties. There is evidence for abnormal immune cell function and cytokine signaling. Some of the abnormalities in immune response may be due to altered cell-to-cell communication by extracellular vesicles released by immune cells and other cell types in the body. We are measuring number and size of vesicles per volume of plasma in order to detect any differences between ME/CFS patients and controls. Furthermore, we are using this information in order to normalize measures of protein and miRNA cargo between individual samples.

Summary of Research:

The Nanoparticle Tracking Analysis (NTA) instrument Malvern NS300 NanoSight was used for the sizing and quantification of extracellular vesicles (EVs) isolated from plasma samples from subject with ME/CFS and healthy individuals. Samples were obtained from individuals recruited at Ithaca College, New York City, and California within an NIH U54 project. Other samples were directly sent to us from Jackson Laboratory as a collaborative project funded by the NIH. We have measured size and numbers to inform Jackson Laboratory for experiments in which the EVs are mixed with cultured cells to observe effects on their function.

We studied an initial set of 70 samples, shown in Fig.1.

A manuscript is currently in preparation that will describe data concerning size, concentration, and cargo in EVs from these samples. There was no difference in the average size or total concentration of EVs between samples from ME/CFS patients vs. controls. A significant increase in the concentration of the 30-130 nm class of EV (exosome type) was observed in the ME/CFS samples in comparison to healthy controls (Figure 1C).

Conclusions and Future Steps:

We are periodically receiving additional samples from Ithaca College, Weill Cornell Medicine, and Los Angeles, where subjects are performing two successive cardiopulmonary exercise tests. We are measuring size and numbers of EVs in plasma before and after such tests, and analysis of cargo in the EVs is underway.

The rationale behind this study is that it is known that EVs increase in blood following exercise by healthy people, and ME/CFS patients are known to have an abnormal response to exercise.

References:

[1] Giloteaux L., A. O'Neal, S.M. Levine, J. Jesus Castro-Marrero, and M.R Hanson. Cytokine profiling of plasma extracellular vesicles in individuals with Myalgic /Chronic Fatigue Syndrome. Oral presentation by L. Giloteaux at the meeting "Accelerating Research on ME/CFS," held at the NIH, Bethesda, MD on April 4-5, 2019.

[2] Giloteaux, L., J. Castro-Marrero., A. O'Neal, J. Grenier, S. Levine, and M.R. Hanson. Cytokine and miRNA profiling of plasma extracellular vesicles in individuals with Myalgic Encephalomyelitis/Chronic Fatigue Syndrome. Poster presentation by L. Giloteaux at the International Society of Extracellular Vesicles (ISEV) 2019 conference held in Kyoto, Japan, April 23rd-28th.

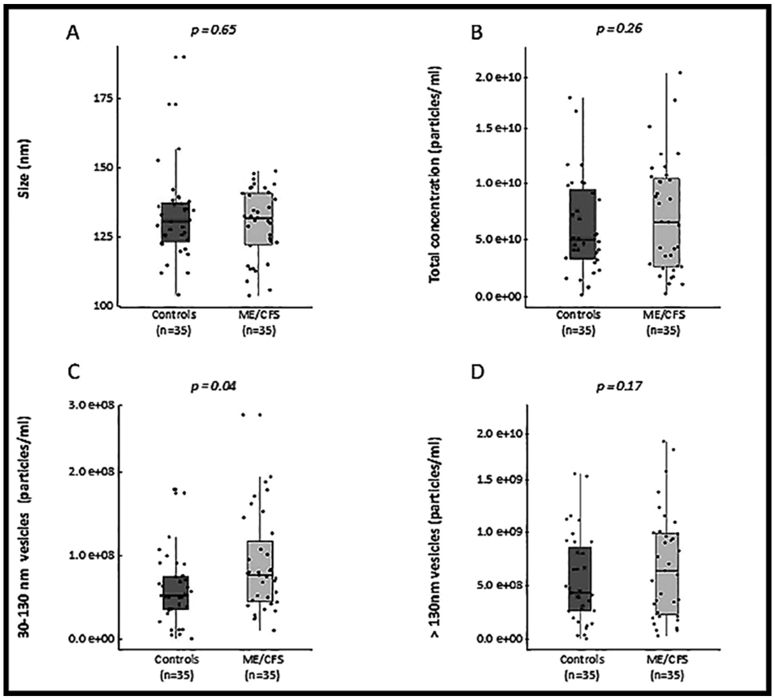

Figure 1: Characterization of EVs by Nanoparticle Tracking Analysis. Size in nanometers (A), total concentration of particles per ml of plasma (B), and the range of concentrations of 30-130 nm vesicles (C) and > 130 nm vesicles (D).

In Vitro Three-Dimensional Engineered Cardiac Tissue Mechanical Stimulation Platform

CNF Project Number: 2619-17

Principal Investigator(s): Jonathan Butcher

User(s): Gaetano Scuderi

Affiliation(s): Biomedical Engineering Department, Cornell University

Primary Source(s) of Research Funding: National Institutes of Health

Contact: jtb47@cornell.edu, gjs95@cornell.edu

Website: http://www.butcherlab.com/

Primary CNF Tools Used: Objet30 Pro 3D printer, Parylene coater, VersaLaser engraver/cutter tool

Abstract:

People who suffer from heart failure have low survival rates since no clinically available cardiac regeneration therapy exists. However, one promising approach is the implantation of tissue engineered myocardium, but due to their immaturity they do not lead to any significant heart function improvements. To improve the maturity of the engineered cardiac tissues (ECT), researchers have attempted to mimic *in vivo* mechanical stimuli. However, current systems have major limitations that lead to only modest improvements in ECT maturity. Therefore, our objective was to develop a superior *in vitro* cardiac tissue platform and mechanical stimulation bioreactor system to ultimately study how various mechanical stimuli affect ECT maturity. Here, we demonstrate the successful development of a novel *in vitro* platform and bioreactor system. We hope to apply this novel system to develop more mature ECTs that can be translated clinically as a viable cardiac regeneration option.

Summary of Research:

In the United States, 750,000 Americans suffer from heart attacks annually with 16% of all cases leading to mortality [1]. Due to the inability for adult mammalian hearts to regenerate, the infarcted region becomes a fibrotic, non-contractile tissue which often leads to congestive heart failure [2]. The gold standard treatment option is heart transplantation, which has major limitations such as an inadequate supply, high risk of donor heart rejection/failure, and need for lifelong immunosuppressants.

Currently, no viable clinical cardiac regenerative therapy is available to restore heart function following a heart attack [3]. One promising cardiac regeneration approach involves the implantation of tissue engineered myocardium to restore heart function. Current tissue engineered myocardium, however, has been unsuccessful at restoring heart function due to the tissue's immature phenotype that has low survivability and poor host integration in adult hearts [3].

Therefore, researchers have turned to investigating ways to improve tissue engineered myocardium maturity that will better integrate with the host tissue. Mechanical stimulation utilizing mechanical anchorage to induce passive tension, passive stretch, and dynamic cyclic stretch have all shown to lead to modest improvements in engineered cardiac tissue (ECT) maturity [4]. However, the current bioreactor systems have many limitations. All systems that dynamically stretch their ECT to mimic *in vivo* mechanical stimuli utilize stiff anchorage points, which prevents the tissues from producing work and can lead to an upregulation of pathological fibrosis/hypertrophic signaling [5]. Likewise, these bioreactor systems often use non-physiological stretching regimens that do not accurately recapitulate normal cardiac development, where a progressive increase in cardiogenic stretch patterns occur to lead to intrinsic maturity improvements [3].

For this project, our objective was to develop a high-throughput *in vitro* ECT platform system and mechanical stimulation bioreactor that allows for the following: 1) anchorage points that allow for contraction and work production, 2) mechanically stretch over a wide range of strain magnitudes (0-50%) and rates (1-5 Hertz), and 3) high-throughput stimulation of 48 ECTs with varying strain magnitudes simultaneously.

Our *in vitro* ECT platform required precise manufacturing of an intricate geometric mold and therefore we turned to Cornell NanoScale Facility's Objet30 Pro 3D printer. This design provided the ability to cast polydimethylsiloxane (PDMS) post constructs that serve as nearly perfectly elastic bioinert anchorage points. PDMS serves as a reliable candidate for ECTs due to its elastic properties, which allows the tissues to contract/deflect the material and therefore produce work [3]. Our ECTs can be cultured on these PDMS constructs (Figure 1).

This PDMS post design allows us to control the bending stiffness that the tissue experiences by restricting any z-direction movements during contractions and serves as a means for the tissue to be stimulated by deflecting the post from above the tissue using a customized mechanical stimulation bioreactor. We validated our platform's ability to create functional ECTs by culturing primary fetal chick cardiac cells on our post platform and compared them to unloaded (non-anchored) control tissues. The loaded ECTs demonstrated aligned cardiomyocytes and non-cardiomyocytes along the axis of tension while the unloaded controls had no inherent alignment (Figure 2).

Our custom high-throughput uniaxial mechanical stimulation bioreactor system for stimulating 48 tissue constructs on a standard 48 well plate was developed using the Objet30 Pro 3D printer (Figure 3). The system uses a hybrid external stepper motor linear actuator. As the linear actuator translates, it moves a customized 3D printed part attached to a steel rod that is attached inside the customized 3D printed box that sits on top of the 48-well plate. A tab grid system then slides along the 3D printed box's linear track and deflects the PDMS posts just above the tissues to apply a stretch. The amount of stretch can easily be modulated using an Arduino Uno system. Likewise, different tab grid systems have been developed that are offset by certain lengths and thus can apply various strains ranging from 0-50% across the 48-well plate simultaneously.

Our next steps are to test out our design by culturing various ECTs and stretching our tissues with varying stretch regimens to determine what types of regimens provide the greatest improvements in cardiac tissue maturity.

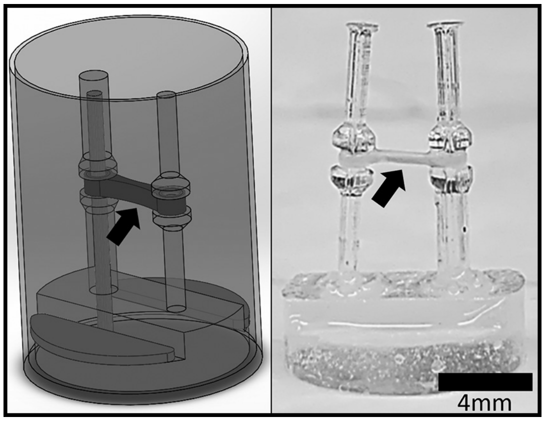

Figure 1: SolidWorks schematic of PDMS construct (left) and fixed ECT after one-week culture on PDMS construct (right). Black arrows point to ECTs.

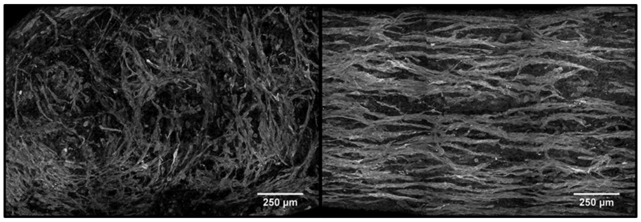

Figure 2: Whole mount immunohistochemical staining of unloaded (left) and loaded (right) ECTs stained for non-cardiomyocytes (red), cardiomyocytes (green), and nuclei (blue). (See pages vi-vii for full color version.)

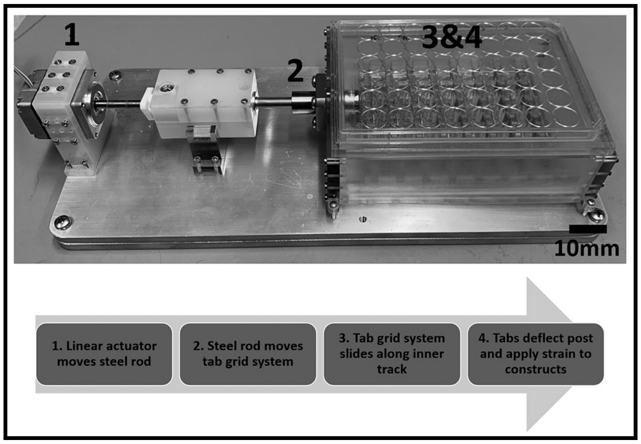

Figure 3: Bioreactor (top) and flow chart of bioreactor operation (bottom).

References:

[1] Mozaffarian, D., et al. Heart disease and stroke statistics—2016 update a report from the American Heart Association. Circulation 133, e38-e48 (2016).

[2] Alcon, A., Cagavi Bozkulak, E., and Qyang, Y. Regenerating functional heart tissue for myocardial repair. Cellular and Molecular Life Sciences 69, 2635-2656 (2012).

[3] Scuderi, G., and Butcher, J. Naturally engineered maturation of cardiomyocytes. Frontiers in Cell and Develop. Bio. 5, (2017).

[4] Radisic, M., et al. Biomimetic approach to cardiac tissue engineering. Philos. Trans. R. Soc. B Biol. Sci. 362, 1357-1368 (2007).

[5] Leonard, A., et al. Afterload promotes maturation of human induced pluripotent stem cell derived cardiomyocytes in engineered heart tissues. J. Mol. Cell. Cardiol. 118, 147-158 (2018).

Evaluating the Role of Tumor-Derived Extracellular Vesicles in Breast Cancer

CNF Project Number: 2706-18
Principal Investigator(s): Lara Estroff
User(s): Minjee Kang

Affiliation(s): Materials Science and Engineering, Cornell University
Primary Source(s) of Research Funding: Human Frontier Science Program
Contact: lae37@cornell.edu, mk2546@cornell.edu
Primary CNF Tools Used: Malvern NS300 NanoSight

Abstract:

Breast cancer frequently metastasizes to bone where it leads to osteolytic bone degradation and poor clinical prognosis. Nevertheless, therapeutic options to interfere with this process are scarce as the underlying mechanisms remain unclear. Previous studies showed that primary breast cancer tumors can alter bone materials properties and bone metastasis even prior to secondary tumor formation, suggesting possible interference with bone mineralization pathways [1]. It is well-known that extracellular vesicles (EVs) shed from tumor cells enter circulation and act as satellites of information transfer among cells. It is unknown, however, if circulating breast tumor-shed EVs contribute to early-stage changes of bone microenvironment. Our project investigates the connections between EV generation, breast cancer malignancy, the binding affinity of EVs in metastatic sites such as the bone.

Summary of Research:

We investigated how tumor-shed EVs interact with a bone-mimetic microenvironment, specifically mineralized collagen fibrils with poorly crystalline apatite crystals, and if EVs bound to the bone-like matrix can promote tumor cell binding to the bone extracellular matrix (ECM). To study interaction between tumor-shed EVs and bone ECM *in vitro*, we prepared bone-mimetic scaffolds composed of mineralized collagen type I fibrils fabricated using a polymer-induced liquid-precursor process.

We used the CNF NanoSight instrument to analyze the size distributions and measure concentrations of EVs shed by breast cancer cell lines. Our findings in Figure 1 indicate that compared to their benign counterparts, cell lines that represent more invasive and metastatic potential shed a greater amount of EVs per cell, with increases in both microvesicles and exosomes.

Next, we loaded labelled tumor-shed EVs into the scaffolds and examined the degree of binding of EVs to the collagen fibrils using confocal microscopy and SEM. The distribution and degree of binding of EVs in the matrix were correlated with various factors including breast tumor cell malignancy, the presence of mineral, and size of EVs. Breast-tumor shed EVs successfully adhered to the bone matrix via ligand-receptor interactions where the degree of binding was dependent upon tumor cell malignancy and vesicle size. EVs adhered slightly better on non-mineralized scaffolds than mineralized scaffolds but the difference was nonsignificant. EVs shed from more malignant breast tumor cells were more effective in binding by 3-8 times to the matrix than those from less malignant cells as shown in Figure 2.

Conclusions and Future Steps:

The adhesion of breast tumor-shed EVs to the bone ECM is associated with their size and parent cell malignancy *in vitro*. These findings suggest a potential role for tumor-shed EVs in preparing a pre-metastatic niche within the bone ECM to which tumor cells are attracted. We anticipate that new understanding of adhesion ability of tumor-shed EVs to the bone ECM will contribute to our understanding of role of EVs in breast cancer bone metastasis.

References:

[1] He F, Chiou AE, Loh HC, Lynch ME, Seo BR, Song YH, Lee MJ, Hoerth R, Bortel E, Willie B, Duda G, Estroff LA, Masic A, Wagermaier W, Fratzl P, Fischbach C. Multiscale characterization of the mineral phase at skeletal sites of breast cancer metastasis. Proc. of the National Academy of Sciences, 114(40), 10542-10547. https://doi.org/10.1073/pnas.1708161114 (2017).

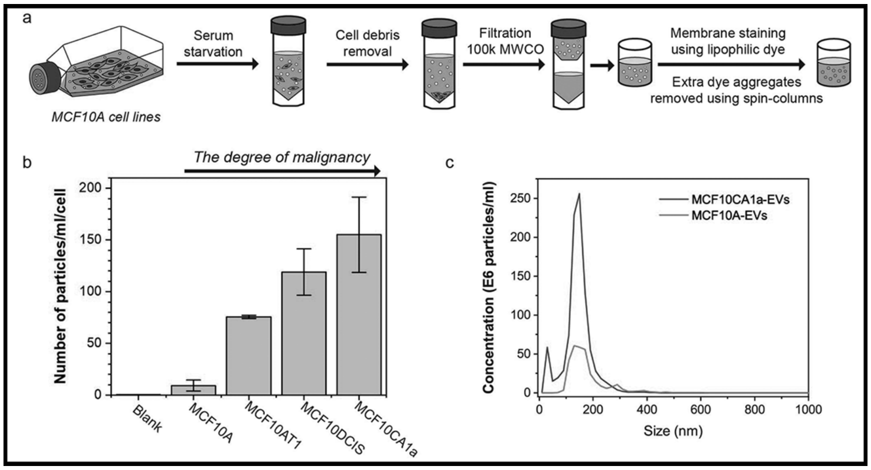

Figure 1: (a) Schematic representation of the collection of extracellular vesicles (EVs). Subconfluent MCF10A cell lines were cultured and serum-starved for 24 h. Media were collected, centrifuged to remove cell debris, and then filtered to concentrate EVs. Fluorescent lipophilic dyes were used to stain membranes of EVs, and the extra aggregates of dyes were removed using spin-columns. (b) Concentration of particles collected from the series of MCF10A cell lines as measured by NanoSight. (c) Size distribution of particles shed from MCF10A cells and MCF10CA1a cells as measured by NanoSight.

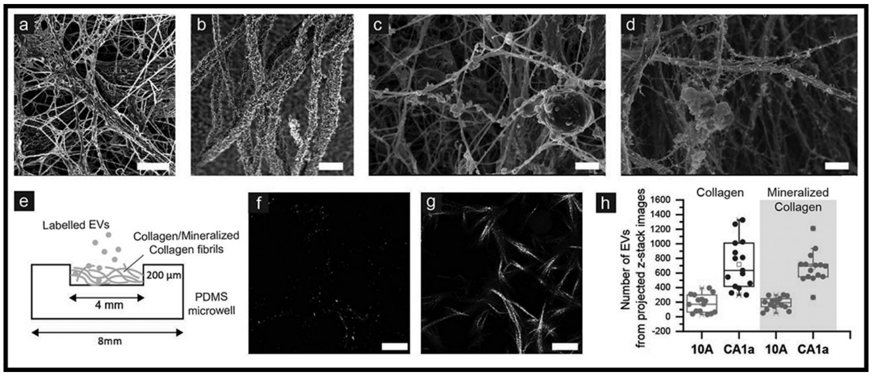

Figure 2: Binding of EVs onto 3D bone-mimetic scaffolds. (a-d) Representative SEM images showing the microstructure of (a) collagen, (b) mineralized collagen prepared via a polymer-induced liquid-precursor process, and MCF10CA1a-shed EVs bound onto (c) collagen fibrils, and (d) mineralized collagen fibrils. Scale bars = 10 µm. (e) Schematic of the bone-mimetic scaffolds used in this study. Collagen or mineralized collagen fibrils were cast into poly(dimethylsiloxane) (PDMS) microwells and fluorescently labeled EVs were incubated into the wells. (f, g) Confocal microscopy images of (f) labeled EVs in green channel and (g) collagen network in reflection mode. (h) Quantification of confocal images to compare the levels of EVs shed from MCF10A cell lines and MCF10CA1a cell lines bound onto collagen and mineralized collagen.

Fabrication of Biological Superhydrophobic Surfaces

CNF Project Number: 2727-18
Principal Investigator(s): Sunghwan Jung
User(s): Ehsan Esmaili

Affiliation(s): Biological and Environmental Engineering, Cornell University
Primary Source(s) of Research Funding: Startup funding
Contact: sj737@cornell.edu, ee287@cornell.edu
Primary CNF Tools Used: ABM aligner, photolithography room

Abstract and Summary of Research:

The CNF photolithography technique has been used to fabricate a microstructure to study the rainfall on biological superhydrophobic surfaces. In this work, we explored raindrop impact at high speeds, which exhibits unexpected drop dynamics: numerous shock-like waves are generated on a spreading drop in the presence of microscopic textures on biological surfaces. Then, the spreading drop with shock-like waves is fragmented soon after it approaches a maximal spreading extent, thereby reducing the residence/contact time more than twofold.

One paper has been prepared and submitted to the PNAS journal, titled as "Shock-like waves and drop fragmentation of a raindrop impacting biological surfaces."

Development of Heparin-Based Coacervate Loaded Liposomes as a Non-Invasive Therapy for Myocardial Infarction

CNF Project Number: 2754-18
Principal Investigator(s): Yadong Wang
User(s): Chia-Wei Yeh

Affiliation(s): Biomedical Engineering, Cornell University
Primary Source(s) of Research Funding: Cornell Startup Funds
Contact: yw839@cornell.edu, cy465@cornell.edu
Primary CNF Tools Used: ABM contact aligner

Abstract:

Cardiovascular disease is one of the major leading causes of death worldwide. Specifically, myocardial infarction (MI), generally known as heart attack, is the main cause of death in cardiovascular disease. Among them, the major cause of death of MI is due to the myocyte necrosis and heart failure. Therefore, it is of particular importance to prevent myocyte necrosis after MI as well as induce infarcted heart tissue to regenerate.

Coacervate is an electrostatically bound complex between cationic and anionic polyelectrolytes. In the extracellular matrix (ECM), glycosaminoglycan such as heparan sulfate proteoglycan (HSPG) binds with several growth factors (GFs) to form HSPG-GF complex. This complex not only serves as reservoir for bonding and stabilization of GFs but also potentiates GFs responsible for maintaining normal cellular function. Due to the similar mechanism of protein-extracellular matrix interaction, it has been shown that heparin-based coacervate is a promising candidate for drug delivery system in biomedical and tissue engineering applications. However, coacervate complex is unstable in the blood stream owing to the relatively weak electrostatic interaction within coacervate droplets, leading to the difficulty to systemically administer coacervate via intravenous injection.

To solve this problem, we aim to encapsulate heparin-based coacervate complex into liposome, namely coacervate vesicles or covesicles in short, for a non-invasive therapy for MI. In this study, polyanion heparin is utilized to complex with vascular endothelial growth factors C (VEGF-C) to form heparin-growth factor complex, which is then mixed with synthetic polycation, poly(ethylene arginyl aspartate diglyceride) (PEAD) to construct VEGF-C loaded coacervate droplets. In order to enhance coacervate complex stability in the blood stream, an on-chip microfluidic device is used to generate covesicles by encapsulating VEGF-C loaded coacervates into liposomes in a well-defined manner. The therapeutic effect of the covesicles will be evaluated on rat myocardial infarction model.

Summary of Research:

Covesicles are successfully generated in the designed microfluidic chip utilizing three phases: outer aqueous phase (OA), inner aqueous phase (IA), and lipid carried organic phase (LO), as shown in Figure 1 and Figure 2. OA contains 15% (vol/vol) glycerol and 5% (w/v) P188 in water, IA contains 15% (vol/vol) glycerol and PEAD/heparin coacervate complex in water, and LO contains 0.2% (wt/vol) DOPC in 1-octanol. Coacervate complex is formed by mixing PEAD solution and heparin solution prior to flow into microfluidic chip.

From Figure 1 and 2, PEAD/heparin coacervate complex is encapsulated by 1-octanol, forming water-in-oil droplets, then further pinched off by OA solution, and forming water-in-oil-in-water double emulsion droplets at the post-junction area. Moreover, covesicles with uniform size and high encapsulation efficiency are observed under the following flow rate: OA: 900 µL/hr, IA: 30 µL/hr, LO: 30µL/hr, as shown in Figure 3. The average diameter of covesicles is 17.87 µm.

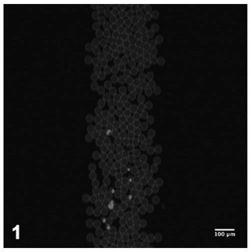

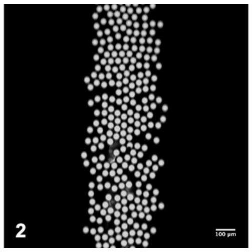

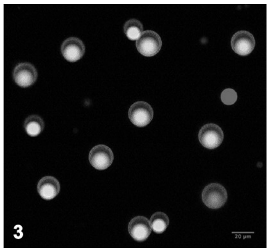

Figure 1, left: *Rhodamine-labeled liposome formed via the designed microfluidic device. Flow rate: OA: 300 µL/hr, IA: 30 µL/hr, LO: 30 µL/hr. Scale bar: 100 µm.* ***Figure 2, middle:*** *FITC-labeled PEAD/heparin coacervate encapsulated in liposome via the designed microfluidic device. Flow rate: OA: 300 µL/hr, IA: 30 µL/hr, LO: 30 µL/hr. Scale bar: 100 µm.* ***Figure 3, right:*** *Covesicles with uniform size and high encapsulation efficiency. Red: rhodamine-labeled lipid. Green: FITC-labeled heparin. Flow rate: OA: 900 µL/hr, IA: 30 µL/hr, LO: 30 µL/hr. Scale bar: 100 µm. (See pages vi-vii for full color versions of all three images.)*

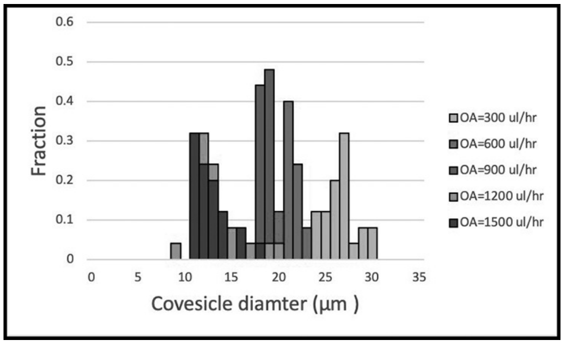

Figure 4: Covesicles diameter distribution vs. OA flow rate.

We are also interested in generating covesicles with various size. Thus, via using different flow rate, the diameter of covesicles ranges from 30 µm to 10 µm is achieved, as shown in Figure 4.

In order to achieve dripping regime during covesicles generation, both of IA and LO flow rate is maintained at 30 µL/hr. As expected, the diameter of covesicles decreases when OA flow rate increases. In our proposed strategy, covesicles less than 10 µm in diameter is our major target.

For next step, we will move forward to encapsulate VEGF-C into covesicles and test the protection effect on VEGF-C.

References:

[1] Deshpande, S., and C. Dekker. "On-chip microfluidic production of cell-sized liposomes." Nature protocols 13.5 (2018): 856.

[2] Deshpande, S., et al. "Spatiotemporal control of coacervate formation within liposomes." Nature Com. 10.1 (2019): 1800.

Characterization of E0771 Exosomes

CNF Project Number: 2780-19
Principal Investigator(s): Cynthia Leifer
User(s): Jingyi Chen, Christopher Wan

Affiliation(s): Microbiology and Immunology, Cornell University
Primary Source(s) of Research Funding: PSOC Pilot Project Funding
Contact: cynthia.leifer@cornell.edu, jc2876@cornell.edu, cw685@cornell.edu
Primary CNF Tools Used: NanoSight

Abstract:

Pathologic activation of the blood clotting system in cancer is associated with systemic thrombotic events as well as transformation, growth and metastasis of various tumors [1,2]. Coagulation is activated primarily by tissue factor (TF). TF is overexpressed in breast tumors *in situ* and in breast cancer cell lines, particularly triple negative cells [3,4]. Overexpression of TF in patient tumors correlates with a poor prognosis [3]. Cancer cells and the tumor microenvironment induce a protumorigenic, pro-angiogenic, and immunosuppressive phenotype in tumor-associated immune cells like macrophages [9]. It is unknown whether breast cancer cell-generated TF-coagulation complexes and PARs regulate macrophage recruitment to tumors or whether they subsequently modulate macrophage behavior in tumors. This is important since macrophage recruitment and regulation contributes to angiogenesis, metastasis and tumor progression [10-12].

We hypothesized that breast cancer-associated hemostatic components regulate macrophage recruitment and their inflammatory, angiogenic and hemostatic activity. To investigate this question, we determined that cancer-derived extracellular vesicles had intrinsic procoagulant activity and conferred that procoagulant activity to macrophages. A key part of our work was quality control of these extracellular vesicles that we subsequently used in our macrophage experiments. We used the NanoSight particle analyzer to characterize the extracellular vesicle populations purified from cancer cell-conditioned and control media. Data obtained using the NanoSight confirmed that we isolated particles 100-200 nm, compatible with extracellular vesicles. Altogether, our data show that breast cancer-derived microparticles confer procoagulant activity to macrophages, which may play a key role in the connection between coagulation and inflammation to regulate tumor growth and anti-tumor immunity.

Summary of Research:

In this project, we used the CNF NanoSight to perform quality control on our cancer-derived and control extracellular vesicles that were then used in additional experiments. Because of the NanoSight data, we demonstrated the procoagulant activity of a mouse breast cancer cell line and found that the vesicles derived from the cells accelerated clotting in mouse plasma.

Overnight incubation of a mouse macrophage cell line with the isolated vesicle fraction from tumor-conditioned, but not cell-free, media increased the procoagulant activity of the mouse macrophage cell line. This supported our hypothesis that tumor cells upregulate procoagulant activity in macrophages. Our goal with using the Cornell NanoScale Facility was to characterize the size distribution of the obtained vesicles.

We found that the microvesicle fraction consisted of a dominant population of particles 100-200 nm, supporting successful isolation of various subsets of extracellular vesicles shed from tumor cells (Figure 1). These data supported several grant applications currently under review.

References:

[1] Khan UT, Walker AJ, Baig S, et al. Venous thromboembolism and mortality in breast cancer: cohort study with systematic review and meta-analysis. BMC Cancer 2017; 17:747.

[2] Cole M, Bromberg M. Tissue factor as a novel target for treatment of breast cancer. Oncologist 2013; 18:14-18.

[3] Vrana JA, Stang MT, Grande JP, et al. Expression of tissue factor in tumor stroma correlates with progression to invasive human breast cancer: paracrine regulation by carcinoma cell-derived members of the transforming growth factor beta family. Cancer Res 1996; 56:5063-70.

[4] Che SPY, Park JY, Stokol T. Tissue Factor-Expressing Tumor-Derived Extracellular Vesicles Activate Quiescent Endothelial Cells via Protease-Activated Receptor-1. Front Oncol 2017; 7:261.

[5] Versteeg HH, Schaffner F, Kerver M, et al. Inhibition of tissue factor signaling suppresses tumor growth. Blood 2008; 111:190-9.

[6] Bourcy M, Suarez-Carmona M, Lambert J, et al. Tissue Factor Induced by Epithelial-Mesenchymal Transition Triggers a Procoagulant State That Drives Metastasis of Circulating Tumor Cells. Cancer Res 2016; 76:4270-4282.

[7] Palumbo JS, Talmage KE, Massari JV, et al. Tumor cell-associated tissue factor and circulating hemostatic factors cooperate to increase metastatic potential through natural killer cell-dependent and -independent mechanisms. Blood 2007; 110:133-141.

[8] Eftekhari R, de Lima SG, Liu Y, et al. Microenvironment proteinases, proteinase-activated receptor regulation, cancer and inflammation. Biol Chem 2018; 399:1023-1039.

[9] Aras S, Zaidi MR. TAMeless traitors: macrophages in cancer progression and metastasis. Br J Cancer 2017; 117:1583-1591.

[10] Gil-Bernabé AM, Ferjancic S, Tlalka M, et al. Recruitment of monocytes/macrophages by tissue factor-mediated coagulation is essential for metastatic cell survival and premetastatic niche establishment in mice. Blood 2012; 119:3164-3175.

[11] Lin L, Chen Y-S, Yao Y-D, et al. CCL18 from tumor-associated macrophages promotes angiogenesis in breast cancer. Oncotarget 2015; 6:34758-34773.

[12] Su S, Liu Q, Chen J, et al. A positive feedback loop between mesenchymal-like cancer cells and macrophages is essential to breast cancer metastasis. Cancer Cell 2014; 25:605-620.

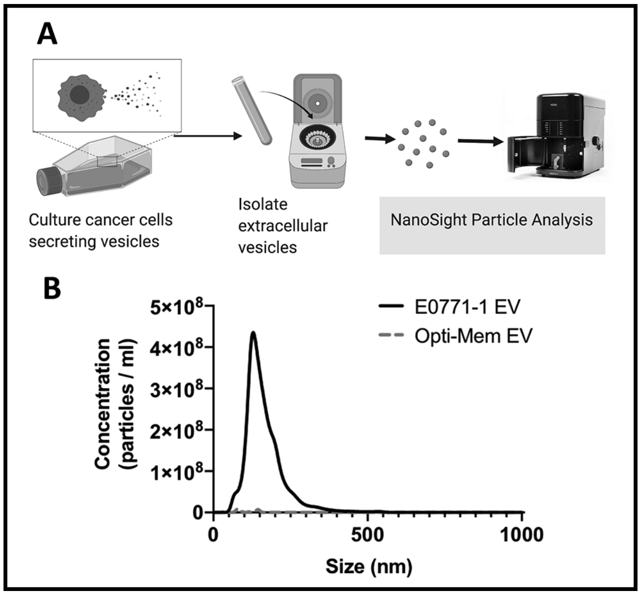

Figure 1: A) Schematic for nanoparticle isolation and analysis using the CNF NanoSight. Mouse mammary cancer cells (E0771) were cultured to produce extracellular vesicles (EV) in Opti-Mem media. Vesicles were isolated by differential centrifugation and subjected to NanoSight particle tracking analysis. B) Example NanoSight results of E0771 EV compared to media only EEV preparations. These data demonstrate isolation of appropriate size EVs from cell cultures and not from media controls. These preparations were used in follow on experiments.

Microcontact Patterning of Single Cardiomyocytes on Shape Memory Polymers

CNF Project Number: 2806-19
Principal Investigator(s): Zhen Ma
User(s): Chenyan Wang

Affiliation(s): Bioengineering, Syracuse University
Primary Source(s) of Research Funding: Carol and Samuel Nappi Research Scholarship
Contact: zma112@syr.edu, cwang40@syr.edu
Website: https://myheart.syr.edu/
Primary CNF Tools Used: ABM contact aligner, Heidelberg mask writer-DWL2000

Abstract:

Investigating the mechanisms of cardiomyocytes remodeling in response to the dynamic mechanical environment is critical for understanding heart disease progression. The aim of our project is to develop a dynamic platform using shape memory polymers (SMPs) and pattern single cardiomyocytes on SMPs to observe their structural and functional remodeling induced by dynamic mechanical stress. To constrain single cardiomyocytes in a predefined shape, extracellular matrix (ECM) proteins need to be deposited on SMPs at the scale of single cell. Making use of the tools at Cornell NanoScale Science and Technology Facility (CNF), we successfully generated rectangular and square patterns at single-cell resolution on SU-8 coated silicon wafers. Using these wafer molds, we fabricated PDMS stamps, and conducted microcontact printing to pattern single cardiomyocytes on the SMPs. Cardiomyocytes showed good confinement within the patterns before and after the application of dynamic mechanical stress.

Summary of Research:

Introduction. SMPs are smart materials that can undergo dynamic shape change stimulated by elevated temperature when they are programmed with internal strain [1]. Microcontact patterning is an efficient tool of controlling the shape of various cell types from tissue to single-cell level to study how the geometry confinement affects the cellular activities [2]. The combination of SMPs and microcontact patterning provides a platform for investigating remodeling of single cardiomyocytes to dynamic change of their geometry.

In this report, we focus on what we have achieved by microcontact patterning facilitated with CNF tools, which include a few steps: 1) design of a photomask with desired pattern shapes, 2) fabrication of Si wafers with opposite patterns by photolithography, 3) cure polydimethylsiloxane (PDMS) on top of wafers to make stamps and coat them with ECM proteins, 4) deposit ECM proteins though direct contact between stamps and SMPs, and 5) cell seeding on top of SMPs.

During this process, photomasks with patterns at high resolution and the efficient pattern transfer from masks to wafers ensure the perfect match of patterns between initial designs and final shapes.

Experimental Process. After estimating the areas of single cardiomyocytes, we designed rectangular and square patterns (areas: 1000 µm^2 and 2000 µm^2, aspect ratios: 1:1 and 1:3) with L-Edit software. Laser writing of photomasks was conducted by Heidelberg mask writer (DWL2000). After chrome etching and series washing steps, photomasks were ready to use. SU-8 50 photoresist was coated on top of a pre-cleaned Si wafer evenly with a photoresist spinner (spreading cycle: 500 rpm at 100 rpm per second for five seconds, spin cycle: 2000 rpm at 300 rpm per second for 30 seconds) to obtain a thickness of about 25 µm. After prebaking at 65°C for three minutes and soft baking at 95°C for seven minutes, the wafer was cooled down to room temperature on a flat surface.

Before exposure, light source with wavelength below 365 nm was filtered out to avoid overexposure of top portion of resist film. After switching on the ABM contact aligner, the photomask was vacuumed on the raised mask frame, and the wafer was vacuumed on the substrate chuck. The mask and wafer were brought into contact by adjusting the position of substrate chuck. After setting exposure timer, the light source was moved on top of the mask to crosslink SU-8.

To test the accurate exposure time for getting optimal patterns, different regions of the wafer were exposed for various time periods. Exposed wafers were post baked at 65°C for one minute and then 95°C for three minutes. Patterns on wafers should be visible after seconds of post bake. After cooled down, wafers were immersed and agitated in SU-8 developer for four minutes to wash off un-crosslinked SU-8. Developed wafers were rinsed with isopropyl alcohol (IPA) and dried with nitrogen. The quality of patterns on wafers was checked under microscope, and optimal patterns should exhibit strong adhesion to the Si substrate and same dimensions as initial designs.

PDMS was cured on top of wafers at 60°C overnight and then cut into small stamps with similar sizes to SMP samples. 20 µL of fluorescence-tagged fibronectin (100 µg per mL) was pipetted on PDMS stamps and incubated at 37°C for one hour. After transfer to an environmental control room with 50% humidity, the fibronectin residual on the stamp was wicked off with KimWipe. Then the SMP was pressed on top of the stamp with a 20 g weight for two minutes to allow fibronectin transfer from the stamp to the SMP. After blocking with 0.4 % Pluronic F-127, single cardiomyocytes were seeded on SMPs at 5×10^4 cells per milliliter. After cultured at 28°C for two days, the patterned cells were transferred to 37°C for 24 hours, and the elevated temperature triggered the shape change of patterns (Figures 1, 2).

Patterned single cardiomyocytes transformed from square to elongated shape (Figures 3, 4).

Conclusion and Future Work:

In summary, we have fabricated Si wafers with single-cell scale patterns at CNF. We made PDMS stamps, and achieved efficient ECM protein transfer to SMPs through microcontact patterning.

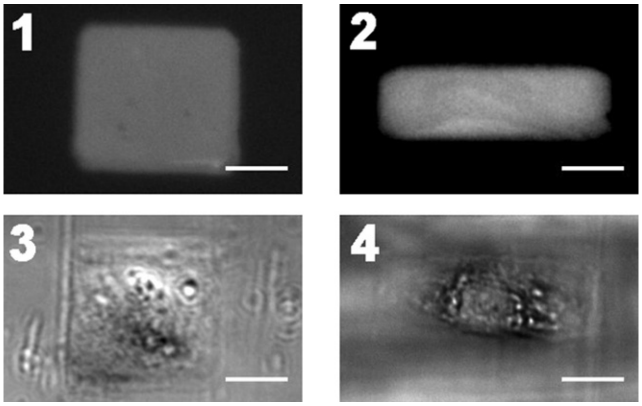

Figure 1: *Fibronectin pattern on SMPs before shape change. Scale bar: 20 µm.* ***Figure 2:*** *Fibronectin pattern on SMPs after shape change. Scale bar: 20 µm.* ***Figure 3:*** *Patterned single cardiomyocyte on SMPs before shape change. Scale bar: 20 µm.* ***Figure 4:*** *Patterned single cardiomyocyte on SMPs after shape change. Scale bar: 20 µm.*

We tested initial seeding of single cardiomyocytes on SMPs, and confirmed that they were elongated after triggering the shape change of SMPs. In future, we will run more cell seeding on our dynamic system to test the consistency of cell remodeling. The sarcomere organization and contractile functions will be quantified as evaluations of cellular responses.

References:

[1] Davis, K. A., Burke, K. A., Mather, P. T. and Henderson, J. H. Dynamic cell behavior on shape memory polymer substrates. Biomaterials 32, 2285-2293 (2011).

[2] Salick, M. R., et al. Micropattern width dependent sarcomere development in human ESC-derived cardiomyocytes. Biomaterials 35, 4454-4464 (2014).

Quantification of Recombinant Outer Membrane Vesicles for Vaccine

CNF Project Number: 2833-19

Principal Investigator(s): David Putnam

User(s): Mariela Rivera-De Jesús

Affiliation(s): Biomedical Engineering, Cornell University

Primary Source(s) of Research Funding: National Institutes of Health (R01AI139664), "Co-Presentation and Delivery of TLR Agonist Combinations with Subunit Antigens to Pathogen-Match the Immune Response" (E888866)

Contact: dap43@cornell.edu, mar524@cornell.edu

Primary CNF Tools Used: Malvern NS300 NanoSight

Abstract:

Bacteria-produced outer membrane vesicles (OMVs) are of great interest in the development of subunit vaccines. One challenge in their use as a vaccine platform is the difficulty of precisely quantifying OMVs. By using nanoparticle tracking analysis system, we can directly quantify the amount of recombinant OMVs produced and better adapt them for further applications. Recombinant ClearColi OMVs were indirectly quantified using bicinchoninic acid (BCA) assay and directly quantified using the Malvern NS300 NanoSight system, at different concentrations determined through the BCA assay. While no correlation was established between BCA-determined protein concentration and NTA-determined particle concentration, we have established a protocol for a direct quantification method of OMVs.

Summary of Research:

Outer membrane vesicles (OMVs) are 20 to 200 nm lipid nanoparticles produced by Gram negative bacteria. These vesicles contain the same surface proteins and sugars that are on the bacterial surface and are strong immunomodulators, an ability that has highlighted OMVs as a potential vaccine platform [1]. Bacteria can be recombinantly modified to produce OMVs with desired characteristics such as reduced toxicity and displaying of surface proteins. Our team is using recombinant bacteria to design a versatile OMV vaccine and investigate the co-presentation of antigens on OMVs. Indirect methods are the most employed, such as quantifying the total protein concentration or the dry mass of the vesicles, but it is important to have a precise measurement of the components of vaccines to produce reproducible results. One method for directly quantifying OMVs is through nanoparticle tracking analysis (NTA), using systems such as NanoSight [2].

Our goal is to develop a more precise method for measuring OMV concentration through NTA. In addition, if possible, we would like to establish a correlation between indirect quantification methods and NTA quantification methods.

Our group had previously modified ClearColi® (CC) BL21(DE3) cells to hypervesiculate through gene knockouts [3]. Three batches of CC OMVs were produced. In brief, liquid CC cultures were centrifuged (4°C, 15 min, 5,000 rcf) and the supernatant passed through a 0.2-mm filter. The filtrate was ultracentrifuged (4°C, 3 hr, 26,000 rpm) and decanted, and the pellets resuspended in PBS. The protein concentration of each batch was determined using the Pierce™ Bicinchoninic Acid (BCA) Protein Assay Kit. Batches were then diluted to 1.50, 1.00, 0.75, 0.50, 0.25, and 0.10 ng/µL according to the BCA assay. Each dilution of each batch was finally measured using the Malvern NS300 NanoSight (five replicates, 1 min each) to determine particle concentration.

Conclusions and Future Steps:

Figure 1 compares the protein concentration measured using the BCA assay and the particle concentration using the NanoSight. Each slope was significantly different from each other, as further highlighted by Figure 2.

Further study is needed to establish a potential correlation between BCA and NTA quantification. Nonetheless, a successful method for measuring OMV concentration through NTA was established. While indirect quantification is enough for in-lab samples, NTA quantification can be applied to sample where a more precise quantification is required, such as determining vaccine dosing.

References:

[1] Jan, AT. Front Microbiol. 2017; 8: 1-11.

[2] Gerritzen, MJH, et al. J. Extracell. 2017; 19(8): 271.

[3] Valentine, JL, et al. Cell Chem Biol. 2016; 23(6): 655-665.

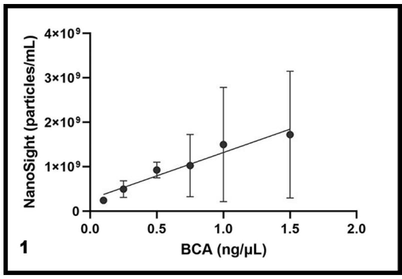

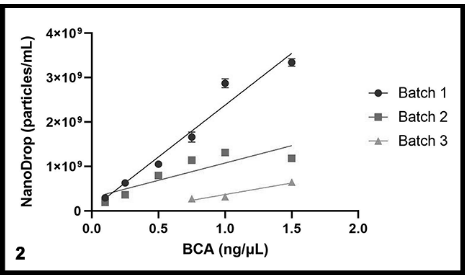

Figure 1. left: Comparison between BCA concentration and NanoSight concentration of CC OMVs, in individual batches. STD calculated by NanoSight. In Batch 3, the concentration of OMVs was too low to be measured below 0.75 ng/µL.

Figure 2, right: Comparison between BCA concentration and NanoSight concentration of CC OMVs, between all batches.

Organic Field Effect Transistor Fabrication

CNF Project Number: 863-00

Principal Investigator(s): John A. Marohn

User(s): Peter Sun, Rachael Cohn

Affiliation(s): Department of Chemistry and Chemical Biology, Cornell University
Primary Source(s) of Research Funding: National Science Foundation
Contact: jam99@cornell.edu, hs859@cornell.edu, rc784@cornell.edu
Website: http://marohn.chem.cornell.edu/
Primary CNF Tools Used: Autostep i-line Stepper, Oxford 80+ Etcher, Oxford ALD FlexAL

Abstract:

We fabricated field-effect transistors with an integrated source-drain electrode silicon wafer with an improved liftoff process and an extra layer of hafnium dioxide (HfO_2).

Summary of Research:

Lead halide perovskites are an emerging class of semiconductors that have shown promising optoelectronic properties. The ability of lead-halide perovskites to maintain exemplary photovoltaic properties while being riddled with structural defects, mobile vacancies, and mobile ions make lead-halide perovskites unique and worth understanding in microscopic detail. Field-effect transistors (FETs) measurements combined with local Kelvin probe force microscopy is a powerful tool to microscopically study charge motion and charge injection in solution-processed semiconductors.

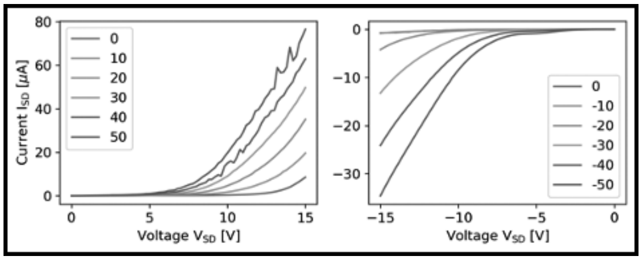

Figure 1: I-V curve for FET made from lead halide perovskite (FAMACs) on substrates fabricated at the CNF. Source-to-drain current (ISD) versus source-to-drain voltage (VSD) at different source-to-gate voltages (VG). Gate voltage sweep direction: 0 V to 50 V and 0 to -50 V.

The transistor substrates consist of gate pads and source-drain pads with interdigitated gold electrodes (5 nm Cr and 30 nm Au) with 5 µm spacing in between. The fabrication was previously developed [1] with a two-step exposure process on Autostep i-line stepper — the gate exposure layer (resist SPR 955 CM 2.1), and the source-drain exposure layer (resist nLOF 2020). The gate pads are etched using the Oxford 80+ etcher, and the gold electrodes are deposited with the odd-hour evaporator. The wafer undergoes a liftoff process and is diced on the DISCO dicing saw.

We have discovered several disadvantages of the previous protocol and improved the fabrication process.

We dramatically increase the yield of the transistors by employing a two-step liftoff process. After being submerged in Microposit Remover 1165 for 12 hours, the wafer is sonicated for six minutes with the solution, followed by a round of IPA spray and water blast cleaning. In the second step, the wafer was sonicated in methanol for three minutes to remove smaller metal particles, subsequently cleaned with IPA and water, and dried with N_2 and on hot plate at 110°C for 60 seconds. The yield improved from 57% to 95%, determined by if the source-drain is shorted due to metal remains on the electrodes.

However, bottom-gate bottom-contact perovskite FETs are difficult to successfully solution process and operate, presumably due to gate voltage induced ion motion and gate material induced material degradation from the widely used gate oxide SiO_2 [2].

Here, we modified and improved our existing FET substrate fabrication recipe to replace the SiO_2 gate with high-K material hafnium oxide, HfO_2, by atomic layer deposition (Oxford ALD FlexAL, 300°C, plasma, HfO_2, 200 cycles). The exposure time and focus are optimized.

We are still in the process of determining the improvement of the HfO_2 layer over the silicon oxide.

Triple cation lead halide perovskite (FAMACs) was solution-processed onto the resulting transistor substrates in a single step process in a glove box using published methods. The resulting films were annealed at 100°C for one hour. Transport properties were measured in the dark and under the vacuum of 5×10^6 mbar. The films showed a noticeable gate effect, which diminished under illumination and repeated measurements (Figure 1). More work is needed to improve the stability of the FETs and understand the effect of gate material and processing on the device performance.

References:

[1] Hoepker, N. C. "Fluctuations Near Thin Films of Polymers, Organic Photovoltaics, and Organic Semiconductors Probed by Electric Force Microscopy", 2013, Ph.D. thesis, Cornell University, Ithaca.

[2] Canicoba, N,. et al. "Halide Perovskite High-K Field Effect Transistors with Dynamically Reconfigurable Ambipolarity", ACS Materials Lett., 2019, 1, 633-640.

Substrate Preparation for Ultrafast Vibrational Spectroscopy Experiments

CNF Project Number: 1936-10
Principal Investigator(s): Poul B. Petersen
User(s): Stephanie Sanders

Affiliation(s): Chemistry and Chemical Biology, Cornell University; Physical Chemistry II, Ruhr-University Bochum, Germany
Primary Source(s) of Research Funding: National Science Foundation
Contact: poul.petersen@rub.de, ses422@cornell.edu
Website: https://www.ruhr-uni-bochum.de/pc2/petersen/
Primary CNF Tools Used: Oxford ALD FlexAL

Abstract:

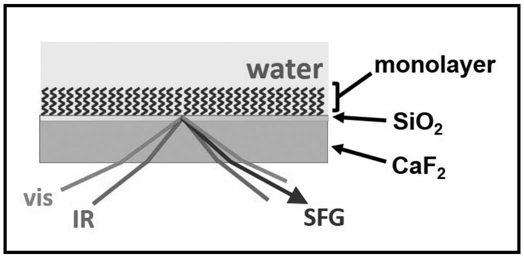

Water is ubiquitous and an active component in many natural and technological processes. Vibrational spectroscopy can be used to probe the structure and dynamics of water in a variety of environments. We use sum-frequency generation, a surface specific vibrational spectroscopy, to probe the structure and dynamics of interfacial water at chemically tunable surfaces. Interfaces with tunable surface character are created with self-assembled monolayers. In order to create substrates compatible for both silane self-assembly and sum-frequency generation, infrared and visible transparent CaF_2 windows are coated with SiO_2. Then after surface functionalization with silane monolayers, the water structure and dynamics at the interfaces can be explored with sum-frequency generation.

Summary of Research:

Water is an active component in many natural and technological processes [1]. Interfaces terminates the H-bonded network of water. We aim to study the structure and dynamics of water at self-assembled monolayers (SAMs) with varying surface character using sum-frequency generation (SFG) spectroscopy. In SFG, an infrared photon interacts with a dipole transition of the molecule and a visible photon excites the molecule to a virtual electronic state where it can undergo an anti-Stokes Raman transition resulting in a photon at the sum of the two incident frequencies being emitted [2,3].

In order to collect SFG spectra of solid-aqueous interfaces, we must probe through the window so the infrared photons are not absorbed by water. However, silica, a common SAMs substrate, also absorbs in the infrared. To create an infrared and visible transparent substrate compatible with SAMs syntheses, we start with a calcium fluoride (CaF_2) window, which is transparent through the visible and infrared. Then approximately 10 nm of SiO_2 is deposited on the CaF_2 window via atomic layer deposition (ALD) with the Oxford ALD FlexAL. The SiO_2 layer is thin enough to not absorb all the IR photons and prevent SFG spectra of the sample from being collected, but thick enough to form a surface compatible with the self-assembly of silanes.

Once the SiO_2 is deposited, hydrophobic, hydrophilic, or mixed monolayer are synthesized with self-assembly of silanes on the surface. Figure 1 shows a schematic of the surface in contact with water. Then, the surfaces and water at the surfaces are analyzed with SFG [2-6].

References:

[1] Ball, P. Life's Matrix: A Biography of Water; University of California Press: Berkeley, 2001.

[2] Barrett, A. R.; Petersen, P. B. Order of Dry and Wet Mixed-Length Self-Assembled Monolayers. J. Phys. Chem. C 2015, 119 (42), 23943-23950.

[3] Vanselous, H.; Petersen, P. B. Extending the Capabilities of Heterodyne-Detected Sum-Frequency Generation Spectroscopy: Probing Any Interface in Any Polarization Combination. J. Phys. Chem. C 2016, 120 (15), 8175-8184.175-8184.

[4] Sanders, S; Vanselous, H; Petersen, P; Water at Surfaces with Tunable Surface Chemistries. J. Phys. Condens. Matter 2018.

[5] Kocsis, I.; Sorci, M.; Vanselous, H.; Murail, S.; Sanders, S.; Licsandru, E.; Legrand, Y-M.; van der Lee, A.; Baaden, M.; Petersen, P. B.; Belfort, G.; Barboiu, M. Oriented chiral water wires in artificial transmembrane channels. Sci. Adv. 2018 4(3), eaao5603.

[6] Sanders, S.E.; Petersen, P.B. Heterodyne-Detected Sum Frequency Generation of Water at Surfaces with Varying Hydrophobicity. J. Chem. Phys., 2019, 150 (20), 204708.

Peptoids as Sequence-Controlled EUV-Photoresists

CNF Project Number: 2733-18
Principal Investigator(s): Christopher Kemper Ober
User(s): Florian Hermann Ulrich Kaefer

Affiliation(s): Department of Materials Science and Engineering, Cornell University
Primary Source(s) of Research Funding: JSR Corporation
Contact: cko3@cornell.edu, fhk28@cornell.edu
Website: https://ober.mse.cornell.edu/
Primary CNF Tools Used: ABM contact aligner, ASML 300C DUV stepper, AFM Bruker Icon, FilMetrics F50-EXR

Abstract:

Sequence-controlled small molecules were synthesized using a peptide synthesizer. The thus obtained peptoids with an average molar mass of 1000 g/mol and a strong alternating sequence of the two used amines were used as positive tone resists for deep ultraviolet (DUV) and extreme ultraviolet (EUV) lithography. In our first experiments we could demonstrate the potential of peptoids as a promising class of new EUV resist, as both the structure of the used amines and the sequence can be adapted to precisely adjust the properties of the photoresist.

Summary of Research:

Introduction. Today's widely used polymeric resists are typically based on random copolymers. These polymers are polydisperse and relatively large in size, with molar masses ranging from 5,000-15,000 g/mol [1]. Characteristics such as these can have a negative impact on resist performance, and therefore it is necessary to explore other architectures for new resist platforms.

Sequence-Controlled Small Molecules. For sequence-controlled polymers, on the other hand, the monomers are arranged in a specific, user-defined order. Monomer sequence regularity strongly influences the molecular, supramolecular, and macroscopic properties of polymer materials, showing promise for the creation of a new type of small molecule photoresist. In this respect, peptoids represent a particularly advantageous group, since they can be specifically varied in their structure, length and sequence of the amines used [2].

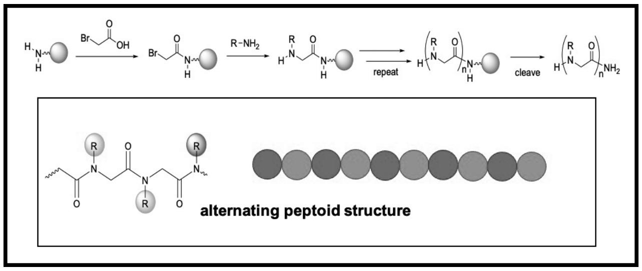

Figure 1: Synthesis of peptoids with an alternating amine sequence.

Peptoid Synthesis. A solid phase peptoid synthesis approach using a 2-chlorotrityl based resin was used [3]. After activating the resin with bromoacetic acid, the first amine solution was added. After the reaction was completed, the second amine, which contains a tert-butyl protecting group, was added and clicked to the resin. These steps were repeated until a peptoid with a total length of ten amines in alternating sequence was obtained, see Figure 1. Subsequently, the peptoid was cleaved from the resin under mild acetic conditions, purified and dried. In order to determine the molar mass and the molecular structure liquid chromatography-mass spectrometry was used.

Characterization and Results:

Preliminary photolithography experiments were performed on the ABM contact aligner and the DUV stepper. For this purpose, the produced peptoid sample with a molar mass of 1000 g/mol and an alternating amine sequence was dissolved, and spin-coated on a silica wafer.

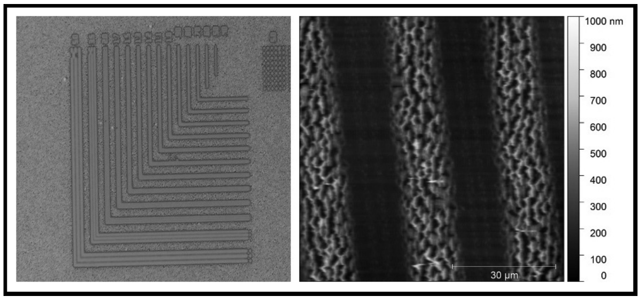

Figure 2: Patterned peptoid film after DUV exposure at the ABM contact aligner. (left) light microscopy image, (right) AFM image.

The resist film thickness was measured by FilMetrics F50-EXR. The made samples were exposed using the ABM contact aligner and developed using a diluted tetramethylammonium hydroxide (TMAH) solution. The obtained pattern was characterized using light microscopy and atomic force microscopy (AFM Bruker Icon), see Figure 2.

The measurements carried out successfully prove that peptoids can be used as DUV photoresist materials. However, the obtained results also show that further optimization of the peptoid structure as well as the photolitographic process requires further optimization. Especially the achieved resolution and the obtained mean roughness of 45 nm have to be improved.

Conclusions and Future Steps:

Sequence controlled peptoids with a molar mass of 1000 g/mol and with strong alternating sequence of the used amines could be synthesized and successfully used as positive tone photoresist using the ABM contact aligner. The obtained patterned films were characterized using light- and atomic force microscopy. However, several challenges still need to be solved. How do we design small molecules to make a photoresist with a desired property? How do we control the nanoscale resolution of the resulting resist? The aforementioned questions shall be studied and answered in the future.

References:

[1] Patterson, K.; Yamachika, M.; Hung, R.; Brodsky, C.; Yamada, S.; Somervell, M.; Osborn, B.; Hall, D.; Dukovic, G.; Byers, J.; Conley, W.; Willson, C. G., Polymers for 157-nm photoresist applications: a progress report. SPIE: 2000; Vol. 3999.

[2] Gangloff, N.; Ulbricht, J.; Lorson, T.; Schlaad, H.; Luxenhofer, R., Peptoids and Polypeptoids at the Frontier of Supra- and Macromolecular Engineering. Chemical Reviews 2016, 116 (4), 1753-1802.

[3] Culf, A. S.; Ouellette, R. J., Solid-phase synthesis of N-substituted glycine oligomers (alpha-peptoids) and derivatives. Molecules (Basel, Switzerland) 2010, 15 (8), 5282-5335.

$PtSe_2$ RF MOSFETs and CMOS Integration

CNF Project Number: 2509-16

Principal Investigator(s): James C.M. Hwang

User(s): Kuanchen Xiong, Lei Li

Affiliation(s): Materials Science and Engineering, Electrical and Computer Engineering; Cornell University

Primary Source(s) of Research Funding: U.S. Office of Naval Research Grant N00014-14-1-0653, Air Force Office of Scientific Research, National Science Foundation EFRI 2-DARE Grant No. 1433459-EFMA, NSF Cooperative Agreement DMR-1539916

Contact: jch263@cornell.edu, kux214@lehigh.edu, LL886@cornell.edu

Primary CNF Tools Used: ABM contact aligner, Autostep i-line stepper, Oxford PlasmaLab 80+ plasma reactor, SC4500 odd-hour evaporator, Oxford atomic layer deposition (ALD)

Abstract:

Few-layer platinum diselenide ($PtSe_2$) is attractive because it has a sizable bandgap, high carrier mobility, air stability, and can be synthesized below 450°C by thermal conversion or molecular beam epitaxy (MBE). In addition, bulk $PtSe_2$ is a semimetal, which can facilitate low-resistance contacts—a challenge for all 2-D devices to date. Taking advantage of these unique properties, we reported CMOS-compatible ultralow-contact-resistance $PtSe_2$ MOSFETs [2]. However, these devices suffer from poor gate modulation due to the relatively thick $PtSe_2$.

To improve gate modulation, we fabricated MOSFETs on trilayer $PtSe_2$ grown by MBE. The MOSFETs are *n*-type with a current on/off ratio of 43 and 1600 at 290 and 80 K, respectively. These results are among the best of transistors based on synthesized $PtSe_2$. Despite the thin $PtSe_2$ layer, doping by contact bias lowers the contact resistance significantly and boosts the current capacity and the on/off current ratio. Temperature-dependent current-voltage characteristics imply a bandgap of approximately 0.2 eV for trilayer $PtSe_2$, which confirms that the semiconductor-semimetal transition of $PtSe_2$ is not as abrupt as originally predicted.

Summary of Research:

Fabrication. The fabrication process is similar to [2] except for the $PtSe_2$ synthesis methods. The detailed structure of a single device is shown in Figure 1(a). After the deposition of Al_2O_3 as the gate dielectric, the chip was cleaned by acetone, isopropyl alcohol, and deionized water, before drying with N_2.

After it was loaded into a DCA Instruments R450 MBE reactor, it was outgassed for 30 min at 130°C, Growth commenced at 200°C under a Pt flux of $9.2 \times 10^{12}/cm^2 \cdot s$ and an Se flux of $1.6 \times 10^{14}/cm^2 \cdot s$. The Pt and Se fluxes are generated by an electron gun and a Knudsen cell, respectively. After growing for 339 s under both Pt and Se fluxes, the $PtSe_2$ was annealed at 400°C for 30 min under the Se flux alone to enhance its crystal quality.

The resulting $PtSe_2$ is approximately three monolayers (2-nm thick) and (001)-oriented with a high degree of in-plane rotational twin formation.

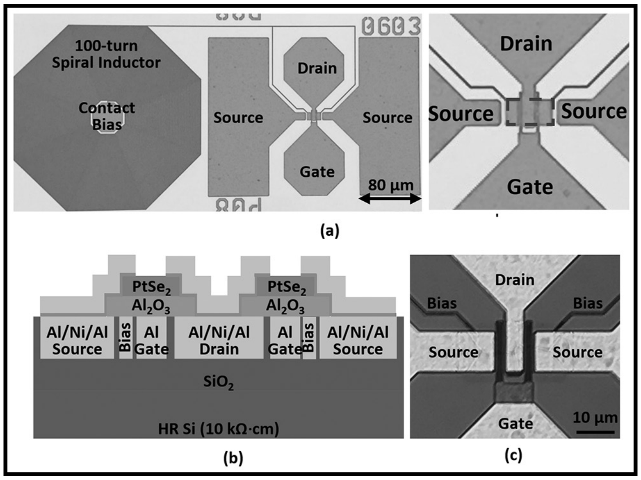

Figure 1: (a) Optical micrograph of individually probable RF MOSFET with source contact biased through a spiral inductor. (b) Cross section schematic. (c) Top-view micrograph of a finished $PtSe_2$ MOSFET.

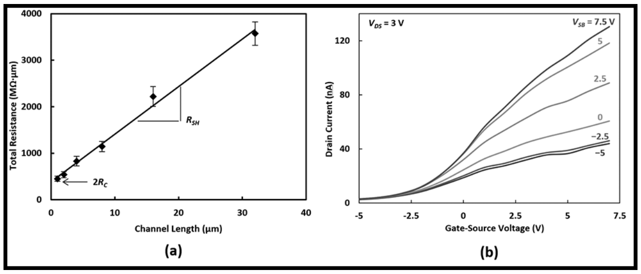

Figure 2: (a) TLM results. (b) Transfer characteristics of a $PtSe_2$ MOSFET under different source contact biases.

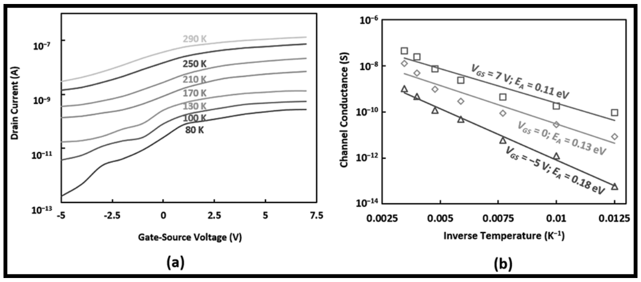

Figure 3: (a) Transfer characteristics of a $PtSe_2$ MOSFET at different temperatures. (b) Channel conductance of a $PtSe_2$ MOSFET between 80 and 290 K.

The trilayer $PtSe_2$ was patterned by photolithography and etched outside the active region by an Oxford PlasmaLab 80+ plasma reactor for 5 s. The flow rates of CF_4 and O_2 were 100 and 20 sccm, respectively. The RF power was 200 W. After $PtSe_2$ etch, the photoresist was stripped by acetone for 30 min. Ni and Al contact layers 50- and 150-nm-thick, respectively, were evaporated by an electron gun.

Figures 1(b) and 1(c) show the cross-section schematic and the top-view micrograph, respectively, of a finished $PtSe_2$ MOSFET.

DC Performance. Figure 2(a) shows the total resistance R_T measured on transfer-length-method (TLM) test structures of different channel lengths. The extraction yields a sheet resistance R_{SH} = 1 × 10^8 Ω/5g and a contact resistance R_C = 2 × 10^8 Ω·μm. Figure 2(b) shows the transfer characteristics of a $PtSe_2$ MOSFET with the drain-source voltage V_{DS} = 3 V and different source contact biases V_{BS}, which helps further reduce the contact resistance as has been demonstrated in [3]. It shows the MOSFET exhibits *n*-type conduction with an on/off ratio of 22. With V_{BS} increasing from 0 to 7.5 V, the on current of the drain I_D^{ON} increases from 60 to 130 nA, while its off current I_D^{OFF} remains the same at 3 nA. Thus, the on/off ratio increases from 22 to 43 mainly due to an increased I_D^{ON}. The results are comparable to $PtSe_2$ grown by chemical vapor deposition.

Thermal Dependence and Bandgap. Figure 3(a) shows the temperature-dependent transfer characteristics of a $PtSe_2$ MOSFET with V_{DS} = 3 V and V_{BS} = 7.5 V. With the ambient temperature decreasing from 290 K to 80 K, the on/off ratio increases from 43 to 1600. This is because I_D^{OFF} decreases much faster than I_D^{ON}, suggesting that they are governed by different activation energies. This difference is confirmed by the Arrhenius plots Figure 3 (b) of the total channel conductance between 80 K and 290 K with V_{DS} = 3 V, V_{BS} = 7.5, and V_{GS} = -5, 0, or 7 V.

The activation energy E_A decreases from 0.18 eV at V_{GS} = -5 V to 0.11 eV at V_{GS} = 7 V. Therefore, the off-state E_A of 0.18 eV should be more indicative of the bandgap of trilayer $PtSe_2$ instead of the on-state E_A.

Future Directions:

First, better MOSFET performance can be expected by growing even thinner $PtSe_2$ uniformly and by thickening the $PtSe_2$ in the contact regions. Second, it is challenging to grow monolayer or bilayer $PtSe_2$ using either MBE or CVD methods. An alternative approach is to use a shadow mask to create the recessed $PtSe_2$ profile.

References:

[1] K. Xiong, et al., "Large-scale fabrication of submicron-gate-length MOSFETs with a trilayer $PtSe_2$ channel grown by molecular beam epitaxy," IEEE Trans. Electron Devices, vol. 67, no. 3, pp. 1-6, March 2020.

[2] L. Li, et al., "Wafer-scale fabrication of recessed-channel $PtSe_2$ MOSFETs with low contact resistance and improve gate control," IEEE Trans. Electron Devices, V65, #10, pp. 4102-08, Oct. 2018.

[3] C. Li, et al., "Black phosphorus high-frequency transistors with local contact bias," ACS Nano, V12, #2, pp. 2118-2125, Jan. 2020.

Fully Transparent FET with High Drain Current and On-Off Ratio

CNF Project Number: 2543-17
Principal Investigator(s): Darrell Schlom
User(s): Jisung Park

Affiliation(s): Department of Material Science and Engineering, Cornell University, Ithaca, NY 14853, USA
Primary Source(s) of Research Funding: Semiconductor Research Corporation
Contact: schlom@cornell.edu, gp359@cornell.edu
Primary CNF Tools Used: PT720/740, PVD75 sputter deposition, Autostep i-line stepper

Abstract:

We report a fully transparent thin-film transistor utilizing a La-doped BaSnO$_3$ channel layer that provides a drain current of 0.468 mA/µm and an on-off ratio of 1.5×10^8. The La-doped BaSnO$_3$ channel is grown on a 100-150 nm thick unintentionally doped BaSnO$_3$ buffer layer on a (001) MgO substrate by molecular-beam epitaxy. Unpatterned channel layers show mobilities of 127-184 cm^{2}V^{-1}s^{-1} at carrier concentrations in the low to mid 10^{19} cm^{-3} range. The BaSnO$_3$ is patterned by reactive ion etching under conditions preserving the high mobility and conductivity. Using this patterning method, a sub-micron-scale thin film transistor exhibiting complete depletion at room temperature is achieved.

Summary of Research:

In summary, a fully transparent submicron TFT based on BaSnO$_3$ has been fabricated with a high drain current and on/off current ratio. This breakthrough is made possible by (1) high mobility bare films in combination with (2) the development of a micrometer-scale etching method that preserves the surface roughness, conductivity, and mobility of BaSnO$_3$ films.

These results demonstrate the tremendous potential of BaSnO$_3$ for the future of transparent electronics. The channel is 0.3 µm long and 0.93 µm wide. This is the first demonstration of a submicron scale BaSnO$_3$-based field effect transistor with complete depletion at room temperature. This result has been published in APL Materials January 2020. Two patent applications have been filed on the reactive ion etching of BaSnO$_3$.

References:

[1] J. Park, H. Paik, K. Nomoto, K. Lee, B.-E. Park, B. Grisafe, L.-C. Wang, S. Salahuddin, S. Datta, Y. Kim, D. Jena, H. G. Xing, and D. G. Schlom, APL Mater. 8, 011110 (2020)

[2] H. J. Kim, U. Kim, H. M. Kim, T. H. Kim, H. S. Mun, B.-G. Jeon, K. T. Hong, W.-J. Lee, C. Ju, K. H. Kim, and K. Char, Appl. Phys. Exp. 5, 061102 (2012).

[3] U. Kim, C. Park, T. Ha, Y. M. Kim, N. Kim, C. Ju, J. Park, J. You, J. H. Kim, and K. Char, APL Mater. 3, 036101 (2015).

[4] J. Yue, A. Prakash, M. C. Robbins, S. J. Koester, and B. Jalan, ACS Appl. Mater. Interfaces 10, 21061 (2018).

[5] J. Park, U. Kim, and K. Char, Appl. Phys. Lett. 108, 092106 (2016).

[6] J. Shin, Y. M. Kim, Y. Kim, C. Park, and K. Char, Appl. Phys. Lett. 109, 262102 (2016).

[7] C. Park, U. Kim, C. J. Ju, J. S. Park, Y. M. Kim, and K. Char, Appl. Phys. Lett. 105, 203503 (2014).

[8] Y. M. Kim, C. Park, T. Ha, U. Kim, N. Kim, J. Shin, Y. Kim, J. Yu, J. H. Kim, and K. Char, APL Mater. 5, 016104 (2017).

[9] Y. M. Kim, C. Park, U. Kim, C. Ju, and K. Char, Appl. Phys. Exp. 9, 011201 (2016).

[10] J. Park, U.S. patent application No. 16/706,126, Docket# 1126-051 (filed, December 6 2019).

[11] J. Park, U.S. patent application No. 16/706,126, Docket# 1126-052 (filed, December 6 2019).

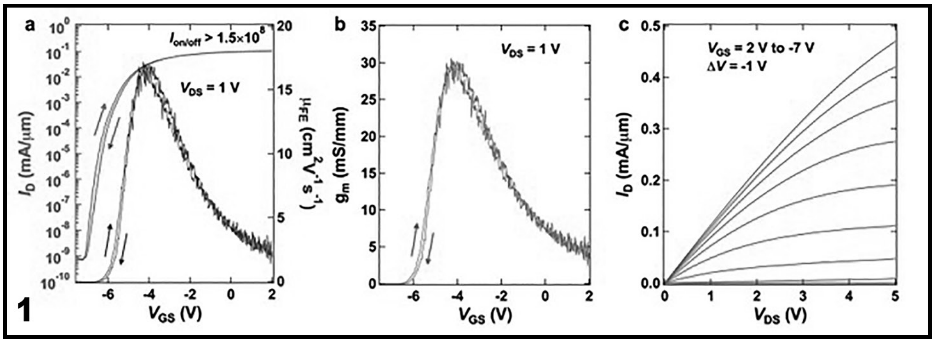

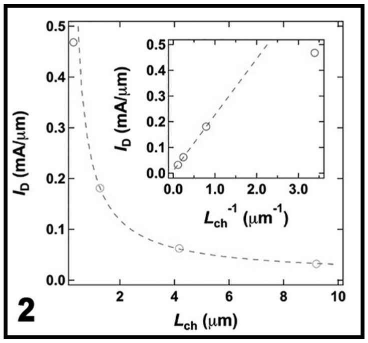

Figure 1, left: (a) The transfer characteristic of the TFT based on La-doped $BaSnO_3$ at V_{DS} = 1 V and the field-effect mobility. The peak field-effect mobility is 17.2 $cm^2V^{-1}s^{-1}$, and the on-off ratio is over 1.5 × 10^8. The subthreshold swing is 0.15 V dec^{-1}. (b) Transconductance of the device at V_{DS} = 1 V. The maximum transconductance is 30.5 mS/mm. (c) The output characteristic of the device at V_{GS} = 2, 1, 0, -1, -2, -3, -4, -5, -6, -7 V. The maximum drain current exceeds 0.467 mA/µm.

Figure 2, right: Drain current dependence on channel length (L_{ch}) when V_{GS} = 2 V and V_{DS} = 5 V. The drain current (I_D) is inversely proportional to the overall channel length except at the shortest channel length, showing little degradation with respect to device scaling. The deviation from linear behavior in the inset at the shortest channel length is likely due to the contact resistance and not short channel effects such as velocity saturation.

Injectable Micro-Scale Opto-Electrically Transduced Electrodes (iMOTEs)

CNF Project Number: 2578-17
Principal Investigator(s): Prof. Alyosha C. Molnar
User(s): Sunwoo Lee, Alejandro J. Cortese, Devesh Khilwani

Affiliation(s): Electrical and Computer Engineering, Cornell University
Primary Source(s) of Research Funding: National Institute of Health
Contact: AM699@cornell.edu, SL933@cornell.edu
Website: https://molnargroup.ece.cornell.edu/

Primary CNF Tools Used: ABM contact aligner, AJA sputter, Westbond 7400A Ultrasonic wire bonder, Oxford 100, Oxford 81, Oxford 82, Unaxis deep Si etcher, Oxford PECVD, Oxford ALD, Anatech, P7 profilometer, ZEISS Ultra and Supra scanning electron microscopes (SEMs)

Abstract:

Recording neural activities in live animals is critical to advancing our understanding of the brain, with far-reaching consequences in healthcare as well as philosophy. Such neural recording can be broadly categorized into two groups — tethered and untethered. An example of tethered neural recording is an electrodes array that can be inserted into the brain, which is then connected to the outside world directly via a wire. Naturally, such a tethered approach is not only inconvenient, but also creates chronic damage due to the residual motion between neurons and electrodes as the brain moves. Hence, there has been much interest in developing tetherless neural recording units.

While RF Coil [1] and ultrasonic approaches [2] have shown promise, the physics of such transduction limits their scaling much below a millimeter. On the other hand, optical techniques, which are becoming increasingly powerful, are nonetheless limited to subsets of neurons in any given organism, impeded by scattering of the excitation light and emitted fluorescence, and limited to low temporal resolution [3].

In this work, we combine the merits of electronics and optics to develop an extremely scaled, untethered electrode unit, where an AlGaAs micro-light emitting diode (µLED) is heterogeneously integrated on top of conventional CMOS. These micro-scale opto-electrically transduced electrodes (MOTEs) are powered by, and communicated through the microscale optical interface (µLED) while the CMOS provides low power amplification and signal encoding. Such MOTEs combine the benefits of optical techniques with high temporal-resolution recording of electrical signals, and are the smallest neural recording units to date (~ 60 µm × 30 µm × 330 µm).

Summary of Research:

Our fabrication starts with a 5 mm × 5 mm, conventional 180 nm CMOS die, which contains the electronics for signal amplification, encoding, and transmission [4]. The CMOS die is then integrated with an aluminum gallium arsenide (AlGaAs) diode, which acts as a photovoltaic (PV) as well as LED, hence abbreviated as PVLED. The PVLED provides an optical link which powers the electronics and transmits encoded signals in optical pulses. The MOTE utilizes Pulse Position Modulation (PPM) for signal encoding for its high information-per-photon efficiency [5], where the spacing between the output pulses is proportional to the measured electric field of neuronal signals across the measurement electrodes. Figure 1 depicts a conceptual deployment of the MOTE [6].

The AlGaAs diodes are first fabricated on a sapphire wafer, to be later released from the sapphire substrate with a sacrificial poly(methyl methacrylate) (PMMA) polymer. In the meantime, the substrate is flattened by Oxford 81 plasma etcher to promote the adhesion between the PVLEDs and the CMOS. Once the PMMA-coated AlGaAs diodes are transferred onto the CMOS die, high vacuum annealing leaves only the PVLEDs array on the CMOS die. To establish the electrical contact between the PVLED and CMOS, we have used ABM contact aligner for photolithography with AZ nLof2020 UV photoresist for efficient lift-off process that ensues after the metal deposition.

After the contact fabrication, the contacts of CMOS and PVLED are connected via similar photolithography process, and to maximize the conformality of the routing metal, we employ the CNF's AJA sputtering system. Following the routing step, each MOTE is etched using Oxford 100 etcher and Unaxis deep reactive ion etch (DRIE) to be separated from the array. Following the etch, each MOTE is encapsulated using Oxford ALD and PECVD for SiO_2, Si_3N_4, and Al_2O_3 deposition.

Finally, the substrate is turned upside down for backside thinning. Figure 2 summarizes the fabrication sequence described herein.

It should be noted that before making much changes are made in fabrication flow, to confirm the functionality of each module (CMOS and the diode), we use the Westbond 7400A Ultrasonic wire bonder for board-level testing. ZEISS Ultra and Supra scanning electron microscopes (SEMs) are also used to inspect the fabricated iMOTE for debugging purposes.

Conclusions and Future Steps:

We have demonstrated that such heterogenous integration fabrication is not only feasible but scalable with high yield (> 80%). The high-quality dielectric deposition tools available at CNF (ALD, PECVD, etc.) allow for excellent cladding that protects the MOTEs in a biological environment (> six months in phosphate buffered saline solution, and > two months in a mouse brain). We plan to continue optimizing the fabrication processes, CMOS circuitries and the PVLED efficiencies so that the MOTEs can be deployed deeper in the brain or to another biological environment. In parallel, we will continue our *in vivo* studies to demonstrate the neural recording based on MOTEs in a mouse brain.

References:

[1] R. R. Harrison, et al., “A Low-Power Integrated Circuit for a Wireless 100-Electrode Neural Recording System,” in IEEE J. Solid-State Circuits, vol. 42, no.1, pp. 123-133, Jan. 2007.

[2] D. Seo, et al., “Neural Dust: An Ultrasonic, Low Power Solution for Chronic Brain-Machine Interfaces,” arXiv:1307.2196, 2013.

[3] W. Yang and R. Yuste, “*In vivo* imaging of neural activity,” Nature Methods, vol. 14, no. 4, pp. 349-359, April 2017.

[4] S. Lee, et al., “A 250 µm × 57 µm Microscale Opto-electronically Transduced Electrodes (MOTEs) for Neural Recording,” IEEE Transactions on Biomedical Circuits and Systems, vol. 12, no. 6, pp. 1256-1266, December 2018.

[5] H. Hemmati, et al., “Deep-Space Optical Communications: Future Perspectives and Applications,” Proceedings of the IEEE, vol. 99, no. 11, pp. 2020-2039, August 2011.

[6] S. Lee, et al., “Fabrication of Injectable Micro-Scale Opto-Electronically Transduced Electrodes (MOTEs) for Physiological Monitoring,” IEEE Journal of Microelectromechanical Systems, submitted.

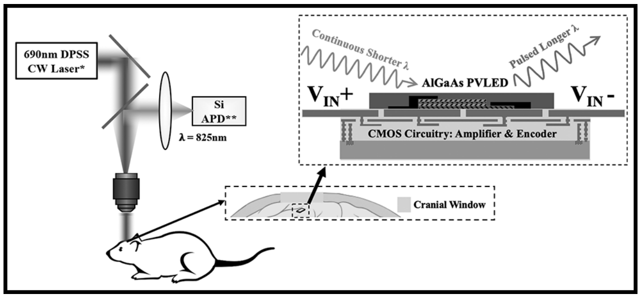

Figure 1: An envisioned employment of the MOTE for neural recording (see ref. [6]).

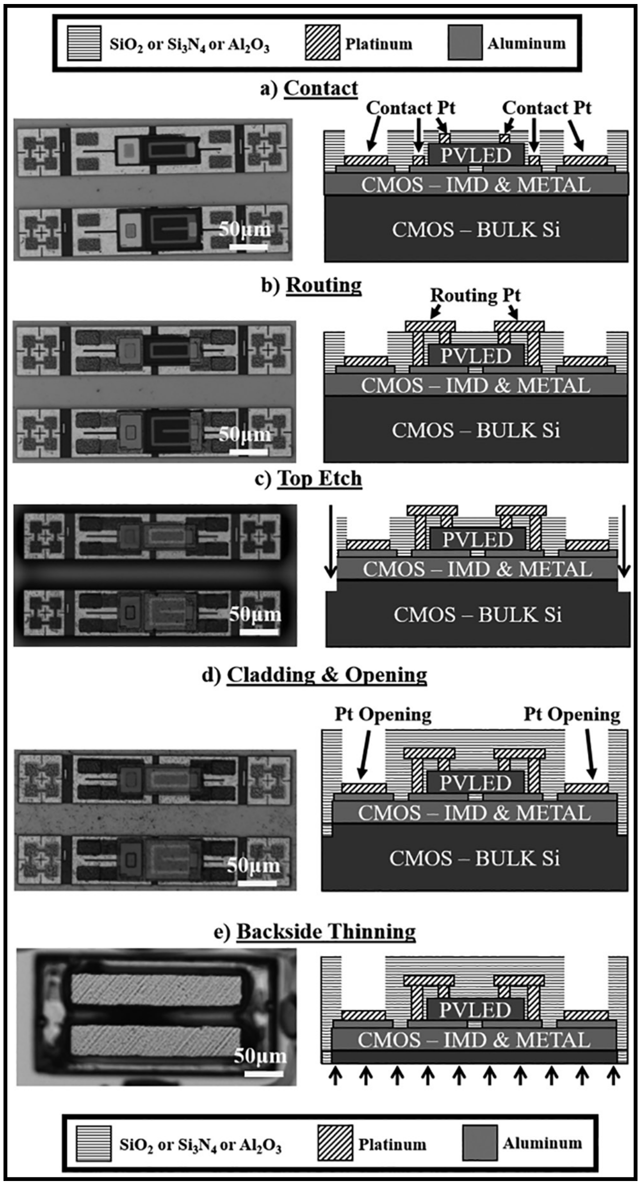

Figure 2: Fabrication flow of MOTE integration where AlGaAs PVLED is integrated on CMOS [6].

Wide-Bandgap p-Channel Transistors Based on GaN/AlN

CNF Project Number: 2800-19

Principal Investigator(s): Debdeep Jena, Huili Grace Xing

User(s): Samuel James Bader, Reet Chaudhuri, Kazuki Nomoto

Affiliation(s): Applied and Engineering Physics, Electrical and Computer Engineering, Materials Science and Engineering; Cornell University

Primary Source(s) of Research Funding: Intel Corporation

Contact: djena@cornell.edu, grace.xing@cornell.edu, sjb353@cornell.edu

Primary CNF Tools Used: SC4500 evaporator, PT 770 ICP/RIE etcher

Abstract:

Wide-bandgap (WBG) p-channel transistors, which can be monolithically integrated with WBG *n*-channel transistors, are the missing piece to the construction of WBG CMOS circuitry, which could provide tightly-integrated control over power and RF electronics. This report demonstrates high on-current *p*-channel devices based on one of the most promising platforms: the GaN/AlN heterojunction.

Summary of Research:

Though gallium nitride (GaN) electronics have advanced rapidly over the last decade to become a major player in the RF and power electronics spaces, *p*-channel devices in GaN have proven difficult to produce. The low hole mobility, poor acceptor efficiency, and hard-to-contact deep valence bands have limited device performance. This highlight celebrates advances on this front achieved in the Cornell NanoScale Science and Technology Facility and reported at the 2019 International Electron Devices Meeting [1].

An epitaxial stack consisting of a p^{++} InGaN cap on a GaN channel on an AlN buffer was grown by molecular beam epitaxy. Pd/Ni ohmic contacts were formed by e-beam evaporation in an SC4500 evaporator. After mesa isolation, the contacts were used as a mask to perform a global recess of the InGaN layer in the PT 770 ICP/RIE etcher. A SiO_2 hard mask was deposited using the Oxford 100 PECVD and patterned to reveal gate recess regions, which were then etched by the PT 770. After mask removal, the SC4500 evaporator was used to put down Mo/Au based gate contacts. All photolithography was performed in the GCA Autostep 200.

Finally, p-channel devices with 600 nm gate recess lengths were measured with up to 100 mA/mm on-current and 1-2 orders of on-off modulation, limited by the Schottky gate leakage. While this leaves significant room to improve upon the gating, the overall device performance compares well with the state-of-art in this field, as shown in Figure 1, demonstrating the promise of GaN/AlN based electronics for a wide-bandgap CMOS future.

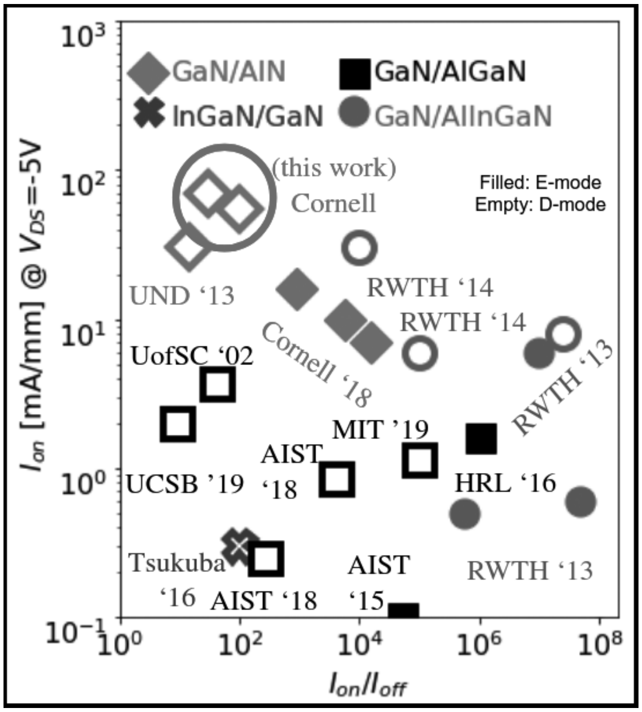

Figure 1: Current-levels and modulation ratios achieved for various p-channel device demonstrations in the III-Nitrides. Noting that this is a rapidly advancing field, it is critical to timestamp this benchmark as drawn from only the publicly available literature as of July 2019. It is seen that GaN/AlN devices enable some of the highest on-currents possible. (See pages vi-vii for full color version.)

References:

[1] S. J. Bader, et al., "GaN/AlN Schottky-gate p-channel HFETs with InGaN contacts and 100 mA/mm on-current," in International Electron Devices Meeting. DOI: 10.1109/IEDM19573.2019.8993532 (2019).

T-Gated AlN/GaN/AlN HEMTs with I_D > 3 A/mm, f_{max} = 230 GHz

CNF Project Number: 2800-19

Principal Investigator(s): Debdeep Jena, Huili Grace Xing

User(s): Austin Hickman, Reet Chaudhuri, Samuel James Bader, Kazuki Nomoto, Lei Li

Affiliation(s): Electronics and Computer Engineering, Materials Science and Engineering; Cornell University

Primary Source(s) of Research Funding: Semiconductor Research Corporation

Contact: djena@cornell.edu, grace.xing@cornell.edu, alh288@cornell.edu

Primary CNF Tools Used: AFM, i-line stepper, PT770 etcher, Oxford 81 etcher, odd hour e-beam evaporator, JEOL 6300 EBL, Oxford PECVD, AJA sputter deposition, Woolam ellipsometer, Zeizz Ultra SEM, Leica critical point dryer, Glen1000 resist stripper, P7 profilometer

Abstract:

In this work, we report record on-current and f_t/f_{max} product for the AlN/GaN/AlN HEMT. The devices demonstrated record on-currents over 3 A/mm with an on-resistance of 1 Ω·mm and excellent saturation. Transfer characteristics revealed I_{on}/I_{off} ratio of 10^3 and peak transconductance of 0.6 S/mm. Bias-dependent S-parameters were measured in the range of 0.05-40 GHz. The extracted f_t/f_{max} = 132/233 GHz (L_G = 45 nm) is the highest f_t/f_{max} product reported on the AlN platform.

Summary of Research:

Next-generation (6G) wireless communication and high-resolution radar systems target high-power operation in the terahertz regime. Gallium nitride high-electron-mobility transistors (GaN HEMTs) are well-suited for this high-power, high-frequency application. However, the conventional AlGaN/GaN heterostructure provides poor quantum confinement of the two-dimensional electron gas (2DEG), generating short channel effects at high frequencies. Additionally, its RF power performance is limited by the breakdown voltage. The AlN/GaN/AlN heterostructure offers material and device design advantages over the conventional AlGaN/GaN HEMT: the AlN buffer tightly confines the 2DEG and offers a higher thermal conductivity path than a thick GaN buffer, and the AlN barrier induces higher density 2DEGs at thinner distances (5 nm). AlN also maximizes the barrier bandgap, improving breakdown voltage.

Recently, fully realized T-gated AlN/GaN/AlN HEMTs were fabricated and characterized. The T-gates were defined via electron-beam lithography using a trilayer resist stack, and Ni/Au (50/200 nm) gate metal was deposited via e-beam evaporation. The resulting structure is shown in Figure 1.

The devices demonstrated record on-currents over 3 A/mm with an on-resistance of 1 Ω·mm and excellent saturation. Transfer characteristics revealed I_{on}/I_{off} ratio of 10^3 and peak transconductance of 0.7 S/mm. All DC characteristics are shown in Figure 2.

Bias-dependent S-parameters were then measured in the range of 0.05-40 GHz. The system was de-embedded via a short-open-load-through (SOLT) impedance standard substrate and on-wafer open/short structures. The device measured for dispersion also demonstrated f_t = 123 GHz, f_{max} = 233 GHz, as shown in Figure 3. This is the highest f_{max} reported for devices on the AlN/GaN/AlN heterostructure, and can be attributed to the incorporation of the T-gate geometry.

This excellent combination of on-current and f_{max} demonstrates the exciting potential for HEMTs on the AlN platform to enable the next generation of high-power, mm-wave communication.

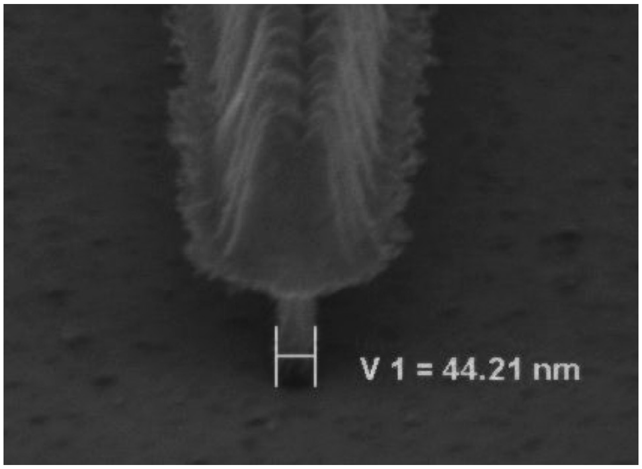

Figure 1: T-gate demonstrating a gate length of 44 nm.

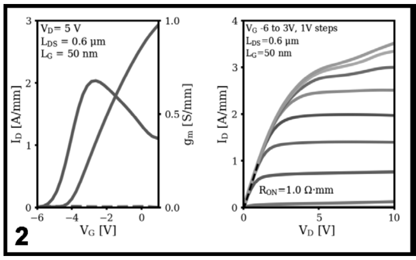

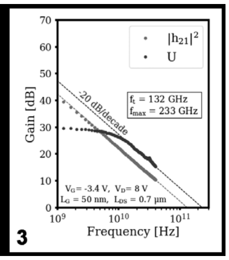

Figure 2, left: *DC characteristics for AlN/GaN/AlN HEMT.* ***Figure 3, right:*** *Small signal characteristics for the T-gated AlN/GaN/AlN HEMT.*

Ultra-Wide Bandgap Power Electronic Devices

CNF Project Number: 2800-19

Principal Investigator(s): Huili Grace Xing

User(s): Wenshen Li, Kazuki Nomoto, Devansh Saraswat, Emma Long

Affiliation(s): School of Electrical and Computer Engineering,
Department of Material Science and Engineering; Cornell University

Primary Source(s) of Research Funding: NSF DMREF Program under Grant 1534303,
AFOSR under Grants FA9550-17-1-0048, FA9550-18-1-0529 and FA9550-18-1-0479

Contact: grace.xing@cornell.edu, wl552@cornell.edu, kn383@cornell.edu, ds2375@cornell.edu, yl3394@cornell.edu

Website: http://grace.engineering.cornell.edu

Primary CNF Tools Used: Oxford PECVD, Oxford ALD, odd-hour and even-hour evaporator, AJA sputtering tool,
PT-770 etcher, Oxford 81 etcher, Gen-1000 etcher, UV-Ozone, Autostep i-line stepper,
ABM contact aligner, Heidelberg mask writer-DWL2000, AFM-Veeco Icon, Oxford ALD FlexAL

Abstract:

Ultra-wide bandgap semiconductor materials, such as beta-phase gallium(III) trioxide (Ga_2O_3), have unprecedentedly high breakdown electric field, thus are considered very promising for use in power electronic devices. Through ingenuous design of the device structure and material interface, we successfully demonstrated high-voltage, low-loss vertical Ga_2O_3 Schottky barrier diodes and fin transistors with record-high performance. The device breakdown voltage shows a significant improvement with the employment of the field-plate technique as edge termination.

Summary of Research:

Beta-phase Ga_2O_3 has been under intensive research as a promising ultrawide-bandgap semiconductor material. It is expected to have a high breakdown electric field of up to 8 MV/cm due to the sizable bandgap of 4.5-4.7 eV, as well as a decent electron mobility of up to ~ 200 $cm^2/V \cdot s$. These properties yield a Baliga's power figure-of-merit higher than GaN and 4H-SiC, thus making Ga_2O_3 a strong material candidate for high power devices. In addition, melt-growth techniques for Ga_2O_3 substrates are available, which promises a cost-effective device platform.

Previously, we have successfully demonstrated Ga_2O_3 trench Schottky barrier diodes with a breakdown voltage (BV) of 2.44 kV [1]. In addition, we realized enhancement-mode vertical fin transistors with a breakdown voltage over 1 kV [2]. Despite the promising performance, the figure-of-merit of the previous devices are still far from the material limit of Ga_2O_3. One of the major reasons is the electric field crowding at the edge of the devices, which leads to premature breakdown. In this work, we improved upon the previous devices by adopting the field plate technique for more effective edge termination.

The fabrication process flow of the field-plated trench Schottky barrier diode prior to the addition of the field plate is largely the same as reported previously. The vertical fin channels were first formed by dry etching using PT-770 etcher. Then, Ti/Au (75/150 nm) cathode ohmic contact was deposited by e-beam evaporation, followed by the deposition of the first Al_2O_3 dielectric of 105 nm by atomic layer deposition using the Oxford ALD tool. After opening of the Al_2O_3 on top of the fin channel by dry etching, Ni (30 nm) Schottky contact and then Ti/Pt (40/40 nm) sidewall coverage were deposited by electron-beam evaporation and sputtering, respectively. To form the field plate, a second ALD Al_2O_3 dielectric layer of 125 nm was deposited. Then, contact holes were formed by dry etching to expose the anode metal. Lastly, the Ti/Al/Cu/Au (10/70/10/60 nm) field-plate metal stack was deposited.

The fabrication process for the field-plated Ga_2O_3 vertical fin transistors is as follows: An n^+ layer was formed on the top surface by Si-implantation and activated at 1000°C to facilitate the source ohmic contact. Submicron fin channels were defined by electron beam lithography and formed by dry etching using a BCl_3/Ar mixture. The resultant fin channels have a near vertical sidewall profile. After dry etching, the Cr/Pt etch mask was removed by Cr etchant and the wafer was treated with HF for 23 min to remove plasma damage. Next, the drain contact (Ti/Au) was deposited before the deposition of the gate stack, consisting of a 35 nm Al_2O_3 gate dielectric by atomic layer deposition (ALD) and a 50-nm Cr gate by sputtering. The gate stack and thick ALD Al_2O_3 spacer was patterned by photoresist planarization and

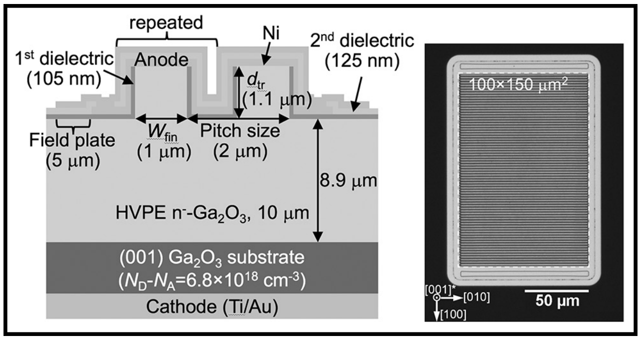

Figure 1: Schematic cross-section and optical top view of the field-plated Ga_2O_3 trench Schottky barrier diodes.

self-aligned etching processes detailed in our previous reports. The source electrode (Ti/Al/Pt) was deposited by sputtering after the spacer formation, simultaneously forming the source-connected field-plate.

The field-plated trench Schottky barrier diodes have a specific on-resistance of 10.5 mΩ·cm². In comparison with the regular SBDs, the field-plated trench SBDs have much lower leakage current as well as a much higher breakdown voltage of 2.89 kV. With addition of the field plate, the destructive breakdown voltage increases by ~ 500 V.

The field-plated trench SBD in this work achieves a power figure-of-merit (BV^2/R_{on}) of 0.80 GW/cm² from DC measurements, which is the highest among all Ga_2O_3 power devices to date [3].

The vertical Ga_2O_3 fin transistors exhibit normally-off operation and a threshold voltage of 1.8 V with a fin channel width of 0.15 µm. The device has an on-off ratio of > 10^8 and a V_{th} of ~ 1.8 V at 0.1 A/cm². The R_{on} is determined to be 25.2 mΩ·cm² from DC measurements. The field-plate helps boost the 3-terminal breakdown voltage from 1 kV to over 2.6 kV, a record high among all Ga_2O_3 transistors [4].

In summary, we have demonstrated improved performance in Ga_2O_3 power diodes and transistors, by using a field-plate technique, marking a significant step forward in the development of high performance Ga_2O_3 power transistors.

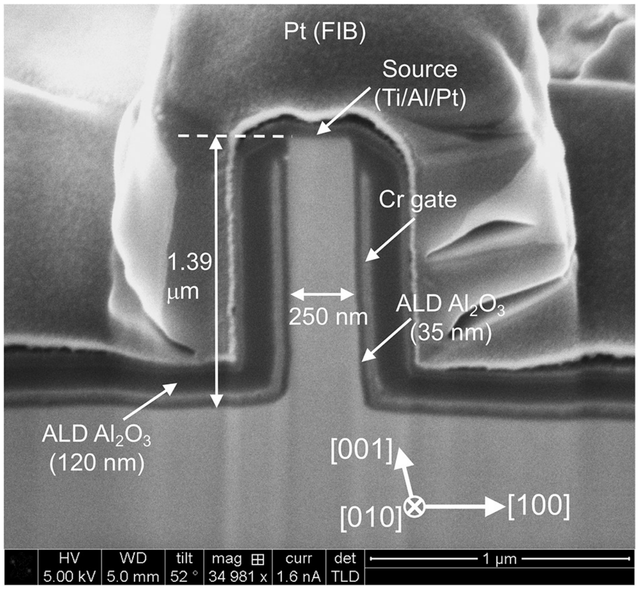

Figure 2: SEM cross-section of the field-plated Ga_2O_3 vertical fin transistors.

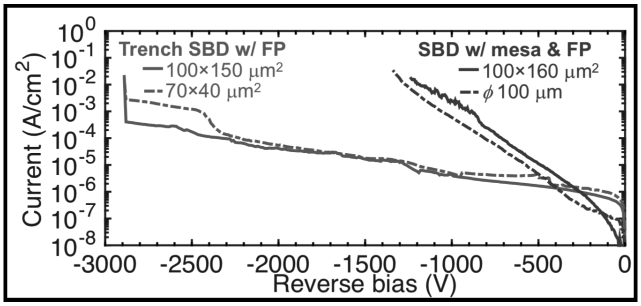

Figure 3: Reverse I-V characteristics of the field-plated Ga_2O_3 trench Schottky barrier diodes.

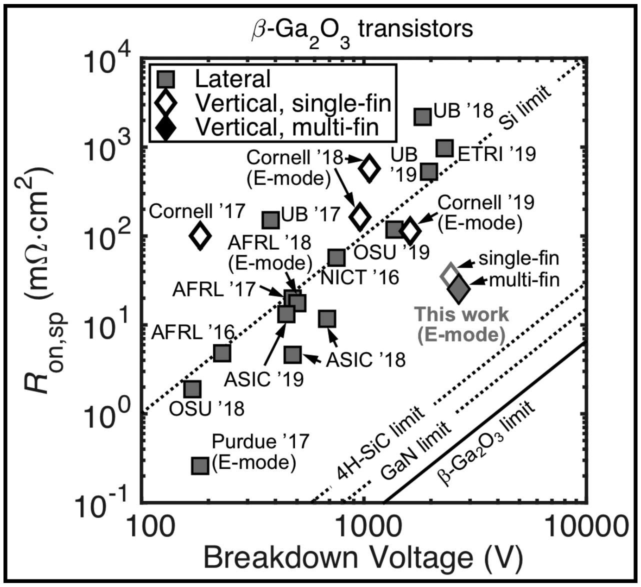

Figure 4: Performance of the field-plated vertical fin transistors in comparison with literature reports.

References:

[1] W. Li, Z. Hu, K. Nomoto, R. Jinno, Z. Zhang, T. Q. Tu, K. Sasaki, A. Kuramata, D. Jena, and H. G. Xing, 2018 IEEE International Electron Devices Meeting (IEDM), pp. 8.5.1, 2018.

[2] Z. Hu, K. Nomoto, W. Li, N. Tanen, K. Sasaki, A. Kuramata, T. Nakamura, D. Jena, and H. G. Xing, IEEE Electron Device Lett. 39, 869 (2018).

[3] W. Li, K. Nomoto, Z. Hu, D. Jena, and H. G. Xing, IEEE Electron Device Lett. 41, 107 (2020).

[4] W. Li, K. Nomoto, Z. Hu, T. Nakamura, D. Jena, and H. G. Xing, 2019 IEEE International Electron Devices Meeting (IEDM), pp. 12.4.1, 2019.

InAlN/GaN HEMTs on Si with Regrown Contacts and f_T/f_{MAX} of 250/204 GHz

CNF Project Number: 2800-19

Principal Investigator(s): Huili Grace Xing, Debdeep Jena

User(s): Kazuki Nomoto, Lei Li, Austin Hickman

Affiliation(s): School of Electrical and Computer Engineering, Cornell University

Primary Source(s) of Research Funding: ComSenTer

Contact: grace.xing@cornell.edu, kn383@cornell.edu

Primary CNF Tools Used: Autostep i-line stepper, Heidelberg mask writer DWL2000, P7 profilometer, FilMetrics, AFM Veeco Icon, Zeiss SEM, PT770, Oxford 81, Oxford PECVD, Oxford ALD, SC4500 evaporators, AJA sputter deposition tools, RTA AG610, JEOL 9500

Abstract:

Depletion-mode high-electron mobility transistors (HEMTs) based on a quaternary barrier $In_{0.17}Al_{0.83}N$/AlN/GaN heterostructure on Si substrate were fabricated. The 55 nm long gate device shows a DC drain current density of 2.8 A/mm, a peak extrinsic transconductance of 660 mS/mm, and balanced current gain cutoff frequency f_T and maximum oscillation frequency f_{MAX} are 250 and 205 GHz, respectively.

Summary of Research:

Gallium nitride high electron mobility transistors (GaN HEMTs) have high breakdown voltages, high two-dimensional electron gas (2DEG) densities, and a high electron saturation velocity. These properties make them ideal for high-power and high-frequency applications, such as switches in power systems and amplifiers in wireless communication systems.

To date, the highest speed GaN HEMTs are demonstrated on SiC substrates, all of which employ regrown ohmic contacts to minimize source/drain resistances. In this report, we have demonstrated the high-frequency and high-power performance capacity of GaN HEMTs on Si substrates. The $I_{D,MAX}$, peak g_m and f_T-f_{MAX} product are among the best reported for GaN HEMTs on Si, which are very close to the state-of-the-art depletion-mode GaN HEMTs on SiC without a back barrier. This highlight celebrates advances on this front achieved in the CNF and published at IEEE Electron Devices Letters [1].

The InAlN/AlN/GaN HEMT structure consists of a 10 nm $In_{0.17}Al_{0.83}N$ barrier, a 1 nm AlN spacer (total barrier thickness: 11 nm), an 800 nm unintentionally doped GaN channel, and AlGaN/AlN buffer and nucleation layers on 200-mm-diameter Si substrate, grown by a Propel® HVM MOCVD system at Veeco Instruments. Room temperature Hall-effect measurements prior to device fabrication showed a 2DEG sheet concentration of 2.27 × 10^{13}/cm^2 and electron mobility of 1430 cm^2/V·s, corresponding to a sheet resistance of 206 Ω/sq.

A schematic cross-section of the InAlN/AlN/GaN HEMT device with regrown n^+ GaN contacts is shown in Figure 1(a). The device fabrication process started with patterning of a SiO_2 mask for n^+GaN ohmic regrowth by PA-MBE. The preregrowth etch depth into the HEMT structure was 40 nm, and regrown n^+GaN was 100 nm with a Si doping level of 7 × 10^{19} /cm^3. Non-alloyed ohmic contact of Ti/Au/Ni was deposited by e-beam evaporation. T-shaped Ni/Au (40/200 nm) gates were formed by electron-beam lithography by JEOL 9500, followed by liftoff. TLM measurements yielded a contact resistance of 0.07 Ω·mm. The device presented here has a regrown n^+GaN source-drain distance L_{sd} of 175 nm, a gate width of 2 × 25 µm, and a gate length L_g of 55 nm. Figure 1(b) shows an angled-SEM image of the fabricated InAlN/AlN/GaN HEMT.

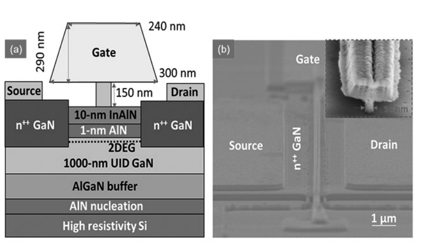

1

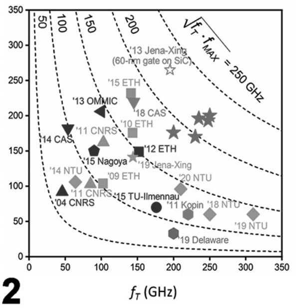

2

Figure 1, left; (a) Schematic cross-section of InAlN/AlN/GaN HEMTs on Si with regrown n^+GaN contacts. (b) An angled SEM image of a fabricated InAlN/AlN/GaN HEMT with an EBL T-gate. ***Figure 2, right:*** *Comparison of the measured* f_T *and* f_{MAX} *of GaN HEMTs on Si substrates. (See pages vi-vii for full color versions.)*

The observed maximum drain current $I_{D,MAX}$ of 2.8 A/mm and the on resistance R_{ON} of 0.6 Ω·mm, along with the peak transconductance g_m of 0.66 S/mm, are among the best in GaN HEMTs on Si, comparable to GaN HEMTs on SiC without a back barrier. At low V_{DS}, these HEMTs typically exhibit a decent I_{ON}/I_{OFF} ratio ~ 10^5; HEMT A has the highest gate leakage among all the tested devices, most likely due to processing non-uniformity. The f_T/f_{MAX} of 250/204 GHz are obtained after de-embedding in HEMT A; in comparison, neglecting the short de-embedding test structure renders similar f_T/f_{MAX} values of 245/187 GHz. In Figure 2, the f_T and f_{MAX} values achieved in this work are compared to other reported GaN HEMTs on Si, as well as the state-of-the-art GaN HEMTs on SiC with similar epi-structures and device dimensions (gate length, barrier materials, and its thickness, no back barrier). It can be seen the present HEMTs are clustered near the upper right corner as desired, with $(f_T \cdot f_{MAX})^{1/2}$ very close to that of the GaN HEMTs on SiC with a comparable gate length.

GaN HEMTs on Si with different geometries were fabricated, measured, and analyzed. The analysis confirms the benefits of n^{++}-GaN source/drain contacts and T-shaped gates, especially in achieving both high f_{MAX} and f_T. With the state-of-the-art regrown ohmics, scaled source-drain separation and T-gates, GaN HEMTs on Si achieve comparable metrics with that on SiC in terms of DC and small-signal performance.

References:

[1] L. Li, K. Nomoto, D. Jena, H. G. Xing, et al., “GaN HEMTs on Si with Regrown Contacts and Cutoff/Maximum Oscillation Frequencies of 250/204 GHz”; IEEE Electron Device Lett., 10.1109/LED.2020.2984727, March. 2020.

Quantum Materials and Technologies

CNF Project Number: 2803-19

Principal Investigator(s): Huili Grace Xing, Debdeep Jena

User(s): John Wright, Zexuan Zhang, Jashan Singhal, Hyunjea Lee, Joseph Casamento

Affiliation(s): Materials Science and Engineering, Electrical and Computer Engineering; Cornell University

Primary Source(s) of Research Funding: National Science Foundation (E2CDA), Semiconductor Research Corporation (nCORE), Office of Naval Research

Contact: djena@cornell.edu, grace.xing@cornell.edu, jgw92@cornell.edu, jac694@cornell.edu, zz523@cornell.edu, js3452@cornell.edu, hl2255@cornell.edu

Primary CNF Tools Used: Autostep 2000 i-line stepper, JEOL 6300, AJA sputter, Veeco AFM, PT-770 etcher, Oxford 81 etcher

Abstract:

The integration of new material properties into electronics devices creates new possibilities for device performance, architecture, and function. We therefore investigate the fabrication and applications of materials with exceptional properties, including superconductivity, ferromagnetism, ferroelectricity, and topologically non-trivial electronic states.

Summary of Research:

With a sizable bandgap higher than that of silicon, two-dimensional (2D) layered materials can be potential candidates for high voltage applications. One of 2D materials, WSe_2 is used for enhancement mode p-channel field effect transistors (FETs) for high voltage devices, being patterned by JEOL 6300 in CNF. Ambipolar transport in back-gate WSe_2 FETs is often reported in literature, which is a feature of junction-less transistors. However, the breakdown voltage of back-gate WSe_2 FETs with overlapping source and drain is found to be limited by the ambipolar transport. In the off-state of WSe_2 p-FETs, the voltage across the overlapping drain and gate creates an electron channel near the drain; electrons are then injected from the drain contact into the electron channel by tunneling and swept to the source by a lateral electric field across the channel, generating high off-state leakage currents. This ambipolar-limited breakdown is confirmed by depositing Al_2O_3, which introduces interface states near the conduction band edge of WSe_2, and the electron current is suppressed since the drain-gate voltage is not able to raise the Fermi-level into the conduction band. With the suppression of the ambipolar transport, WSe_2 p-FETs show improved breakdown voltages up to -100 V (Figure 1), corresponding to a critical electric field in WSe_2 higher than 200 kV/cm.

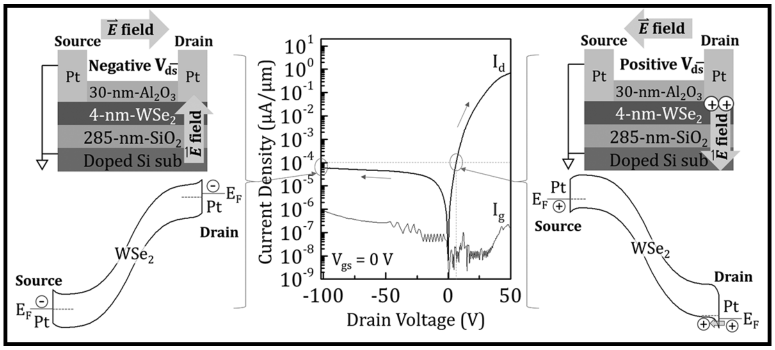

Figure 1: Off-state leakage currents and corresponding energy band diagram cartoons of the WSe_2 p-FET.

Epitaxial ferroelectric semiconductor devices have promise in applications of low power transistors and nonvolatile memories. Their realization has been largely hindered due to material development issues. Our goal was to utilize a novel epitaxial ferroelectric material system, $LuFeO_3$, integrated on GaN to achieve an epitaxial ferroelectric semiconductor field-effect transistor (FE-FET). With the utilization of CNF equipment such as the SC4500 odd hour electron beam evaporator, AG 610 rapid thermal annealer, AJA ion mill, Veeco Dimension Icon atomic force microscope, and GCA Autostep 200 DSW i-line wafer stepper, we have taken the steps toward achieving that goal.

$LuFeO_3$ is intended to act as a ferroelectric gate dielectric and a two-dimensional electron gas (2DEG) formed from a conduction band offset at the $Al_{0.25}Ga_{0.75}N$-GaN interface serves as the semiconductor electron channel.

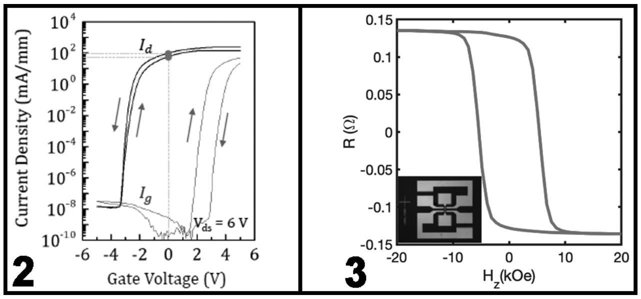

Figure 2, left: I_d-V_{gs} and I_d-V_d characteristics of the $LuFeO_3$-GaN Fe-FET device, showing 2DEG depletion and hysteretic behavior, as well as saturation. Figure 3, right: Hall resistance of Pt/Mn_4N Hall bar (Inset: photo of the measured device).

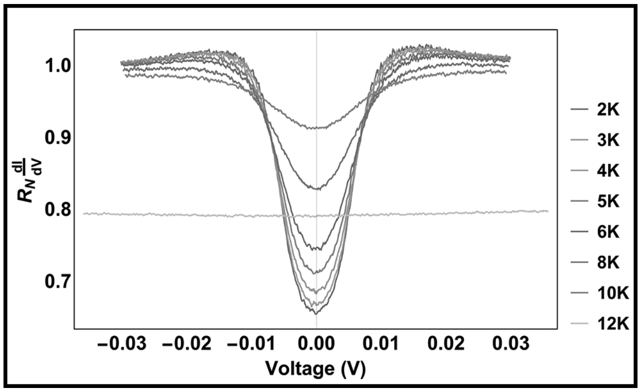

Figure 4: Differential conductance of a NbN/2DEG/NbN device fabricated using a nitrogen polar GaN/AlN quantum well. (See pages vi-vii for full color version.)

Drain current, gate voltage (I_d-V_{gs}) electrical data show a high on-off ratio (10^6) and depletion of the 2DEG in the negative bias regime with counterclockwise hysteretic behavior (Figure 2). These results show effective device patterning, etching, and electrical contact to the electron channel. This is a significant step toward a Fe-FET involving $LuFeO_3$-GaN based heterostructures.

Seamless integration of ferromagnet on semiconductor such as GaN is a promising route towards future energy efficient applications because it provides the unique opportunity to merge memory and logic components. To this end, we have focused on the epitaxial integration of various magnetic phases of MnxNy with wide bandgap semiconductors (GaN and SiC) [1]. Ferrimagnetic Mn_4N layers were grown using molecular beam epitaxy technique on different substrates including cubic MgO, $SrTiO_3$ and hexagonal GaN, SiC. Structural and magnetic characterization was done with the help of various CNF tools and they were found to differ significantly on different substrates [2]. Particularly, Mn_4N layers grown on MgO exhibits strong perpendicular magnetic anisotropy (PMA) and smooth surface.

For spintronic applications based on spin orbit torque (SOT), heavy metal Pt was sputtered on MBE grown Mn_4N and further patterned into test structures such as Hall bars through photolithography, ion mill and lift off process. An image of the patterned structure could be seen in inset of Figure 3.

Transport properties were measured on patterned devices where a square hysteresis loop in field dependent Hall resistances was observed (Figure 3). Such hysteresis loop is typical of a PMA magnetic thin film with high structural quality. At this stage, however, SOT switching of Pt/Mn_4N hasn't been demonstrated, possibly due to (1) poor interface quality between Pt and Mn_4N caused by air exposure or (2) insufficient spin injection considering the large strength of PMA in Mn_4N. Future steps would include optimizing Pt/Mn_4N structure along these directions.

Topological superconductivity can be engineered by utilizing topologically trivial S-wave superconductors to induce correlated electronic states in non-superconducting topological electronic systems, such as the quantum Hall state in high mobility two-dimensional electron gases (2DEG). To explore these phenomena we have grown epitaxial nitride superconductor/semiconductor heterostructures utilizing nitrogen polar GaN/AlN quantum wells with superconducting NbN contacts. The structure places the 2DEG in closer proximity to the surface then would be the case with the more conventional metal-polar nitride AlN/GaN quantum well, while also reducing the tunneling barrier between the superconducting top contact and the 2DEG. Once the structure is grown by MBE the NbN is selectively etched to create devices wherein the 2DEG in the GaN quantum well forms a conducting channel with NbN contacts.

Figure 4 shows the differential conductance of a NbN/2DEG/NbN device at temperatures around the superconducting transition temperature of the NbN film, which is approximately 12K. We see evidence that below 12K the 0V differential conductance is reduced, which is due to the opening of an energy gap at the fermi level in the NbN.

Further work will focus on placing the 2DEG in even closer proximity to the superconductor to increase the proximity induced correlated states, which will be evidenced by an increase in the 0V differential conductance.

References:

[1] S. Dhar, et al. Appl. Phys. Lett. 86, 112504 (2005).

[2] Z. Zhang, et al. AIP Advances 10, 015238 (2020).

Neural Probe Utilizing Micro-Coil Magnetic Stimulation with CMOS Technology Integration for Spatially Programmable Neurostimulation

CNF Project Number: 2847-19

Principal Investigator(s): Alyosha Molnar

User(s): Edward Szoka

Affiliation(s): Department of Electrical and Computer Engineering, Cornell University

Primary Source(s) of Research Funding: National Institutes of Health

Contact: molnar@ece.cornell.edu, ecs227@cornell.edu

Primary CNF Tools Used: Oxford ALD FlexAL, AJA sputter deposition, ABM contact aligner, Unaxis 770, PT770 etcher, Oxford 100

Abstract:

Neural prostheses have been effective in treating neurological disorders using electrical stimulation through micro-electrodes [1]. However, micro-electrode neurostimulation suffers from the inability to selectively activate neurons based on orientation [2] as well as maintaining long-term functionality [3]. Magnetic stimulation produced by micro-coil devices avoid these issues as the induced electric fields are asymmetric and magnetic fields can pass through biological materials allowing for complete encapsulation [4,5]. Mixed-signal circuitry is integrated into the proposed micro-coils by fabricating the design in a 180 nm CMOS technology process. Further nanofabrication techniques are applied to release the proposed micro-coils from the original chip packaging to produce a neural probe with spatially programmable micro-coil magnetic stimulation sites. Preliminary *in vitro* patch-clamp recordings of retinal tissue with programmed micro-coil magnetic stimulation sites has shown controlled neural behavior. Further research exploring the programmable stimulation site regions are ongoing.

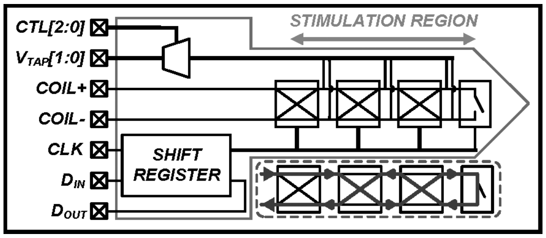

Figure 1: High-level diagram of the proposed programmable micro-coil neural probe with an example of programmed current direction.

Summary of Research:

The proposed micro-coil system is shown in Figure 1. The programmable stimulation sites are implemented by using a programmable switching network to direct the micro-coil current flow. The switching network can be programmed into four states: pass straight through, cross over, short-circuit, or open-circuit. The switches are implemented as pass gates with the NFETs sized at W/L of 1.5 mm/180 nm and PFETs sized at W/L of 2 mm/180 nm. The switches are sized to have a maximum resistance of 2W. With the trace resistance approximately 4W, the maximum coil resistance is 18W, allowing safe operation of the FETs while driving the micro-coil with 100 mA of current. The micro-coil is programmed using a shift register where the programming bits are buffered and routed down the probe to the switching networks. For electrical verification the coil segments are broken out to a multiplexer and brought off-chip to validate the current direction based off the voltage drop throughout the micro-coil.

The micro-coils are released and thinned down from the original chip packaging through a series of nanofabrication steps. Aluminum oxide and chrome are deposited (to serve as silicon etching and oxide etching masks respectively) and patterned using conventional photolithography and a combination of wet-etch and plasma etching. The oxide is etched in a CHF_3/O_2 oxide plasma etch using the Oxford 100 to expose the silicon surface. The exposed topside silicon is etched in the Unaxis 770 using a deep reactive-ion etching (DRIE) process down to the desired thickness of the neural probe (75 µm). The chips are flipped upside-down and the bulk silicon is etched in the same DRIE process until the micro-coils are released from the rest of the chip. The nanofabrication process to release the micro-coils is shown in Figure 3. The released micro-coils are then wire bonded to a carrier PCB, the wire bonds are protected with epoxy, and the entire assembly is coated with around 2 µm of Parylene-C to further encapsulate the micro-coil.

The micro-coils were fabricated in a 180 nm 1P6M CMOS process with a probe length and width of 1.9 mm and 0.1 mm respectively. A micrograph and scanning electron microscope (SEM) image of the micro-coil is shown in Figure 3.

Preliminary biological testing has been done using a patch clamp recording electrode in conjunction with the micro-coil in mouse retinal tissue. The recorded neuron was located at the tip of the micro-coil probe. Stimulation trials were done by driving the micro-coil with twenty ramp current waveforms spaced 200 ms apart. Figure 4 shows the neural response of the clamped neuron at the first and fourth stimulation sites (next to the neuron and 750 μm away). The data shows that stimulation near the neuron elicited indirect stimulation as there was immediate suppression of neural activity for 100 ms followed by a spike train for all twenty stimulation pulses. Stimulation further away from the neuron showed neural behavior that was more akin to natural behavior than evoked responses.

Conclusions and Future Steps:

Through the use of CMOS technology and nanofabrication techniques an insertable neural probe utilizing micro-coil magnetic stimulation with spatially programmable stimulation sites has been created. Preliminary biological testing with patch clamp measurements has shown repeatable evoked neural responses, however further testing utilizing a multi electrode array needs to be done to characterize the stimulation site regions. Future designs are also being created to utilize micro-coils with more turns to decrease the necessary stimulation current as well as incorporating current driving circuitry to independently drive each micro-coil.

References:

[1] S. J. Bensmaia and L. E. Miller, "Restoring sensorimotor function through intracortical interfaces: progress and looming challenges," Nature Reviews Neuroscience, vol. 15, no. 5, pp. 313-325, 2014.

[2] M. H. Histed, V. Bonin, and R. C. Reid, "Direct activation of sparse, distributed populations of cortical neurons by electrical microstimulation," Neuron, vol. 63, no. 4, pp. 508-522, 2009.

[3] V. S. Polikov, P. A. Tresco, and W. M. Reichert, "Response of brain tissue to chronically implanted neural electrodes," Journal of Neuroscience Methods, vol. 148, no. 1, pp. 1-18, 2005.

[4] S. W. Lee, F. Fallegger, B. D. F. Casse, and S. I. Fried, "Implantable microcoils for intracortical magnetic stimulation," Science Advances, vol. 2, no. 12, 2016.

[5] S. W. Lee, K. Thyagarajan, and S. I. Fried, "Micro-coil design influences the spatial extent of responses to intracortical magnetic stimulation," IEEE Transactions on Biomedical Engineering, vol. 66, no. 6, pp. 1680-1694, June 2019.

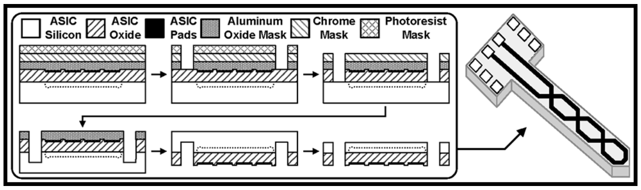

Figure 2: Nanofabrication process to release the micro-coils from the rest of the chip. Mask layers that are no longer being used are etched away between the shown process steps.

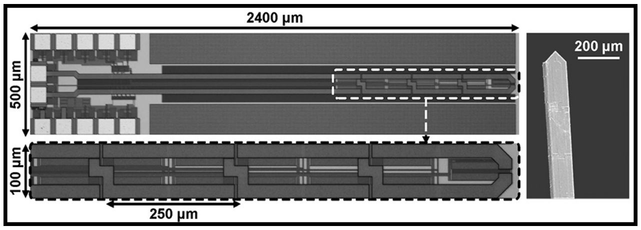

Figure 3: Unreleased micro-coil die photo with enhanced view of the stimulation region as well as an SEM image of a released micro-coil.

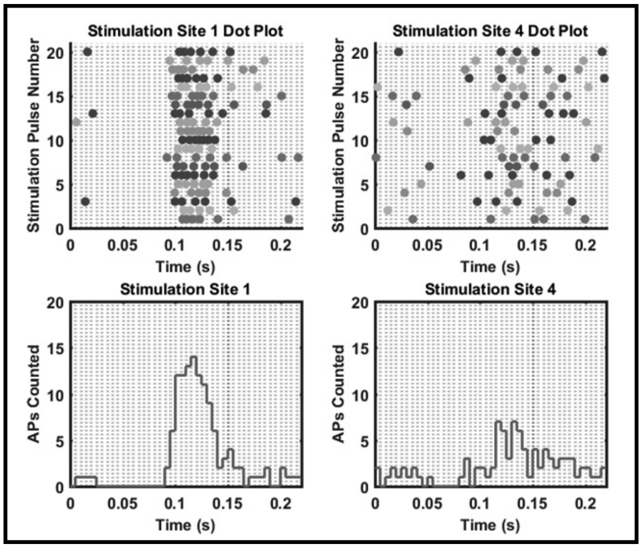

Figure 4: Dot plot and action potential count of patch clamp measurements from one neuron during stimulation at two different programmed sites. (See pages vi-vii for full color version.)

One-Component Molecular Glass Photoresists for EUV Lithography

CNF Project Number: 386-90

Principal Investigator(s): Christopher Kemper Ober

User(s): Yusuke Otsubo

Affiliation(s): Materials Science and Engineering, Cornell University

Primary Source(s) of Research Funding: JSR Corporation

Contact: c.ober@cornell.edu, yo237@cornell.edu

Primary CNF Tools Used: Zeiss Supra SEM, ASML 300C DUV stepper, ABM contact aligner

Abstract:

Extreme ultraviolet (EUV) lithography has entered into high volume manufacturing (HVM) phase in 2019. However, meeting the increased requirements for the photoresists still remains a challenge. As the feature size decreases, it is becoming more difficult to meet the requirements using conventional organic polymer-based chemically amplified resists (CAR). In this context, development of new photoresist material platforms with high resolution maintaining high sensitivity and low roughness is highly demanded. Our group has previously shown that molecular glass photoresist system has the excellent potential as a high-resolution photoresist platform. We are currently attempting to improve the performance of molecular glass photoresist by introducing photoacid generator (PAG) moieties into the resist molecules, making it completely one-component system. In this report, our preliminary results of deep ultraviolet (DUV) patterning with newly developed one-component molecular glass photoresists are described.

Summary of Research:

Introduction. EUV lithography has already been in HVM phase. Throughout the next decade, a resolution of sub-10 nm half pitch (HP) will be the industry-wide target. In the era of sub-10 nm HP, which is comparable with polymeric materials, it is obvious that conventional CAR system reaches the technical limitation.

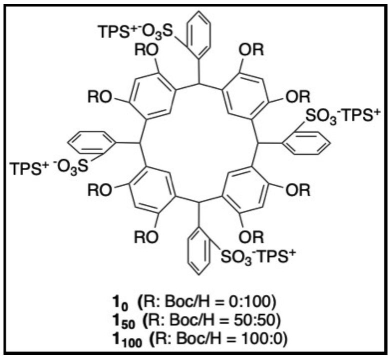

Figure 1: Chemical structures of the molecular glass photoresists used in the study.

Our group has previously reported utilization of amorphous small organic molecules, known as molecular glasses, as new photoresist platform [1,2]. Smaller, well-defined size of molecular glass resists compared to CAR was shown to be advantageous for achieving high resolution and low roughness patterning. However, perfect uniformity in component has yet to be achieved, as the previous systems required PAG as additive. In this work, we are attempting to develop completely one-component molecular glass photoresists, assuming that perfect uniformity in component as well as in size will give more homogeneous films, and therefore high resolution and low roughness patterning.

Material Design and Synthesis. Photoresist material has to meet several requirements including solubility, film forming ability and etch resistance. Especially for molecular glasses, which has low molecular weight and therefore higher tendencies to crystalize than polymers, additional care for crystallization should be paid because it will cause pattern deformation in lithography. To prevent crystallization, it is important to keep glass-transition temperature (T_g) much higher than temperature in post- and pre-exposure baking steps.

We have previously demonstrated that resorcin[4]arene-based molecular glass photoresists show high T_g due to its rigid and phenolic structures [2]. Herein we designed and synthesized novel one-component molecular resists by introducing PAG moieties on the rim of resorcin[4]arene core in varying substitution degree (Figure 1). The sulfonate groups were covalently bounded to the core in order to limit the diffusion of generated photoacid. The synthesis can be done only in three steps from reasonable commercially available reagents and basic laboratory techniques. This would allow feasible industrial scale production at low cost.

The synthesized photoresists could be dissolved in gamma-butyl lactone (GBL), a common spin-coating solvent regardless of their degree of substitution.

The solutions in GBL remained clear and did not give any precipitation even after one months at room temperature.

Photolithographic Performance Evaluation. Thin films could be fabricated by spin-coating 5 wt% GBL solutions onto unprimed 4-inch silicon wafers. The formed films did not show any obvious cracks. DUV exposure was performed using ABM contact aligner equipped with 248 nm filter and the exposed films were developed using isopropanol (IPA). Obtained pattered films were observed with optical microscope (Figure 2). Although much more improvement needs to be made, the microscopic images showed vague positive-tone patterns obtained without any PAG as additive. These preliminary results encourage us to explore one-component molecular glass system more.

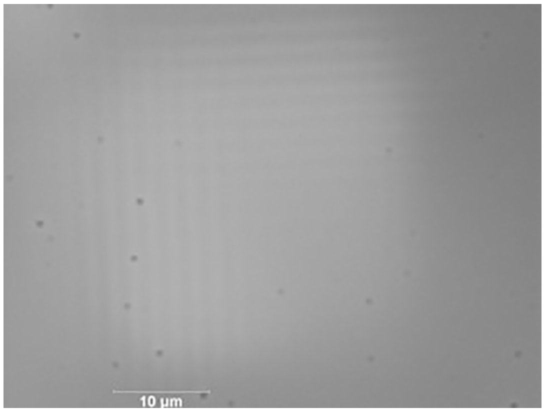

Figure 2: Optical microscope images of patterned film with 150. Prebake: 150°C/60s; Exposure: 20 mJ/cm^2; Development: isopropanol 120s.

Conclusions and Future Steps:

Novel resorcin[4]arene-based one-component photoresist materials have been successfully synthesized. They showed good film formation and positive-tone patterning ability with DUV exposure. Further improvements to obtain high contrast pattern from both material and process sides is underway.

References:

[1] J. Dai, S. W. Chang, A. Hamad, D. Yang, N. Felix, C. K. Ober Chem. Mater. 2006, 18, 3404-3411.

[2] S. W. Chang, R. Ayothi, D. Bratton, D. Yang, N. Felix, H. B. Cao, H. Deng, C. K. Ober J. Mater. Chem. 2006, 16, 1470-1474.

Amorphous Bi-Ti-O Thin Film Dielectrics

CNF Project Number: 1400-05
Principal Investigator(s): R. Bruce van Dover
User(s): Rita Sun

Affiliation(s): Materials Science and Engineering, Cornell University
Primary Source(s) of Research Funding: Air Force Office of Scientific Research
Contact: vandover@cornell.edu, rs2537@cornell.edu
Primary CNF Tools Used: FilMetrics

Abstract:

Amorphous bismuth titanate (Bi-Ti-O) composition spread thin films were fabricated using off-axis reactive RF co-sputtering. Continuous compositional spreads allow for high-throughput analysis techniques. Optical reflectometry and profilometry were applied on reference single-element samples and Bi-Ti-O composition spreads to generate composition maps. Metal contacts were deposited on the samples for dielectric properties measurement. Dielectric constant, dissipation factor and current-voltage characteristics reveal the potential of amorphous Bi-Ti-O thin films as a novel dielectric for application in capacitive circuit elements.

Summary of Research:

The investigation of new candidate thin film dielectric materials has been of great importance in capacitive circuits applications for various electronic devices. A good dielectric material exhibits a high dielectric constant and a low dissipation factor that gives low leakage current. These features increase the effective capacitance of the capacitive circuit elements. Besides, amorphous thin films are preferable over polycrystalline materials, since they are generally cheaper and easier to fabricate, especially on modern circuitry that has nanoscale features. Polycrystalline dielectrics are also expected to show a lower breakdown field than that of amorphous dielectrics due to the presence of grain boundaries. [1]

Amorphous bismuth titanate (Bi-Ti-O) thin films can be considered as a potential candidate thin film dielectric material. Crystalline $Bi_4Ti_3O_{12}$ has been reported to show a high dielectric constant and low dissipation factor [2]. Furthermore, to investigate composition-dependent trends of dielectric properties, a composition-spread technique for thin film growth can be applied for high-throughput analysis of a wide range of compositions [3].

In this work, amorphous Bi-Ti-O composition spread thin films were synthesized by off-axis reactive RF magnetron sputtering to investigate the composition-dependence of dielectric properties.

Optical reflectometry was performed on Bi-Ti-O composition spread thin films by FilMetrics in the Cornell NanoScale Science and Technology Facility (CNF). Profilometry was performed on calibration Bi-O and Ti-O samples to help obtain composition maps of samples. The thickness of Bi-Ti-O thin films was measured by profilometry. An array of silver contacts was deposited on Bi-Ti-O thin films as top electrodes for the characterization of dielectric properties. Silver dot contacts were deposited by thermal evaporation in CNF. Capacitance, dissipation factor and current-voltage characteristics were measured using a high-throughput setup which consists of an LCR meter and an electric probe with an automatic stage.

Figure 1 shows the capacitance map as a function of the sample position (Bi-rich region on the left, Ti-rich region on the right) on the Bi-Ti-O thin film. The data shown was measured at 10 kHz, while values that were too high or too low to be realistic are shown in white color. High capacitance values can be observed in the central region and the Ti-rich side of the Bi-Ti-O composition spread thin film.

Figure 2 and Figure 3 illustrate the dielectric constant and the dissipation factor of Bi-Ti-O as a function of composition. It can be seen that Bi-Ti-O thin film with a Bi:Ti ratio of roughly 1:1 appears to exhibit a high dielectric constant while maintaining a low dissipation factor.

Figure 4 shows the maximum breakdown field as a function of composition. Addition of Ti in $Bi_{1-x}Ti_xO_y$ up

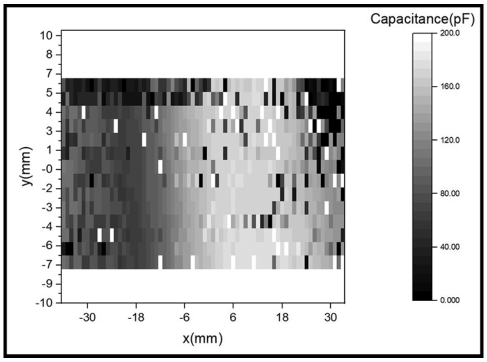

Figure 1: Capacitance map of Bi-Ti-O thin film as a function of sample position (Bi-rich region on the left, Ti-rich region on the right).

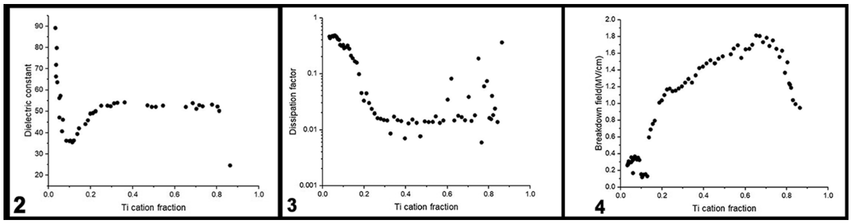

***Figure 2, left:** Dielectric constant of Bi-Ti-O as a function of Ti cation composition. **Figure 3, middle:** Dissipation factor of Bi-Ti-O as a function of Ti cation composition. **Figure 4, right:** Breakdown field of Bi-Ti-O as a function of Ti cation composition.*

to x around 0.7 increases the breakdown field of the sample, which can result in a good maximum stored charge of approximately 8 $\mu C/cm_2$.

Conclusions and Future Steps:

The dielectric properties of amorphous Bi-Ti-O composition spread thin films were examined. Amorphous Bi-Ti-O was found to show good potential as a dielectric material. However, using the profilometry data to characterize the composition as a function of the sample position is a rough approximation. More accurate data can be obtained from optical reflectometry, which can be further used to characterize the refractive index of samples. Furthermore, laser spike annealing can be performed on the samples to form stable and metastable phases in addition to the as-deposited amorphous phase [4], which can be enable the investigation of the effect of different crystalline phases on dielectric properties of Bi-Ti-O thin films.

References:

[1] Naoi, T. A., Paik, H., Green, M. L., and Dover, R. B. V. (2015). Dielectric properties of amorphous Zr-Al-O and Zr-Si-O thin films. Journal of Advanced Dielectrics, 05(01), 1550010. doi: 10.1142/s2010135x15500101.

[2] Alfonso, J., Olaya, J., Bedoya-Hincapié, C., Toudert, J., and Serna, R. (2014). Annealing Effect on the Structural and Optical Properties of Sputter-Grown Bismuth Titanium Oxide Thin Films. Materials, 7(5), 3427-3434. doi: 10.3390/ma7053427.

[3] van Dover, R. B., Schneemeyer, L. F., Fleming, R. M., and Huggins, H. A. (1999). A high-throughput search for electronic materials-thin-film dielectrics. Biotechnology and bioengineering, 61(4), 217-225.

[4] Bell, R. T., Jacobs, A. G., Sorg, V. C., Jung, B., Hill, M. O., Treml, B. E., and Thompson, M. O. (2016). Lateral Temperature-Gradient Method for High-Throughput Characterization of Material Processing by Millisecond Laser Annealing. ACS combinatorial science, 18(9), 548-558.

Three-Dimensional Printing with Silica Cages

CNF Project Number: 1645-08
Principal Investigator(s): Tobias Hanrath
User(s): Jen-Yu Huang

Affiliation(s): Robert F. Smith School of Chemical and Biomolecular Engineering, Cornell University
Primary Source(s) of Research Funding: National Science Foundation
Contact: th358@cornell.edu, jh2486@cornell.edu
Primary CNF Tools Used: ZEISS Supra and Ultra SEMs, Leica supercritical dryer

Abstract:

Material scientists have now developed an extensive library of nano-sized building blocks, offering a vast panel of properties (optic, magnetic, plasmonic, catalytic, etc.). Nevertheless, combining these building blocks for the realization of multifunctional materials while controlling their structure from the nano- to the micro- and all the way to the macroscale still remains an open challenge in order to fully exploit their potential. In parallel, new material processing techniques such as 3D printing technologies are emerging for the fabrication of macroscopic highly engineered parts and devices. In this work, newly discovered silica nanocages are combined with digital light processing 3D printing technique for the rapid fabrication of mesoporous parts with arbitrary shapes and tunable internal structures. Complementary strategies are then deployed for the implementation and deliberate positioning of various functionalities throughout 3D printed objects with high control on the microstructure and macroscopic architecture of the superstructures. This approach paves the road for innovative device concepts and designs, that will benefit from the unique properties of nanomaterials and from the micro-and macroscale manufacturing capability of 3D printers.

Summary of Research:

In this work, silica cages were made compatible with digital light processing 3D printing, through our reported photoresponsive ligand on inorganic core (PLIC) concept [1].

Making use of the printed cage-based mesoporous materials, we developed a hitherto unknown internal 3D printing approach. Here, the porosity of an already printed 3D part serves as a scaffold for the subsequent printing of a second 3D material directly within the first. To demonstrate this concept, we printed a second metal structure within the pores of the first silica structure. As illustrated in Figure 1, a 3D block of silica cages was first printed as described before and then soaked for 30 minutes in a solution of silver nitrate (0.1 M in 10:1 v/v ethanol:toluene), and two photoinitiators, namely TPO (0.05 M) and Darocur 1173 (0.5 M). In this case, TPO acts as a sensitizer for Darocur 1173, which serves as the electron donor for the reduction of Ag^+ to Ag^0.

A light pattern was then projected in the form of three lines to locally reduce silver, which remained embedded in the original 3D silica block (Figure 1d-f). The 3D printing of a second, more active material within a 3D printed mesoporous silica block opens a whole new scope of opportunities. Through this approach, the two materials are entangled with each other, which means that the structure of the scaffold or host material will influence the structure and therefore properties of the guest material.

As an example, deliberately varying the porosity of the silica host could allow to tune the electrical conductivity along the metal lines. Furthermore, the entanglement of the two materials also means that interactions between them such as charge transport, are possible and may even benefit from their high interfacial area. This approach can readily be extended to a large variety of materials offering a wealth of unique properties.

For instance, printing two different catalytic materials within a porous silica scaffold could result in a highly tunable platform with controlled symmetry and flux for tandem catalysis applications. The whole 3D printing toolbox can thereafter be put to practice for the positioning of active centers within the host scaffold with a great degree of freedom.

References:

[1] Huang, J.-Y. et al. Three-Dimensional Printing of Hierarchical Porous Architectures. Chem. Mater. acs.chemmater.9b02761, doi:10.1021/acs.chemmater.9b02761 (2019).

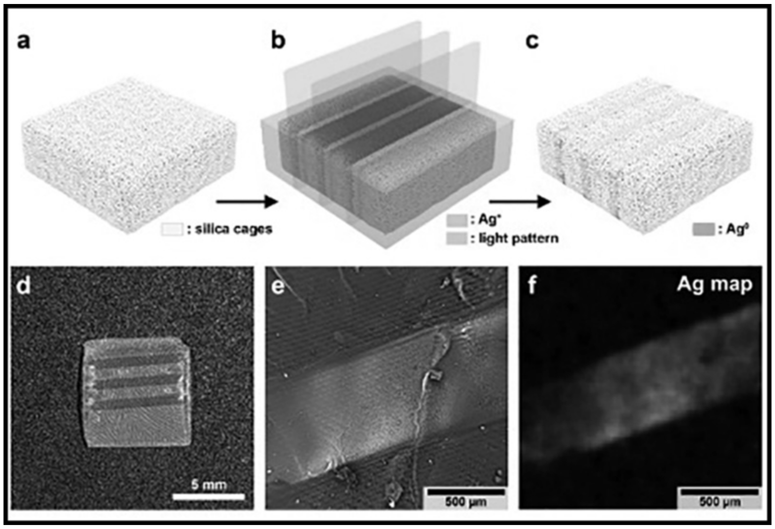

Figure 1: a-c, Illustration of the process of printing silver within a primary part printed with porous silica cages. First, a block of silica cages without additional functionalization is printed (a). The block is immersed in a solution of silver nitrate and photoinitiators. A light pattern in the shape of lines is then projected onto this block (b), resulting in the localized reduction of Ag^+ ions into Ag^0 (c). d, Photograph of the resulting block of silica cages exhibiting three lines of metallic silver. Backscattered electron-based SEM image (e) and EDS map (f) of a silver line embedded in the porous silica matrix.

Nanometer-Scale Area-Selective Formation of Polymer Brushes

CNF Project Number: 1757-09
Principal Investigator(s): Christopher Kemper Ober[2]
User(s): Yuming Huang[2], Hai Tran[1,2]

Affiliation(s): 1. Chemical and Biomolecular Engineering, 2. Materials Science and Engineering; Cornell University
Primary Source(s) of Research Funding: National Science Foundation
Contact: cko3@cornell.edu, yh839@cornell.edu
Website: https://ober.mse.cornell.edu/index.html
Primary CNF Tools Used: E-beam resist spinners, JEOL 9500, FilMetrics F50-EXR, Oxford 81 etcher, Zeiss Ultra SEM, optical microscope

Abstract:

The topological control of mixed polymer brushes can be realized via multi-steps surface-initiated polymerizations on a pattern fabricated by e-beam lithography, which is known for its fine resolution and precision. Patterned binary polymer brushes were produced on silicon wafers by area-selective deposition of two different initiators, using patterned e-beam resists as the masks. As a result, "nano-spikes" made of rod brushes were formed, surrounded by soft coil brushes. This platform has unique dual properties and thus can be used in various applications such as cytoskeleton mimicry and molecular recognition.

Summary of Research:

Introduction. Polymer brushes are polymer chains that have one end covalently bonded to a substrate, such as a silicon wafer. Due to the unusual molecular arrangements, polymer brushes have demonstrated interesting surface properties and thus has been one of the main research focus in polymer science [1]. Potential applications such as metal oxide surface functionalization, optoelectronics, and medical diagnosis have been studied in the past decades. However, there is an increasing need for location-specific functionalization of these metal oxide surfaces as patterning techniques advances in the lithography industry. As such, incorporating e-beam lithography with the vapor phase surface-initiated polymerization can be a possible solution to the aforementioned demands.

Previously we have reported a new approach to nano-pattern rod-like polymer brushes with high persistence length using the equipment in Cornell NanoScale Facilities (CNF). This year we have made further advancement by incorporating our knowledge in combining rod-coil polymer brushes in a single system, which will provide enhanced phase separation and unique mechanochemical surface properties [2]. This report provides a novel pathway in fabricating nano-patterned rod-coil mixed polymer brushes on a silicon wafer, which will result in surfaces with dual properties, chemical functionality, and responsive behavior under different stimulations.

Fabrication. The mixed polymer brushes were patterned on a silicon wafer by multi-steps fabrication process and area-selective deposition of surface-bound initiators for polymerizations.

E-beam Resist Mask Preparation. Patterned e-beam resist mask (~150 nm) was prepared through JEOL 9500. The sample was then etched ~ 10 nm using Oxford 81 etcher to remove residual debris in the unmasked area.

Synthesis of the Rod Brushes. The deposition of a silane initiator on the treated substrate was carried out in a closed chamber under vacuum and elevator temperature. The initiator was allowed to vaporize and thus reacting with the exposed metal oxide surfaces. Afterward, the resist mask was removed by organic solvents. Subsequently, surface-initiated ring-opening polymerization of poly-*y*-benzyl-*L*-glutamate (PBLG), a rod-like polymer, was synthesized under vacuum and elevated temperature.

Synthesis of the Coil Brushes. The deposition of α-bromoisobutyryl bromide (BiBB) functionalized silane initiator was deposited onto the remaining unreacted area under similar conditions, followed by surface-initiated atom-transfer radical polymerization of poly(*N*-isopropylacrylamide) (PNIPAM), obtaining a thermo-responsive coil polymer brushes with low persistence length.

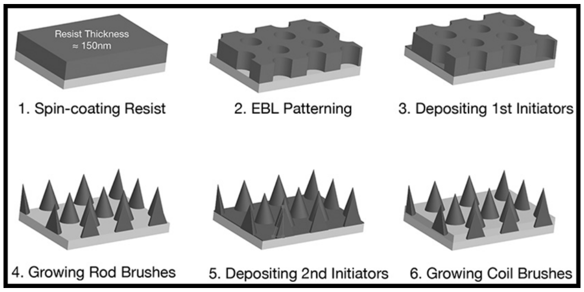

Figure 1: Schematic illustration of the fabrication process.

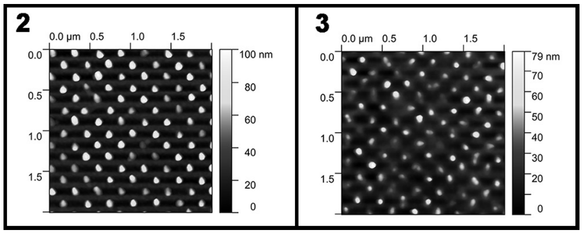

***Figure 2 left:** AFM image of the patterned PBLG rod brushes.*
***Figure 3, right:** AFM image of the mixed PBLG-PNIPAM brushes.*

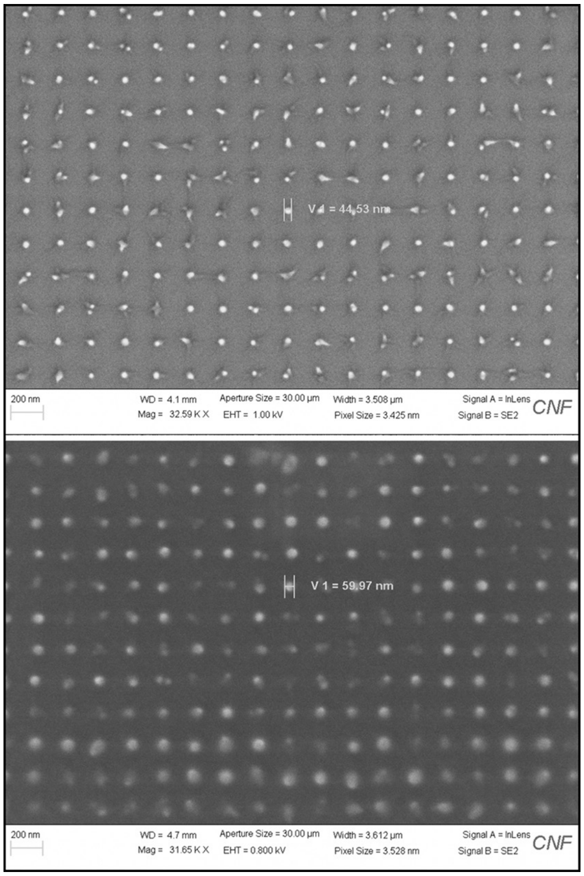

Figure 4: SEM images of the PBLG brushes (top) without PNIPAM and (bottom) with PNIPAM brushes.

A schematic illustration of the whole fabrication process is shown in Figure 1.

Characterization and Results:

The e-beam resist thickness was measured by FilMetrics F50-EXR. The patterned e-beam resist was examined using Zeiss Ultra SEM. The patterned PBLG rod brushes were characterized using atomic force microscopy (AFM) for height measurement (Figure 2), and Zeiss Ultra scanning electron microscopy (SEM) for topological analysis. The resulting surfaces with mixed rod-coil brushes were analyzed with AFM (Figure 3) and SEM (Figure 4) to compare the differences.

In conclusion, we demonstrated a process for precisely control the spatial arrangement of mixed rod-coil polymer brushes. In the near future, we plan to examine how the addition of thermo-responsive PNIPAM brushes in the system would affect the surface properties. We also plan to explore the use of these surfaces for biological applications, such as cell membrane support and molecular recognition.

References:

[1] Chen, W. L.; Cordero, R.; Tran, H.; Ober, C. K., 50th Anniversary Perspective: Polymer Brushes: Novel Surfaces for Future Materials. Macromolecules 2017, 50 (11), 4089-4113.

[2] Tran, H.; Zhang, Y.; Ober, C. K., Synthesis, Processing, and Characterization of Helical Polypeptide Rod-Coil Mixed Brushes. ACS Macro Lett 2018, 7 (10), 1186-1191.

Nanotube Transistor Arrays on a TEM Substrate

CNF Project Number(s): 2486-16, 2858-19
Principal Investigator(s): Jonathan S. Alden
User(s): Jonathan S. Alden, Joshua S. Alden

Affiliation(s): Esper Biosciences, Inc.; McGovern Center, Cornell University

Primary Source(s) of Research Funding: National Institutes of Health, Esper Biosciences, Inc.

Contact: jonathan.alden@gmail.com, ja698@cornell.edu

Primary CNF Tools Used: Low pressure chemical vapor deposition (LPCVD) furnaces (oxide, nitride), Autostep i-line stepper, ABM contact aligner, SC4500 evaporators, Oxford 80 RIE

Abstract:

We use photolithography to fabricate nanotube transistor devices on substrates with thin nitride windows, which can be imaged using transmission electron microscopy (TEM). Our device architecture permits us to characterize a given nanotube both electrically, and by high-resolution TEM. In low-dimensional systems, such as nanotubes, where nanoscale surface and defect structure can have profound influences on the electrical properties, we expect this combined nanoscale imaging and electrical characterization to yield insights that will inform the design of nanoscale sensors.

Summary of Research:

The study of low-dimensional materials, such as carbon nanotubes, graphene, and molybdenum disulfide, has been an area of growing interest over the past decades, in part due to their promise as molecular sensors. Due to their one-to-few-atom thickness, the properties of such materials often depend sensitively on surface adsorbates, substrate-surface interaction and defect structure. Improving sample cleanliness, for example, enabled the first observations of spin-orbit coupling in carbon nanotubes [1] and, more recently, the fractal quantum Hall effect, known as Hofstadter's butterfly, in graphene [2]. In order to understand these nanoscale structures and subsequently design improved sensors, a device architecture is needed that combines the atomic-level characterization afforded by TEM with the electronics characterization ability enabled by a gated, transistor-like geometry. We demonstrate that we can produce arrays of gated nanotube sensors devices, with reasonably high yield that can be characterized afterwards by TEM. Our design also keeps parasitic capacitance from our electrodes to the highly resistive silicon substrate low enough to enable electronic measurements of our transistors at MHz bandwidth.

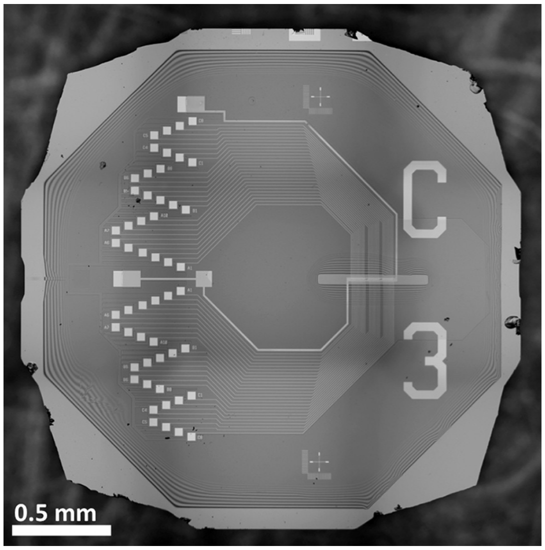

Figure 1: Optical image of microfabricated TEM grid with 26 pairs of source-drain electrodes, a top gate, and a thin nitride window for TEM imaging after top-gate is removed via chemical etching.

We fabricate nanotube devices on TEM grids using a combination of photolithography and standard nanotube growth and transfer techniques [3]. Figure 1 shows one of such devices, having 26 source-drain electrode pairs and two top gates. Between a few of the electrode pairs are individual nanotubes, which have been transferred prior to the deposition of a gate dielectric, and top-gate. The device fabrication involves using nine masks to define the various structures, which have been designed to yield nanotube devices with good gating characteristics, as well as low capacitive coupling between nearby electrodes.

The outline of the fabrication procedure is as follows. We begin by using low pressure chemical vapor deposition (LP CVD) to deposit the low-stress nitride on a 300 µm-thick silicon substrate, which will ultimately become our TEM window. We later deposit electrodes, and use backside alignment followed by reactive ion etching (RIE) to expose rectangles on the back of the wafer which will later be used for a potassium hydroxide (KOH) through-etch. Arrays of parallel nanotubes are grown by CVD on a separate quartz substrate, coated with poly(methyl methacrylate) (PMMA), lifted off with KOH, and transferred onto the device substrate [3], where unwanted areas are patterned and etched using RIE. We use atomic layer deposition (ALD) to deposit a gate dielectric, after which we pattern and evaporate a gold top-gate. The surface is then coated with a KOH protection layer, and the devices are placed in hot KOH, which etches the silicon exposed on the back, to both release individual grids and to etch the silicon away from behind the nitride window. Later, the nanotube devices will be imaged through this window using TEM. The protection layer is then removed, and the grids are cleaned with oxygen plasma. Our fabrication process typically yields at least one electrically-connected, gated nanotube on 75% of the TEM grids.

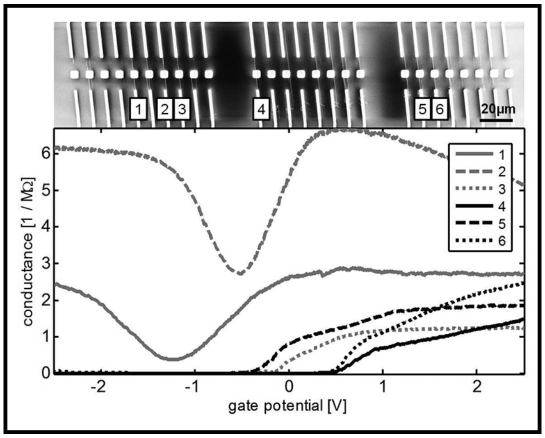

Figure 2: Upper: Scanning electron microscope image of nanotubes between source-drain electrodes, passing over thin nitride windows. Lower: Corresponding conductance measurements as a function of top gate voltage showing six conducting nanotubes with varying characteristics.

Figure 2 shows an SEM image of nanotubes patterned between the source-drain electrode pairs, imaged prior to top-gate deposition. The squares in the center are thin nitride windows for low-background TEM imaging. After completion of the device fabrication, these nanotubes are characterized electrically, shown in the lower portion of Figure 2. All of these nanotubes can be gated to have resistance lower than 1MΩ (50kΩ/μm) showing that they have a low defect density, and good coupling to the top gate. Nanotubes 1 and 2 can be seen to be metallic, while nanotubes 3-6 are semiconducting.

Furthermore, we can probe the electrical characteristics at high speeds in the megahertz (MHz) range. Previous research has shown that single charge fluctuations in a dielectric can be detected by semiconducting carbon nanotubes as random telegraph signals [4]. As shown in Figure 3, our devices are also capable of measuring such signals, but at higher speeds with rise times less than 1 μs. After characterizing the nanotubes electronically, we can etch away the gold top-gate, and image them by TEM to determine, for example, the nanotube diameter. Figure 3 shows one such nanotube, which can be seen to be single-walled (single dark lines running parallel to the arrows), and 4 nm in diameter (the width between those lines).

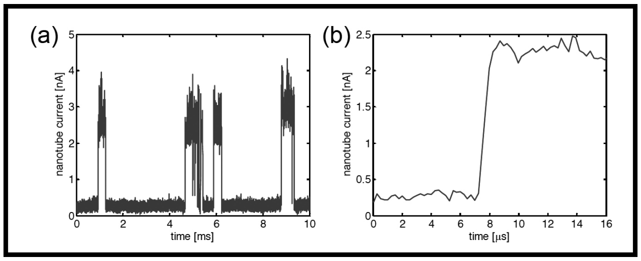

Figure 3: High-speed measurement of nanotube random telegraph signal showing (a) fluctuations in nanotube current and (b) measured rise time of less than 1 μs.

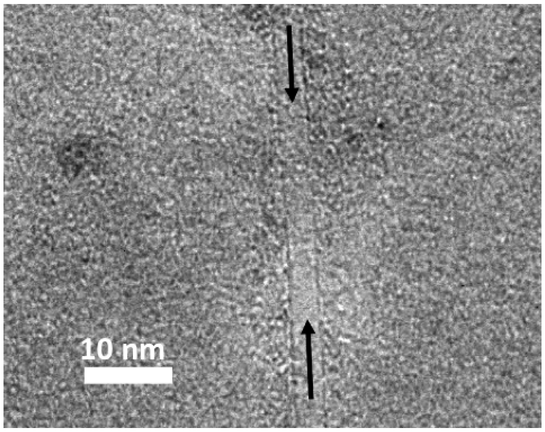

Figure 4: TEM image of a nanotube imaged through a thin nitride window, after top-gate removal.

Conclusions and Future Steps:

In principle, our fabrication procedure can be applied to many different CVD-grown low-dimensional materials with only minor modifications, and may lead to the development of improved nanoscale sensors capable of high-speed molecular sensing.

References:

[1] F. Kuemmeth, et al., Nature 452 448-452 (2008).
[2] C. R. Dean, et al., Nature 497, 598-602 (2013).
[3] L. Jiao, et al., J. Am. Chem. Soc. 130, 12612-12613 (2008).
[4] T. Sharf, et al., Nano Lett. 14 (9) 4925-4930 (2014).

Antifouling Topographies to Combat Microbial Biofilms

CNF Project Number: 2505-16
Principal Investigator(s): Dacheng Ren[1,2,3,4]
User(s): Huan Gu[1,2]

Affiliation(s): 1. Biomedical and Chemical Engineering, 2. Syracuse Biomaterials Institute, 3. Department of Civil and Environmental Engineering, 4. Department of Biology; Syracuse University, Syracuse, 13244 New York, USA

Primary Source(s) of Research Funding: National Institutes of Health (NIH), National Science Foundation (NSF)

Contact: dren@syr.edu, hugu@syr.edu
Website: https://renlab.syr.edu/

Primary CNF Tools Used: Heidelberg mask writer DWL2000, ABM contact aligner, Plasma-Therm UNAXIS 770 deep silicon etcher, MVD 100

Abstract:

Bacteria can adhere and develop multicellular structures (known as biofilms) on medical devices, which are the primary cause of hospital-acquired infections (HAI) and biofouling. Once mature biofilms are established, they are hard to eradicate, leading to the persistence of biofilm-mediated medical challenges. In this project, we aim to develop a strategy to address these challenges using biocompatible shape memory polymers (SMPs) with defined surface topography. The surface topography is introduced onto the surface of SMPs using photolithography and soft lithography. This strategy can prevent bacterial adhesion and remove mature biofilms on-demand, and therefore, providing prolonged antifouling properties. By challenging these new antifouling surfaces with *Pseudomonas aeruginosa* biofilms, these topographies demonstrate 99.9% biomass reduction compared to the static and flat controls. Similar potent antifouling effects are also observed against biofilms of *Staphylococcus aureus* and a uropathogenic strain of *Escherichia coli*. The data included in this report has been published in the Journal of ACS Applied Materials and Interfaces [1].

Summary of Research:

To fabricate well-defined surface topography on SMPs, we used poly(dimethylsiloxane) (PDMS) surfaces with complementary topography as molds (Figure 1). These PDMS surfaces were created using photolithography and soft lithography by following the protocol described by Hou, et al. [2]. In detail, the configuration of the patterns was designed using the software L-Edit (Tanner Research, Monrovia, CA, USA) to create hexagonal shapes with side length (L) of 5, 10, 15, 20, 30, 40, or 50 µm and inter-pattern distance (D) of 2, 5, 10, 15, or 20 µm.

This design was first written onto a photomask using a photomask writer (Heidelberg Mask Writer - DWL2000) and then transferred onto silicon wafers coated with photoresist S1813 using the ABM contact aligner. The hexagonal holes on silicon wafers were etched to obtain approximately 10 µm deep features using a Plasma-Therm Unaxis 770 deep silicon etcher.

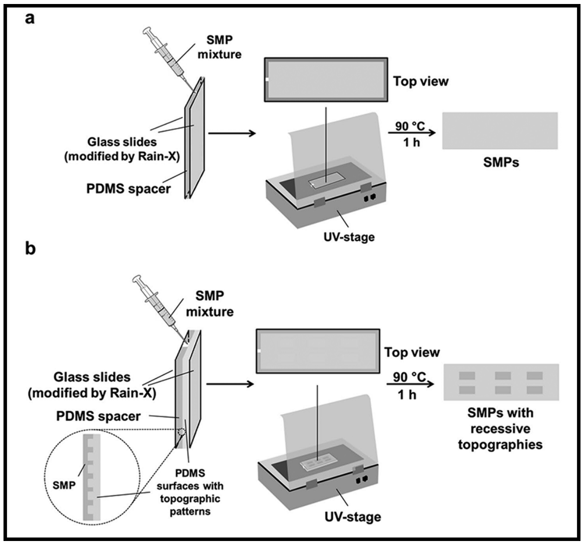

Figure 1: Schematic illustration of the process for preparing SMPs without (a) or with (b) surface topography.

To minimize PDMS residues in each round of soft lithography, silicon wafers were coated with (tridecafluoro-1,1,2,2,-tetrahydrooctyl)trichlorosilane (FOTS) prior to use as templates. Silicon elastomer mixtures (base : cure agent (wt/wt) = 10 : 1; Sylgard® 184, Sigma-Aldrich, St. Louis, MO, USA) were applied onto the silicon wafers and polymerized at 60°C for 24 h. PDMS surfaces with recessive hexagonal patterns were then gently peeled off and used as molds.

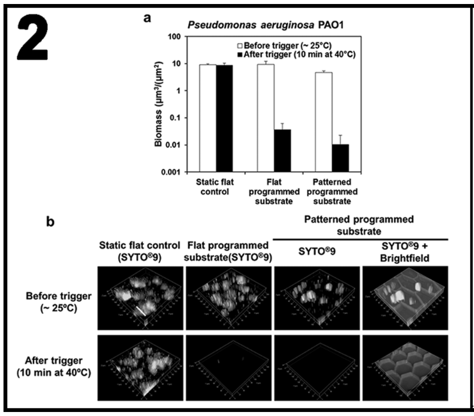

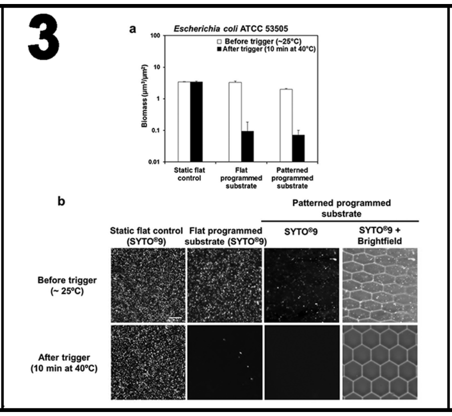

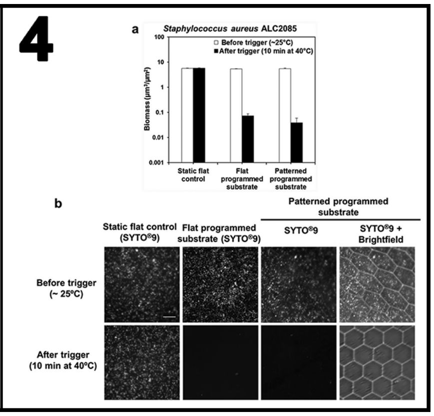

Figure 2, left: *Effects of static flat control and programmed substrates on the biofilm formation and mature biofilms of* P. aeruginosa *PAO1. Figure 2 shows the biomass (a) and representative fluorescence images (b) of* P. aeruginosa *PAO1 biofilms on different surfaces before and after trigger (10 min incubation at 40°C) (Bar = 50 μm) [1]. (Reproduced with permission from the Journal ACS Applied Materials and Interfaces.)* ***Figure 3, middle:*** *Effects of static flat control and programmed substrates on the biofilm formation and mature biofilms of* E. coli *ATCC53505. Figure 3 shows the biomass (a) and representative fluorescence images (b) of* E. coli *ATCC53505 biofilms on different surfaces before and after trigger (10 min incubation at 40°C) (Bar = 50 μm) [1]. (Reproduced with permission from the Journal ACS Applied Materials and Interfaces.)* ***Figure 4, right:*** *Effects of static flat control and programmed substrates on the biofilm formation and mature biofilms of* S. aureus *ALC2085. Figure 4 shows the biomass (a) and representative fluorescence images (b) of* S. aureus *ALC2085 biofilms on different surfaces before and after trigger (10 min incubation at 40°C) (Bar = 50 μm) 1]. (Reproduced with permission from the Journal ACS Applied Materials and Interfaces.)*

The SMP used in this study was synthesized by mixing t-butyl acrylate (tBA), poly(ethylene glycol) n dimethacrylate (PEGDMA), and photoinitiator 2,2-dimethoxy-2-phenylacetophenone (DMPA) (wt:wt:wt = 9:1:0.04). Flat or topographically patterned substrates were prepared by injecting the mixture between two glass slides with a 1 mm thick PDMS spacer using a syringe, being pre-polymerized under 365 nm UV irradiation for 10 min, followed by a thermal post-cure for 1 h at 90°C to maximize the conversion of monomers [3] (Figure 1). We programmed the shape change of SMPs by incubating dog bone shaped flat or topographically patterned substrates at 50°C for 5 min and then gradually stretching using a manual stretcher to 1.5 times of the original length. This temporary shape was fixed via approximately 5 min cooling at room temperature. We triggered shape recovery by incubating these SMP substrates with their temporary shape in pre-warmed 0.85% NaCl for 10 min at 40°C. Flat static control (samples that do not undergo shape change when heated) were also prepared.

By comparing the biomass of 48 h *P. aeruginosa* PAO1 on the three different surfaces that are flat static controls, flat and topographically patterned programmed surfaces, recessive hexagonal patterns were found to significantly prevent biofilm formation with 50.9 ± 7.2% and 51.9 ± 7.3% reduction in biomass compared to that on flat programmed substrates and static flat control, respectively ($p < 0.001$ for both, one way ANOVA adjusted by Tukey test; Figure 2a). No significant difference was found between static flat controls and flat programmed substrates (both around 9 $\mu m^3/\mu m^2$; $p = 0.93$). Shape recovery induced movement of recessive hexagonal patterns triggered more profound effects on removing the established biofilms. For instance, the biomass on topographically patterned programmed substrates was 0.01 ± 0.01 $\mu m^3/\mu m^2$ after shape recovery. This represents a 469-fold reduction of biomass compared to the biomass before shape recovery (4.7 ± 0.7 $\mu m^3/\mu m^2$), and 909-fold reduction compared to the 48 h *P. aeruginosa* PAO1 biofilm biomass (9.1 ± 0.8 $\mu m^3/\mu m^2$) on static flat controls without topographic patterns and shape change. These results were obtained by quantifying fluorescence images using COMSTAT4 (Figure 2b). Similar results were observed in preventing the biofilm formation and removing mature biofilms of two other microorganisms, *E. coli* and *S. aureus* (Figures 3 and 4).

In summary, we developed new antifouling surfaces based on shape memory triggered changes in surface topography. This strategy was found effective for the prevention and removal of established biofilms of multiple species. Future studies are needed to understand the underlying mechanism and develop biocompatible polymers for *in vivo* use with tailored temperature and duration of heating to achieve multiple cycles of shape change.

References:

[1] Gu, H., Lee, S. W., Buffington, S. L., Henderson, J. H., and Ren, D. On-Demand Removal of Bacterial Biofilms via Shape Memory Activation. ACS Appl Mater Interfaces 8, 21140-21144, doi:10.1021/acsami.6b06900 (2016).

[2] Hou, S., Gu, H., Smith, C., and Ren, D. Microtopographic Patterns Affect *Escherichia coli* Biofilm Formation on Poly(dimethylsiloxane) Surfaces. Langmuir, doi:10.1021/la1046194 (2011).

[3] Yakacki, C. M., Willis, S., Luders, C., and Gall, K. Deformation limits in shape-memory polymers. Adv Eng Mater 10, 112-119, doi:DOI 10.1002/adem.200700184 (2008).

[4] Heydorn, A., et al. Quantification of biofilm structures by the novel computer program COMSTAT. Microbiology-Uk 146, 2395-2407 (2000).

Encapsulation of Photocathodes in Two-Dimensional Materials

CNF Project Number: 2584-17
Principal Investigator(s): Melissa A. Hines
User(s): William J.I. DeBenedetti

Affiliation(s): Department of Chemistry and Chemical Biology, Cornell University
Primary Source(s) of Research Funding: Center for Bright Beams, an NSF-funded Science and Technology Center (STC), National Science Foundation
Contact: Melissa.Hines@cornell.edu, wjd74@cornell.edu
Website: http://hines.chem.cornell.edu
Primary CNF Tools Used: SC4500 odd-hour evaporator, YES CV200RFS oxygen plasma asher

Abstract:

We are developing a new technique for encapsulating highly reactive photocathodes in an atomically thin membrane that protects them from oxidation and degradation without affecting their photoemission properties or chemical purity.

Summary of Research:

Photocathodes are materials that eject electrons under illumination. By their very nature, high-performance photocathodes must be made from materials that lose electrons easily — in other words, materials that are easily oxidized. For example, many photocathodes are either coated with alkali metals (e.g., Cs/GaAs) or comprised of alkali metals (e.g., Cs_3Sb). This presents a technical challenge, as exposure to even trace amounts of O_2 or H_2O will destroy or degrade the photocathode. For highest performance, the photocathodes must also be atomically flat and extremely homogeneous.

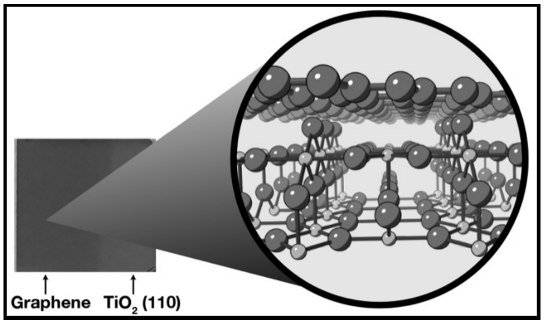

Figure 1: Optical image of TiO_2(110) with single-layer graphene on left side. The inset is a model of single-layer graphene on TiO_2(110).

To meet these challenges, we are developing a technique to produce a graphene-encapsulated photocathode. The key challenge in this project is ensuring that every step of the fabrication leaves no residue on the surface, as even monolayer levels of contamination could significantly reduce photoelectron transmission and beam brightness.

In the first step of fabrication, commercial two-dimensional materials, which are grown on a copper foil, are coated with a thin gold layer in the SC4500 thermal/e-beam evaporator. The two-dimensional material on the backside of the copper foil is then removed using 100W of oxygen plasma in the YES oxygen plasma asher. The copper foil is then removed with an aqueous etchant, allowing the graphene side of the gold-coated graphene to be adhered to a low energy substrate. The gold film is then removed by a second aqueous etch.

Deposition and Characterization of ALD Dielectric Materials for Metal-Insulator-Semiconductor AlGaN/GaN High Electron Mobility Transistors

CNF Project Number: 2684-18

Principal Investigator(s): Fatemeh Shahedipour-Sandvik

User(s): Benjamin McEwen

Affiliation(s): SUNY Polytechnic Institute, College of Nanoscale Science and Engineering

Primary Source(s) of Research Funding: Army Research Laboratory

Contact: sshahedipour-sandvik@sunypoly.edu, mcewen@sunypoly.edu

Primary CNF Tools Used: Oxford FlexAL ALD, Woollam spectroscopic ellipsometer

Abstract:

We continue our investigation of atomic layer deposition (ALD) for gate dielectric materials in AlGaN/GaN metal-insulator-semiconductor high electron mobility transistors (MISHEMTs). Al_2O_3, Si_3N_4, and SiO_2 were each tested. Pre- and post-deposition processes are found to greatly affect the quality of the dielectric and the dielectric/semiconductor interface. In particular, deposition of dielectric material as the first step in the fabrication process flow was found to be important. All devices fabricated with dielectric deposited after ohmic metallization exhibited high leakage currents and poor gate control. This presents a problem for Al_2O_3 MISHEMTs, since the Al_2O_3 has a relatively limited thermal budget and degrades at the temperatures necessary for ohmic metallization of GaN (~850°C).

Summary of Research:

The next generation of (Al)GaN power switches will likely require MIS gates in order to operate as normally-off devices with low leakage and high gate swing. Adding a gate dielectric however, complicates the process flow as additional considerations for stability of the dielectric during subsequent processing must be made, and the additional dielectric/semiconductor interface may contain a high density of interface trap states (D_{it}), leading to issues such as high dynamic on resistance (R_{ON}) and premature breakdown.

To determine the effect of forming a gas (95% N_2/5% H_2) anneal on the Al_2O_3/GaN interface, unintentionally doped (UID) GaN was grown on c-plane sapphire using metal-organic chemical vapor deposition (MOCVD) — 20 nm of Al_2O_3 was deposited using the Oxford FlexAL ALD system at CNF; the substrate was maintained at 300°C during the deposition.

Temp (°C)	1 min	10 min	20 min
600	X		X
475		X	
350	X	X	X

Table 1: Forming gas annealing conditions applied to Al_2O_3 after deposition.

After the deposition, samples were annealed in forming gas for a range of temperatures and times, as outlined in Table 1. MIS capacitors were subsequently fabricated, and the conductance method was used to extract the D_{it}. The D_{it} of the samples annealed at 350°C for 10-20 min was found to be over an order of magnitude less than that of the sample annealed at 600°C for 20 min and approximately half an order of magnitude less than the samples with as-deposited material, annealed at 350°C for 1 min, annealed at 475°C for 10 min, and annealed at 600°C for 1 min.

This indicates that annealing in forming gas for long times at lower temperatures is beneficial, while the material starts to degrade at higher temperatures. As ohmic metallization temperatures for GaN are ~ 850°C, this means Al_2O_3 must be deposited after the ohmic metallization [1].

To compare the necessary ohmic-first Al_2O_3 MISHEMTs with dielectric-first Si_3N_4 and SiO_2 MISHEMTs (these materials have high thermal budget), MISHEMTs were fabricated, using the Oxford FlexAL ALD system at CNF to deposit all dielectric materials; ~ 15 nm of each material was deposited, as measured using the Woollam spectroscopic ellipsometer at CNF.

As shown in Figure 1, in all cases, several orders of magnitude reduction in gate leakage current relative to a Schottky-gated HEMT was observed. However, the sample with Al_2O_3 gate dielectric (deposited after ohmic metallization) exhibited poor gate control, and instead showed a high I_{DS} regardless of the applied V_{GS} (Figure 2). It is believed that this is due to a highly defective and/or contaminated interface between the dielectric and semiconductor, imparting a high fixed positive surface charge, making it impossible to deplete the 2DEG channel before dielectric breakdown [2].

In order to potentially recover the GaN surface and improve the quality of the dielectric/semiconductor interface, surface cleaning treatments were performed on GaN; using X-ray photoelectron spectroscopy (XPS), it was found that a cleaning procedure consisting of consecutive NH_4OH, HCl, and HF resulted in the lowest surface coverage of carbon and oxygen on the GaN [2]. This cleaning procedure was applied to Al_2O_3/AlGaN/GaN MISHEMT devices prior to dielectric deposition.

After ohmic contact metallization, samples were cleaned with NH_4OH, HCl, and HF immediately before being loaded in the Oxford FlexAL ALD chamber at CNF; 8 nm of Al_2O_3 was deposited at 300°C. Completed devices exhibited more gate control than devices fabricated in the same run with only acetone/IPA clean prior to Al_2O_3 deposition, but high $I_{OFF} \sim 190$ mA/mm was measured at $V_{DS} = 10$ V, compared to $I_{ON} \sim 340$ mA/mm at $V_{DS} = 10$ V and $V_{GS} = 0$ V.

Even with surface treatments, the surface is not fully recovered, and additional measures must be taken to preserve the semiconductor surface if Al_2O_3 is to be a viable gate dielectric.

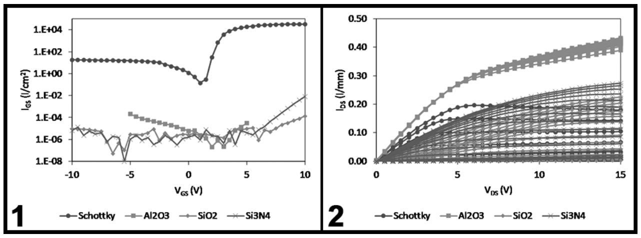

Figure 1, left: *Gate leakage current for Al_2O_3, Si_3N_4, and SiO_2 MISHEMTs compared with conventional Schottky gate HEMT. $V_{DS} = 5.5$ V.* ***Figure 2, right:*** *Output characteristics for Al_2O_3, Si_3N_4, and SiO_2 MISHEMTs compared with conventional Schottky gate HEMT. The highest curves are at $V_{GS} = 0$ V, subsequent curves incremented V_{GS} down by 0.5 V. (See pages vi-vii for full color versions of both figures.)*

This is the subject of ongoing research.

References:

[1] B. McEwen, I. Mahaboob, E. Rocco, K. Hogan, R. Green, F. Nouketcha, T. Murray, V. Kaushik, A. Lelis, F. Shahedipour-Sandvik. "Investigation of the Effects of Forming Gas Annealing on Al_2O3/GaN Interface," submitted.

[2] B. McEwen, I. Mahaboob, K. Hogan, E. Rocco, V. Meyers, S. Tozier, A. Lelis, R. Green, F. Nouketcha, F. Shahedipour-Sandvik. "Effects of Semiconductor Surface Treatments and Dielectric Anneal on the Electrical Characteristics of GaN-Based Metal-Insulator-Semiconductor Devices." Poster presented at: 13th International Conf on Nitride Semiconductors; 2019 Jul 7-12; Bellevue, WA.

Scissionable Polymer Photoresist for Extreme Ultraviolet Lithography

CNF Project Number: 2751-18
Principal Investigator(s): Christopher Kemper Ober
User(s): Jingyuan Deng, Abhaiguru Ravirajan

Affiliation(s): Materials Science and Engineering, Cornell University
Primary Source(s) of Research Funding: INTEL Corporation
Contact: c.ober@cornell.edu, jd966@cornell.edu, ar2362@cornell.edu
Primary CNF Tools Used: ASML 300C DUV stepper, JEOL-6300 e-beam lithography, P10 profilometer

Abstract:

Extreme ultraviolet (EUV) is one of the most promising methods to create nano-size patterns below 10 nm. Numerous EUV resists have been developed in last decades to accommodate EUV lithography. The main challenge of EUV lithography lies in RLS tradeoff, which specify the tradeoff among resolution (R), line edge roughness (L) and sensitivity (S). In addition, EUV lithography suffers from low photon numbers, which may cause stochastic issues. In this work, we developed chemically amplified chain scissionable polymers to tackle these issues. Polyphthalaldehyde (PPA) based photoresists have been synthesized and their lithographic performance have been investigated.

Summary of Research:

Scissionable polymers are polymers that will depolymerize under different stimuli including acid, base, and free radicals [1]. These polymers have been investigated in the development of photoresists and other degradable materials. This work focuses on the poly(phthalaldehyde), PPA, family of scissionable polymers. The PPA backbone consists of acetal linkages that are very sensitive to acids. Upon exposure to acids, the polymer chain depolymerizes to its corresponding monomers. This depolymerization behavior makes PPAs excellent candidates as photoresist materials. Several new architectures are being explored. For example, PPAs with tethered photoacid generators (PAG)s, which release acid upon irradiation, depolymerize upon exposure followed by a post exposure bake step. The depolymerized monomers in exposed areas could be easily removed using appropriate organic solvents while the unexposed areas remain unchanged. Therefore, both unsubstituted and substituted PPAs may equally serve as a positive tone photoresist.

This study focuses on the development of low exposure dose, sensitive PPA photoresists, which do not suffer from materials stochastic issues related to non-uniformities at nanoscale present in multi-component systems for EUV lithography. In order to improve the lithographic performance of the PPA photoresists, the structure of the polymer backbone as well as photoacid generators (PAG)s are being investigated and tailored for EUV lithography. Aryl sulfonates were prepared as non-ionic PAGs for PPA photoresists [2]. The steric and electronic nature of the aryl sulfonate PAGs can be easily tuned to optimize acid generation efficiency and their compatibility with a polymer photoresist matrix.

Results and Discussions:

The homogenous solution of PPA polymers and PAGs were prepared and spin coated on a silicon wafer. The coated silicon wafers were then exposed using ASML 300C DUV stepper. After exposure, the exposed film was baked and developed. The resulting line-space patterns were characterized using AFM and SEM. The images are shown in Figure 1 and 2, respectively.

Summary:

In summary, preliminary results were obtained with chain scissionable photoresists. With these results in hand, the lithographic performance of newly developed functionalized PPAs will be investigated under DUV, e-beam, and EUV to pursue higher resolution and improved LER.

References:

[1] Yardley, R. E.; Kenaree, A. R.; Gillies, E. R. Macromolecules 2019, 52, 6342.

[2] Sulc, R.; Blackwell, J. M.; Younkin, T. R.; Putna, E. S.; Esswein, K.; DiPasquale, A. G.; Callahan, R.; Tsubaki, H.; Tsuchihashi, T. Proc. SPIE, 2009; 7273, 72733.

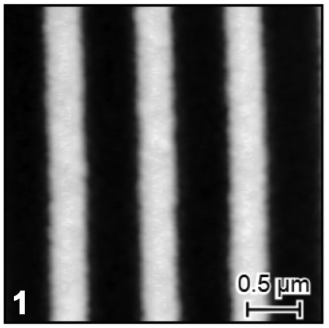

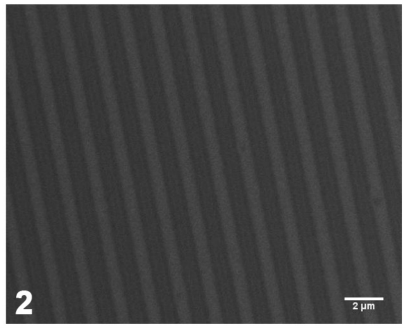

Figure 1, left: *1:1 Line space pattern with feature size 512 nm observed under AFM after exposure of 100 mJ/cm^2 deep UV exposure. As seen from these figures, the line edge roughness was relatively rough. The acid diffusion, which caused this roughness, could be alleviated by changing the chemical structure of the photoacid generator. Next, we plan to explore the resolution limit of these photoresists with different photoacid generators using e-beam, and EUV. These samples are currently under preparation.*

Figure 2. right: *1:1 Line space pattern with feature size 512 nm observed under SEM after exposure of 100 mJ/cm^2 deep UV exposure.*

Mitigating Etch-Induced Fencing of Platinum with Sacrificial Layers

CNF Fellows Program

Principal Investigator(s): Vince Genova[1], David Lisham[2]

CNF Fellow: Kyle J. Dorsey[3]

Affiliation(s): 1. Cornell NanoScale Science and Technology Facility, 2. Plasma-Therm LLC,
3. School of Applied and Engineering Physics, Cornell University

Primary Source(s) of Research Funding: Cornell NanoScale Science and Technology Facility

Contact: genova@cnf.cornell.edu, kjd96@cornell.edu

Primary CNF Tools Used: AJA International, GCA AS200 i-line stepper

Abstract:

Lithographic patterning of platinum is challenging because platinum does not readily form volatile etch products. Most approaches toward patterning platinum rely on physical etch mechanisms. Low-energy sputtered platinum has a short mean-free path and high surface mobility, so it readily redeposits on the sidewalls of etch masks. When the etch mask is removed, the sidewall-deposited platinum remains adhered to the wafer in a phenomenon known as "fencing." We describe a lithographic approach to mitigate the effects of platinum etch fencing by utilizing sacrificial layers to lift off the residual fences during etch mask stripping. The central elements of the process are described schematically in Figure 1. A sacrificial layer is prepared with considerable undercut underneath the etch mask as shown in Figure 1(a). The redeposition of platinum from the edge of the feature can be considered a point source. The flux of platinum should then vary as cos *θ*. Therefore, very little platinum is redeposited underneath the resist, enabling it to be lifted off in solvent.

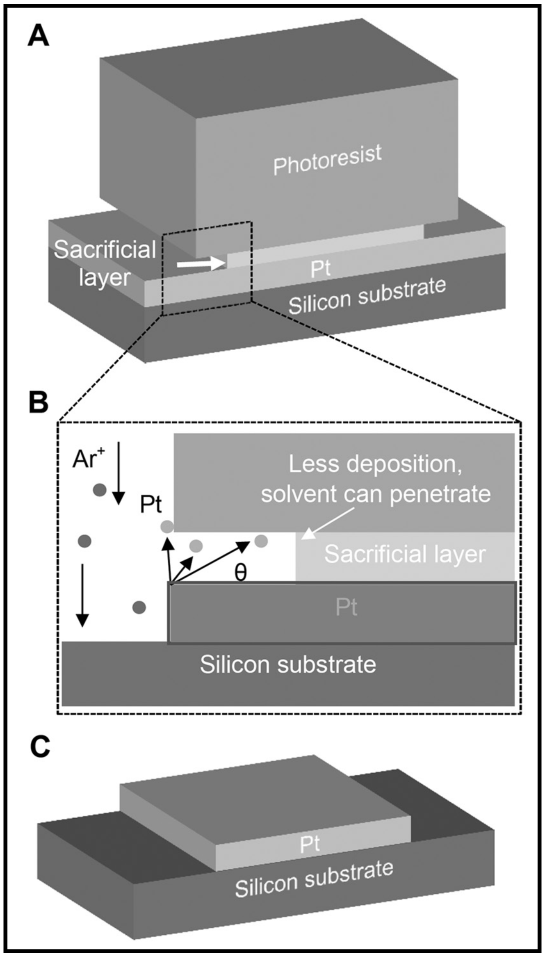

Figure 1: Central elements of the process are described schematically.

Summary of Research:

Platinum films were prepared on silicon wafers by DC sputtering (AJA International). *In situ*, the wafers were cleaned with an Ar plasma, then sequentially coated with 2 nm Ti adhesion layer and 100 nm Pt at 3 mTorr. The sacrificial layer (to be described in subsequent sections) was deposited or spin-coated. The etch mask was patterned by photolithography (GCA AS200 i-line stepper, 5x) in SPR700-1.2 photoresist. The pattern consists of lines and spaces at equal pitch ranging from 0.5 µm to 20 µm. The platinum was etched in an argon ion-milling system at normal incidence with 600V bias. Etching proceeded in 15 second increments with 30 second cooldowns between bursts to prevent overheating. Eight etch/cool cycles were needed to clear through 100 nm of Pt.

The primary sacrificial layer investigated is Microchem LOR resist. This material dissolves in developer solution, producing an undercut profile concurrently with the lithography process. The thickness is controlled by spin-coating and viscosity, and the undercut rate is controlled by soft-bake temperature. After etching, the photoresist was dissolved in heated 1165 stripper (~50°C) with

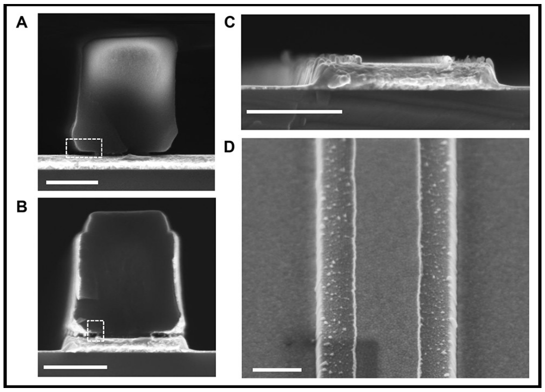

Figure 2: Complete process flow.

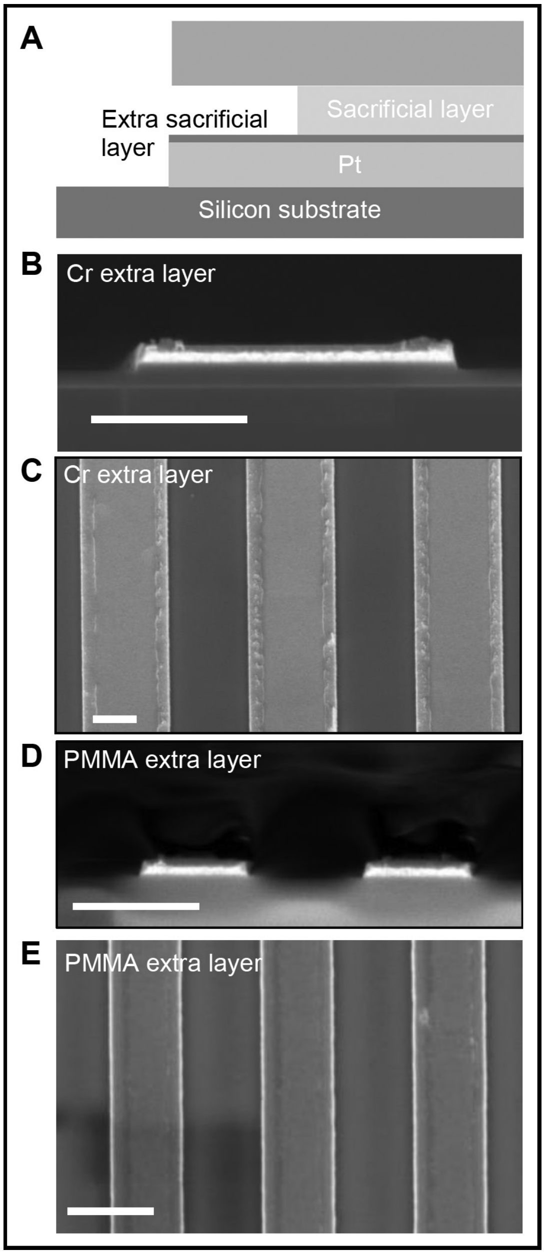

Figure 3; Results of the platinum features after removing the extra sacrificial layer.

ultrasonic agitation for 30 minutes, followed by rinsing in acetone, isopropanol, and DI water.

Results:

We investigated ultra-thin layers of LOR, which simplifies process by having easier to prepare films, eliminating an etch step, and remaining easy to remove. The LOR was prepared by mixing LOR 1A in a 1:1 volumetric ratio with cyclopentanone. This mixture was mixed on a magnetic stir plate for an hour prior to coating. The wafers were spun with this solution at 3500 RPM for 30 seconds and baked at 185°C. At this temperature, the LOR produces an undercut rate of 4 nm/sec in 2.38N developer. The complete process flow with this sacrificial layer is described in Figure 2.

Figure 2a shows the completed structure. The LOR thickness is 40 nm, and the development time produces a 200 nm undercut. After milling, the sidewalls are coated in Pt, as shown in Figure 2b. However, the corners of the completed feature are not coated. This enables separation of the sidewall from the substrate. After removal, the finished structures are shown in cross section in Figure 2c and in angled imaging in Figure 2d. There is some residual platinum, but none of it is thicker than the LOR thickness. Moreover, there are no large regions of retained sidewall as there were for the silicon nitride case.

The remaining Pt particles can be removed by inserting an additional sacrificial layer in between the platinum and the undercut resist, as shown in Figure 3a. The thickness of this additional layer should be very thin as to avoid generation of new, larger fences. It should also not dissolve during photolithography development or resist coating. We investigated two extra sacrificial layers, 10 nm of chromium (sputtered, 3 mTorr) and 10 nm of PMMA.

Figure 3 reports the results of the platinum features after removing the extra sacrificial layer. Figures 3b and 3c show the effects of removing the 10 nm of Cr post-milling with Cr etchant CE-200. There are small additional fences remaining, but fewer large residues compared to the approach without the extra layer. Figures 3d and 3e show the effects of using ultra-thin PMMA films as the extra layer. Compared to the Cr layer, the PMMA films simplify the process since it is removed concurrently with the photoresist in the 1165 bath. This approach has improved residues compared to the Cr-based approach and the process without any extra layers at all.

Future Work:

Future work will focus on further refinement of the sacrificial underlayer approach. It shows promise as a simple route to fence-free platinum etching. An additional interesting experiment involves conformal sacrificial layers deposited over the imaging resist. This conformal layer covers the entire sidewall of the resist pattern. If chosen appropriately, it can lift off the sidewall fences in a single process step. Work is ongoing using ALD-deposited aluminum oxide, which can be deposited conformally at low temperatures and is readily dissolved in TMAH-based photoresist developer.

Flexible Exoskeletons for Magnetically Actuated Microscopic Robots using Atomic Layer Deposition

CNF Project Number: 900-00

Principal Investigator(s): Paul L. McEuen[1,2], Itai Cohen[1,2]

User(s): Tanner Pearson[3], Kyle Dorsey[3], Edward Esposito[1], Sierra Russell[4], Baris Bircan[3]

Affiliation(s): 1. Laboratory of Atomic and Solid State Physics, Cornell University; 2. Kavli Institute for Nanoscale Science, Cornell University; 3. School of Applied and Engineering Physics, Cornell University; 4. College of Nanoscale Sciences, SUNY Polytechnic Institute

Primary Source(s) of Research Funding: This work was supported by National Science Foundation (NSF) grant DMR-1435829, Air Force Office of Scientific Research (AFSOR) multidisciplinary research program of the university research initiative grant FA2386-13-1-4118, Cornell Center for Materials Research (CCMR) through NSF MRSEC program (DMR-1719875), ARO grant W911NF-18-1-0032, NSF Major Research Instrumentation Award DMR- 1429155, the National Science Foundation under Grant No. NNCI-1542081, and the Kavli Institute at Cornell for Nanoscale Science

Contact: plm23@cornell.edu, itai.cohen@cornell.edu, tgp34@cornell.edu, kjd96@cornell.edu, epe3@cornell.edu, srussell@sunypoly.edu, bb625@cornell.edu

Primary CNF Tools Used: Oxford FlexAL ALD, Arradiance ALD, Autostep AS200 i-line stepper, CVC e-beam evaporators, Oxford 81/82 etchers, PT770/PT740 etchers, Anatech Asher, Zeiss SEMs, Veeco AFM, Tencor P7 profilometer, FilMetrics UV, Woollam ellipsometer, DISCO dicing saw, Heidelberg DWL2000, AJA sputterer

Abstract:

One of the grand challenges in robotics is to create truly microscopic robots, i.e. those too small to be resolved by the naked eye. We attack this problem by combining programmable magnetic panels with nanometer-thick flexible materials to make micron-scale, magnetically controlled robots and smart assemblies. The ideal material for this flexible exoskeleton must be elastic, possess high intrinsic strength, and integrate easily into standard microfabrication processes. We employ atomic layer deposition (ALD) to synthesize films down to 2 nm thickness to create membranes, metamaterials, and machines [1]. We demonstrate that these ALD films behave elastically under repeated deformation and have fJ-scale bending stiffness. We further incorporate magnetic panels to controllably actuate simple mechanisms and machines. These results establish ultrathin ALD films as flexible materials for microscopic actuating systems. Our current pursuit focuses on improving functionality of these systems by encoding them with magnetic information. This idea can be implemented to program dipole orientations in individual magnetic panels, enabling more complex modes of actuation for executing specific tasks [2]. Moreover, patterned magnetic multipoles can be utilized for smart self-assembly via specific binding [3]. Ultimately, the use of magnetic programing techniques to design actuating systems based on ALD films will provide a unique platform for constructing and manipulating microscopic robotic systems.

Summary of Research:

ALD is an ideal technique for scaling mechanical systems to micron-scale dimensions. We have developed an entire fabrication strategy around ALD, including lithography, etching, release, and integration. ALD films are grown conformally on a sacrificial layer of aluminum, as shown schematically in Figure 1. The devices consist of lithographically patterned regions of ALD membranes and thicker panels of other materials that provide rigid structure and additional functions such as mirrors or magnets. The devices are fabricated at wafer scales at yields exceeding 90%. The wafer is diced and devices are released by immersing in dilute base, followed by rinsing in water. Upon release, all experiments are

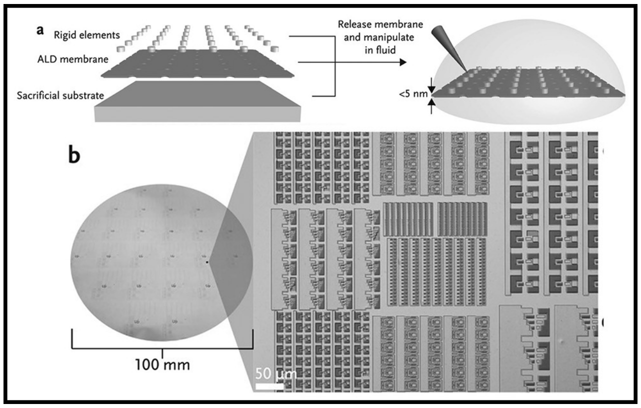

Figure 1: (a) Schematic of the fabrication and release processes. (b) Photograph of a 100 mm wafer with myriad ALD devices.

carried out in aqueous environments, often with added surfactant, to avoid stiction of the free membranes.

We investigated the mechanical properties of these films by measuring the bending stiffness of over 60 magnetically actuated glass hinges. Ferromagnets with saturated in-plane moments are patterned on panels at the ends of the hinges. The panels are deflected when we apply an out-of-plane magnetic field B, and the bending stiffness is determined by measuring the corresponding deflections of the hinges. Scaling the thickness from 2 nm to 8 nm, we find bending stiffnesses spanning nearly two orders of magnitude, with the lowest being in the femtojoule range. We additionally find the Young's modulus of ALD glass to be 90 ± 10 GPa. This value is comparable to values for bulk material (70-80 GPa), indicating that even at 2 nm thickness, the films behave mechanically similar to macroscopic counterparts.

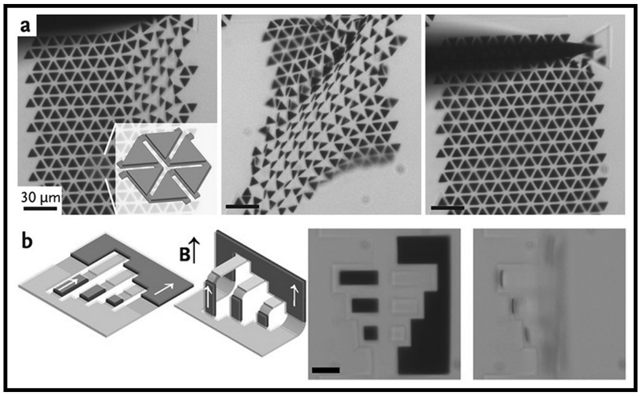

Figure 2: (a) Biaxially stretchable mechanical metamaterial. (b) Magnetically actuated pop-up staircase.

We additionally use ALD membranes to fabricate a range of microscopic actuatable systems (Figure 2). Glass and platinum sheets can be patterned into geometries that allow parts of the sheet to bend/buckle out of its fabrication plane, producing highly stretchable and auxetic metamaterials. Moreover, ferromagnetic panels can be introduced to create magnetically actuated machines that function with exquisitely small forces and torques. These span from pop-up book style devices that can be snapped shut, to muscle mimetic load bearing mechanisms.

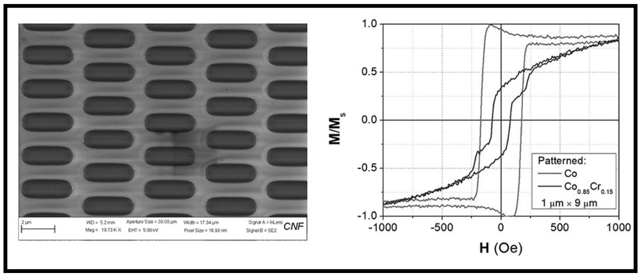

Figure 3: (a) SEM image of lithographically patterned Co. (b) Magnetic hysteresis loops of similarly patterned Co and CoCr.

Our recent efforts focus on improving functionality of these actuatable systems by encoding them with magnetic information. This idea can be implemented to program dipole orientations in individual magnetic panels, enabling more complex modes of actuation for executing specific tasks. In order to achieve magnetic writing capabilities, we must define the appropriate combination of magnetic materials and writing technique. Using the AJA magnetron sputterer in CNF, we have investigated materials such as Co, CoCr alloys, and Co/Pt multilayers and measured their magnetic properties via vibrating sample magnetometry (VSM) and magnetic force microscopy (MFM). Additionally, we have patterned these films to understand the effects of shape anisotropy on their magnetic properties (Fig.3).

We are currently using these results to determine viable approaches for magnetic recording. One promising method would rely on the disparity of the in-plane coercivity between Co and CoCr. One could use a large field to orient Co, a high coercive field material, in one direction, and subsequently use a smaller field to write CoCr, a softer material, in the opposite direction without affecting the Co. Leveraging shape anisotropy, one could repeat this process along an orthogonal axis to achieve four unique magnetic orientations. This simple magnetic writing scheme for magnetic panels combined with a flexible and robust exoskeleton deposited using ALD would facilitate the design of microscopic actuating systems for smart self-assembly and robotics.

References:

[1] K. J. Dorsey, T. G. Pearson, E. Esposito, S. Russell, B. Bircan, Y. Han, M. Z. Miskin, D. A. Muller, I. Cohen, P. L. McEuen, Adv. Mater. 2019, 31, 1901944.

[2] J. Cui, T. Huang, Z. Luo, P. Testa, H. Gu, X. Chen, B. J. Nelson, L. J. Heyderman, Nature 2019, 575, 164.

[3] R. Niu, C. X. Du, E. Esposito, J. Ng, M. P. Brenner, P. L. McEuen, I. Cohen, PNAS 2019, 116 (49), 24402.

Water Propagation on a Surface with Buried Nanochannels

CNF Project Number: 2123-12

Principal Investigator(s): Shalabh C. Maroo

User(s): Sajag Poudel, An Zou, Manish Gupta

Affiliation(s): Department of Mechanical and Aerospace Engineering, Syracuse University, Syracuse, NY 13244

Primary Source(s) of Research Funding: National Science Foundation Career Award NO. 1454450, Office of Naval Research Grant NO. N000141812357

Contact: scmaroo@syr.edu, sapoudel@syr.edu, azou@syr.edu, magupta@syr.edu

Website: http://maroo.syr.edu

Primary CNF Tools Used: Heidelberg mask writer (DWL 2000), manual photoresist spinner, Gamma coat-develop tool, GCA auto stepper, ASML stepper, YES image reversal oven, ABM contact aligner, SÜSS MA6-BA6 contact aligner, e-beam evaporator, Oxford PECVD, GSI PECVD, Glen 1000 Plasma, Anatech resist strip, Oxford 81/82 etcher, Oxford 100 etcher, Plasma-Therm deep silicon etcher, Unaxis 770 deep silicon etcher, optical microscope, scanning electron microscope, atomic force microscope

Abstract:

We investigated the wicking of a finite water drop sitting on a surface with well-defined cross-connected buried nanochannels by experiments and analytical models. The wicking process is composed of wicking-dominant and evaporation-dominant regimes, with each further divided into two subregimes. The wicking is initially governed by surface tension and viscous forces, and later by hydrodynamic dissipation within the droplet sitting on the top surface due to the finite liquid supply. The work reported here is part of a journal article published in Journal of Physical Chemistry C [1].

Summary of Research:

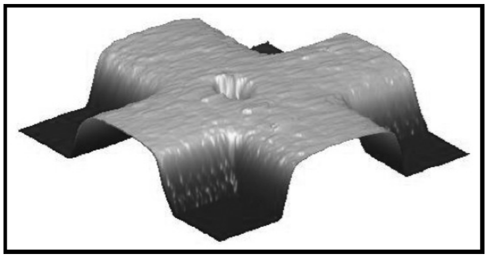

Figure 1: Atomic force microscope (AFM) image of the profile of channels and pores.

Wicking is the phenomenon in which liquid propagates in a porous medium primarily due to the surface tension, curvature, and the solid-liquid intermolecular attraction force. Wicking plays a significant role in various areas, such as thin film evaporation, printing, oil processing, etc. Superior wickability of a porous medium is a major motivation to employ them in phase-change heat transfer applications, which is widely accepted as one of the most promising solutions to the increasing demand of high heat flux removal. Here, we present an experimental work of water propagation on a surface with buried nanochannels. The geometry of the nanochannel being well controlled and defined makes it a perfect candidate to conduct such investigation due to: (1) accurately modeled capillary pressure without having to predict the meniscus shape; and (2) easily achieved long wicking distance as the evaporation is hindered.

The buried cross-connected nanochannels were fabricated on a silicon (Si) substrate by etching patterned sacrificial metal layers buried under a 300 nm thick silicon dioxide (SiO_2) film from plasma enhanced chemical vapor deposition (PECVD). The channel geometry was determined by the pattern of sacrificial layers, which was attained by a lift-off process. The cross-connected channels, made from two sets of channels perpendicular to each other, allow for ease of liquid exchange inside the channels. Further, at each intersect of the channels, a 2 µm pore was fabricated allowing liquid present above the surface to flow into the channels. Figure 1 shows an atomic force microscope (AFM) image of the surface (channel width: 5 µm, spacing: 5 µm, height: 728 nm).

In wicking experiments, the spreading of a 2-µL water droplet on a sample with buried nanochannels was recorded using a high speed camera. The volume of the droplet was generated and controlled by a string pump. Using a vertical-translation stage, the sample was raised until it touched the droplet, after which the droplet starts to spread on the surface, as well as wick into the channels before eventually drying out due to evaporation. The water propagation during wicking were characterized by three parameters: wicking radius

(R_w, defined as radius of the entire wetted area), droplet base radius (R_d, defined as radius of the droplet sitting above nanochannels), and wicking distance (w_d, defined as difference between above two). Figure 2 shows a schematic of these parameters. Both R_w and R_d were obtained from image analysis of the high-speed video and were measured with time.

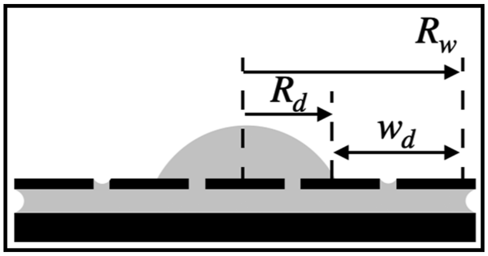

Figure 2: Schematic of definition of wicking radius (R_w) and droplet base radius (R_d).

Figure 3 shows the evolution of R_w and R_d. The wicking process can be divided into two distinct regimes: initial wicking-dominate (regime I) and later evaporation-dominant regime (II). Each of these two regimes can be further divided into two subregimes. When the droplet comes in contact with the surface (defined as t = 0), it spreads on the top of the surface immediately; water starts wicking into the channels as well, causing both R_d and R_w to increase fast in the first subregime I-A. The end of subregime I-A is defined by the time ($t = t_d$) when R_d reaches its maximum. In subregime I-B, the water menisci in the channels continues to advance radially outward and reaches a maximum wicking radius at $t = t_{max}$; while the R_w remains nearly constant during this period. Beyond t_{max}, the wicking process transitions to regime II where evaporation dominates, causing the meniscus front recede and dry out eventually due to the finite water supply from the droplet.

In subregime II-A, the water evaporated from menisci in the channels and pores is balanced by the water supply from the droplet, leading to a nearly constant R_w. The R_d maintains at its maximum as well, with a decrease in droplet height due to the shrink in volume. After the droplet height reaches a certain minimum value, water front above nanochannels starts to recede, leading to a decreased R_d and therefore subregime II-B where evaporation flux in menisci in channels overwhelms water supply from the droplet, causing R_w to decrease and eventually dry out.

The data of wicking distance (w_d) in regime I are in good agreement with two analytical models which can be used to predict wicking distance evolution in nanochannels. In regime I-A, the w_d can be predicted by Xiao's model [2] where the flow is governed by surface tension (flow driving force) and viscous forces (flow resistance) with unlimited liquid supply. Due to the finite droplet volume, the w_d deviates from this prediction in regime I-B, but is in good agreement with prediction from Ruijter's model [3], where the hydrodynamic dissipation within droplet was considered as the dominant reason behind the loss of surface during spreading.

Conclusions and Future Steps:

The wicking in buried nanochannels is composed of wicking-dominant and evaporation-dominant regimes. The wicking is initially governed by surface tension and viscous forces, and later by hydrodynamic dissipation within the droplet sitting on the top surface.

References:

[1] S. Poudel, A. Zou, S.C. Maroo, J. Phys. Chem. C, 123: 23529-23534 (2019).

[2] R. Xiao, R. Enright, E.N. Wang, Langmuir, 26: 15070-075 (2010).

[3] M.J. de Ruijter, J. De Coninck, G. Oshanin, Langmuir, 15: 2209-2216 (1999).

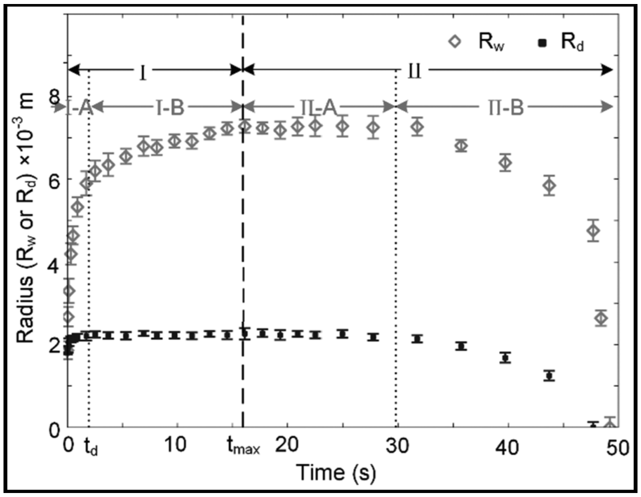

Figure 3: Evolution of wicking radius (R_w) and droplet base radius (R_d) for wicking of 2 µl droplet.

Quantum Optomechanical Coupling in Hexagonal Boron Nitride Membranes

CNF Project Number: 2126-12

Principal Investigator(s): Gregory D. Fuchs

User(s): Nikhil Mathur

Affiliation(s): Applied and Engineering Physics, Cornell University

Primary Source(s) of Research Funding: National Science Foundation (DMR-1719875)

Contact: gdf9@cornell.edu, nm648@cornell.edu

Website: http://fuchs.research.engineering.cornell.edu/

Primary CNF Tools Used: Heidelberg DWL2000, ASML DUV stepper, Oxford 81 etcher, P10 profilometer, SC4500 evaporator, Zeiss scanning electron microscope (SEM)

Abstract:

We report on the fabrication, electrostatic actuation, and optical detection of micro-mechanical resonator devices composed of a hexagonal boron nitride (hBN)/graphene membrane covering a 285 nm-deep circular hole. The mechanical resonant frequency of the fundamental mode is 11 MHz, with a *Q* factor of 2000. We also used a focused ion beam (FIB) to create defects in suspended hBN membranes and then used confocal laser-scanning microscopy to study single-photon photoluminescence from the exposed regions. By resonantly driving a membrane in which quantum emitters are embedded, we hope to take advantage of strong defect-strain coupling to explore the physics of a hybrid quantum system.

Summary of Research:

Solid-state single-photon sources are an essential component of emerging quantum technologies. Point defects in hBN are a bright source of single-photons at room temperature with interesting coupling to strain in the crystal. This strong coupling has been used to statically tune defect emission [1,2] and it gives hBN the potential to be used in a hybrid quantum system entangling single photons with single phonons [3].

To study the dynamic optomechanical coupling of an hBN defect to a driven membrane, we first design devices that achieve high strain through electrostatic actuation. To fabricate these devices, we use DUV photolithography to etch a pattern of holes and trenches into SiO_2 and then align a second layer of patterned photoresist to evaporate Ti/Au electrodes at the top and bottom of the holes. Figure 1 shows a scanning electron micrograph of such a device before transferring the heterostructure membrane over the electrodes. After the photolithography, we use a polymer-assisted exfoliation method to transfer a multilayer hBN/graphene heterostructure over the hole such that the graphene is in contact with only the top electrodes and suspended above the bottom electrode (Figure 2). By applying voltage across the electrodes, the electrostatic force deflects the suspended membrane and the induced strain shifts the optical transition energy of defects within the hBN flake.

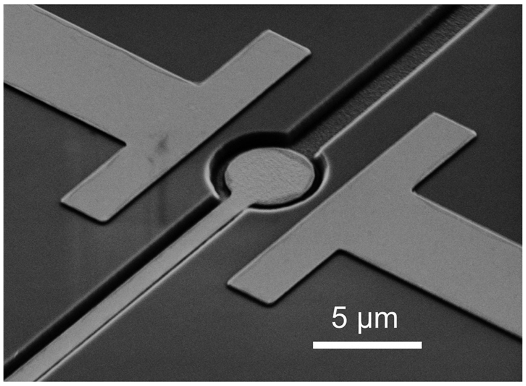

Figure 1: SEM of the fabricated device substrate onto which the heterostructure membrane was transferred. The trenches are etched 285 nm into the SiO_2 substrate and a 30 nm film of Ti/Au is evaporated to define the electrodes.

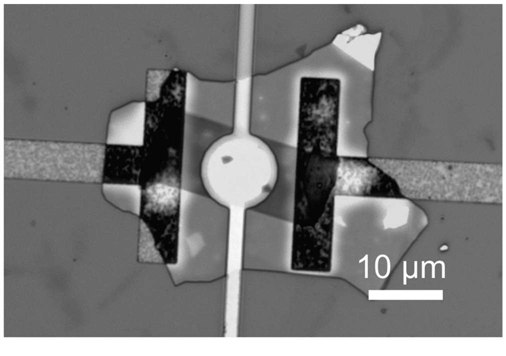

Figure 2: Optical micrograph of a 25 nm thick hBN/graphene heterostructure membrane exfoliated onto the device substrate. (See pages vi-vii for full color version.)

We detect motion of the membrane using interferometric techniques by focusing a 637 nm laser onto the center of the membrane while the device is under high vacuum (< 10^{-5} Torr). When the membrane is vibrating, the optical phase difference created by

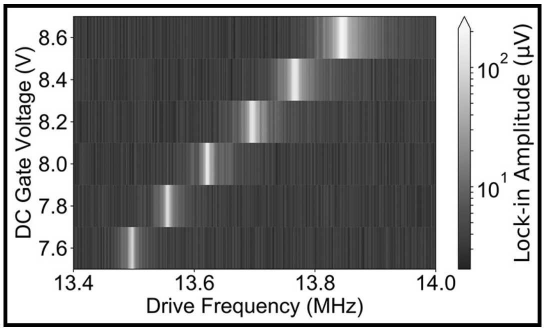

Figure 3: Lock-in sweep data showing the mechanical resonance at varying DC offset voltages.

the gap between the membrane and bottom electrode fluctuates and thus so does the reflection intensity. We direct the reflected light onto a high-frequency photodiode, whose voltage is the input to a lock-in amplifier with the electrostatic drive as the reference. When we sweep the driving frequency while monitoring the lock-in signal, we detect the fundamental resonant mode at around 11 MHz. Additionally, by applying a DC offset, the static pre-tension can be used to tune the resonant frequency and improve the resonator *Q* factor (Figure 3).

Although much progress has been made in creating optically stable defects in hBN, most methods produce emitters at random positions [4]. To integrate and couple the emitters with other structures, defects must be created with nanometer precision and reproducible properties. We have made significant progress on this front by producing arrays of quantum emitters at deterministic locations. Using a gallium FIB [5], we mill shallow circular pits 300 nm across and 5 nm deep on exfoliated hBN (Figure 4a), suspended over trenches to avoid background fluorescence induced by the substrate. We then anneal the devices for 30 minutes at 850°C in a N_2 environment.

Using a confocal laser-scanning microscope, we measure photoluminescence from the milled regions (Figure 4b). Upon close inspection, we observe high-purity single-photons from several defect-based emitters close to the perimeter of each milled circle. Autocorrelation statistics from one of these quantum emitters is shown in Figure 4c.

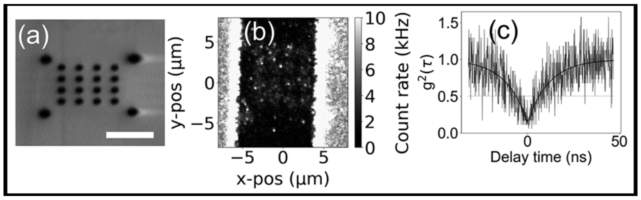

Figure 4: a) SEM of a suspended multilayer hBN membrane, patterned with an array of circular pits milled using a gallium FIB. Scale bar is 5 μm. b) Photoluminescence map of FIB-exposed region. c) Second-order autocorrelation function of the emission from an isolated defect, fit to a two-level model. The measurement of g(2)*(τ = 0) < 0.5 indicates that the source is emitting single-photons.*

Conclusions and Future Steps:

While driving on resonance, we will be able to scan the interferometry laser position over the entire membrane and achieve high spatial resolution of the mechanical mode. We can then infer the strain profile using a finite element model of the device. We will then create isolated point defects in the hBN using the FIB method discussed and will be able to quantify the shift in the optical transition, elucidating the potential for hBN to be used in quantum optomechanical devices.

References:

[1] N. Mendelson, M. Doherty, M. Toth, I. Aharanovich, T. T. Tran, "Strain-Induced Modification of the Optical Characteristics of Quantum Emitters in Hexagonal Boron Nitride" Adv. Mater. 2020, 1908316 (2020).

[2] G. Grosso, H. Moon, B. Lienhard, S. Ali, D. K. Efetov, M. M. Furchi, P. Jarillo-Herrero, M. J. Ford, I. Aharonovich, and D. Englund, "Tunable and high purity room-temperature single photon emission from atomic defects in hexagonal boron nitride" Nat. Commun. 8, 705 (2016).

[3] X. Guo, Z.-Q. Yen, T. Li, "High-speed quantum transducer with a single-photon emitter in an atomically thin resonator" arXiv:1712.09245 (2017).

[4] I. H. Abidi, N. Mendelson, T. T. Tran, A. Tyagi, M. Zhuang, L. T. Weng, B. Özyilmaz, I. Aharonovich, M. Toth, Z. Luo, "Selective Defect Formation in Hexagonal Boron Nitride" Adv. Opt. Mater. 7, 1900397 (2019).

[5] J. Ziegler, R. Klaiss, A. Blaikie, D. Miller, V. R. Horowitz, B. J. Alemán, "Deterministic Quantum Emitter Formation in Hexagonal Boron Nitride via Controlled Edge Creation" Nano Lett. 19, 3, 2121-2127 (2019).

Making a Microfluidic Device to Mimic Flow Through Porous Medium

CNF Project Number: 2385-15
Principal Investigator(s): Brian Kirby
User(s): Katherine Polhemus

Affiliation(s): Mechanical and Aerospace Engineering, Cornell University
Primary Source(s) of Research Funding: IGERT Program for Earth Energy
Contact: kirby@cornell.edu, kcp44@cornell.edu
Primary CNF Tools Used: CAD software L-Edit, hot press, CorSolutions Microfluidic Probe Station

Abstract:

With the rapid depletion of known oil reserves, detecting properties of the oil reservoirs and optimizing oil extraction is critical. By measuring the aqueous properties of the reservoirs, decisions can be made on which reservoirs to drill and the available quantity of oil to extract, with minimal environmental impact. Utilizing particles in testing can provide a variety of information about the reservoir. The objective of the proposed work is to characterize the behavior of particles at the oil-water interface in order to optimize their use as subsurface sensors. In order to complete the optimization, a microfluidic model for the environment needs to be developed. This past year's work involves making microfluidic devices to mimic water flowing through the subsurface and oil trapped in pores. The design and mold to make the mold was developed in the CNF first using photolithography to create a mold with negative photoresist which was used to make microfluidic channels out of polydimethylsiloxane and later using positive photoresist and etching to create a mold to make microfluidic channels out of polypropylene.

Summary of Research:

The work in the CNF has consisted of using microfabrication techniques to make a microfluidic device. Using the CAD software L-Edit to make patterns to transfer to a mask using the Heidelberg mask writer, in the past year, we have made two types of masks: one for positive photoresist and the other for negative photoresist. The first set of microfluidic devices used the negative photoresist (SU-8) to make a mold. The process of making a mold with photoresist (photolithography) consist of the steps; 1) Pour and spin photoresist onto a wafer (using CNF spinner), 2) Bake photoresist (using CNF hot plates), 3) Wait time, 4) Expose photoresist (using ABM contact aligner), 5) Second wait time, 6) Development of photoresist.

At the end of the process, we have a mold out of SU-8 on top of a wafer. In the Kirby research group's lab, we made microfluidic devices by pouring PDMS on top of the mold and baking, then attaching, the molded PDMS to a glass slide through plasma cleaning. Unfortunately for our application, we need the PDMS to be very hydrophobic and PDMS was not hydrophobic enough for the experiments. Therefore, we switched to making devices out of a polypropylene — a much more hydrophobic material. To make molded polypropylene pieces we used hot embossing, which is done on the CNF hot press.

Because of the large pressure applied during embossing, we needed a stronger mold than SU-8, so we switched to making molds out of silicon. To make a mold out of silicon, a positive photoresist is spun instead of negative and after the photolithography process, the wafer is etched on the deep reactive ion etcher in the CNF. The mold is used in the CNF hot press to hot emboss the pattern onto polypropylene. Another piece of polypropylene is pressed to a thinner thickness using the using the hot press. Finally, the device is bonded together using the hot press. We also used the CorSolutions Microfluidic Probe Station as a connection method for tubes to the device, which allowed us to flow oil and particles into the device.

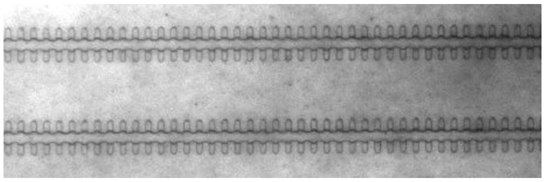

Figure 1: Oil-water contact line in polypropylene device.

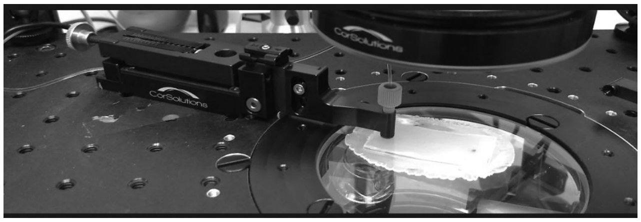

Figure 2: Device on CorSolution station.

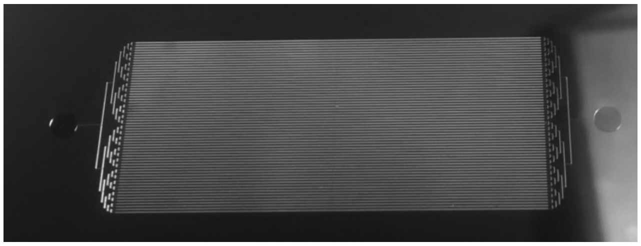

Figure 3: Etched silicon mold for hot pressing.

The Role of Smart Water in Oil Recovery

CNF Project Number: 2385-15
Principal Investigator(s): Brian Kirby
User(s): Julia Radzio

Affiliation(s): Mechanical and Aerospace Engineering, Cornell University
Primary Source(s) of Research Funding: Cornell Engineering Learning Initiatives (ELI)
Contact: kirby@cornell.edu, jr932@cornell.edu
Website: http://blogs.cornell.edu/kirbyresearch/
Primary CNF Tools Used: CRC hot press, CorSolutions Microfluidic Probe Station

Abstract:

Global oil demand and consumption continues to increase yearly, but current oil recovery techniques lack the efficiency needed to extract most of the oil in reservoirs. The use of nanoparticles as sensors for the available quantity of oil to extract has been demonstrated in experimental laboratory evaluations with core samples. This report will discuss how microfluidic devices were used to provide a controlled environment for studying how particles partitioned between oil and flooding fluids. Smart water was injected into the devices at various flow conditions in order to determine favorable circumstances for particles to enter the pockets of the channels. Solutions that contained less than 50% water to ethanol minimized particle clogging at the inlets and T-intersections of the devices. At 2.5 µL/min, the contact line between the oil and smart water remained stable and boluses did not appear. The hydrophobicity of the walls of the inlets negatively affected the flow of particles in smart water solutions. These flow conditions will ultimately allow for the particle concentration at the inlet and outlet of microfluidic devices to be measured, which will inform the effectiveness of particles as sensors for oil in a reservoir.

Summary of Research:

With the rapid depletion of known oil reserves, detecting properties of oil reservoirs and optimizing oil extraction is critical. Global oil demand and production continues to increase every year, with the rate of oil consumption in 2018 having grown to an above average 1.4 million barrels per day [1]. Nanoparticles can serve as sensors for the interiors of oil reservoirs by partitioning into oil or releasing nanoreporters upon contact with oil [2]. Microfluidic devices can provide a micro-scale environment to analyze singular effects in pores by modeling partially saturated rock with crude oil [3]. Laminar flow in the microchannels of the devices allows for experiments that can be reliably repeated and observed over a pore network [3].

The microfluidic device that is utilized to mimic subsurface conditions is fabricated from two layers of polypropylene in the Cornell NanoScale Facility. To manufacture a mold for forming the channels, a Si wafer is patterned with SPR-220-7 using standard photolithography techniques and deep reactive ion etching. The mold is used to emboss a polypropylene square on a CRC Hot Press at 166.6°C at 200 lbf (pound-force) for 2.5 minutes, after which the embossed piece is bonded to blank polypropylene square with a thickness between 0.17 mm and 0.24 mm at 149.5°C at 9 lbf above the baseline force for six minutes. As seen in Figure 1, the design features 16 parallel, bifurcating channels that allow for uniform, low flow rates for the given syringe pump range. The depth and width of the main channels was approximately 20 µm, and the pockets were rounded with a side width of 13 µm and placed apart from each other every 13 µm.

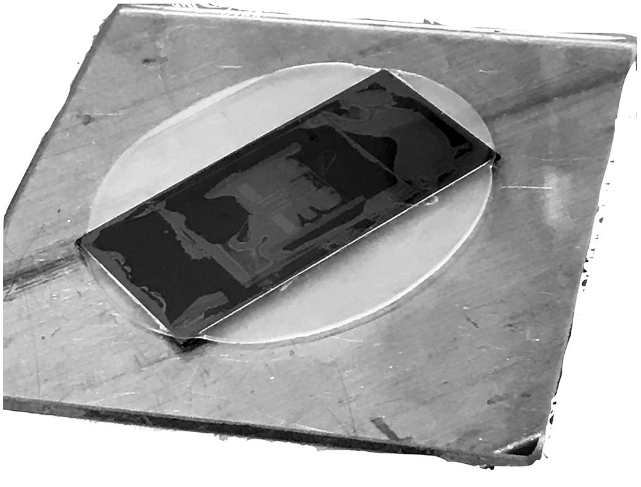

Figure 1: Silicon wafer patterned with 16 channel design.

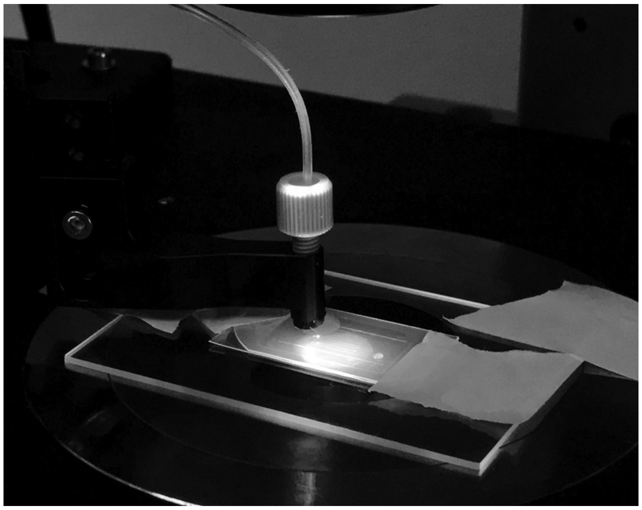

Figure 2: Experimental setup close-up of CorSolutions arm connector.

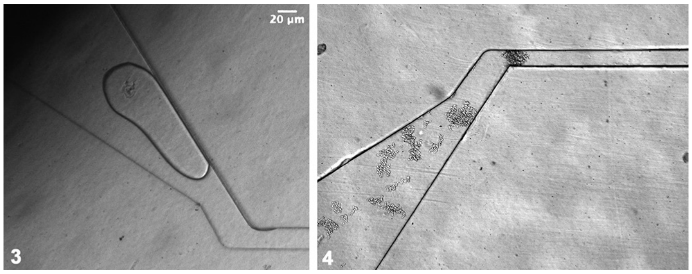

Figure 3, left: *Oil bolus attached to wall of inlet of microfluidic device.*
Figure 4, right: *Particles clustered at the narrowing of the inlet for 25% water: 75% ethanol solution.*

The formation of oil boluses in the inlet of the microfluidic devices after water-ethanol solutions were injected was investigated. Boluses that formed at any point in the device would lead to particles dispersing at an uneven rate and would lead to clogs in the channels of the device. Undecane, oil, and water-ethanol were sequentially injected into a device using a Tygon® tube as shown in Figure 2 (CorSolutions). Boluses at the inlet were qualified as a distinct second phase that appeared to fill the center of the inlet or as singular bubbles of oil that remained attached to the inlet wall for the duration of the trial as seen in Figure 3.

For every flow rate, 25% water: 75% ethanol had inlets free of boluses. The contact line between oil and the injected solution was most stable for 2.5 µL/min, as it took the longest amount of time for the oil to be displaced from the pockets compared to 5 and 10 µL/min. The 25% water: 75% ethanol solution containing microparticles was injected in a new device at 10 µL/min. 2 µm particles clumped together immediately at the inlet and the first T-intersection for all three trials as shown in Figure 4, but there was no evidence of boluses in the inlet.

Conclusions and Future Steps:

Because the devices were primed with oil, it was expected that the particles would partition from the injected solution to the oil in the pockets. As the particles had a tendency to attach to the walls of the inlet and to each other at T-intersections, no particles were able to flow into the channels of the devices at a variety of water-ethanol solutions and flow rates. Qualitative data presented in this report suggests that smart water consisting of 25% de-ionized water and 75% ethanol prevents boluses from forming in the inlet of the device. However, the hydrophobicity of the solution and the surface of the channels causes particles to cluster at the inlet and clog flow into the channels.

Future work will focus on changing the composition of the smart water with a surfactant that allows particles to partition into the oil in the pockets, and ultimately serve as a sensor for oil.

References:

[1] British Petroleum. (2019). BP Statistical Review of World Energy 2019. (Report No. 68).

[2] Sireesha, M., Babu, V. J., Kiran, S. K., and Ramakrishna, S. (2018). A Review on Nanomaterial Revolution in Oil and Gas Industry for Enhanced Oil Recovery Methods. Res Dev Material Sci. 4 (1).

[3] Gogoi, S., and Gogoi, S. B. (2019) Review on microfluidic studies for EOR application. Journal of Petroleum Exploration and Production Technology.

Atomically Thin Actuator-Enabled Micro-Machines and Micro-Structures

CNF Project Number: 2416-16

Principal Investigator(s): Itai Cohen, Paul L. McEuen

User(s): Qingkun Liu, Wei Wang, Baris Bircan, Michael F. Reynolds

Affiliation(s): Kavli Institute at Cornell for Nanoscale Science, School of Applied and Engineering Physics, Laboratory of Atomic and Solid-State Physics, Department of Physics; Cornell University

Primary Source of Research Funding: National Science Foundation Grant DMR-1719875; DMR-1435829 Army Research Office Grant W911NF-18-1-0032

Contact: itai.cohen@cornell.edu, plm23@cornell.edu, ql59@cornell.edu, ww459@cornell.edu, bb625@cornell.edu

Primary CNF Tools Used: Oxford ALD FlexAL, Arradiance ALD Gemstar-6, Oxford 81/100 etchers, ABM contact aligner, SC 4500 odd-hour, AJA sputter, AJA ion mill, Oxford Cobra ICP etcher, Heidelberg DWL2000

Abstract:

The ability to actuate an object at the microscale is an important technological aspect of manufacturing micro-robots and micro-machines. Here we demonstrate that micro-actuators made by atomically thin layers of metals and dielectrics could bend in response to electrical or chemical signals. The electrical micro-actuators could work in both volatile and shape memory regimes depending on the applied voltages, enabling electrically programmable three-dimensional structures and artificial cilia. The chemo-responsive actuators allow for self-folding three-dimensional origami structures activated by the pH of the aqueous solution.

Summary of Research:

Our team has developed atomically thin actuators that can bend in response to electrical and chemical stimuli. This approach makes it possible to create complex structures, machines, and microrobots by using origami design principles at the microscale.

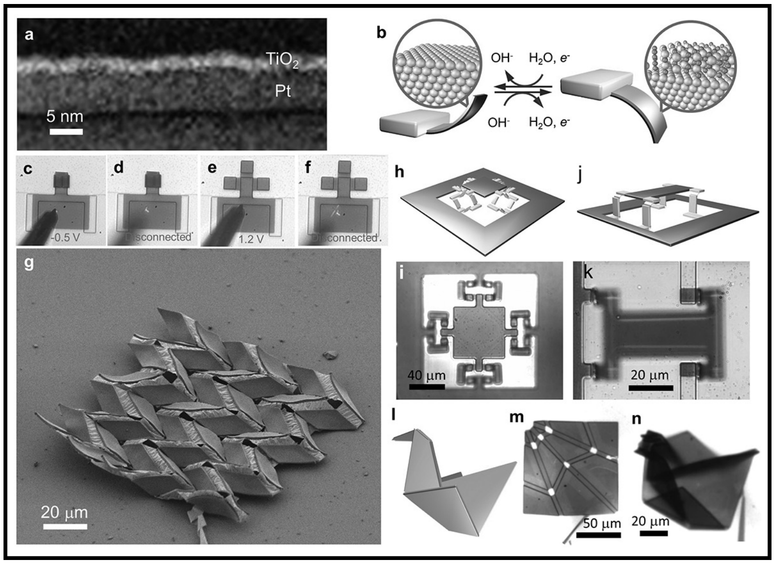

Figure 1: Electrically programmable shape memory actuator-enabled micro-devices. (See cover for Figure 1g in full color. Used with permission.)

Our team first discovered a microscale multistable electrochemical shape memory actuator that "memorizes" a continuous range of shapes, which is distinct from only one or two stable shapes of the conventional shape memory materials associated with the transformation of crystal structures [1]. The core of the device comprises of an electrochemically active platinum membrane capped on one side by an inert layer (Figure 1a). To achieve a continuous range of shapes, the team developed a technique based on applying voltage to shift the electrochemical balance between platinum and a surrounding electrolyte in order to drive oxygen ions through one surface of the platinum membrane (Figure 1b). This electrochemical redox reaction of platinum creates a differential in stress between the two sides of the actuator, causing the structure to cycle and maintain a submicron bending radius for a long time (Figure 1c-f).

This electrical programmability of nanometer-thin membranes can be harnessed to create three dimensional shapes that can be reversibly erased and rewritten by short electrical pulses. We then localized the bending position by patterning rigid polymeric panels (Figure 1g). Origami principle could be employed to design micro-machines owing to the capability of the bidirectional folding of actuators by reversing the deposition order of the platinum and inert layers. We demonstrate electrically reconfigurable micro-origami motifs and bistable microactuators (Figure 1h-n).

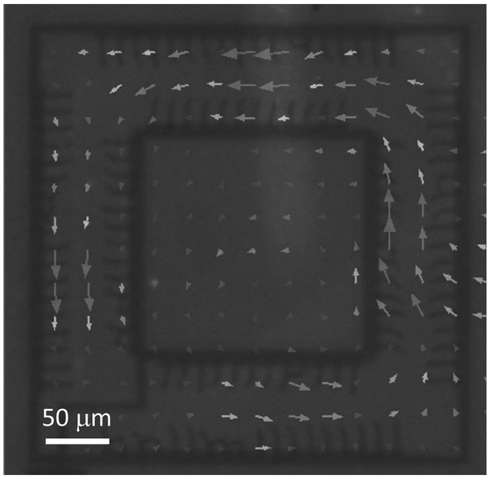

Figure 2: Electrical artificial cilia-pumped flow pattern with its direction indicated by arrows. (See pages vi-vii for full color version.)

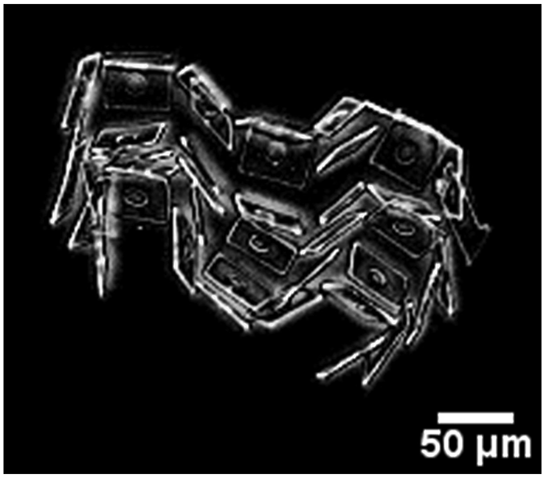

Figure 3: A spacer Miura-ori fold made using ultra-thin, self-folding atomic layer deposited sheets.

The manufacturing process is fully compatible with the microelectronic fabrication technology, making it easy to integrate with control circuit. These results could lead to new micro- or nano- electromechanical systems for robotic applications.

Besides the shape memory effect, the atomically thin platinum/titanium membrane could work as a volatile actuator. The actuators bend due to the difference in stress between the platinum and titanium layers that stems from the electrochemical adsorption of oxygen species on the surface of platinum. By harnessing this new type of electrical micro-actuator, our team developed electrically controllable artificial cilia that efficiently pump fluid in a steady unidirectional flow (Figure 2).

Individually addressable micro-scale robotic cilia have the potential to enable unprecedented control over microfluidic environments. They could be used to sort microscale particles, control chemical reactions, and transport viscoelastic materials. Such systems could also be used to better understand biological processes such as neurotransmitter transport in the brain, as well as clearing in the liver and lungs. The electrical nature of these artificial cilia makes it possible to integrate control circuits and power sources, allowing for sequential and addressable generation of arbitrary flow patterns. We envision that this technology will find broad applications. For example, in addition to ushering unparalleled control of fluids moving over surfaces, such electrically programmable artificial cilia could serve as actuators for aquatic microscale robots.

Our team also developed chemo-responsive micro-actuators that enable self-folding three-dimensional micro-architectures using origami principle. The mapping of an arbitrary three-dimensional shape to an origami fold pattern requires the assignment of fold angles ranging from -180° to +180°. Therefore, bidirectional folding action is essential in creating a complete platform for origami-based self-assembly.

Our previous work achieved unidirectional folding with atomically thin sheets of hard materials [2], but could not be used to fabricate complex geometries that required bidirectional folding. To address this problem, our team has developed a scalable microfabrication process to create microscale bidirectional folds using 4 nm thick atomic layer deposition SiN_x - SiO_2 bilayer films [3]. Strain differentials within these bilayers result in bending, producing microscopic radii of curvature. To take advantage of this intrinsic curvature, we photolithographically pattern these bilayers and localize the bending using 1 μm thick panels of rigid SU-8 polymer. This allows us to fabricate a variety of complex micro-origami devices, ranging from relatively simple geometries with six folds to more complex ones with nearly 100 folds, such as the spacer Miura-ori fold seen in Figure 3.

Upon release, these devices self-fold according to prescribed patterns. Our approach combines automated lithography mask design with easily scalable planar microfabrication methods, making it easy to fabricate and deploy micro-origami devices en masse. This work has been compiled into a manuscript and submitted for publication.

References:

[1] Liu, Q., Wang, W., Reynolds, M., Miskin, M., Cao, M. C., Muller, D. A., McEuen, P. L. Cohen, I., Electrically Programmable Micro-Scale Shape Memory Devices, APS March Meeting, 2020.

[2] Miskin, M., Dorsey, K., Bircan, B., Han, Y., Muller, D., McEuen, P., and Cohen, I. Graphene-based bimorphs for micron-sized autonomous origami machines. Proceedings of the National Academy of Sciences, 115: 466-470 (2018).

[3] Bircan, B., Miskin, M., Dorsey, K., McEuen, P. and Cohen, I., Bidirectional Folding with Nanoscale Sheets for Autonomous Micro-Origami, 2018.

Integration of III-V Microscale Light-Emitting Diodes for Cell-Sized Optical Wireless Electronics

CNF Project Number: 900-00

Principal Investigator(s): Paul L. McEuen[1,2]

User(s): Yanxin Ji[3], Alejandro J. Cortese[1], Conrad Smart[1]

Affiliation(s): 1. Laboratory of Atomic and Solid State Physics, 2. Kavli Institute at Cornell for Nanoscale Science, 3. Electrical and Computer Engineering; Cornell University

Primary Source(s) of Research Funding: Cornell Center for Materials Research with funding from the NSF MRSEC program (DMR-1719875), Air Force Office of Scientific Research (AFSOR) multidisciplinary research program of the university research initiative Grant FA2386.13-1-4118

Contact: plm23@cornell.edu, yj323@cornell.edu, ajc383@cornell.edu, cs2239@cornell.edu

Primary CNF Tools Used: Odd hour evaporator, ABM contact aligner, Oxford 81 etcher, AJA sputter deposition tool, P10 profilometer, RTA-AG610, Heidelberg mask writer DWL2000

Abstract:

Opto-electric circuits comprising light emitting diodes, photovoltaic cells, electric circuits etc. have attracted increasing attention and have found broad applications in fields ranging from displays to bio-integrated systems. A transfer technique to integrate optical and electrical devices together is required. Here we present a 4-inch wafer-scale aligned transfer method for integrating micro-LEDs with silicon circuits. This method demonstrates both high transfer yield and high alignment accuracy.

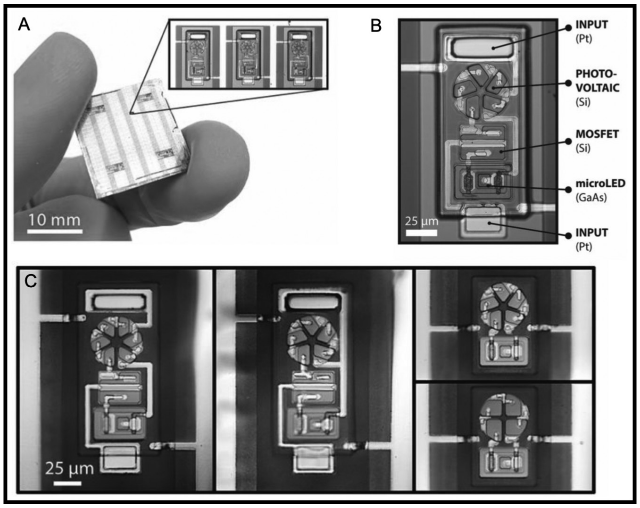

Figure 1: (A) Image of a chip containing thousands of integrated optical wireless integrated circuit (OWIC) sensors. (B) Optical image of an OWIC sensor with components labeled. (C) Image of various OWIC sensors with different functions.

Summary of Research:

Inorganic microscale light-emitting diodes (micro-LEDs) are broadly used in optoelectronic systems because of their high efficiency, color purity and reliability. Our group has recently developed a platform combining both inorganic micro-LEDs and electric circuits: optical wireless integrated circuits (OWICs) [1] (Figure 1). The OWIC sensors are approximately 100 µm across, which is microscopic in size, and can be used for a wide range of applications such as biosensing.

To integrate the micro-LEDs and silicon-based devices into the same circuit, a challenge must be met: high quality inorganic micro-LEDs are commonly grown on non-silicon substrates such as gallium arsenide (GaAs), while the electric circuits are fabricated on silicon substrates. Therefore, effective transfer methods are required. We develop an approach for transferring GaAs micro-LEDs from their native substrates to silicon substrate at wafer scale.

The micro-LEDs are fabricated on a commercially purchased 4-inch GaAs LED epitaxial wafer. The epitaxial structure is composed by p-GaAs layer, multiple quantum wells (active region) and n-GaAs layer. We first etch the GaAs epitaxial structure down to the n-GaAs layer to expose GaAs by citric acid wet etching. We then deposit the Ti/Pt metallic contact on the p-GaAs layer using the odd-hour evaporator. Following that, Au/Ge/Ni metallic contacts are deposited on the n-GaAs layer using the AJA sputter deposition system. We then etch the GaAs epitaxial structure down to the bulk substrate to outline the micro-LEDs using citric acid wet etching. In the end, the GaAs wafer is annealed in RTA-AG610 for better n-contact.

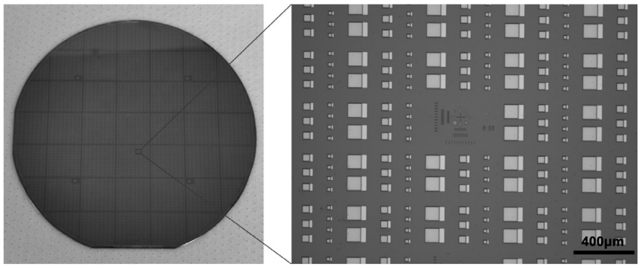

Figure 2: Fabricated GaAs micro-LEDs on a 4-inch GaAs wafer.

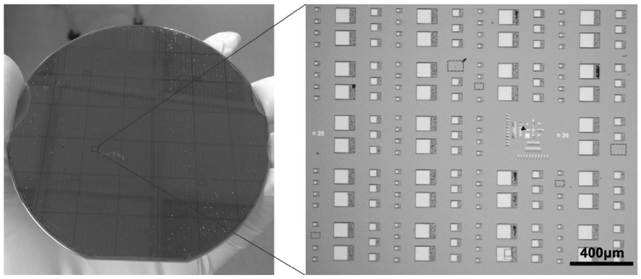

Figure 3: Transferred GaAs micro-LEDs on a 4-inch silicon wafer.

Figure 2 shows micro-LEDs of various sizes.

We then spin-coat PMMA onto the micro-LEDs as the protection layer and bond the 4-inch GaAs wafer with a transparent carrier wafer using a low melting-point thermal plastic polymer. Then we place the stack into citric acid to etch away the bulk GaAs substrate. After that, we have micro-LED arrays attached to the transparent carrier wafer. We then build up an aligning and bonding system based on the ABM contact aligner and a homemade heat stage. Using the aligning and bonding system, we first align the micro-LEDs with the features on the target substrate and then bring the micro-LEDs into contact with the target silicon substrate.

In the end we melt the thermal plastic polymer on a heat stage allowing the removal of the carrier substrate. The polymer residue is etched away in acetone. The result is aligned micro-LEDs transferred onto a 4-inch silicon wafer (Figure 3).

The transfer yield of this method is promising.

We transferred micro-LEDs in varied sizes to a bare silicon substrate (no adhesion layer) with high yield. The dashed boxes in Figure 3 indicate the few missing micro-LEDs, which are a small fraction of the total. The alignment accuracy is quantified by thousands of alignment marks distributed across the wafer. They show our method has reasonably precise alignment (~1μm). This wafer-scale transfer method will make possible new classes of integrated wireless sensors and optoelectronic devices fabricated across a full 4-inch wafer.

References:

[1] Cortese, Alejandro J., et al. "Microscopic sensors using optical wireless integrated circuits." Proceedings of the National Academy of Sciences (2020).

Optomechanical Sensing in the Nonlinear Saturation Limit

CNF Project Number: 1997-11
Principal Investigator(s): Qiang Lin
User(s): Usman A. Javid

Affiliation(s): The Institute of Optics, University of Rochester, Rochester NY
Primary Source(s) of Research Funding: National Science Foundation (Grant No. ECCS-1842691, ECCS-1351697, and EFMA-1641099)
Contact: qiang.lin@rochester.edu, usman.javid@rochester.edu
Primary CNF tools used: JEOL 9500, Unaxis 770 deep silicon etcher

Abstract:

The leap from former bulky electronic and optical components to integrated devices has revolutionized computing, information processing and sensing technologies. Compact chip-scale devices allow confinement of light into sub-wavelength volumes to enable strong light matter interactions. The interaction of light with mechanical motion has enabled design of highly sensitive opto-mechanical sensors that are used in many areas of scientific research. These sensors have a limited dynamic range of sensing in order to allow for high sensitivity of detection. Here, we demonstrate that the dynamic range can be enhanced by a new measurement technique using a suspended silicon microdisk resonator that supports high-*Q* optical and mechanical modes.

Summary of Research:

Interaction of light with mechanical motion has enabled many interesting phenomena including cooling and mechanical lasing, quantum state control of light and mechanical motion, nonlinear and chaotic dynamics and so on [1]. Light-matter interactions inside optical microcavities have been shown to be excellent sensors [2]. For instance, these devices have been used in force sensing [3], acceleration and gyration measurements [4], electric magnetic fields sensors [5], scanning-probe microscopy [6], chemical and biological sensors [7], and so on. In most sensors there is a trade-off between the sensitivity that determines the smallest change in the input that can be detected, and the dynamic range that determines the largest change in the input that can be transduced without saturation. Cavity based optical sensors rely on the change in the resonance frequency of the cavity mode due to the change in the environment. This is manifested in the change in the transmission of an optical signal through the cavity. The nonlinear nature of the Lorentzian lineshape of the cavity mode puts an upper limit on the maximum change in its resonance frequency that can be measured. Increasing this dynamic range requires increasing the cavity linewidth which decreases the sensitivity to the resonance shift, manifesting the sensitivity-dynamic range trade-off mentioned earlier. Here we demonstrate a technique that extends the dynamic range beyond the traditional limit.

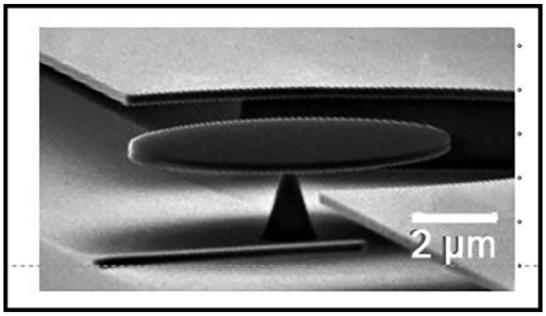

Figure 1: SEM image of the silicon microdisk resonator.

The scanning electron microscopic (SEM) image in Figure 1 shows a high-*Q* silicon microdisk resonator fabricated from a standard silicon-on-insulator (SOI) wafer using electron-beam lithography (JEOL 9500). The microdisk has a radius of about 4 µm and thickness of 260 nm. A C_4F_8/SF_6 chemistry was utilized in an inductively coupled plasma-reactive ion etching (ICP-RIE) process on the Unaxis 770 deep silicon etcher. The recipe was optimized for smooth device sidewalls, which reduces scattering losses and improves the optical quality (*Q*) of the device. Additionally, a hydrofluoric acid (HF) undercut was employed to suspend the silicon microdisk above the oxide layer.

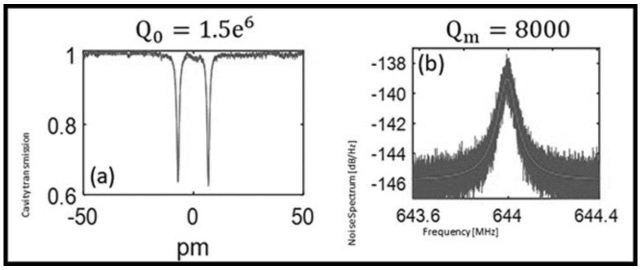

Figure 2: (a) Spectrum of an optical resonance of the microdisk with an intrinsic Q *of 1.5 million. (b) Thermal noise spectrum of the mechanical breathing mode with a* Q *of 8000 measured in vacuum.*

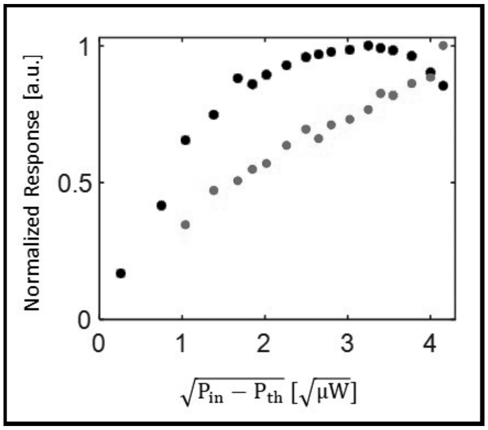

Figure 3: Measured modulation amplitude for increasing pump power using only the first harmonic (black) and the first three harmonics (grey). P_{th}*: Lasing threshold power,* P_{in}*: Input laser power.*

This undercut was done in several steps using a dilute HF bath to precisely control the undercut. The pedestal width is estimated to be between 100 and 200 nm. The resonator supports optical modes with quality factor as high as 1.5 million as shown in Figure 2(a). The device also supports a radial breathing mechanical mode with a resonance frequency of 644 MHz and a Q-factor of around 8000 in vacuum as shown in Figure 2(b).

Typically, in a sensing experiment, a modulation signal is applied to the cavity to modulate the resonance frequency in time. In optomechanical systems, this can be done by coherent oscillations induced by radiation pressure [8]. In this case, the cavity starts coherent mechanical oscillations after a power threshold is reached and the mechanical energy increases linearly with the input optical power. Theoretically, the dynamics can be modelled as a harmonic oscillator with time dependent resonance frequency. In the limit where the mechanical resonance frequency exceeds the cavity linewidth, we have shown that the mechanical motion can be estimated unambiguously by the first three harmonics of the modulation [9]. This is a new technique that allows the measurement of modulation amplitudes that exceed the ordinarily achievable dynamic range, given by the cavity linewidth.

We run a pump-probe experiment where a low-Q resonance drives these mechanical oscillations while a high-Q mode acts as a probe to measure the modulation amplitude. We compare the measured modulation amplitude using the traditional method using only the first harmonic, and our proposed approach using the first three harmonics of the modulation signal. Figure 3 shows the results. We can clearly see that the measurement using the traditional approach of using only the first harmonic saturates while our technique gives a linear response proving an increase of dynamic range. We measure a maximum modulation amplitude of over six times larger than the dynamic range would ordinarily allow.

Conclusions:

We have demonstrated a new sensing technique for micro-resonator based optomechanical sensors. Experimentally, we have shown how our proposed approach can extend the dynamic range of these sensors far beyond what is traditionally achievable.

References:

[1] M. Aspelmeyer, T. J. Kippenberg, and F. Marquardt, Rev. Mod. Phys. 86, 1391 (2014).

[2] M. R. Foreman, J. D. Swaim, and F. Vollmer, Adv. Optics Photonics 7, 168-240 (2015).

[3] E. Gavartin, P. Verlot, and T. J. Kippenberg, Nat. nanotechnology 7, 509 (2012).

[4] J. Li, M.-G. Suh, and K. Vahala, Optica 4, 346-348 (2017).

[5] S. Forstner, S. Prams, J. Knittel, E. Van Ooijen, J. Swaim, G. Harris, A. Szorkovszky, W. Bowen, and H. Rubinsztein-Dunlop, Phys Review Letters 108, 120801 (2012).

[6] Y. Liu, H. Miao, V. Aksyuk, and K. Srinivasan, Opt. Express 20, 18268-18280 (2012).

[7] Y. Sun and X. Fan, Anal. Bioanalytical Chemistry 399, 205-211 (2011).

[8] H. Rokhsari, T. J. Kippenberg, T. Carmon, and K. J. Va-hala, Opt. Express 13, 5293-5301 (2005).

[9] U. Javid, et al., Conference on Lasers and Electro-Optics (CLEO) 2020. (In preparation).

Photon-Level Tuning of Photonic Nanocavities

CNF Project Number: 1997-11

Principal Investigator(s): Qiang Lin

User(s): Mingxiao Li, Yang He, Jingwei Ling

Affiliation(s): Electrical and Computer Engineering, University of Rochester

Primary Source(s) of Research Funding: National Science Foundation (NSF) (EFMA-1641099, ECCS-1810169, and ECCS-1842691); the Defense Threat Reduction Agency-Joint Science and Technology Office for Chemical and Biological Defense (grant No. HDTRA11810047)

Contact: qiang.lin@rochester.edu, mli53@ur.rochester.edu, yhe26@ur.rochester.edu, jling8@ur.rochester.edu

Primary CNF Tools Used: JEOL 9500, AJA ion mill

Abstract:

We report an all-optical approach for extremely efficient tuning of a high-*Q* lithium niobate photonic crystal nanocavity, with a significant resonance tuning rate of 88.4 MHz/photon.

Summary of Research:

Controlling photonic functionalities by purely optical means is a long-term goal of nonlinear optics, which has been pursued for decades. Unfortunately, natural optical media generally exhibit fairly weak optical nonlinearities. Photonic crystal (PhC) nanocavities are able to strongly confine optical waves inside a small volume, thus particularly suitable for enhancing nonlinear optical interactions [1]. To date, PhC nanocavities have been applied on a variety of device platforms for optically tuning/switching the cavity properties [2-6]. However, it remains fairly challenging to achieve device control with only photon-level optical energy, which represents the ultimate efficiency of nonlinear optics. Here we report a lithium niobate (LN) PhC nanocavity that exhibits an optical *Q* as high as 1.41 million, more than one order of magnitude higher than previously reported [7-9]. With this device, we are able to demonstrate extremely efficient wavelength tuning of the device, with a resonance tuning rate as high as 88.4 MHz/photon, and nearly 100% preservation of the resonance quality.

Figure 1 shows the device, which was fabricated on a 300-nm-thick x-cut single-crystalline LN thin film, and patterned by JEOL 9500. We optimized the nanobeam width, layer thickness, lattice constant, and the shape of the elliptical holes to achieve a photonic bandgap of 26 THz covering optical frequency from 183 to 209 THz, for the transverse-electric-like (TE-like) polarization with the guided mode dominantly lying in the device plane. Simulations by the finite element method show that the cavity mode exhibits a radiation-limited optical *Q* of 1.23 × 10^8, with an effective mode volume as small as $0.78(\lambda/n)^3$.

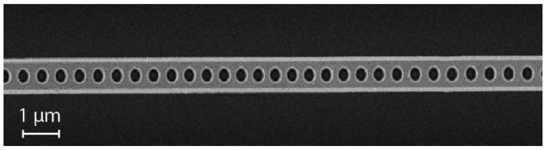

Figure 1: SEM image of a fabricated LN PhC nanobeam.

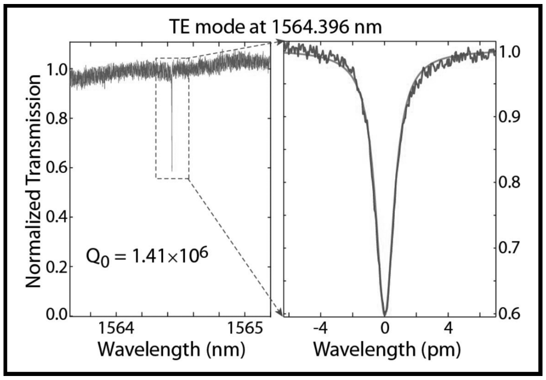

Figure 2: Laser-scanned transmission spectrum of a fabricated LN PhC nanobeam with the experimental data shown in blue and the theoretical fitting shown in red. (See pages vi-vii for full color version.)

Detailed experimental characterization of the fabricated device, as shown in Figure 2, shows that the device exhibits a high-quality cavity mode at 1564.396 nm in the telecom band, with an intrinsic optical *Q* factor as high as 1.41 million. This value is more than an order of magnitude larger than what was previously reported on LN nanophotonic devices [7-9]. To the best of our

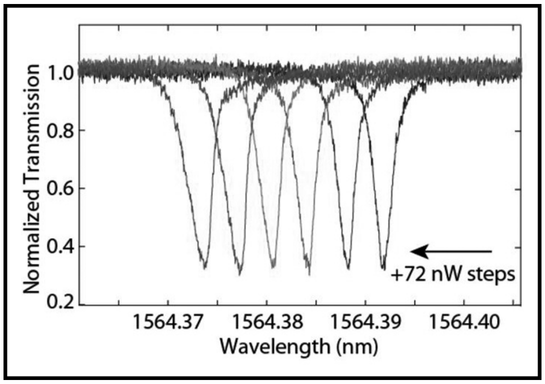

Figure 3: Measured transmission spectra of cavity exhibit strong resonant wavelength tuning with increasing intra-cavity power. (See pages vi-vii for full color version.)

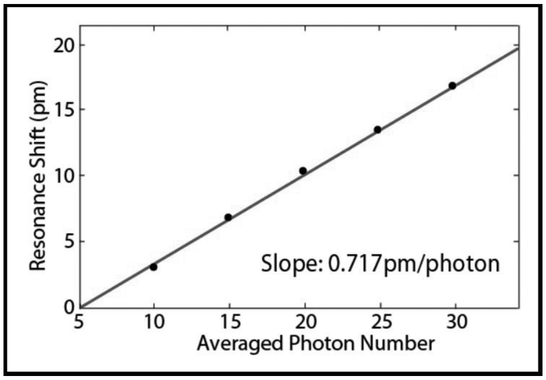

Figure 4: Linear resonant wavelength tuning as a function of intra-cavity power. The measured tuning efficiency is 88.4 MHz/photon, or equivalently 0.67 GHz/aJ.

knowledge, this is the second single-crystalline PhC nanocavity, other than silicon ones [10], that is able to exhibit an intrinsic optical Q above one million.

The extremely high optical Q, together with the tiny effective mode volume, of the device would result in dramatic enhancement of nonlinear optical interactions inside the cavity, thus allowing us to explore efficient nonlinear photonic functionalities. An intriguing nonlinear optical property of LN is the photorefractive effect [11], which manifests an intensity-dependent decrease of refractive index. We thus expect that the cavity resonance can be self-tuned by optical power launched into the device. To show this phenomenon, we maintain an external coupling efficiency of 65% (accordingly, loaded optical Q around 8.9×10^5). We continuously scanned the laser wavelength across the resonant wavelength back and forth and monitored the transmission of the device. As shown in Figure 3, when the input optical power increases from 72 nW to 432 nW, the cavity resonance wavelength continuously shifts towards blue.

As the laser wavelength was scanned back and forth in a periodic triangular fashion over a spectral range of 150 pm, the input power of 432 nW results in an averaged optical energy of about 3.96 aJ inside the cavity, which corresponds to an average of only 30 photons. Figure 4 shows the induced resonance shift as a function of average number of photons inside the cavity. It shows a clear linear dependence, with a tuning slope of 0.717 pm/photon, corresponding to 88.4 MHz/photon. Therefore, about 2.4 photons on average inside the cavity are able to shift the whole cavity resonance, clearly showing the extreme efficiency of the induced resonance tuning.

In summary, we demonstrated a LN photonic crystal nanobeam resonator with optical Q as high as 1.41 million. With this device, we were able to demonstrate efficient tuning of the cavity resonance, with a significant tuning rate of 88.4 MHz/photon and nearly 100% preservation of the resonance quality.

References:

[1] M. Soljacic and J. D. Joannopoulos, "Enhancement of nonlinear effects using photonic crystals," Nature Mat. 3, 211 (2004).

[2] M. Notomi, et al., "Nonlinear and adiabatic control of high-*Q* photonic crystal nanocavities," Opt. Express 15, 17458 (2007).

[3] I. Fushman, et al., "Ultrafast nonlinear optical tuning of photonic crystal cavities," Appl. Phys. Lett. 90, 091118 (2007).

[4] C. Husko, et al., "Ultrafast all-optical modulation in GaAs photonic crystal cavities," Appl. Phys. Lett. 94, 021111 (2009).

[5] K. Nozaki, et al., "Sub-femtojoule all-optical switching using a photonic-crystal nanocavity," Nature Photon. 4, 477 (2010).

[6] K. Nozaki, et al., "Ultralow-power all-optical RAM based on nanocavities," Nature Photon. 6, 248 (2012).

[7] S. Diziain, et al., "Second harmonic generation in free-standing lithium niobate photonic crystal L3 cavity," Appl. Phys. Lett. 103, 051117 (2013).

[8] L. Cai, et al., "Photonic crystal slab fabricated on the platform of lithium niobate-on-insulator," Opt. Lett. 39, 2094 (2014).

[9] H. Liang, et al., "High-quality lithium niobate photonic crystal nanocavities," Optica 4, 1251 (2017).

[10] T. Asano, et al., "Photonic crystal nanocavity with a *Q* factor exceeding eleven million," Opt. Express 25, 1769-1777 (2017).

[11] P. Günter and J. P. Huignard, eds., Photorefractive Materials and Their Applications (Springer, New York, 2006).

Ultra-Low Threshold Broadband Soliton Frequency Comb Generation

CNF Project Number: 2364-15

Principal Investigator(s): Michal Lipson[1]

User(s): Xingchen Ji[2]

Affiliation(s): 1. Department of Electrical Engineering, Columbia University, New York, NY 10027;
2. School of Electrical and Computer Engineering, Cornell University, Ithaca, NY 14853

Primary Source(s) of Research Funding: Defense Advanced Research Projects Agency

Contact: ml3745@columbia.edu, xj53@cornell.edu

Primary CNF Tools Used: PECVD, e-beam lithography, Oxford 100 etcher,
AJA sputter deposition, mask writer, furnace, Oxford 82 etcher

Abstract:

We measure a record-low threshold power down to 73 µW for parametric oscillation using resonators with intrinsic *Q* of 31.8 ± 4.4 million and demonstrate a broadband single soliton comb spectrum spanning 1097 nm-2040 nm (126 THz). The resonator compact profile is designed to minimize higher order modes excitation.

Summary of Research:

Microresonator-based frequency comb generation has recently attracted interest due to potential applications in spectroscopy, precision metrology and biomedical imaging [1-8]. However, the thresholds for these broadband frequency combs are limited by loss due to surface scattering [9,10].

Here we demonstrate an ultra-low threshold broadband single soliton frequency comb. It is generated with a resonator based on highly multimode Si_3N_4 waveguides for decreasing loss due to surface scattering and adiabatic bends to suppress higher order modes excitation.

Figure 1(a) shows the schematic of the device. The microresonator has a free spectral range (FSR) of 174 GHz and a cross section of 730 nm × 2600 nm which supports more than 8 modes (Transverse electric (TE) modes are shown in Figure 1 inset). A bus waveguide with the same dimension is used to couple to it. In the coupling section, the bending radius starts large (~ 900 µm) and then gradually reduces to a small value (~ 80 µm). The bending radius changes adiabatically, which allows us to have a small bending radius and also suppress excitation of higher order modes. Full 3D finite-difference time-domain (FDTD) simulations (Lumerical FDTD) depicted in Figure 2 show that higher order modes in our adiabatic bends design are suppressed compared with a regular ring resonator with constant bending radius.

We achieve a broadband single soliton comb spectrum spanning 1097 nm-2040 nm (126 THz) and measure a record-low threshold power down to 73 µW for parametric oscillation using resonators with intrinsic

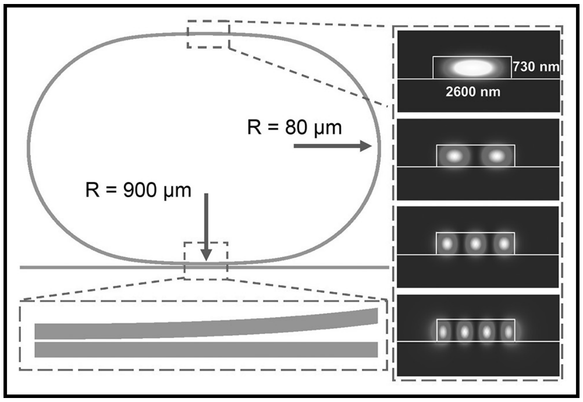

Figure 1: Schematic of our microresonators with adiabatic bends design. The bending radius starts large (~ 900 µm) and then gradually reduces to a small value (~ 80 µm). Inset shows the transverse electric (TE) modes supported by the waveguide and only the fundamental mode is excited in the adiabatic bends design.

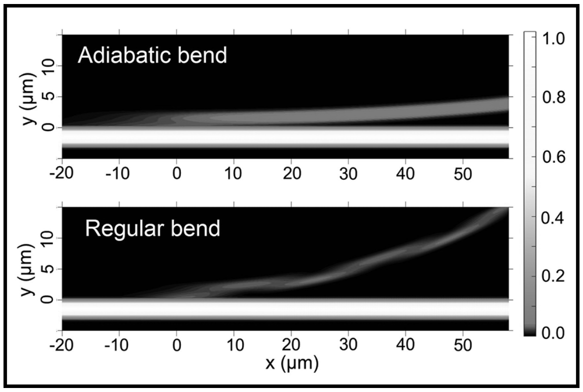

Figure 2: FDTD simulations of the adiabatic bends design (top) and the regular ring resonator with constant bending radius (bottom). Note that higher order modes have been excited in the regular ring and not in our adiabatic bends design.

Q of 31.8 ± 4.4 million. One can see that despite the large waveguide dimensions, we can still engineer the dispersion. In order to test the devices, we launch a laser source transmitted through a fiber polarization controller into the inverse nanotaper of our chip using a lensed fiber and collect the output through another inverse nanotaper using a collimating lens. We then split the collected light such that one of the outputs is used to monitor the generated comb spectrum and the other one is sent to a fast photodiode (> 12.5 GHz) to monitor transmission. We measure the output power in the first generated four-wave-mixing sidebands for different pump powers to determine the threshold for parametric oscillation.

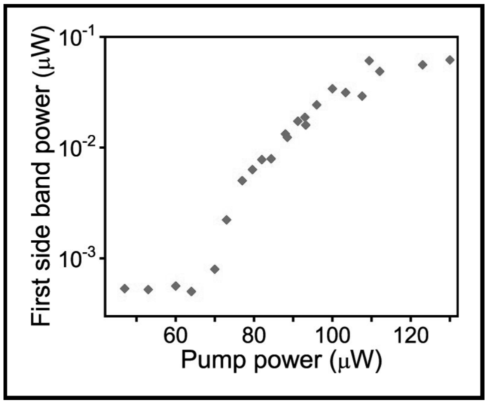

Figure 3: Output power in the first generated side band as a function of pump power. In this device, parametric oscillation is observed for pump power down to 73 μW.

Figure 3 shows the data for a device with an intrinsic *Q* of 32.8 million pumped at the resonance near 1560 nm. Parametric oscillation is observed with pump power down to 73 μW which is close to the theoretical limit of 70 μW. We generate a soliton-mode locked comb with the thermal tuning method as demonstrated in [11]. A narrow wavelength division multiplexing (WDM) filter centered at the pump wavelength is used to increase the dynamic range of the optical spectrum analyzer (OSA). Limited by the wavelength range of a single OSA, we obtain the spectrum in two shots under the same experimental condition (shown in Figure 4). Soliton state is maintained the same throughout the experiment.

In conclusion, we measure a record-low threshold power down to 73 μW for parametric oscillation using resonators with intrinsic *Q* of 31.8 ± 4.4 million.

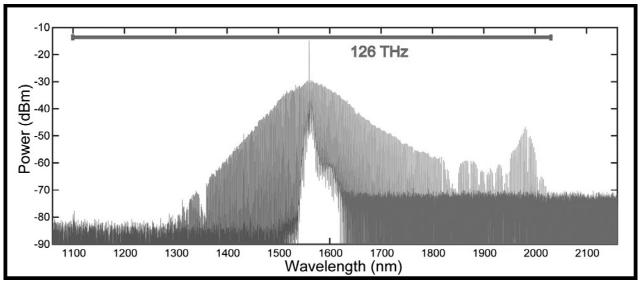

Figure 4: Broadband single soliton frequency comb spanning 1097 nm-2040 nm (126 THz) using highly multimode microresonators. Note that blue and red parts are the same single soliton state measured by two OSAs and dips in the spectrum (at 1350 nm and 1850 nm for example) are due to the WDM filter defects.

We achieve a broadband single soliton comb spectrum spanning 1097 nm-2040 nm (126 THz) using highly multimode waveguides by suppressing excitation of higher order modes with adiabatic bends. Utilizing highly multimode structures, we have more flexibility in the waveguide design (i.e. dispersion engineering). This work provides a method for using ultra high-*Q* multimode microresonators for applications such as spectroscopy and precision metrology.

References:

[1] T. J. Kippenberg, A. L. Gaeta, M. Lipson, and M. L. Gorodetsky, Science 361, eaan8083 (2018).

[2] A. L. Gaeta, M. Lipson, and T. J. Kippenberg, Nat. Photonics 13, 158-169 (2019).

[3] M.-G. Suh, Q.-F. Yang, K. Y. Yang, X. Yi, and K. J. Vahala, Science 354, 600-603 (2016).

[4] A. Dutt, C. Joshi, X. Ji, J. Cardenas, Y. Okawachi, K. Luke, A. L. Gaeta, and M. Lipson, Sci. Adv.4, e1701858 (2018).

[5] X. Ji, X. Yao, A. Klenner, Y. Gan, A. L. Gaeta, C. P. Hendon, and M. Lipson, Opt. Express 27, 19896-19905 (2019)

[6] M. H. P. Pfeiffer, C. Herkommer, J. Liu, H. Guo, M. Karpov, E. Lucas, M. Zervas, and T. J. Kippenberg, Optica 4, 684-691 (2017).

[7] M. Karpov, M. H. Pfeiffer, J. Liu, A. Lukashchuk, and T. J. Kippenberg, Nat. Commun. 9, 1146 (2018).

[8] Q. Li, T. C. Briles, D. A. Westly, T. E. Drake, J. R. Stone, R. B. Ilic, S. A. Diddams, S. B. Papp, and K. Srinivasan, Optica 4, 193-203 (2017).

[9] X. Ji, A. B. Felippe, S. P. Roberts, A. Dutt, J. Cardenas, Y. Okawachi, A. Bryant, A. L. Gaeta, and M. Lipson, Optica 4(6), 619 (2017).

[10] M. H. P. Pfeiffer, J. Liu, A. S. Raja, T. Morais, B. Ghadiani, and T. J. Kippenberg, Optica 5(7), 884 (2018)

[11] C. Joshi, J. K. Jang, K. Luke, X. Ji, S. A. Miller, A. Klenner, Y. Okawachi, M. Lipson, and A. L. Gaeta, Opt. Lett. 41, 2565 (2016).

Development of Single and Double Layer Anti-Reflective Coatings for Astronomical Instruments

CNF Project Number: 2458-16

Principal Investigator(s): Gordon Stacey[1]

User(s): Bugao Zou[2], Nicholas Cothard[2], Mahiro Abe[3]

Affiliation(s): 1. Department of Astronomy, 2. Department of Applied and Engineering Physics, 3. Department of Physics; Cornell University

Primary Source(s) of Research Funding: NASA Grant NNX16AC72G

Contact: stacey@cornell.edu, bz332@cornell.edu, nc467@cornell.edu, ma797@cornell.edu

Primary CNF Tools Used: Oxford PECVD, Anatech resist strip, Oxford 82 & 100 etchers, manual resist spinners, resist hot strip bath, Plasma-Therm deep silicon etcher, ASML 300C DUV stepper

Abstract:

We are developing microfabricated, silicon-substrate based mirrors for use in cryogenic Fabry-Perot Interferometers (FPIs) for astronomical instruments in the mid-infrared to sub-mm/mm wavelength regime. These mirrors consist of silicon substrates that are lithographically patterned with metal mesh reflectors on one side and metamaterial anti-reflection coatings (ARC) on the other side. In the past year we published a paper in the Journal of Low Temperature Physics that illustrates the design of the CCAT-prime Epoch of Reionization Spectrometer instrument and how the microfabricated FPI fits in the module and enables our scientific goals. Currently we are refining our ARC fabrication recipe to improve the quality and accuracy of the microfabricated structures. Optical performance measurements for our samples are ongoing using Fourier transform spectrometers.

Summary of Research:

The goal of the project is to develop microfabricated, silicon-substrate based mirrors for use in cryogenic Fabry-Perot interferometers for astronomical instruments in the mid-infrared to sub-mm/mm wavelength regimes. The mirrors consist of high-purity, float-zone, 500-µm-thick silicon wafers that are lithographically patterned with frequency-selective, gold mesh reflectors. We use a combination of inductive and capacitive meshes to maintain uniform high reflectance and hence nearly uniform resolving power over the FPI bandwidth. Due to the high index of refraction of silicon, the other side of the mirror must be patterned with an ARC to achieve broadband capability and to mitigate contaminating resonances from the silicon surface [1,2].

The bulk of our work this year has been the development of the fabrication methods of the ARC. Figure 1 shows our current recipe for a two-layer ARC. First, silicon dioxide is deposited on the wafer using the Oxford plasma enhanced chemical vapor deposition (PECVD) tool. Then, two layers of photoresist are patterned correspondingly to be etched into a two-layer oxide pattern using the Oxford 100 etcher. We use either the ABM contact aligner or the ASML stepper to pattern the photoresist depending on the feature sizes of our structures. After that, the two-layer silicon structure is formed by etching the wafer using the Plasma-Therm

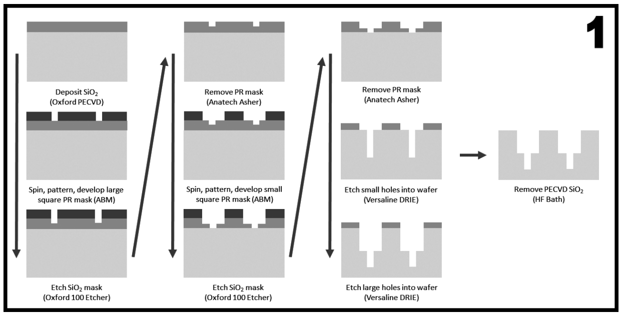

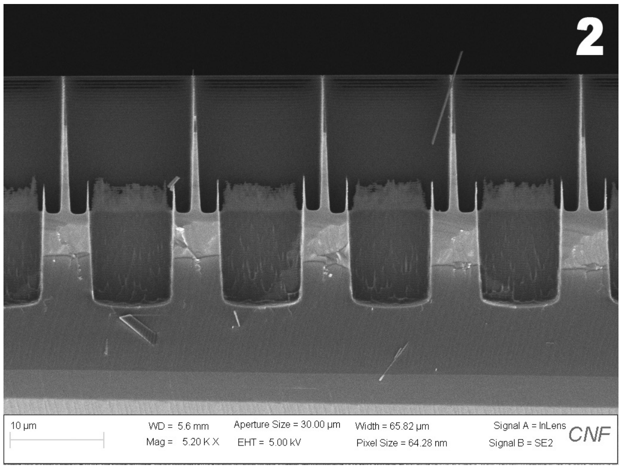

***Figure 1, top:** Process flow for fabricating a double-layer ARC on a silicon wafer. **Figure 2, bottom:** SEM image taken using CNF's Zeiss Ultra SEM showing the two-layer structure of anti-reflection coatings.*

deep silicon etcher using the oxide layer as the etch mask. A scanning electron microscope (SEM) image of the cross section of the ARC is shown in Figure 2.

Unwanted fence-like structures can be found at the boundary of two silicon layers. We believe they are caused by the passivation layer generated during silicon etch processes. We found that an external thermal oxidation postprocessing step can remove these structures. We are currently working to improve our control of this method and we are also looking for other methods to prevent the formation of this structure.

In addition, our fabrication process for metal mesh reflectors has been improved over this past year. We have successfully deposited 10-micron scale capacitive and inductive gold meshes on samples using AZ nLOF 2020 photoresist and the CHA evaporator. The lift-off procedure is done using heated Microposit 1165 Remover.

We have fabricated both ARC and metal mesh reflectors on several optical quality silicon wafers and are now measuring their frequency dependent transmittances in the mid-infrared to sub-mm/mm wavelength regimes using Fourier transform spectrometers. Our progress on these devices is discussed in a paper published in Journal of Low Temperature Physics which illustrates the design of the CCAT-prime Epoch of Reionization Spectrometer instrument and how the microfabricated FPI fits in the module and enables spectroscopic observations of the early universe [1].

The silicon-substrate based mirrors that are developed in CNF will be used in the upcoming scanning FPI instrument Prime-Cam in the CCAT-prime observatory, which is located at 5600 meters elevation on Cerro Chajnantor in the Atacama Desert in Chile [3]. CCAT-prime will use our FPI for one of its main science goals, that is to study the Epoch of Reionization of the universe via [CII] intensity mapping in the 750-1500 µm regime. Our instrument will enable the intensity mapping observations by providing high-sensitivity, wide-field, broadband spectroscopy. These measurements will tell us about how the first stars and galaxies evolved in the early universe.

Conclusions and Future Steps:

In the past year we have made great steps towards achieving our goals at CNF. We have demonstrated our ability to fabricate double-layer ARCs for different wavelengths and metal meshes with different feature sizes. We have used many of the fabrication and metrology tools at CNF. Our next steps are to better characterize our etched geometries and improve our metamaterial ARCs. We will be using Fourier transform spectrometers to measure our samples optical performance and using the results to iterate on our fabrication design.

References:

[1] Cothard, N.F., Choi, S.K., Duell, C.J., et al. The Design of the CCAT-prime Epoch of Reionization Spectrometer Instrument. J Low Temp Phys, https://doi.org/10.1007/s10909-019-02297-1 (2020).

[2] N.F. Cothard, M. Abe, T. Nikola, G.J. Stacey, G. Cortes-Medellin, P.A. Gallardo, B.J. Koopman, M.D. Niemack, S.C. Parshley, E.M. Vavagiakis, K. Vetter, "Optimizing the efficiency of Fabry-Perot interferometers with silicon-substrate mirrors," Advances in Optical and Mechanical Technologies for Telescopes and Instrumentation III (2018).

[3] http://www.ccatobservatory.org/

Fabrication, Characterization, and Application of All-Glass, 1 cm Diameter Metalens Working at Visible Wavelength

CNF Project Number: 2471-16

Principal Investigator(s): Professor Federico Capasso

User(s): Joon-Suh Park

Affiliation(s): John A. Paulson School of Engineering and Applied Sciences, Harvard University

Primary Source(s) of Research Funding: Defense Advanced Research Projects Agency (Grant no. HR00111810001)

Contact: capasso@seas.harvard.edu, parkj@g.harvard.edu

Website: https://www.seas.harvard.edu/capasso

Primary CNF Tools Used: Heidelberg DWL2000, HamaTech mask chrome etch 1, ASML 300C DUV stepper, Gamma automatic coat-develop tool, CHA Mark 50 e-beam evaporator, Trion Minilock III ICP etcher, Plasma-Therm dual chamber 770, Oxford 81, Oxford 82, Oxford 100, P10 profilometer, DISCO dicing saw, Zeiss Ultra SEM

Abstract:

Using deep-ultraviolet (DUV) projection lithography, we demonstrate mass-production of one-centimeter diameter, all-glass metalenses working in the visible wavelength. Characterization of the metalens by comparing its point-spread-function with that of the ideal lens and conventional refractive lenses with similar size and focal lengths are performed.

Summary of Research:

Recent advances in aerial drones and cube satellites have increased the demands for better optics for their on-board imaging systems. One of the approaches for better imaging is increasing the amount of light collected into the system by increasing the diameter of the lens. However, increasing the diameter of the lens meets two important tradeoffs for their application purposes: the increase of aberration and the weight of the lens. Simply increasing the diameter of a refractive lens increases the spherical aberration, which then needs to be corrected by using costly methods such as tailoring the lens surface to an aspheric. Also, the weight of the bulk refractive optics volumetrically scales with diameter, which renders it less advantageous when payload is of a concern.

Metasurfaces, a new category of optical elements that can tailor the optical effects of the outgoing light by placing subwavelength-spaced structures on a two-dimensional surface, can provide alternative solutions for refractive optics [1]. Although many prior metasurface works used high-refractive index materials such as TiO_2, SiN, GaN or amorphous Si to achieve phase control [1,2], here we use low-refractive index material, fused silica (SiO_2), as a base material to design and fabricate a centimeter diameter metasurface functioning as a lens (metalens) working in the visible wavelength.

We fabricate the metalenses on a 4-inch fused silica wafer using DUV (248 nm, KrF) projection lithography. After writing a reticle of the metalens with Heidelberg DWL 2000 mask writer, the pattern on the reticle is exposed onto the chrome (100 nm thick)-coated fused silica substrate spin-coated with DUV-24P ARC and UV210 resist. The patterned resist is then used as an etch mask to transfer the pattern to the chrome layer using chlorine plasma. As chlorine etch chemistry has high selectivity against SiO_2, the substrate works as an etch stop layer. With the patterned chrome as etch mask, we then etch into the SiO_2 substrate using fluorine plasma. The fluorine etch chemistry has high selectivity between chrome and SiO_2, which allows high-aspect ratio etching of SiO_2. The fluorine etching is stopped when the etch depth reaches 2 µm, which is determined by surface profilometry. The residual chrome is then etched away using chlorine plasma, leaving only SiO_2 pillars on the substrate. The schematic of the process is depicted in Figure 1, and the scanning electron microscope imaging result of fabricated SiO_2 pillars is shown in Figure 2.

The fabricated metalens is capable of imaging in the visible wavelength, as shown in Figure 3. We further compare the metalens' point-spread-function along its optic axis at metalens' design wavelength ($\lambda = 633$ nm) with similar off-the-shelf refractive lens counterparts with similar diameter and focal length; an aspheric lens (Edmund Optics, 33-944) and a plano-convex lens (Thorlabs Inc., LA1213-A). As shown in Figure 4, the fabricated metalens show good focusing around its focus compared to that of the refractive optics. The Strehl ratio of the metalens' focal spot is measured to be 0.95, which indicates the fabricated metalens is diffraction-limited. The results are published to Nano Letters [3].

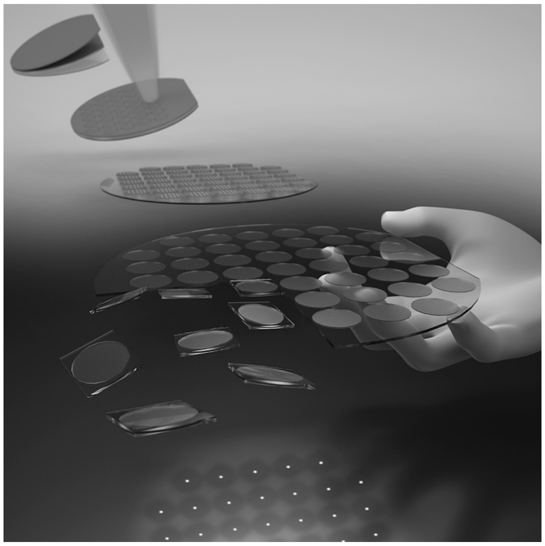

Figure 1: Schematic of fabrication process. A 4-inch diameter fused silica wafer goes through metal evaporation, DUV projection lithography, etching, and dicing to make 45 1-centimeter diameter metalenses per wafer.

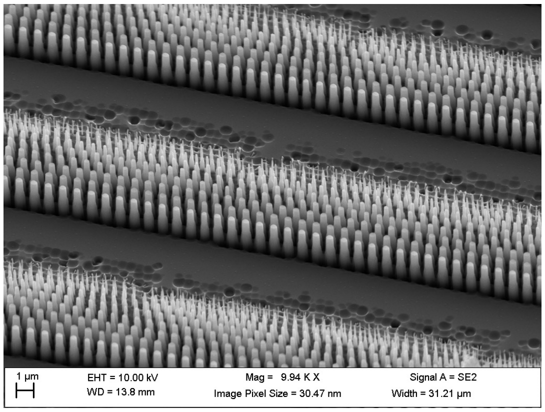

Figure 2: SEM image of silica nanopillars constituting the fabricated metalens.

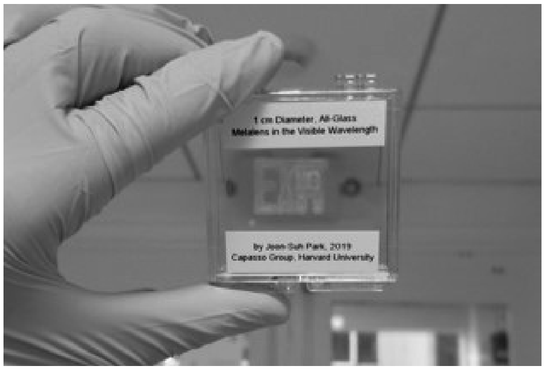

Figure 3: Photograph of a metalens, diced to a 11 mm × 11 mm square from initially fabricated 4-inch wafer, imaging a red-lit emergency exit sign. The image of the "Exit" sign is clearly visible through the metalens.

Conclusions and Future Steps:

We demonstrated a proof-of-concept mass-manufacturing of centimeter-scale metalens working in the visible wavelength and showed that it does not experience spherical aberrations as its refractive counterparts. However, our metalens is chromatic by design: the focal length varies with incident wavelength. We are investigating methods to design and fabricate a larger diameter metalens and an achromatic metalens that is compatible with conventional integrated circuit chip fabrication techniques.

References:

[1] Alan She, Shuyan Zhang, Samuel Shian, David R. Clarke, and Federico Capasso, "Large area metalenses: design, characterization, and mass manufacturing," Opt. Express 26, 1573-1585 (2018).

[2] Mohammadreza Khorasaninejad, Wei Ting Chen, Robert C. Devlin, Jaewon Oh, Alexander Y. Zhu, and Federico Capasso, "Metalenses at visible wavelengths: Diffraction-limited focusing and subwavelength resolution imaging," Science 352, 1190 (2016).

[3] Joon-Suh Park, Shuyan Zhang, Alan She, Wei Ting Chen, Peng Lin, Kerolos M. A. Yousef, Ji-Xin Cheng, and Federico Capasso, "All-Glass, Large Metalens at Visible Wavelength Using Deep-Ultraviolet Projection Lithography," Nano Lett. 19, 12, 8673-8682 (2019).

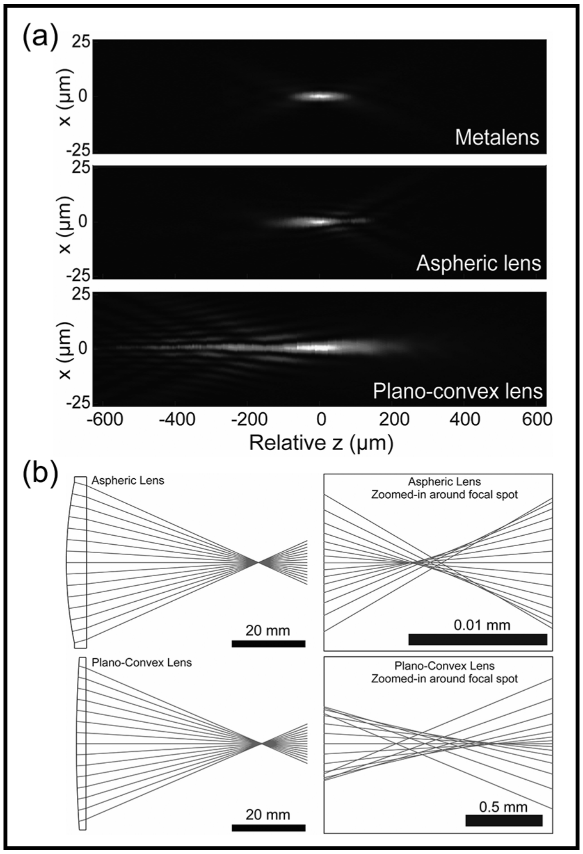

Figure 4: (a) Comparison of point-spread-functions along the optical axis near the focus between a metalens, an aspheric lens (Edmund Optics, 33-944), and a plano-convex lens (Thorlabs Inc., LA1213-A), respectively, with 633 nm wavelength incidence. The refractive lenses are off-the-shelf commercial glass lenses with similar diameter and focal length with those of the metalens. (b) Ray-tracing diagram of refractive lenses derived from data provided by manufacturers.

Tunable Semiconductor Metasurfaces for Active Lensing

CNF Project Number: 2472-16

Principal Investigator(s): Gennady Shvets

User(s): Melissa Bosch, Steven He Huang, Maxim Radikovich Shcherbakov

Affiliation(s): School of Applied and Engineering Physics, Department of Physics; Cornell University

Primary Source(s) of Research Funding: Office of Naval Research (ONR) and National Science Foundation (NSF)

Contact: gs656@cornell.edu, mb2583@cornell.edu, hh623@cornell.edu, mrs356@cornell.edu

Website: http://shvets.aep.cornell.edu

Primary CNF Tools Used: JEOL 9500, Zeiss Ultra SEM, Oxford Cobra ICP etcher, Oxford PECVD

Abstract:

Optically thin metamaterials, or metasurfaces, provide strong modulations to spatial and spectral properties of light. We engineer metasurfaces based on high index low-loss semiconductors, which exhibit narrowband and/or tunable optical resonances for near-infrared photonic applications. We report on the design, fabrication, and characterization of resonant silicon metasurfaces and thermally-tunable germanium metasurfaces to demonstrate active lensing. By virtue of their scalability and compactness, semiconductor metasurfaces present a promising alternative to traditional optical elements.

Summary of Research:

Silicon Metasurfaces. Semiconductor resonators, such as germanium and silicon, are attractive candidates for efficient metadevices owing to their high refractive index, infrared transparency, and support of strong localized Mie-type resonance modes [1,2].

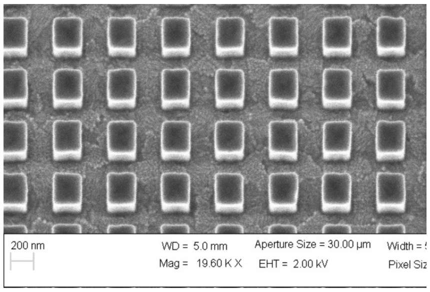

Figure 1: SEM of a typical α-Si-based near-IR resonant metasurface on a SiO_2/ITO substrate.

Our project focuses on the design and fabrication of resonant amorphous silicon (α-Si) meta-surfaces with sub-50 nm feature sizes, suitable for various applications where compact and efficient light modulation is needed. An example of a typical α-Si metasurface under study is shown in Figure 1, consisting of an array of rectangular α-Si patches on a fused silica substrate, with the gap between adjacent resonators governing the *Q*-factor of the optical resonance.

In one application, we employ α-Si metasurfaces towards the design and fabrication of a metalens with tunable focus. Metalenses with tunable functionalities are critical to the miniaturization of vision and imaging technologies such as spatial light modulators and adaptive optics; however, most metalenses have static functionalities preset by their geometries. By selecting three constituent resonator geometries that impart phase shifts in increments of $2\pi/3$, the spatial phase profile for a converging metalens is achieved. To enable tunability, the meta-atoms are designed to have a locally-adjustable optical phase response dependent on the permittivity of the surrounding media, and the lens is encapsulated in a liquid crystal (LC) cell, which offers an absolute shift up to 0.7 in the in-plane permittivity upon application of an external electric field.

For metasurface fabrication, amorphous silicon (α-Si) films are deposited onto ITO-covered fused silica substrates using plasma-enhanced chemical vapor deposition (Oxford PECVD), and film surface is treated with SurPass 3000 adhesion promoter. HSQ 6% was spun and baked to form a 100 nm thick layer over the α-Si, coated with DisCharge anti-charging layer, e-beam exposed at a dose of 250 µC/cm^2 (JEOL 9500FS), and developed in MIF 300 solution for 120 s. The pattern was transferred to the α-Si layer using reactive ion etch (Oxford Cobra). The resulting samples were characterized with a scanning electron microscope (Zeiss Ultra). The project is currently in the LC encapsulation stage. Our simulations predict a focal spot position shift from +8 mm to -8 mm in response to the maximum permittivity modulation of the LC, as shown in Figure 2.

Germanium Metasurfaces. Next, we utilize the large thermo-optic coefficient of germanium (Ge) [3] to demonstrate a resonant Ge-based metalens, which can be controlled by heat. The metalens building blocks are high aspect-ratio anisotropic double-pillar Ge meta-

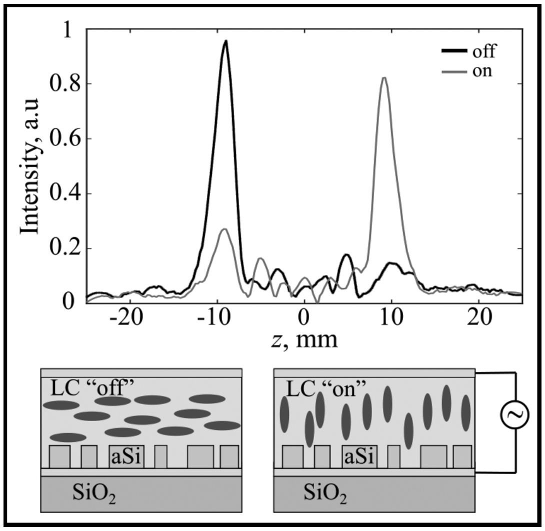

Figure 2: Top, simulated intensity of light transmitted through the α-Si metalens, plotted along the optical axis of the lens. The lens acts as a converging lens with +8 mm focus in the absence of an external electric field (black line) and acts as a diverging lens with a -8 mm focus in the presence of an external electric field (light gray line). Bottom, schematic of an α-Si metalens design.

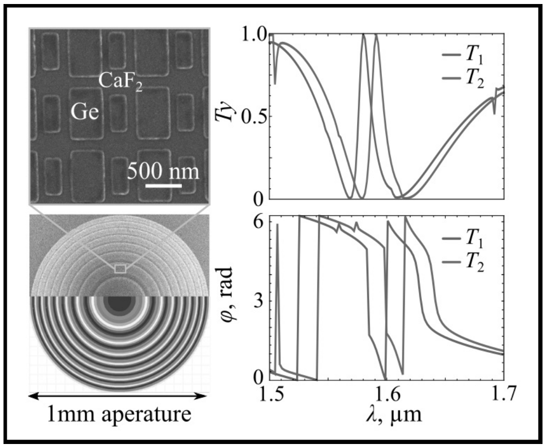

Figure 3: Top Left, zoomed-in SEM of one of the fabricated metalens phase steps. Bottom Left, an SEM of the fabricated 8-step spherical metalens. The lower half of the lens is color-coded according to its eight phase steps. Right, simulated temperature-dependent transmission and phase spectra for one of the meta-atom geometries (zone 8).

atoms, as shown in Figure 3. Such structures support high quality-factor resonances which can be excited by one of the principal linear polarizations of an incident light and whose spectral positions can be widely tuned by heating the metasurface [4]. The meta-atom geometries are selected to impart the required hyperbolic phase profile for a spherical lens, while simultaneously optimized to exhibit high efficiency contrast with thermal tuning. The selection therefore enables control over the intensity of the focused light. Representative transmission and phase spectra of the meta-atoms are presented in Figure 2. We verify the tunable metalens concept experimentally by fabricating and characterizing a Ge metasurface patterned on a quartz substrate. The device fabrication consisted of seven steps: e-beam evaporation of 630 nm of Ge (CVC SC4500); standard PMMA spin-coat, baking, and e-beam exposure at 1000 μC/cm^2 (JEOL 9500FS); development in MIBK:IPA 1:3; e-beam evaporation of a 30 nm chrome (Cr) mask; liftoff in room-temperature sonicated acetone for 20 min; pattern transfer to the Ge layer through HBr reactive ion etching (Oxford Cobra); and removal of residual Cr mask with argon ion milling (AJA Ion Mill).

Figure 3 presents an SEM image of one of the meta-atom geometries of fabricated metalens. The experimental focal spot tuning is shown in Figure 4; by increasing the temperature of the fabricated metasurface, a continuous intensity modulation of the focal spot of the metalens is demonstrated, with up to 55% intensity modulation achieved by increasing the temperature from 25-125°C.

References:

[1] Soref, Richard. "Mid-infrared photonics in silicon and germanium." Nature photonics 4.8 (2010): 495.

[2] Frey, Bradley J., Douglas B. Leviton, and Timothy J. Madison. "Temperature-dependent refractive index of silicon and germanium." Optomechanical technologies for Astronomy. Vol. 6273. International Society for Optics and Photonics, 2006.

[3] Bosch, M., Shcherbakov, M. R., Fan, Z., and Shvets, G. (2019). Polarization states synthesizer based on a thermo-optic dielectric metasurface. Journal of Applied Physics, 126(7), 073102.

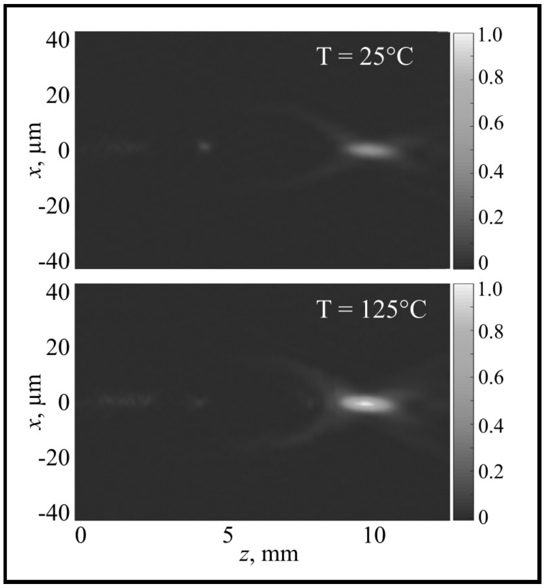

Figure 4: Experimental temperature-dependent focal spot profiles of the metalens. Top, focusing profile of the metalens at a temperature of 25°C. Bottom, focusing profile of the metalens at a temperature of 125°C.

Si-on-Sapphire Metasurfaces for High Harmonic Generation and Laser Machining

CNF Project Number: 2472-16

Principal Investigator(s): Gennady Shvets

User(s): Giovanni Sartorello, Maxim Radikovich Shcherbakov

Affiliation(s): Department of Applied and Engineering Physics, Cornell University.

Primary Source(s) of Research Funding: Office of Naval Research (ONR) Grant No. N00014-17-1-2161, Air Force Office of Scientific Research (FA-9550-16-1-0069 and FA9550-16-1-0013), CCMR NSF MRSEC program (DMR-1719875)

Contact: gs656@cornell.edu, gs664@cornell.edu, mrs356@cornell.edu

Website: shvets.aep.cornell.edu

Primary CNF Tools Used: JEOL 9500, Oxford Cobra ICP, SC-4500, wet benches

Abstract:

We used a silicon-on-sapphire (SOS) platform to fabricate several metasurfaces for nonlinear optical experiments in the mid-infrared (MIR). One series of experiments aims to use the metasurfaces for high-efficiency third harmonic generation (THG) and the generation of higher-order harmonics (HHG). Another one aims to use high laser irradiance and the localized hotspots that form within nanostructures to perform nanoscale machining by accurately controlling laser-induced damage. All samples were fabricated by electron-beam lithography (EBL) performed with the JEOL 9500, e-beam deposition of a chromium mask in one of the SC-4500 evaporators, and HBr etching in the Oxford Cobra ICP etcher.

Summary of Research:

We work in nonlinear optics with sources in the MIR, and our aim is the efficient generation of optical harmonics — light with a multiple of the original MIR frequency [1]. Harmonics generation in solid-state materials is commonly used in laser systems, and has promising applications both in the sciences (such as for solid-state attosecond lasers) and in everyday life (for example in telecommunications) [2].

Nonlinear metasurfaces, planar arrays of thin subwavelength structures, have emerged as a platform for nonlinear generation and nonlinear light control [3,4]. Their parameters, such as geometric properties, refractive index and local phase profile can be adjusted to perform, in a compact form factor, functions that ordinarily require bulky materials or gases [5].

Our metasurfaces are based on dielectric resonators, rectangular silicon structures of dimensions w_x, w_y, w_z arranged in a lattice of period p_x, p_y. Adjusting these dimensions controls the resonance spectral position as well as its width, both of which must match experimental requirements. At resonance, greatly increased coupling of the fundamental light to the metasurfaces increases the amount of energy available for nonlinear processes, resulting in much increased nonlinear generation. It also changes the energy distribution of the electrons in the material, potentially with a time dependence, which, if correctly exploited, can further enhance the emission of harmonics. The result is, potentially, not only highly efficient HG in a compact, ultrathin system, but also the emission of higher-order harmonics that are normally obtained in gases. Usually, suitable periods are a little less than the wavelength, x/y dimensions are smaller than that, and the thickness of the structures is even smaller. Deeply subwavelength thicknesses relax phase matching conditions for the generation of harmonics and prevent the harmonics themselves from being excessively reabsorbed.

We fabricate our samples starting from commercially available silicon-on-sapphire substrates. Our structures are arranged in square or rectangular arrays a few hundred µm to 1 mm to the side. We fabricate several such arrays in a grid on each sample, each with a slightly differing pattern or rescaled by a certain amount, to give a distribution of resonance wavelengths, allowing us to compare resonant and nonresonant behavior and account for slight deviations during fabrication.

Each substrate, etched down to the correct thickness in the Oxford Cobra ICP etcher with HBr, was coated in PMMA 495 A4 on a spinner, baked on the hot plates, and exposed in the JEOL 9500 EBL machine. The pattern was developed with 1:3 MIBK:IPA and a subsequent IPA wash. A Cr mask 40-50 nm thick was then deposited with one of the SC-4500 evaporators. Lift-off followed with sonication in acetone, leaving a patterned Cr mask on the bare Si. Etching around the mask down to the sapphire was again done with the Oxford Cobra. The mask was finally removed with chromium etchant in a wet bench.

This year, we fabricated several series of samples, which have been used to study THG with chirp-dependent

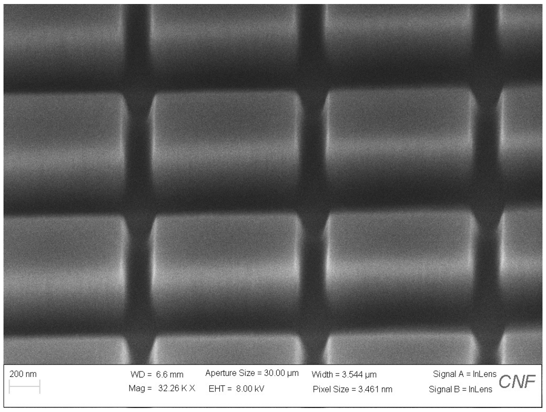

Figure 1: SEM detail of a Si nonlinear metasurface, a 1.16 × 1.16 μm^2 array of 0.99 × 0.75 × 0.3 μm^3 structures.

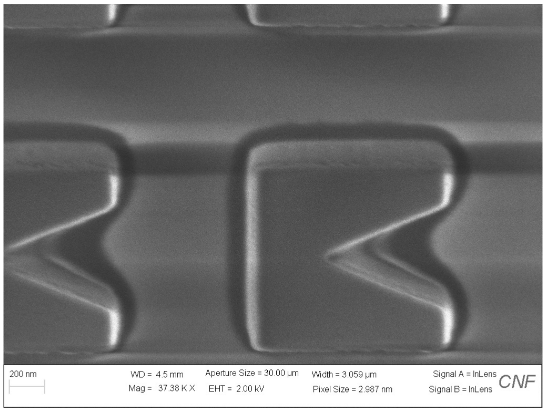

Figure 2: SEM detail of a Si laser machining metasurface, a 1.94 × 1.95 μm^2 array of 1.08 × 1.15 × 0.3 μm^3 structures. The notch is 0.72 μm deep.

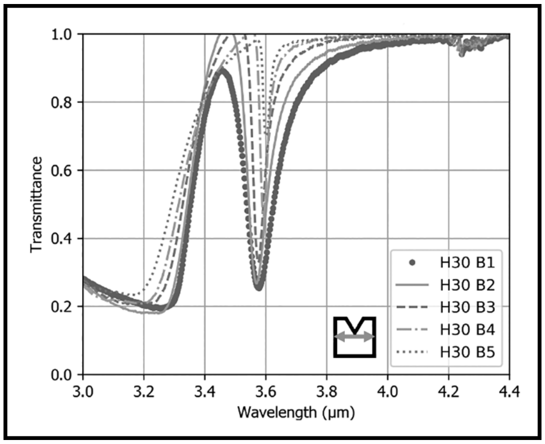

Figure 3: Transmittance FTIR spectra of the laser machining metasurface. The array detail in Figure 3 is "B1" in the legend. Inset: polarization of the incident wave.

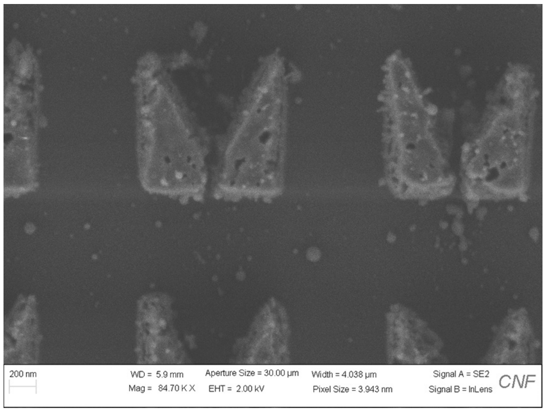

Figure 4: Early example of laser machining shown on a previously fabricated sample. Image credit: Melissa Bosch.

behavior induced by tuning the chirp of the incident pulses as well as HHG experiments. An example of a metasurface for HG is shown in Figure 1.

All HG metasurfaces are simple rectangular resonators, because there is no particular need for a more complex shape for the purposes of the project. The resonator shape, however, can be used to increase field concentration in a particular spot of the resonator. Sharp features or restriction points create hot spots, which are used extensively in nanoscale resonators. The high field concentration may cause damage, usually an unwanted problem, which we want to exploit to machine coupled resonators separated by very small gaps.

We fabricated square resonators with notches (Figure 2), then used laser pulses to cause the structures to break at the notch position, where field concentration is the highest. The resonant behavior of these structures pre-machining, which exemplifies that of all samples in this report, is shown in Figure 3.

The intended outcome is shown in a preliminary result, separately obtained on an older sample, in Figure 4.

Conclusions and Outlook:

We have successfully used a SOS platform to fabricate a number of Si resonator meta-surfaces, which we have used for a variety of nonlinear experiments in the MIR. We will continue to develop the platform to reach higher harmonic orders and greater efficiency. We have also developed a promising platform for nanoscale laser machining, whose behavior we will study and improve as necessary to achieve small, well defined and controlled features.

References:

[1] Boyd, R. W., "Nonlinear Optics", Academic Press, 2008.

[2] Garmire, E., "Nonlinear optics in daily life", Opt. Express, 21(25), 30532, 2003.

[3] G. Li, S. Zhang, and T. Zentgraf, "Nonlinear photonic metasurfaces," Nat. Rev. Mater., vol. 2, no. 5, p. 17010, 2017.

[4] A. Krasnok, M. Tymchenko, and A. Al "Nonlinear metasurfaces: a paradigm shift in nonlinear optics," Mater. Today, vol. 21, no. 1, pp. 8-21, Jan. 2018.

[5] M. R. Shcherbakov, K. Werner, Z. Fan, N. Talisa, E. Chowdhury, and G. Shvets, "Photon acceleration and tunable broadband harmonics generation in nonlinear time-dependent metasurfaces," Nat. Commun., vol. 10, no. 1, p. 1345, 2019.

Silicon Metasurfaces for Magneto-Optics

CNF Project Number: 2472-16

Principal Investigator(s): Gennady Shvets

User(s): Daniil Shilkin, Maxim Radikovich Shcherbakov, Melissa Bosch

Affiliation(s): School of Applied and Engineering Physics, Department of Physics; Cornell University

Primary Source(s) of Research Funding: Office of Naval Research (ONR), Air Force Office of Scientific Research, and National Science Foundation (NSF)

Contact: gs656@cornell.edu, ds2232@cornell.edu, mrs356@cornell.edu, mb2583@cornell.edu, shilkin.daniil@physics.msu.ru

Website: http://shvets.aep.cornell.edu

Primary CNF Tools Used: JEOL 9500, Zeiss Ultra SEM, Oxford Cobra ICP Etcher, Oxford PECVD, SC4500 Evaporator, CHA Evaporator

Abstract:

E-beam lithography is applied to fabricate arrays of optically resonant silicon disks followed by covering them with a nickel film to be used in magneto-optical measurements.

Summary of Research:

Electron-beam lithography is often applied to produce semiconductor optical metasurfaces with a typical feature size of 100 nm or below [1,2]. Below are the results of applying this technique to fabricate dense arrays of optically resonant amorphous silicon (α-Si) disks on a glass substrate followed by covering the structure with a thin nickel film to be used in magneto-optical measurements [3]. The pattern presented three 0.5 × 0.5 mm^2 arrays with a constant period of 400 nm and the varied diameter of the disks (Figure 1). The desired height of the disks was 135 nm, and the desired nickel thickness was 5 nm. The resist was hydrogen silsesquioxane (HSQ). Fused silica glasses with a thickness of 0.5 mm were used as substrates.

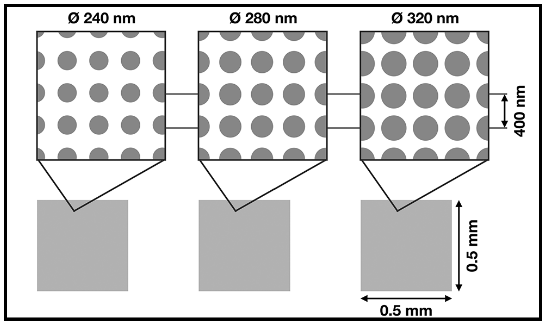

Figure 1: Scheme of the pattern.

The substrates were covered by α-Si using the Oxford plasma enhanced chemical vapor deposition (PECVD) system. The parameters were fixed at the following values: temperature 200°C, microwave power 10 W, pressure 1 Torr, SiH_4/Ar 25/475 sccm. The deposition rate, measured close to the substrate center, was found to depend on the substrate dimensions and varied from 10.6 nm/min (for 1-inch circles) to 11.6 nm/min (for 10 × 10 mm^2 squares). For the desired samples, 135 nm thick films were fabricated. The film thicknesses were measured by FilMetrics F50-EXR using the dispersion data obtained by the Woollam spectroscopic ellipsometer.

The fabricated α-Si films were covered with the resist layer by spin coating. The standard procedure resulted in a non-uniform deposition of the film: the profile of the vacuum holder appeared on the resist layer. This was overcome by placing an aluminum disk on the chuck and fixing the substrates with a Kapton® tape.

The e-beam exposure was performed using JEOL 9500. The files were prepared by standard methods including the proximity effect correction. In every session, the pattern was exposed with a number of different base doses. The other varied parameters included the beam current and the shot spacing, the resist thickness, the baking temperature and time, the choice of the charge dissipative layer, the choice of the developer, and the developing time. These parameters are discussed below.

After the pattern development, samples were etched using Oxford Cobra HBr etcher with the parameters fixed at the following values: HBr/Ar 20/7 sccm, RIE/ICP 30/1500 W, pressure 11 mTorr. The etching rate of 178 ± 2 nm/min was measured using 400-nm-thick films by etching for different times.

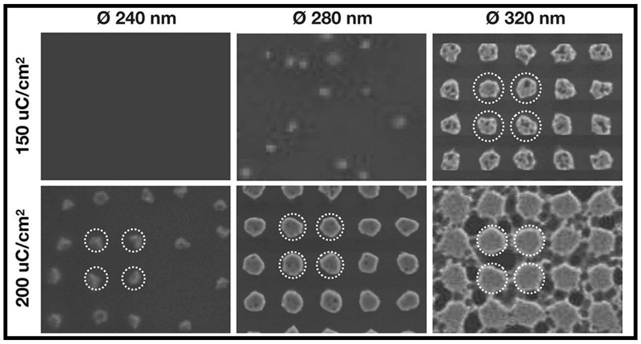

Figure 2: SEM of one the first fabricated samples. Circles indicate the diameter set in the pattern.

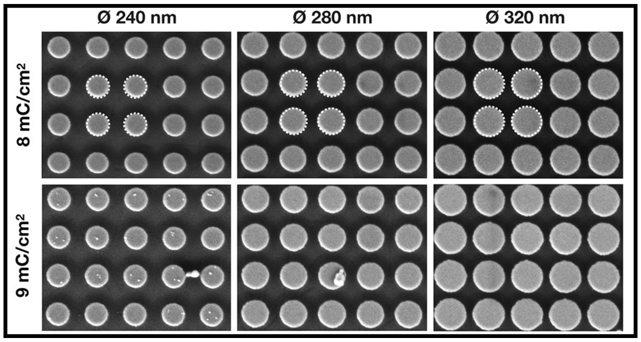

Figure 3: SEM of the last fabricated sample. Circles indicate the diameter set in the pattern.

For samples with the silicon thickness of 135 nm, the etching time of 50 s provided full etching outside of the mask with no cut-off. The presence of the resist residue on top of the disks was not desired, but not critical for our purpose.

The resulting structures were covered by a 5 nm nickel film using the SC4500 odd-hour evaporator. The thermal source was used with the deposition rate set to 0.5-1.0 Å/s.

Figure 2 shows scanning electron microscope (SEM) images of one of the first samples that was fabricated as follows. The 6% HSQ solution was spin coated at 3000 rpm for 60 s with the lid opened. The resist was baked at 170°C for 2 min and covered with DisCharge by spin coating at 3000 rpm for 60 s. The beam current was 1 nA; the shot spacing was 6.5 nm. The pattern was developed in 300 MIF for 2 min, rinsed in water and blow dried. The SEM images were obtained after plasma etching for 43 s and spin coating DisCharge. The fabricated disks appeared to exhibit irregular shapes with either dimensions reduced (at low doses) or disks merged (at higher doses). The optimal dose was found to depend on the diameter of the disks.

These issues were solved as follows. First, the shapes were found to be smoother when a gold film is used instead of the DisCharge. The gold was deposited after the resist baking using CHA thermal evaporator with the deposition rate set to 1.0 Å/s. Second, the use of the 'salty' developer instead of MIF 300 significantly increased the contrast of the resulted pattern. Finally, using a thinner (30 nm) resist provided the best correspondence between the set and the obtained disk diameters.

Figure 3 shows SEM images of the last sample that was fabricated as follows. The 2% HSQ solution was spin coated at 4000 rpm for 60 s with the lid closed. The resist was baked at 115°C for 70 s and covered with a 13 nm gold film. The beam current was 20 nA; the shot spacing was 5 nm. Directly after the exposure, the gold was removed by wet etching for 30 s in gold etch, the sample was rinsed in water and put into 'salty' developer for 1 min, then rinsed in water, rinsed in isopropyl alcohol (IPA), and blow dried by nitrogen. The SEM images were obtained after plasma etching for 50 s and nickel film deposition. The fabricated disks have a smooth circular shape with the dimensions very close to the set values at a single optimal dose for all of the diameters (the size variations are less than SEM accuracy).

The established metasurface fabrication approach is scalable; thereby promising versatile platforms for ultrathin optical devices poised to find use in free-space and integrated photonics.

Acknowledgements:

This work was supported by the Office of Naval Research (ONR) under Grant No. N00014-17.1-2161, by the Air Force Office of Scientific Research (FA-9550-16-1-0069 and FA9550-16-1.0013), and by the Cornell Center for Materials Research with funding from the NSF MRSEC program (DMR-1719875).

References:

[1] Z. Dong, et al. Nano Letters 17(12), p.7620-7628 (2017).
[2] A. Martins, et al. Optics Express 26(8), p.9573-9583 (2018).
[3] M.G. Barsukova, et al. ACS Photonics 4(10), p.2390-2395 (2017).

On-Chip Monolayer WSe_2 Microring Laser Operating at Room Temperature

CNF Project Number: 2524-17
Principal Investigator(s): Jaime Cardenas
User(s): Marissa Granados-Baez

Affiliation(s): The Institute of Optics, University of Rochester, Rochester, NY, 14627
Primary Source(s) of Research Funding: University of Rochester
Contact: jaime.cardenas@rochester.edu, mgranad2@ur.rochester.edu
Website: https://www.hajim.rochester.edu/optics/cardenas/
Primary CNF Tools Used: JEOL 9500, Logitech Orbis CMP, SÜSS MA6-BA6 contact aligner, Oxford 100 & 81 etchers

Abstract:

We demonstrate lasing at room temperature of monolayer WSe_2 integrated with a silicon nitride ring resonator. Signatures of lasing are shown by a 'kink' in the L-L plot and a linewidth narrowing of 30% when reaching threshold.

Summary of Research:

Monolayers of transition-metal dichalcogenides (TMDCs) are excellent materials to produce nanolasers since they are direct bandgap emitters and lack the need of lattice matching making them easy to integrate with planar devices. However, previously demonstrated TMDC nanolasers emit perpendicularly to the plane of their cavity into free space [1-4] and are thus challenging to integrate on chip. Integrated nanolasers are one of the key devices for fully integrated optical circuits, which require sources, modulators, and detectors interconnected with waveguides and electronics in a single chip. Modulation, detection and propagation of light have been demonstrated using TMDCs and other 2D materials. The waveguide coupled 2D material laser demonstrated here will ultimately enable photonic devices with sources, detectors, modulators, and sensors integrated in multiple photonic layers that can be monolithically integrated with electronics.

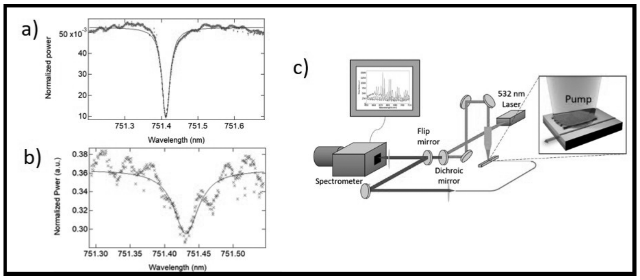

Figure 1: a) Ring resonace at 751.41nm with Q = 350,000-200,000. b) Ring resonance after monolayer transfer with Q = 95,000. c) Experimental setup to pump from the top and collect the chip's output from the side.

We demonstrate lasing from a monolayer tungsten diselenide (WSe_2) monolithically integrated with a high Q, chipscale silicon nitride microring resonator. This integration enables efficient light emission coupled to an on-chip waveguide. The device consists of a silicon nitride microring resonator with a radius of 13 µm coupled to a Mach-Zehnder Interferometer (MZI). We use the MZI to decrease the number of resonant modes since the gain threshold for lasing increases proportionally with the number of resonant modes of the cavity. Depending on the length of the MZI arms, resonances of the ring can be suppressed.

Our device is designed to suppress every other resonance of the ring, increasing its Free Spectral Range (FSR) by a factor of two. The width and thickness of the waveguide are 0.5 µm and 0.3 µm, respectively. The ring and bus waveguide are separated by a gap of 0.35 µm. Mechanically exfoliated WSe_2 is transferred using a PDMS-based all dry transfer technique [5] and placed on top of the microring resonator. Before the monolayer is transferred, the microring has an intrinsic *Q* of 350,000 (Figure 1a). After the monolayer transfer the intrinsic quality factor of the ring is 95,000 (Figure 1b) showing a strong interaction of the ring with the monolayer.

We fabricate the silicon nitride microring resonator by depositing 300 nm of silicon nitride via low-pressure chemical vapor deposition (LPCVD) on 4 µm of oxide thermally grown on a silicon wafer. The ring and bus waveguide are patterned with electron-beam lithography. A fill pattern that serves as a chemical mechanical polishing (CMP) stop layer is written with contact lithography. The nitride is etched in an inductively coupled plasma reactive ion etcher (ICP-RIE) using a CHF_3/O_2 chemistry. The device is clad with 1 µm of silicon dioxide via plasma enhanced chemical vapor deposition (PECVD). We polish the upper cladding down to a thickness of 0 to 20 nm using CMP to increase the interaction between the optical field in the resonator and the WSe_2 monolayer. The smooth surface after the CMP step also improves the adhesion of the WSe_2 flake.

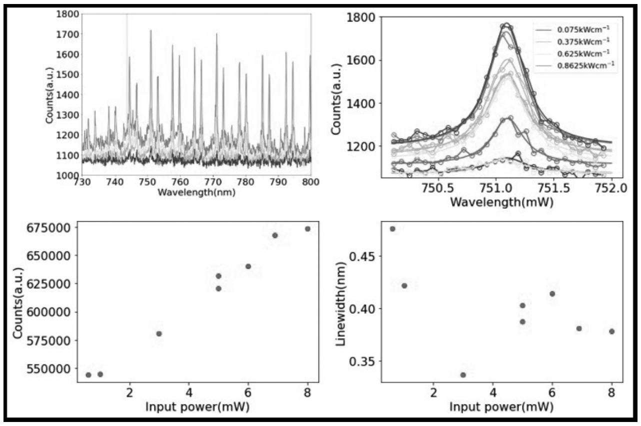

Figure 2: a) Spectrum for increasing input power. b) Lorentzian function fitting for a peak at 751.05 nm at different input powers. c) L-L plot showing a 'kink' between 1 mW and 3 mW of input power. d) Linewidth vs input power plot showing linewidth narrowing between 1 mW and 3 mW of input power.

We demonstrate optically pumped lasing emitted at a central wavelength of 751.05 nm by a monolayer of WSe_2. We focus the pump laser (CW Ti:Sapphire at 701 nm) emission that is coupled from the ring to the bus waveguide with a lensed optical fiber at the output of the chip. The collected emission is measured with a spectrophotometer (Figure 1c). The collected spectra (Figure 2a) show the expected WSe_2 broad PL spectrum centered at ~ 749 nm with peaks that match the ring resonances. All the measurements were done at a room temperature of 22°C.

The laser emission is identified by the behavior of the 'light-light' or L-L curve and the linewidth narrowing of particular peaks. We fitted a Lorentzian line shape to the individual peaks (Figure 2b) to obtain the FWHM values and output intensity values. The plot of the output light intensity (defined as the integrated area under the peak) vs. the input power in Figure 2c shows a 'kink' between 1 mW and 3 mW. For the same range of input power, the input vs. linewidth plot in Figure 2d shows progressive narrowing from 0.48 nm to 0.38 nm. The linewidth narrows by 30%. Linewidth narrowing indicates a laser like behavior of the emission coupled to the ring and later to the bus waveguide.

Conclusions and Future Steps:

In conclusion, our device demonstrated the possibility to integrate the photoluminescence of monolayer TMDCs and produce integrated laser emission at room temperature enabling a lasing platform that is scalable to arrays of on-chip lasers. Since integrated modulation and detection can also be achieved with 2D materials, our integrated laser opens the possibility to a fully integrated and complete optical circuit using the properties of 2D materials.

References:

[1] Wu, S., et al. Monolayer semiconductor nanocavity lasers with ultralow thresholds. Nature 520, 69-72 (2015).

[2] Ye, Y., et al. Monolayer excitonic laser. Nature Photon.9, 733-737 (2015).

[3] Li, Yongzhuo; Zhang, Jianxing; Huang, Dandan; Sun, Hao; Fan, Fan; Feng, Jiabin; Wang, Zhen; Ning, C. Z. Nature Nanotechnology 12,987-992 (2017).

[4] Javerzac-Galy, J., Kumar, A., Schilling, R.D., Piro, N., Barbone, M., Goykman, I., Khurgin, J.B., Ferrari, A.C., and Kippenberg, T. J., "Excitonic emission of monolayer semiconductors near-field coupled to high-*Q* microresonators," arXiv preprint arXiv:1710.04294 (2017).

[5] C.Chakraborty; K.M. Goodfellow; S.Dhara; A.Yoshimura; V.Meunier; A.N.Vamivakas Nano Lett. 2017, 17, 2253-2258 (2017).

Single-Shot, Multiple I/O Photonic Chip to Fiber Array Packaging Using Fusion Splicing

CNF Project Number: 2524-17

Principal Investigator(s): Jaime Cardenas[2]

User(s): Juniyali Nauriyal[1], Meiting Song[2], Jaime Cardenas[2]

Affiliation(s): 1. Department of Electrical and Computer Engineering, University of Rochester, Rochester, N.Y. 14627, USA; 2. The Institute of Optics, University of Rochester, Rochester, N.Y. 14627, USA

Primary Source(s) of Research Funding: Technology Development Fund, University of Rochester

Contact: jaime.cardenas@rochester.edu, jnauriya@ur.rochester.edu

Primary CNF Tools Used: GSI, furnace, ASML stepper 3000, Oxford 82, Oxford 100, Gamma

Abstract:

We show a novel multiple I/O photonic packaging method for 4-fiber array using fusion splicing. We demonstrate a minimum loss of 2.5 dB per facet with a variation of +/-0.1 dB through a 4-fiber array.

Summary of Research:

With increase in parallelism and switching in data communication and increasing integration between electronics and optics, highly efficient communication links are needed. However, packaging of integrated devices with multiple I/O ports in a single run remains a challenge. To keep up with the highly data driven communication systems, a low-cost and low-loss packaging technique for photonic integrated circuits with multiple port devices like switches, interferometers and modulators [1,2]. Current packaging methods for multiple I/O photonic chip utilize packaging of a single fiber individually. This process is inefficient while packaging many output ports, however, as the parallelism between electronics with optics increases, multiple I/O ports will be required for switching. In a silicon photonics foundry, packaging each fiber individually consumes equipment time and increases packaging cost of a single chip. We introduce a packaging technique for packaging multiple fibers (2,4) at once using a CO_2 laser to splice the fiber-array to the photonic integrated circuit.

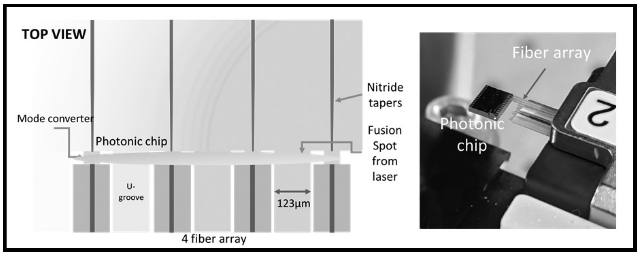

Figure 1: Left; Schematic representation of the top view of the method shows the fusion splicing spot from the CO_2 laser and the u-grooves for aligning fiber arrays. Right; A photograph of a packaged photonic device to a fiber array on a holder.

Multiple packaging methods use special fixtures, fabrication steps and tools for aligning fiber arrays to a photonic chip, however, these methods use optical adhesive for packaging the devices which shrinks during curing and leads to misalignment losses. Most techniques also use special fixtures like v-grooves, specialized connectors or polymer lids/waveguides with optical adhesive for packaging photonic devices with multiple I/Os [3-5]. The v-grooves are used for passive alignment of the fiber to the chip, however, packaging of the fiber array is still done using optical adhesives. Optical adhesives shrink during curing and since alignment tolerances are tight, it becomes challenging to achieve low losses with high scalability. Fabrication of v-grooves requires very precise etch rates and increases fabrication steps.

We demonstrate a novel photonic packaging method for permanent optical edge coupling between a fiber-array and a photonic chip using fusion splicing which is low-loss, low-cost, robust, and scalable to high volume manufacturing without using an optical adhesive. We fabricate u-grooves on the chip for placement of fiber arrays with a pitch of 250 µm as shown in Figure 1. These u-grooves help in the placement of the fiber, which is coupled to the oxide mode converter [6]. The oxide mode converter matches the modes between a SMF-28 optical fiber (mode size of 10.4 µm) to a waveguide (mode size < 1 µm). We engineer the geometry of the two sides of the oxide mode converter to maximize the coupling from the waveguide nanotaper to the cleaved optical fiber.

We fabricate silicon nitride waveguide devices using standard CMOS compatible, microfabrication techniques. A 5 µm thick layer silicon dioxide is deposited via a plasma-enhanced chemical vapor deposition (PECVD) on the silicon wafer and 309 nm of silicon nitride are deposited via low pressure chemical vapor deposition. The waveguides are patterned with standard DUV optical lithography at 248 nm and etched using a fluorine chemistry in an inductively coupled plasma reactive ion etcher. We clad the devices with 5 µm of silicon dioxide using plasma enhanced chemical vapor deposition. We then pattern the chip structure with u-grooves and deep-etch the silicon to a depth of about 100-120 µm. After dicing, we remove the silicon substrate underneath the oxide mode converter to optically isolate it.

We fusion splice an entire fiber-array of four fibers to the mode-converter using a CO_2 laser in a single shot to achieve high manufacturing scalability. We use a cylindrical lens to focus the beam of the CO_2 laser in one dimension to a width ~ 3 mm. As the beam is focused into a line, it is aligned at the fiber to mode converter interface and then radiated with CO_2 laser for 1 sec at ~ 10W of laser power. The width (3 mm) is selected to enable fusing a 12-fiber array in a single shot for future applications. Fusing multiple fibers at once significantly decreases the time and the cost involved in packaging a single chip. Fusing the fiber array and the chip together using radiative heating leaves no residue behind and forms a permanent bond, not requiring extra fixtures or adhesives for durability.

We fuse cleaved 1, 2 and 4-fiber arrays to the oxide mode converter using a single shot from the CO_2 laser and measure a coupling loss of 1.2 dB, 2.2 dB and 2.5 dB per-facet respectively. A waveguide propagation loss of 0.4 dB was subtracted from the measured loss. We expect to see a decrease in the coupling loss after the application of an optical adhesive [7]. We measure variation of ± 0.1 dB through a 4-fiber array at 1550 nm and ± 0.05 dB through a 2-fiber array at 1550 nm as shown in Table 1.

Photonic packaging has the potential to achieve manufacturing scalability at industry level using single shot fusion splicing using a CO_2 laser, which is cost and time efficient. We envision that this method can be fully automated using passive alignment techniques to enable efficient, fast and low-cost fiber array to chip packaging in high volume applications. To provide more mechanical stability, the fiber array can be fused to the chip at multiple spots eliminating the need for optical adhesives.

References:

[1] L. Schares, B. G. Lee, F. Checconi, R. Budd, A. Rylyakov, N. Dupuis, F. Petrini, C. L. Schow, P. Fuentes, O. Mattes, and C. Minkenberg, "A Throughput-Optimized Optical Network for Data-Intensive Computing," IEEE Micro 34, 52-63 (2014).

[2] X. Wang, W. Jiang, L. Wang, H. Bi, and R. T. Chen, "Fully Embedded Board-Level Optical Interconnects from Waveguide Fabrication to Device Integration," J. Lightwave Technol. 26, 243-250 (2008).

[3] T. Barwicz, N. Boyer, S. Harel, T. W. Lichoulas, E. L. Kimbrell, A. Janta-Polczynski, S. Kamlapurkar, S. Engelmann, Y. A. Vlasov, and P. Fortier, "Automated, self-aligned assembly of 12 fibers per nanophotonic chip with standard microelectronics assembly tooling," in 2015 IEEE 65th Electronic Components and Technology Conference (ECTC) (2015), pp. 775-782.

[4] M. Papes, P. Cheben, D. Benedikovic, J. H. Schmid, J. Pond, R. Halir, A. Ortega-Moñux, G. Wangüemert-Pérez, W. N. Ye, D.-X. Xu, S. Janz, M. Dado, and V. Va.inek, "Fiber-chip edge coupler with large mode size for silicon photonic wire waveguides," Opt. Express, OE 24, 5026-5038 (2016).

[5] R. Hauffe, U. Siebel, K. Petermann, R. Moosburger, J.-R. Kropp, and F. Arndt, "Methods for passive fiber chip coupling of integrated optical devices," in 2000 Proceedings. 50th Electronic Components and Technology Conference (Cat. No.00CH37070) (2000), pp. 238-243.

[6] J. Nauriyal, M. Song, R. Yu, and J. Cardenas, "Fiber-to-chip fusion splicing for low-loss photonic packaging," Optica, OPTICA 6, 549-552 (2019).

[7] W. N. Ye and Y. Xiong, "Review of silicon photonics: history and recent advances," Journal of Modern Optics 60, 1299-1320 (2013).

No of fiber	Coupling loss per-facet (dB)	Deviation (dB)
1	1.2	0
1	2.2	(+/-)0.05
2	2.3	
1	2.5	(+/-)0.1
2	2.6	
3	2.7	
4	2.7	

Table 1: Coupling losses for 1, 2, and 4-fiber arrays.

Precise Phase Measurement with Weak Value Amplification on Integrated Photonic Chip

CNF Project Number: 2524-17

Principal Investigator(s): Jaime Cardenas

User(s): Meiting Song

Affiliation(s): The Institute of Optics, University of Rochester

Primary Source(s) of Research Funding: DRS, Andrew Jordan LLC

Contact: jaime.cardenas@rochester.edu, msong17@ur.rochester.edu

Website: https://www.hajim.rochester.edu/optics/cardenas/

Primary CNF Tools Used: Low pressure chemical vapor deposition (LPCVD), plasma-enhanced chemical vapor deposition (PECVD), JEOL 9500, ASML stepper, Oxford 100 ICP-RIE, AJA sputterer

Abstract:

We show, for the first time, phase measurement with weak value amplification on an integrated photonic chip. We demonstrate 9 dB improvement of signal over an on-chip Mach-Zehnder interferometer with equal amount of detected optical power.

Summary of Research:

Weak value amplification has shown the ability to make sensitive measurements with a small portion of the light signal, including beam deflection measurement of 400 frad with 63 µW out of 3.5 mW light power [1], frequency sensitivity of 129 kHz/√Hz with 85 µW out of 2 mW [2] and temperature sensor with 4-fold enhancement [3]. By introducing a perturbation and post-selection of the light, weak value amplification can amplify the signal to overcome technical noises, resulting in a higher signal-to-noise ratio (SNR) with less power. However, tabletop setups are space consuming and vulnerable to environmental changes. By taking this technique to the integrated photonics regime, we can largely improve its robustness and compactness, making it a good candidate for precision metrology.

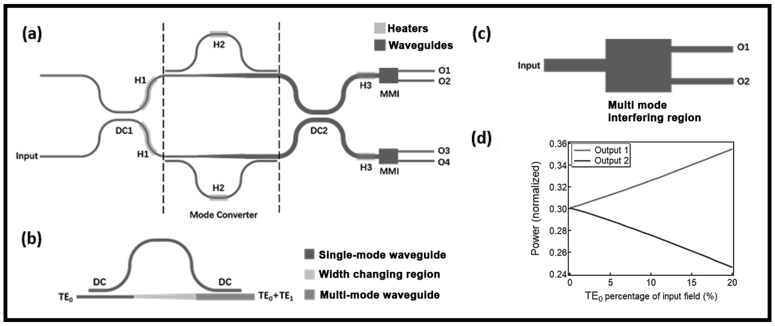

Figure 1: (a) Layout of device with heaters (not to scale). DC: direction-al coupler; H: heater; MMI: multi-mode interferometer; O: output. (b) Layout of a multimode interferometer. (c) Layout of a multi-mode interferometer. (d) Output power of MMI vs ratio of TE_0 and TE_1 mode.

We used an integrated Mach-Zander interferometer (MZI) followed by a multi-mode interference waveguide (MMI) (Figure 1(a)) to achieve weak value measurement. To introduce the misalignment, in other words, a spatial phase tilt in a waveguide, we designed the structure in Figure 1(b) to couple a small part of the light in TE_0 to TE_1. This is based on the fact that the Hermite-Gaussian expansion of a free space tilted beam is mainly a combination of fundamental and first order modes [4]. Since eigenmodes of a waveguide are similar to Hermite-Gaussian modes, we applied the theory on waveguide eigenmodes TE_0 and TE_1.

We design a multimode coupler to couple light from fundamental mode to higher order mode. As shown in Figure 1(b), the lower waveguide is a single mode waveguide, which transits to a multimode waveguide through an adiabatic taper. The upper waveguide couples a slight portion of light from TE_0 in lower waveguide. Then it couples back in to the lower waveguide, but to TE_1 mode, since the TE_1 mode supported by the lower waveguide is designed to be phase matched with TE_0 in the upper waveguide.

Another necessary component is needed to measure the "location shift" at the dark port, which translates to measuring the ratio of TE_0 and TE_1 modes. We used an MMI (multi-mode interferometer, Figure 1(c)) as simulation (Figure 1(d)) shows that its output power is dependent on the ratio of the input TE_0 and TE_1 modes.

We then fabricated the device with CMOS-compatible processes. The fabrication started with a 4-inch silicon wafer with 4 µm of thermally grown silicon dioxide. We deposited a layer of 289 nm silicon nitride with low pressure chemical vapor deposition (LPCVD). Then we used e-beam lithography to pattern the waveguides and etched the silicon nitride with inductively coupled plasma reactive ion etching (ICP-RIE). As cladding on the waveguides, we deposited 2.6 µm of silicon dioxide with plasma enhanced chemical vapor deposition (PECVD). Finally, we sputtered 100 nm of platinum with lift-off method for heaters.

We compare our weak value device with a standard on-chip MZI with same footprint working in quadrature. We launch 1 mW of laser power at 1570 nm with a tapered optical fiber. The phase signal is introduced by applying a modulated 1V, 10 kHz voltage to the heater 1. The outputs are imaged onto a balanced detector and we measure the signal on an RF spectrum analyzer.

We demonstrate 9 ± 1.9 dB signal improvement over the regular MZI in the weak value device with equal amount of detected optical power. When detected powers are 14 µW, weak value device has a signal of 66.17 dBm, while the regular MZI shows 75.33 dBm. For the regular MZI to also show a signal of 66.17 dBm, it requires a higher detected power of 40.5 µW.

Conclusions and Future Steps:

In conclusion, we have shown that on-chip weak value device is a good candidate for phase related metrology, including temperature drift and frequency shift. As it provides higher signal with same amount of optical power, it can monitor the optical signal in a system without consuming a large portion of the light. On the other hand, in a detector saturation limited system, weak value device is able to further increase the signal.

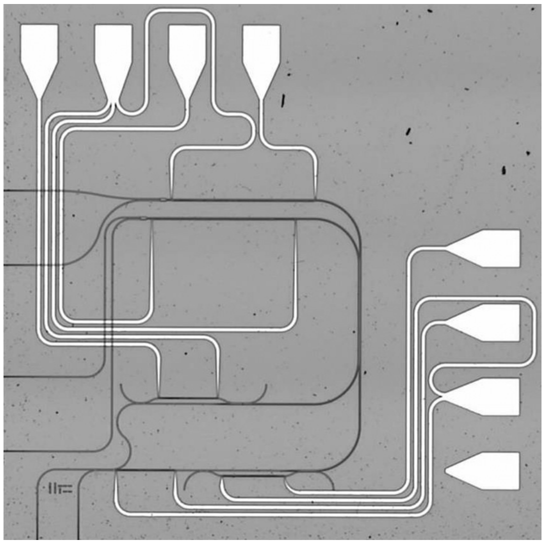

Figure 2: Microscope capture of the device. The device is wrapped around to reduce footprint.

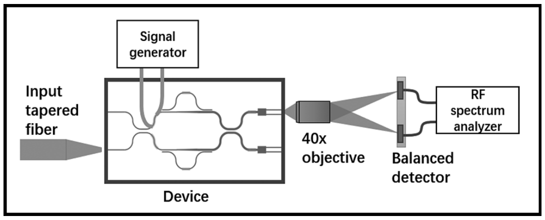

Figure 3: Illustration of testing setup.

References:

[1] P. B. Dixon, D. J. Starling, A. N. Jordan, and J. C. Howell, "Ultrasensitive Beam Deflection Measurement via Interferometric Weak Value Amplification," Phys. Rev. Lett. 102, 173601 (2009).

[2] D. J. Starling, P. B. Dixon, A. N. Jordan, and J. C. Howell, "Precision frequency measurements with interferometric weak values," Phys. Rev. A 82, 063822 (2010).

[3] L. J. Salazar-Serrano, D. Barrera, W. Amaya, S. Sales, V. Pruneri, J. Capmany, and J. P. Torres, "Enhancement of the sensitivity of a temperature sensor based on fiber Bragg gratings via weak value amplification," Opt. Lett., OL 40, 3962-3965 (2015).

[4] J. Steinmetz, K. Lyons, M. Song, J. Cardenas, and A. N. Jordan, "Precision frequency measurement on a chip using weak value amplification," in Quantum Communications and Quantum Imaging XVII (International Society for Optics and Photonics, 2019), Vol. 11134, p. 111340S.

High Transmission Plasmonic Metasurfaces in the Visible Band

CNF Project Number: 2525-17
Principal Investigator(s): Chunlei Guo
User(s): Jihua Zhang, Ran Wei

Affiliation(s): The Institute of Optics, University of Rochester
Primary Source(s) of Research Funding: Bill and Melinda Gates Foundation (OPP1119542)
Contact: chunlei.guo@rochester.edu, jzh119@ur.rochester.edu, rwei@ur.rochester.edu
Website: http://www2.optics.rochester.edu/workgroups/guo/about.html
Primary CNF Tools Used: JEOL 9500

Abstract:

Metasurfaces are two-dimensional nanoantenna arrays that can control the propagation of light at will. In particular, plasmonic metasurfaces feature ultrathin thicknesses, ease of fabrication, field confinement beyond the diffraction limit, and ultrafast performances. However, the technological relevance of plasmonic metasurfaces operating in the transmission mode at optical frequencies is questionable due to their limited efficiency. The state-of-the-art efficiency of geometric plasmonic metasurfaces at visible and near-infrared frequencies, for example, is ≤ 10%. Here, we report a multipole-interference-based transmission-type geometric plasmonic metasurface with a polarization conversion efficiency that reaches 42.3% at 744 nm, over 400% increase over the state of the art. The efficiency is augmented by breaking the scattering symmetry due to simultaneously approaching the generalized Kerker condition for two orthogonal polarizations. In addition, the design of the metasurface proposed in this study introduces an air gap between the antennas and the surrounding media that confines the field within the gap, which mitigates the crosstalk between meta-atoms and minimizes metallic absorption.

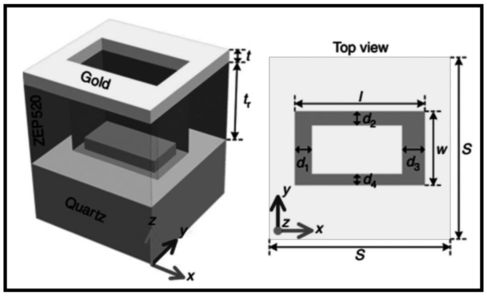

Figure 1: Schematic showing the designed multipole meta-atom, which consists of a gold nanoaperture and a gold nanorod separated by a perforated ZEP520 layer. In the meta-atom, S = 320 nm, l = 230 nm, w = 130 nm, t = 35 nm, and t_r = 180 nm. The multipole response of this meta-atom can be tuned by introducing an air gap between the nanorod and ZEP520 sidewalls, i.e., a noncomplementarity between the nanorod and the nanoaperture. The dimension of the air gap is denoted by $d_{1,2,3,4}$ in four sides.

Summary of Research:

In this work [1], we use multipole meta-atoms that support not only electric dipole and magnetic dipole but also an electric quadrupole and a magnetic quadrupole to construct an ideal half-wave plate. In multipole meta-atoms, it is possible to completely suppress backscattering for both orthogonal polarizations by satisfying the so-called generalized Kerker condition [2] and maintain the π-phase difference. We propose a multipole meta-atom design consisting of a metallic nanoaperture and a metallic nanorod separated by a perforated dielectric layer, as shown in Figure 1. The dimension of the nanorod and thus the multipole response can be modified by introducing a small air gap between the nanorod and the dielectric spacer separating adjacent meta-atoms, i.e. non-complementarity.

We also explore the advantages of the noncomplementary design of meta-atoms compared with complementary design, i.e. with no airgap between the nanorod and the nanoaperture. First, the introduction of non-complementarity is the key to engineering the multipole interference and enhancing the transmittance of light with cross-polarization ($T_{cross\text{-}CP}$), which, in most applications, is preferred for wavefront control of the transmitted light. As a result, we achieve an overall enhancement in the $T_{cross\text{-}CP}$ of the noncomplementary design. The peak efficiency is increased to 45.5% at a peak wavelength of 751 nm, i.e., $T_{cross\text{-}CP}$ is increased by > 10% compared with complementary design.

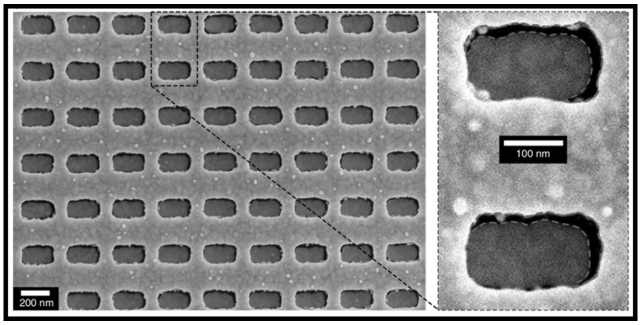

Figure 2: SEM image of a fabricated MPM and an enlarged view of two meta-atoms. The dashed lines mark the edges of the air gap.

Figure 3: Holography images at 750 nm for the noncomplementary design. (See pages vi-vii for full color version.)

Another evident advantage is the reduced near-field coupling between the meta-atoms. Both designs support good orientation-controlled phase responses. However, the $T_{cross\text{-}CP}$ amplitude of the complementary design significantly changes as a function of orientation angle of the meta-atom, while the noncomplementary meta-atom has higher and relatively flat amplitudes, representing reduced field coupling between meta-atoms.

Figure 2 shows scanning electron microscopy (SEM) images of the fabricated noncomplementary metallic plasmonic metasurfaces (MPM) using e-beam lithography on JEOL 9500 at CNF. The MPM has also been further tested on two applications, a beam deflector and a hologram, respectively. The beam deflector is realized by introducing a phase gradient on the surface, here the unit cell we used consists of eight subunits with an orientation step of 22.5°. The measured extinction ratio (ER) peaks at 7.8 dB at ~ 745 nm and exceeds 0 dB between 660 and 850 nm.

Both the peak transmission efficiency (E_p) and ER are significantly higher than the values of the current state-of-the-art MPMs ($E_p \leq 10\%$, ER ≤ 0 dB) in the visible and near-infrared regions in realizing various functionalities [3].

Another application that we demonstrate with the proposed design is a high efficiency hologram. Figure 3 shows experimental holography images in the far field at $\lambda = 750$ nm obtained from a noncomplementary design. The hologram efficiencies are measured to be 37%, which is better than those of the state-of-the-art GMs in the visible and near infrared regions [4]. The hologram is broadband as well, which shows holography images at various wavelengths.

Conclusions and Future Steps:

A significant increase in the transmission efficiency of plasmonic geometric metasurfaces is facilitated by tuning the multipole response of individual meta-atoms and by minimizing the crosstalk between meta-atoms. The maximum efficiency of the metasurfaces is on the long-wavelength side of the visible spectrum, 744 nm.

However, the demonstrated high efficiency exceeds that of the state-of-the-art over a wide wavelength range of 630-970 nm, i.e., in the red color range of the visible (visible covers 380-780 nm) and near-infrared regions. This concept and these techniques can be used for shorter visible wavelengths or longer-wavelength regions by tuning the dimensions of the meta-atom. This concept can be used for dielectric metasurfaces as well.

Furthermore, reflective-type metasurfaces can benefit from the generalized Kerker, no-front-scattering condition. On the other hand, perfect and selective light absorption can be achieved by eliminating both reflection and transmission, using the generalized Kerker approach.

In the future, even higher-order multipoles can also be included to improve the performance of MPMs [5].

References:

[1] Zhang, Jihua, et al. "Plasmonic metasurfaces with 42.3% transmission efficiency in the visible." Light: Science and Applications 8.1 (2019): 1-13.

[2] Liu, W., and Kivshar, Y. S. Generalized Kerker effects in nanophotonics and metaoptics [Invited]. Opt. Express 26, 13085-13105 (2018).

[3] Wen, D. D., et al. Metasurface for characterization of the polarization state of light. Opt. Ex. 23, 10272-10281 (2015).

[4] Wan, W. W., Gao, J., and Yang, X. D. Metasurface holograms for holographic imaging. Adv. Opt. Mater. 5, 1700541 (2017).

[5] Kruk, S., et al. Invited article: broadband highly efficient dielectric metadevices for polarization control. APL Photonics 1, 030801 (2016).

Description of the Exploratory Etching and Electrodeposition Project

CNF Project Number: 2527-17

Principal Investigator(s): Dr. David Crouse

User(s): Golsa Mirbagheri

Affiliation(s): Electrical and Computer Engineering Department, Clarkson University
Primary Source(s) of Research Funding: CFM, Clarkson University
Contact: dcrouse@clarkson.edu, mirbagg@clarkson.edu
Primary CNF Tools Used: Oxford 82, Oxford 100, ASML, Gamma, PECVD, Cobra

Abstract:

This project is a continuing project. We will be finishing the fabrication of the hyperbolic metamaterial structure and designing a 2nd generation of the filter that uses more of a photonics crystal resonant material within a Bragg stack. Both the hyperbolic metamaterial structure and the 2nd generation devices have compelling properties. Both show very little dispersion — meaning that their performance is not affected by the angle of incidence to the optical signal.

Summary of Research:

During the last year, we have further designed the hyperbolic metamaterial device and have performed much more optimization and have taken into account practical design considerations. We are now fabricating the structure at the Cornell NanoScale Science and Technology Facility (CNF) at Cornell University.

We have developed a fabrication plan and are now implementing the plan, with masks designed and fabrication processes in development. Based on what we have learned, we are now investigating a 2nd generation device that does not use metal wires, but uses resonant cavities in the three middle layers of the Bragg stack. The resulting structure will have far less polarization dependence, will absorb less radiation, will be far easier to fabricate and manufacture, and will have a larger tuning range that allows for it to be used within pixelated wavelength filters for hyperspectral imaging applications.

We have been performing preliminary testing on the resonant cavities and have a preliminary design for operation in the midwavelength infrared range of 3-5 µm. The Bragg stack will use silicon and silicon dioxide, and potentially silicon nitride — all CMOS compatible devices — as well as having all structure features with sizes amenable to optical lithography.

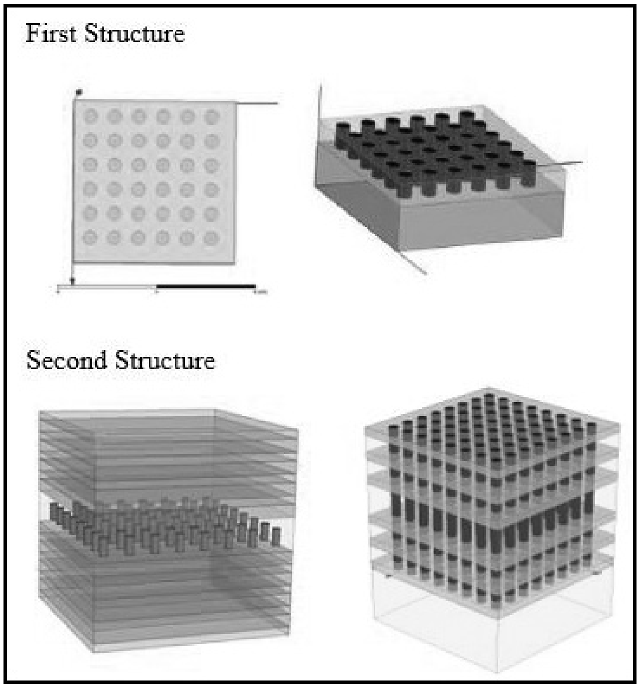

Figure 1: First Structure: The 1.5 µm SiO_2 film was deposited, patterned and etched. The holes were 0.5 µm, electroplated with Cu. Second Structure: Alternative layers of SiO_2 and Si are deposited, patterned and etched (all through the layers), then holes electroplated with Cu.

Metamaterial Spectrometer: A Low SWaP, Robust, High Performance Hyperspectral Sensor for Land and Atmospheric Remote Sensing

CNF Project Number: 2661-18
Principal Investigator and User: Lori Lepak

Affiliation(s): Phoebus Optoelectronics LLC
Primary Source(s) of Research Funding: National Aeronautics and Space Administration (NASA)
Contact: llepak@phoebusopto.com
Website: www.phoebusopto.com
Primary CNF Tools Used: ASML DUV stepper, Oxford 81 etcher, Logitech CMP, Zeiss Supra SEM

Abstract:

Since 2003, Phoebus Optoelectronics has enabled custom R&D solutions in the fields of Plasmonics, Metamaterials, Antennas, and Sensors. We work closely with our customers throughout device development, from simulation and design, to prototype realization, testing, and small volume manufacturing. Our R&D portfolio spans the spectral ranges of visible light, infrared, terahertz, and microwave radiation, for applications in high resolution imaging systems, wavelength and polarization filtering, tunable optical components, beam forming and steering, solar cells, renewable energy devices, and chemical and biological toxin sensors. We routinely partner with large, industry-leading businesses to develop products in all of these areas, jointly performing advanced testing and working together to scale up to medium- and large-volume manufacturing. Our agile team makes extensive use of the resources at the CNF for our nano/micro fabrication and testing, to provide cost efficiency and rapid turnaround.

In the present report, we discuss the ongoing development of a metamaterial-based hyperspectral imaging filter.

Summary of Research:

Phoebus uses the resources of the CNF to fabricate plasmonic chips patterned with a metamaterial surface to enable Extraordinary Optical Transmission (EOT), a phenomenon unique to metastructures in which light is transmitted through apertures much smaller than the incident wavelength, at anomalously large intensities relative to the predictions of conventional aperture theory. EOT was first observed by T.W. Ebbesen in 1998 [1]. Since its founding in 2003, Phoebus has successfully harnessed EOT by incorporating metasurfaces into devices used to perform light filtering [2,3], photon sorting [4,5], polarimetric detection [6], high speed optical detection [7], and SPR plasmonic sensor chips [8].

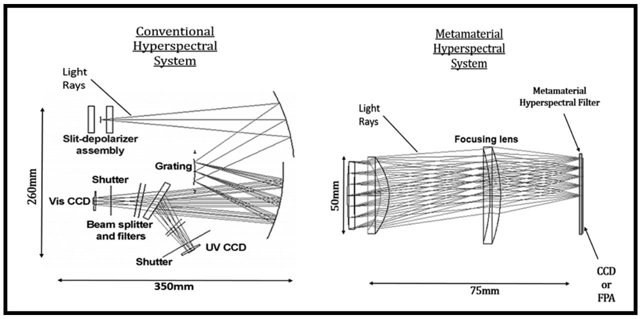

Figure 1: Phoebus's Metamaterial Spectrometer (MS) technology (right) eliminates much of the size and weight of conventional hyperspectral spectrometer technologies (left). Note the significant difference in scale of the two images.

In our current project, we are developing a hyperspectral imaging system, shown schematically in Figure 1. Our technology (Figure 1b) uses a metasurface to precisely target very narrow spectral bands of interest, enabling a significant reduction in the size and number of optical components relative to current state-of-the-art imaging systems (Figure 1a), which in turn will enable integration of our high-performance sensor onto weight-sensitive platforms (i.e., satellites) far more readily than existing systems. Our initial goal is to detect and image trace gases in the Earth's atmosphere in the midwave infrared (MWIR) region (defined as 3-5 µm wavelength), while reducing adjacent channel latency to less than 10 ms.

Using the ASML DUV stepper, an entire wafer can rapidly be lithographically patterned with arrays of metastructures, as shown in Figure 2. In general, the optimal feature size and period of these metastructures depends primarily upon the desired wavelength of operation and the refractive indices of the constituent materials. In the MWIR, typical feature sizes are on the order of ~ 1 µm. As we can see in the optical microscope image in Figure 3, the ASML can easily produce highly uniform, large-area arrays of test features of an appropriate size. Equally critical for photonics applications, relatively narrow spaces between these features can be etched with moderately high aspect ratios, to form structures with nearly vertical sidewalls, as shown in Figure 4. These vertical structures both minimize optical losses, and ensure that the real fabricated devices will perform as closely as possible to the optimal designs predicted by simulations.

Conclusions and Future Steps:

Our overall metasurface technology can be easily adapted to other spectral ranges, from the visible to the microwave, by substituting appropriate materials, and scaling feature sizes in proportion to the desired wavelength of imaging. In addition to fabricating the MWIR device, we have completed the design of a visible-wavelength counterpart of the current technology, and are about to begin fabrication using all of same tools as the MWIR project, plus the Oxford PECVD and AJA sputter tool to deposit the thin films. Thus, the extensive resources of the CNF are enabling us to rapidly develop our Metamaterial Spectrometer technology for a broad range of imaging and sensing applications.

References:

[1] Ebbesen, T.W., et al., “Extraordinary optical transmission through sub-wavelength hole arrays.” Nature, (1998). 391(6668): p. 667-669.

[2] Crouse, D. “Numerical modeling and electromagnetic resonant modes in complex grating structures and optoelectronic device applications.” Electron Devices, IEEE Transactions on 52.11 (2005): 2365-2373.

[3] Crouse, D., and Keshavareddy, P. “Polarization independent enhanced optical transmission in one-dimensional gratings and device applications.” Optics Express 15.4 (2007): 1415-1427.

[4] Lansey, E., Crouse, D., et al. “Light localization, photon sorting, and enhanced absorption in subwavelength cavity arrays.” Optics Express 20.22 (2012): 24226-24236.

[5] Jung, Y.U; Bendoym, I.; Golovin, A.B.; and Crouse, D.T. “Dual-band photon sorting plasmonic MIM metamaterial sensor.” Proc. SPIE 9070, Infrared Technology and Applications XL, 90702X (June 24, 2014); doi:10.1117/12.2050620.

[6] Crouse, D., and Keshavareddy, P. “A method for designing electromagnetic resonance enhanced silicon-on-insulator metal-semiconductor-metal photodetectors.” J. of Optics A: Pure and Applied Optics 8.2 (2006): 175.

[7] Mandel, I.; Gollub, J.; Bendoym, I; Crouse, D. Theory and Design of a Novel Integrated Polarimetric Sensor Utilizing a Light Sorting Metamaterial Grating. Sensors Journal, IEEE, (2012): Vol. PP, 99.

[8] Lepak, L., et al. “Handheld chem/biosensor using extreme conformational changes in designed binding proteins to enhance surface plasmon resonance (SPR)” Proc. SPIE 9862, Advanced Environmental, Chemical, and Biological Sensing Technologies XIII, 9862-7 (April 17, 2016); doi:10.1117/12.2222305.

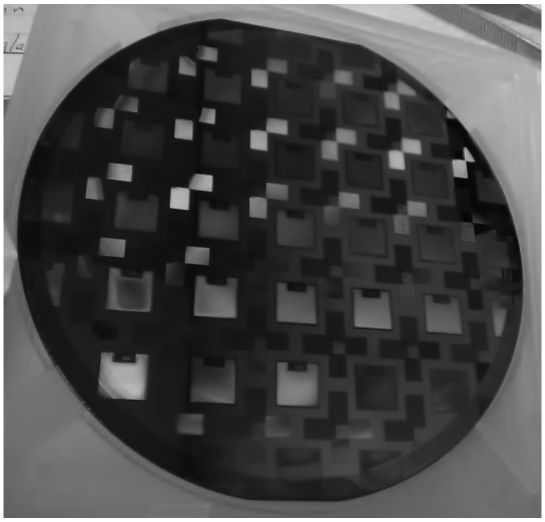

Figure 2: Wafer lithographically patterned with optical metastructures, using the ASML DUV stepper. (See pages vi-vii for full color version.)

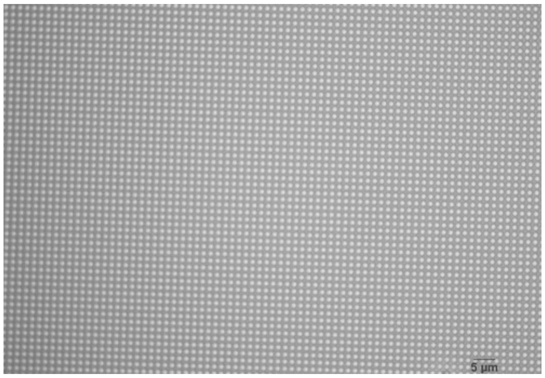

Figure 3: Optical microscope image of test pattern of array of ~ 1 µm pillars, lithographically patterned on the ASML DUV stepper.

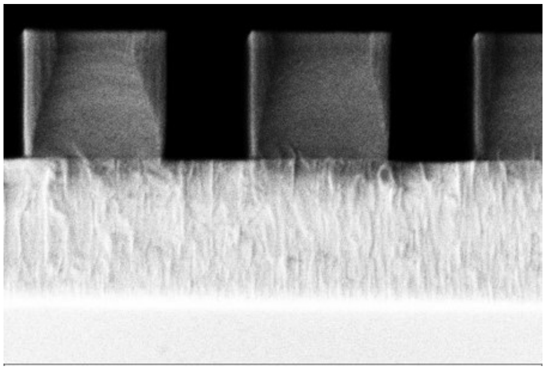

Figure 4: SEM image (cross section) of etched pillars with near-vertical sidewalls. Imaged at ~ 90 kX in the Zeiss Supra SEM, the grain structure of the etch stop layer is clearly visible.

Metasurface-Integrated Graphene for Mid-Infrared Optical Devices

NF Project Number: 2472-16
Principal Investigator(s): Gennady Shvets
User(s): Aditya Mahalanabish, Minwoo Jung

Affiliation(s): School of Applied and Engineering Physics, Department of Physics; Cornell University
Primary Source(s) of Research Funding: Office of Naval Research (ONR) and National Science Foundation (NSF)
Contact: gs656@cornell.edu, am2952@cornell.edu, mj397@cornell.edu
Website: http://shvets.aep.cornell.edu
Primary CNF Tools Used: JEOL 9500, CVC SC4500 evaporator, Zeiss Supra/Ultra SEM, PT740 or Anatech resist strip

Abstract:

Plasmonic metasurfaces, when integrated with graphene, can greatly enhance the absorption of incident radiation into graphene through resonant field enhancement. This metasurface structure can be obtained simply by patterning graphene itself, or it may take a form of thin metallic film periodically patterned on graphene. The former approach was used to achieve an on/off notch filter of mid-infrared radiation with narrow linewidth, and the latter approach was used to make a high-responsivity and ultrafast graphene photodetector.

Summary of Research:

Graphene Based Mid-IR High *Q* Active Notch Filter. Graphene's high electronic mobility and ultrawide tunability owing to the linear Dirac electronic dispersion makes it an exceptional candidate for optoelectronic applications. However, its inherent weak absorption of only 2.3% of normally incident light in the visible and infrared spectrum acts as a bottleneck. To enhance its optical absorption, we can make use of the strong absorption properties of localized surface plasmon resonance (LSPR) in graphene. Nanopatterning of monolayer graphene using e-beam lithography and subsequent etching using RIE or FIB can be used to produce structures like nanorings and nanodisks [1], which support LSPR and have been reported to show an enhanced absorption of 25% [2]. For our structure, shown in Figure [1], we design a nano patterned graphene structure that maintains electrical connectivity and thus foregoes the requirement of an ion gel layer [1,2] — reducing the complexity in fabricating and handling such an optoelectronic device.

The device is fabricated in a total of four steps: (1) gold alignment marks and electrodes are deposited on CaF_2 (the substrate), (2) the heterostructure of graphene/hBN/graphene is transferred on to the substrate carefully to make sure each graphene layer is connected to one set of electrodes only, (3) the resonator pattern is etched on the top graphene using e-beam lithography, and (4) the graphene is etched through the developed PMMA, to get the required pattern using PT740 or the Anatech resist strip.

Figures 1 and 2 show two different fabricated resonator designs for the device. Device fabrication is at the stage of optimizing the etch recipe for graphene.

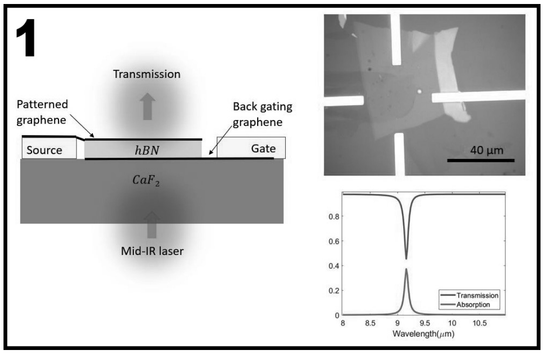

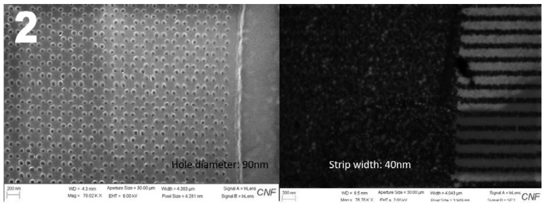

Figure 1, top: Left, schematic of the mid-IR notch filter showing the heterostructure stack. Top right, fabricated device under optical microscope, the opaque material visible in between the electrodes is the hBN layer. Bottom right, simulated mid-IR spectra of the fabricated device with the top graphene having a hexagonal pattern of holes (see Figure 2).

Figure 2, bottom: Left, SEM of developed pattern of hexagonal lattice of holes on PMMA covering the top graphene before plasma etch. Right, SEM of another possible 1D resonator pattern, rectangular strips etched on graphene, transferred on Si/SiO_2 substrate.

Graphene Photodetector with High Responsivity Enhanced by Plasmonic Metasurface. In a similar way, we resonantly boost the absorption into graphene by integrating a gold metasurface with graphene.

While graphene photodetectors enhanced by plasmonic metasurfaces are previously demonstrated [3], we aim for even greater enhancement by (1) interdigitating the source and drain and (2) using high-quality exfoliated graphene. Especially, the latter advancement is expected to give a huge improvement on the quality of detector performance, as the previous works were mostly done with CVD graphene with lower quality.

As depicted in the Figure 3 inset, we place graphene-hBN stack on top of the pre-fabricated gold metasurface structures deposited on SiO_2-Si substrate. The gold metasurfaces are fabricated by using e-beam lithography. We use PMMA for the e-beam resist, and deposit 7 nm of Cr and 43 nm of gold using CVC SC4500 evaporators.

The device is under characterization, and here we report on its optical characterization. The photocurrent measurement is to be done in a near future.

Figure 3 shows the reflection spectra of the gold metasurfaces with and without the graphene-hBN stack. While there are some modifications to the resonance structure due to the phonon bands of hBN, the original reflection dips are well-conserved. Thus, we expect that the absorption enhancement would be maintained at the similar order of magnitude even under the perturbation by hBN. We introduce this additional hBN layer for better graphene quality. The current experiment will be followed by the electrical characterization of the devices.

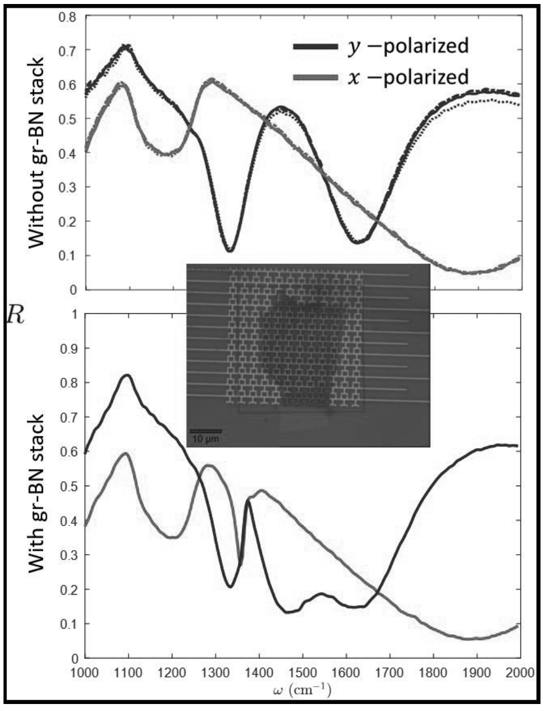

Figure 3: Optical characterization of photodetector device. Top, reflection spectra without graphene-BN stack on top of metasurface. Bottom, reflection spectra with graphene-BN stack on top of metasurface. Inset (middle), an optical microscopy image of a device with graphene-BN stack.

References:

[1] Fang, Z. Y.; Thongrattanasiri, S.; Schlather, A.; Liu, Z.; Ma, L. L.; Wang, Y. M.; Ajayan, P. M.; Nordlander, P.; Halas, N. J.; de Abajo, F. J. G. Gated Tunability and Hybridization of Localized Plasmons in Nanostructured Graphene. ACS Nano, 7, 2388-2395 (2013).

[2] Fang, Z.; Wang, Y.; Schlather, A. E.; Liu, Z.; Ajayan, P. M.; de Abajo, F. J. G.; Nordlander, P.; Zhu, X.; Halas, N. J. Active Tunable Absorption Enhancement with Graphene Nanodisk Arrays. Nano Lett., 14, 299-304 (2013).

[3] Y. Yao, R. Shankar, P. Rauter, Y. Song, J. Kong, M. Loncar, and F. Capasso; High-Responsivity Mid-Infrared Graphene Detectors with Antenna-Enhanced Photocarrier Generation and Collection. Nano Letters 14 (7), 3749-3754 (2014).

III-N Photonic Devices

CNF Project Number: 2801-19

Principal Investigator(s): Debdeep Jena

User(s): Kevin Lee, Shyam Bharadwaj, Ryan Page, Jimy Encomendero

Affiliation(s): Electrical and Computer Engineering, Materials Science Engineering; Cornell University

Primary Source(s) of Research Funding: National Science Foundation

Contact: djena@cornell.edu, sb2347@cornell.edu, kl833@cornell.edu, rlp238@cornell.edu, jje64@cornell.edu

Primary CNF Tools Used: ABM contact aligner, electron-beam evaporators, Plasma-Therm inductively coupled plasma reactive ion etcher (PT 770), electron-beam lithography, atomic layer deposition, plasma-enhanced chemical vapor deposition

Abstract:

Lifi communication using III-Nitrides visible light sources has drawn huge attention recently. Our goal is to build monolithic integration of field effect transistor (FET) with blue light emitting diodes (LEDs). We use plasma-assisted molecular beam epitaxy (PA-MBE) to grow a buried tunnel junction blue LED with a n-i-n channel sitting on top. The resulting device we called "light emitting FET (LEFET)" shows successful gate modulation and on/off ratio of five orders. Light output signal can be switched up to 30 kHz.

Summary of Research:

The LEFET structure is grown on a n-type metal polar free-standing GaN substrate with dislocation density ~ 10^6 cm^{-2} by PA-MBE. The detailed structure is presented in Figure 1(a). First, a 125 nm Si-doped GaN layer is grown with [Si] = 10^{19} cm^{-3}. After initial n-GaN layer, p-GaN with Mg doping of 3 × 10^{19} cm^{-3}. This completes the buried tunnel junction for hole injection. The active region contains three periods of InGaN multiple quantum wells (MQWs) with blue emission at 467 nm. Later, the n-i-n FET region is grown using unintentional doped GaN (uid-GaN) sandwiched between two n-GaN layers.

The sample was processed into devices consisting of various numbers of vertical n-FET nanowires or fins of varying dimensions on top of 55 × 55 µm^2 LED mesas.

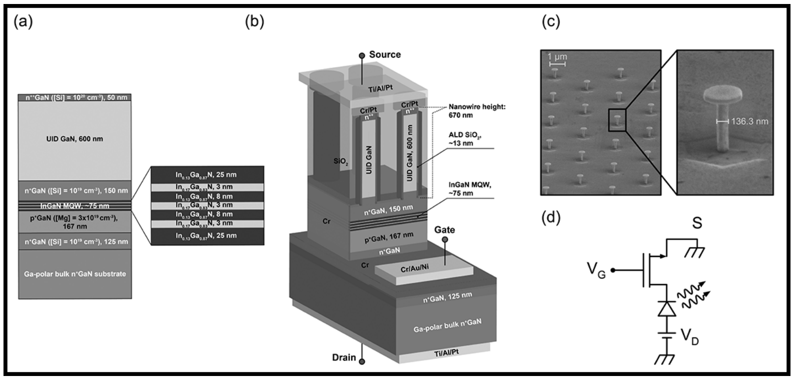

Figure 1: (a) Schematic epitaxial layer structure for the device discussed in this study. The structure consists of a vertical n-i-n GaN FET sitting above a bottom-TJ homojunction InGaN LED. (b) Schematic of a fabricated nanowire LEFET structure, showing source, gate, and drain contacts for biasing the device, and dielectrics for isolation. (c) SEM image of the nanowire LEFET structure. (d) Circuit diagram of the LEFET.

A schematic of a processed nanowire LEFET is shown in Figure 1(b). First, 55 × 55 µm^2 LED areas were isolated through inductively-coupled plasma reactive ion etching (ICP-RIE) down to the n$^+$GaN nucleation layer. Next, nanowires and fins were defined on the mesa surface through electron beam lithography (EBL).

The etch process for nanowire/fin definition consisted of first an ICP etch (using Cr/Pt as an etch mask as well as top source contact) followed by a wet etch in AZ400K to make the sidewalls vertical for efficient lateral gating (see Figure 1(c)). The fins were defined with long edge along the m-plane direction in order to allow for adequate wet etching. Then, SiO$_2$ was deposited by atomic layer deposition (ALD) as a gate dielectric for the nanowire/fin FETs.

Next, Cr was sputtered as the sidewall gate metal, followed by e-beam evaporation of large Cr/Au/Ni pads for electrically contacting the gate. The undesired sputtered Cr above the source contact of the fins and wires was etched away after a planarization process, after which SiO$_2$ was blanket deposited by plasma-enhanced chemical vapor deposition (PECVD) to isolate the rest of the sidewall gate metal. This SiO$_2$ was then planarized to again expose the Cr/Pt wire/fin source contact, after which thick source pads (Ti/Al/Pt) for probing were deposited. Gate isolation for the FET wires/fins between different devices (which still had their gates shorted together by the sputtered Cr at this point) and contact holes for the thick gate pads were realized together with an SiO$_2$ etch followed by a Cr etch.

Finally, a Ti/Al/Pt back contact was deposited with a window left free of metal for collecting light from the back side.

After device processing, electrical and optical measurements were performed, with results for a 500 nm × 50 µm single-fin device shown in Figures 2 and 3, respectively. Circular transfer length method (cTLM) measurements shown in Figure 2(a) reveal low contact and sheet resistances: 9.34 × 10^{-6} Wcm^2 for the top source contact, and 185 Ω/sq for the n^{++}GaN contact layer underneath, resulting in negligible voltage drops across these regions. I$_D$-V$_G$ and I$_D$-V$_D$ measurements on the 500 nm × 50 µm single-fin device are shown in Figures 2(b) and (c), respectively, with current density values shown on the plots normalized to the area of the finFET.

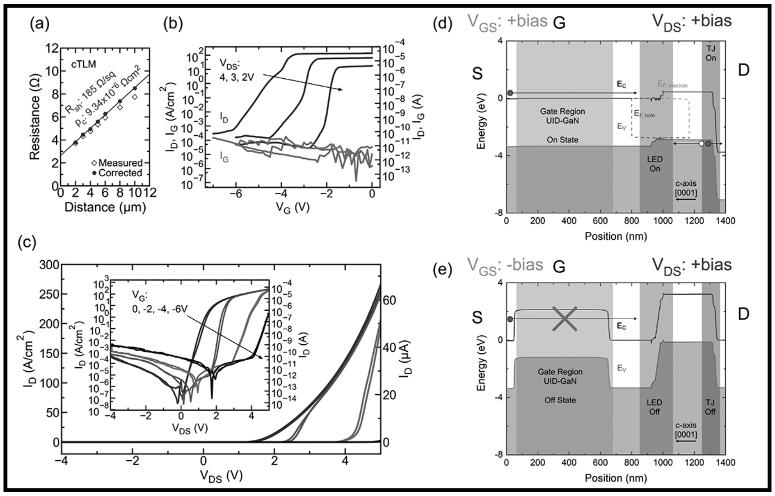

Figure 2: (a) Circular TLM data for the source contact of the LEFET. (b) I_DV_G measurement for a single-fin device with fin dimensions of 500 nm × 50 µm and LED dimensions of 55 × 55 µm^2. Current density is calculated using the area of the fin. (c) Linear I_DV_D characteristic (with log-scale in inset) showing reduction in on current of ~ 100x at V_{DS} = 5 V as V_G is reduced from 0 V to -6 V. (d), (e) Qualitative depiction of band diagrams for the device in the on and off states, respectively. With a fixed positive V_{DS}, switching V_G from positive to negative biases modulates electron conduction across the FET channel, and allows voltage to drop across the diode.

The measured electroluminescence (EL) spectra are shown in Figure 3, demonstrating the optical modulation enabled by the FinFET. Figures 3(a) and (b) show the effect of the drain voltage on the emission spectra in linear and log scales for the 500 nm × 50 µm single fin device at a fixed V$_G$ = 4V for V$_{DS}$ between 10V and 13V. Figures 3(c) and (d) demonstrate the desired modulation of the EL spectra through gating of the GaN FinFET.

In summary, we have demonstrated a new technique for achieving monolithic integration of n-FETs and LEDs, using vertical fin-and nanowire-FETs and bottom tunnel junction blue LEDs. This platform allows for strong gate control (~ 5 orders of magnitude on/off for I$_D$) without limiting the on-wafer LED active area, and does not require regrowth.

Optical switching behavior up to 30 kHz is demonstrated in the first prototype, with room for improvement through use of InGaN heterojunction TJs.

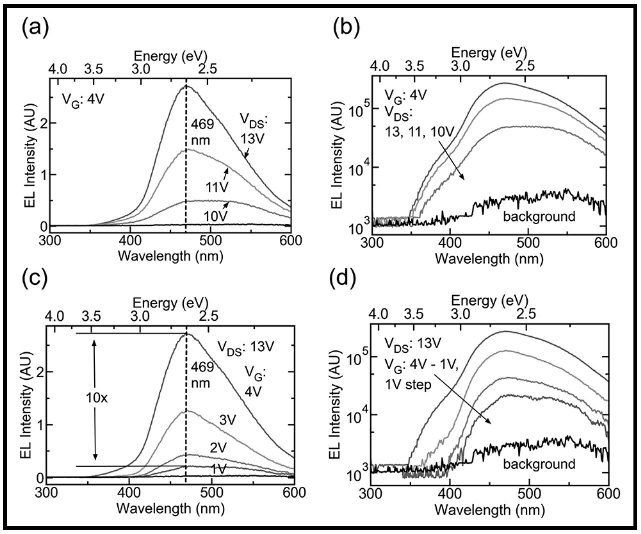

Figure 3: (a), (b) Linear and log scale plots, respectively, of electroluminescence (EL) intensity versus wavelength for a single-fin device, with V_G fixed at +4V. The EL intensity rises as expected with increasing V_{DS} as the level of forward bias across the diode is increased. (c), (d) Linear and log scale plots, respectively, of EL intensity versus wavelength for the same device, with V_{DS} fixed at 13V. A factor of 10 reduction in EL intensity is observed as V_G is decreased from +4V to +1V, demonstrating the gate's ability to limit electron transport into the LED.

Self-Torque in Ferromagnetic using ST-FMR and Harmonic Measurements

CNF Project Number: 111-80

Principal Investigator(s): Robert A. Buhrman

User(s): Qianbiao Liu

Affiliation(s): Applied and Engineering Physics, Cornell University

Primary Source(s) of Research Funding: Department of Defense; Intelligence Advanced Research Projects Activity

Contact: buhrman@cornell.edu, ql63@cornell.edu

Primary CNF Tools Used: ASML, JEOL 6300, Veeco AFM

Abstract:

Spin-orbit torque in heavy metal/ferromagnet heterostructures with broken spatial inversion symmetry provides an efficient mechanism for manipulating magnetization using a charge current. We report the presence of a spin torque in a single ferromagnetic. According to the fitting results of ST-FMR and Harmonic measurements, it is clear the spin orbit torque that should come from the SHE and anomalous spin orbit torque of FM induced σz with σy spin current. However, there still remains a main problem to further clarify about the original of non-equilibrium spin accumulation between bottom Cu/FM interface and top FM/Cu interface.

Summary of Research:

When a charge current passes through a ferromagnet (FM) due to the imbalance in electron density of states at the Fermi level and scattering asymmetry between spin-up and spin-down electrons, it becomes polarized, thereby generating a net spin current flowing in the charge current direction. In addition to longitudinal charge and spin currents, transverse charge and spin currents are also generated by the anomalous Hall effect (AHE), leading to charge and spin accumulation at the side surfaces or edges at steady state. So far, the study of AHE has mainly been focused on charge accumulation because it can be detected directly as a voltage signal, and very little attention has been devoted to the spin accumulation. Recently, several groups have attempted to exploit the AHE-induced spin accumulation and related spin torque (ST) for magnetization switching applications in FM/nonmagnet (NM)/FM trilayers which, compared to spin-orbit torque (SOT) generated by the spin Hall effect (SHE), offers the possibility of controlling the spin polarization direction by manipulating the magnetization direction of one of the FM layers. However, there still remains a main problem to further clarify about the original of non-equilibrium spin accumulation between bottom Cu/FM interface and top FM/Cu interface.

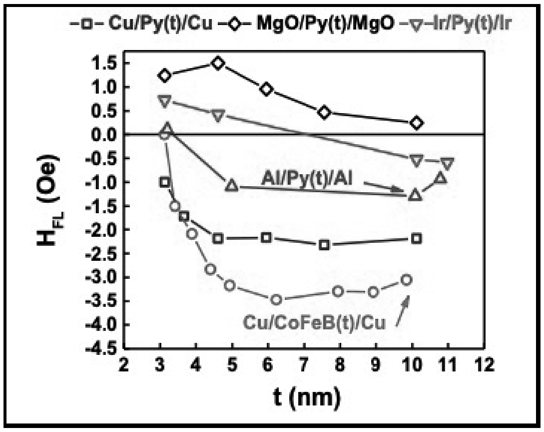

Figure 1: FM thickness dependence of H_{FL0}.

We fabricated a series of Hall bar devices. We will discuss the spin torque, and the H_{FL0} values of all samples are shown on Figure 1. We get similar results with the ST-FMR results. The field-like torque in Cu/Py/Cu is opposite with MgO/Py/MgO, and the Ir/Py/Ir fall in between Cu/Py/Cu and MgO/Py/MgO. The torque in Cu/CoFeB/Cu have the same signal with Cu/Py/Cu. And the torque efficiency increases with increasing the FM thickness. All of these results mean the σ_y from the bulk effect. The possible mechanism is bulk SHE or the anomalous spin orbit torque.

References:

[1] Z.Luo, Q.Zhang, Y.Xu, Y.Yang, X.Zhang and Y.Wu, Spin-Orbit Torque in a Single Ferromagnetic Layer Induced by Surface Spin Rotation. Phys. Rev. Appl. 11, 064021 (2019).

Spin Pumping and Non-Uniform Magnetic Excitation in Spin-Torque FMR Studies of the Spin Hall Effect

CNF Project Number: 111-80

Principal Investigator(s): Robert A. Buhrman

User(s): Ryan Tapping

Affiliation(s): Applied and Engineering Physics, Cornell University

Primary Source(s) of Research Funding: Cornell Center for Materials Research

Contact: buhrman@cornell.edu, rct76@cornell.edu

Primary CNF Tools Used: GCA 5x stepper, AJA sputtering tool

Abstract:

Spin-torque ferromagnetic resonance (ST-FMR) is a technique that was first used to show a surprisingly strong spin Hall effect (SHE) in certain heavy metals (HM) [1]. This method has since been widely deployed in the study of spin-orbit torques in HM/FM bilayers. However, recently it is unclear that ST-FMR always provides accurate, quantitative measures of the damping-like spin-torque efficiency ξ_{DL}, principally because of the unsettled role of spin-pumping and the inverse SHE in ST-FMR, but also because of the assumption that only the uniform mode is excited. Here we report on an extensive ST-FMR study of Pt/FM and HM/spacer/FM trilayers chosen such that the spin pumping effect is both strong and variable. We show that spin pumping, when significant, subtracts from the antidamping torque signal, resulting in $\xi_{FMR} < \xi_{DL}$. These results explain why ST-FMR often underestimates ξ_{DL} in comparison to quasi-static second harmonic results, the latter of which are generally confirmed by ST switching of MTJs.

Summary of Research:

Thin film samples were deposited onto 100 mm silicon wafers using our magnetron sputtering system. Structures were composed of, from bottom to top, Ta(1)/HM(t_{HM})/FM(t_{FM})/MgO(2)/Ta(1) with numbers in parenthesis representing the thickness of the layer in nanometers and t_{HM} and t_{FM} are the thicknesses of the heavy metal (HM) and ferromagnetic (FM) layers, respectively. Stacks were then patterned into 20 × 10 µm^2 micro-strips using photolithography with the 5X g-line stepper at CNF and etched using our own ion milling system. The contacts were made using the AJA sputtering system at CNF. The schematic of our devices and measurement is shown in Figure 1.

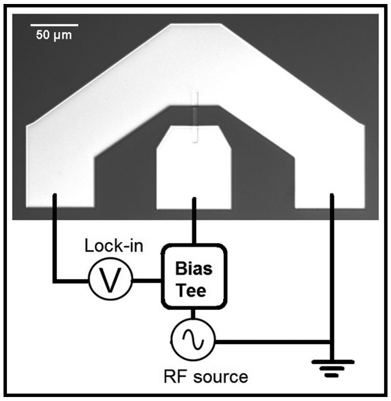

Figure 1: Microstrip with dimensions 20 × 10 µm^2 after fabrication and a schematic of the ST-FMR measurement.

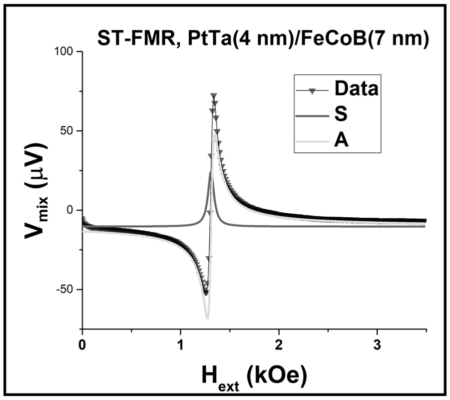

Figure 2: Example of voltage output from ST-FMR and a magnetic field sweep. The Lorentzian is fit with symmetric and antisymmetric components shown.

The spin torque efficiency (ξ) in these samples was determined using spin-torque ferromagnetic resonance (ST-FMR) [1,2]. A microwave frequency (RF) current is driven through the microstrip, which induces magnetic precession in the ferromagnetic layer via spin transfer torque. A magnetic field is swept at 45° to the microstrip and the voltage is measured by a lock-in amplifier. A lineshape analysis is done by fitting a Lorentzian function with symmetric (S) and antisymmetric (A) components as shown in Figure 2. The ratio of the prefactors S and A yield ξ_{FMR}.

Traditionally, spin pumping is not taken into account, and without the presence field-like torque ξ_{FMR} would be the same as the damping-like torque efficiency ξ_{DL}. Experimentally we achieve samples without a strong field-like torque by insertion of a Hf spacer layer between the HM and FM layers in the case of Pt based samples such as $Pt_{0.9}Ta_{0.1}$ [2]. However, when spin pumping is accounted for, the expression for ξ_{FMR} becomes more complicated as shown by the equation in Figure 3. Here we have separated two terms for the damping-like spin torque efficiency: one for the value obtained from the traditional analysis of the FMR signal, and one for the value obtained from the portion of the signal due to spin pumping. The entire portion of the signal subtracted from the FMR ξ_{DL} is due to spin pumping. Importantly, we can see some terms that would cause this signal to become larger such as higher HM resistivity samples and samples with thicker HM and FM layers.

We expected that the $Pt_{0.9}Ta_{0.1}$ alloy is a good HM for showing spin pumping because of its higher resistivity and large spin torque efficiencies as a Pt system. The result of an ST-FMR measurement of an 8 nm $Pt_{0.9}Ta_{0.1}$ sample with varying FeCoB thickness is shown in Figure 4. Here we see that the signal inferred from traditional FMR analysis is $\xi_{DL} = 0.064$. However, it is clear that ξ_{FMR} changes as a function of FM thickness. This is due to spin pumping and has the predicted behavior of subtracting from the signal and increasing in magnitude as the FM layer becomes thicker, as predicted in Figure 3. A quantitative analysis yields $\xi_{DL} = 0.34$ as measured from the spin pumping signal. This is much larger than the signal from traditional ST-FMR and agrees more closely with values obtained from similar Pt-based alloy systems [4] and with our own second harmonic measurements of $Pt_{0.9}Ta_{0.1}$ of around $\xi_{DL} = 0.3$ as well. Using different thicknesses of $Pt_{0.9}Ta_{0.1}$ we also observed spin pumping effects that were in relative strength to the thickness of the HM layer.

Conclusions and Future Steps:

We show that the spin pumping signal affects ST-FMR by subtracting from the signal and thus causing an underestimation of the damping-like spin torque efficiency of the HM layer if using only traditional analysis. In the $Pt_{0.9}Ta_{0.1}$ system, there is a clear suppression of the signal and it behaves in accordance with the equation in Figure 3.

$$\xi_{\mathrm{FMR}} = \xi_{\mathrm{DL}}^{\mathrm{FMR}} - \frac{\xi_{\mathbf{DL}}^{\mathbf{SP}}\, e^{-\frac{t}{\lambda_{\mathrm{Hf}}}}}{\rho_{\mathrm{N}}} \frac{A}{(\Delta\rho/\rho)_{\mathrm{SMR}}} \left(B t_{\mathrm{F}} \mathrm{t}_{\mathrm{N}} + \frac{{\xi_{\mathrm{DL}}^{\mathrm{FMR}}}^{2}}{B t_{\mathrm{F}} t_{\mathrm{N}}} \right)$$

$$A = \frac{h}{e}\frac{\gamma\mu_0}{32\pi} \tanh\left(\frac{t_N}{2\lambda_N}\right) \frac{\sigma_{\mathrm{F}} t_{\mathrm{F}}}{\sigma_{\mathrm{N}} \mathrm{t}_{\mathrm{N}} + \sigma_{\mathrm{F}} t_{\mathrm{F}}} \frac{1}{\alpha} \frac{\sqrt{H_{\mathrm{R}}(H_{\mathrm{R}} + 4\pi M_{\mathrm{eff}}))}}{(H_{\mathrm{R}} + 2\pi M_{\mathrm{eff}})} \quad B = \frac{\mu_0 e M_s}{\hbar} \sqrt{1 + \frac{4\pi M_{\mathrm{eff}}}{H_{\mathrm{R}}}}$$

Figure 3: The equation used for ST-FMR analysis with a spin pumping model.

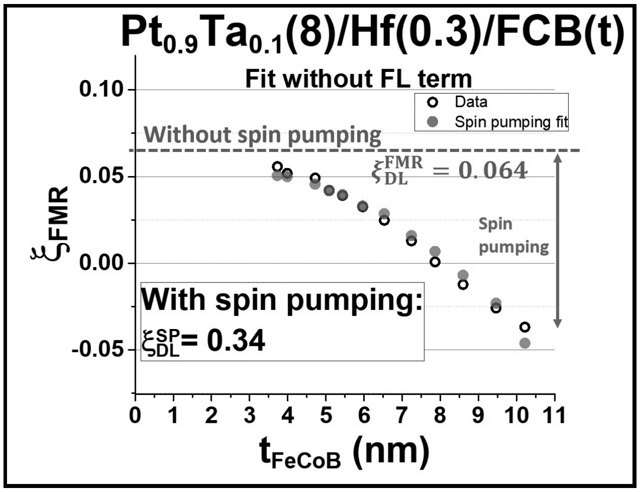

Figure 4: ST-FMR signal from an 8 nm $Pt_{0.9}Ta_{0.1}$ sample with Hf spacer and FeCoB. Fits to the data without the spin pumping model and with the spin pumping model are both shown.

Quantitative analysis yields results that agree well with other measurements, unlike the original analysis methods used which underestimate ξ_{DL}. We plan to do more experiments with different HM layers and also to fabricate more samples where we manipulate parameters such as the resistivity and also the spin torque signal itself with varying spacer layers. We expect to be able to model those results as well as those that also include a field-like torque term.

References:

[1] Luqiao Liu, et al. Phys. Rev. Lett. 106, 036601 (2011).

[2] Chi-Feng Pai, et al. Phys. Rev. B. 92, 064426 (2015).

[3] Yongxi Ou, et al. Phys. Rev. B 94, 140414 (2016).

[4] L. Zhu, D.C. Ralph, and R.A. Buhrman, Phys. Rev. Applied 10, 031001 (2018).

Spin Torque Efficiency of Cobalt Iron Boron

CNF Project Number: 598-96

Principal Investigator(s): Daniel Ralph

User(s): Thow Min Cham

Affiliation(s): Laboratory for Atomic and Solid State Physics, Cornell University

Primary Source(s) of Research Funding: National Science Foundation/Division of Materials Research, Agency for Science Technology and Research (Singapore)

Contact: dcr14@cornell.edu, tc676@cornell.edu

Primary CNF Tools Used: Autostep i-line stepper, AJA sputter deposition, DISCO dicing saw

Abstract:

A spin polarized current is generated in a ferromagnet via the anomalous Hall effect (AHE) when an electric field is applied. The polarisation of the spins depend on the polarisation direction of the spin majority band, which can be controlled by applying an external magnetic field. Unlike spin currents generated in heavy metals where the spin polarisation is constrained by symmetry to be in plane, an out-of-plane component may be present. This enables high efficiency spin torque switching of magnets with perpendicular magneto-anisotropy. In this project, we investigate the charge to spin conversion efficiency of cobalt iron boron (CoFeB).

Summary of Research:

We quantify the spin torque efficiency of CoFeB by measuring the spin torque induced oscillation of a second CoFeB layer with perpendicular magnetic anisotropy, separated from the in-plane magnetised source layer by a titanium spacer layer. Similar work has been done using both CoFeB and permalloy spin source layers [1].

The CoFeB(4nm)/Ti(2nm)/CoFeB(1nm) heterostructures were first deposited by magnetron sputtering. Hall bars were then defined and etched out of the deposited thin film heterostructure using photolithography (Autostep i-line stepper) and ion-milling. Following this, a second level of photolithography was done and a second round of magnetron sputtering (AJA sputter deposition), to deposit titanium and platinum contact pads. A schematic of the heterostructure is shown in Figure 1. The fabricated devices were then measured on a projected field magnet probe station, where a sinusoidal voltage was applied across the hall bar and the transverse hall voltage whilst sweeping the external field strength and direction.

The longitudinal electric field generates a spin polarized current in the source layer, which flows in the transverse direction into the upper readout layer. As the spin polarized current travels into the ferromagnet, the local magnetization causes transverse components to dephase and transfer spin angular momentum in the process, applying a torque on the ferromagnet. This torque is also known as the anti-damping (AD) torque, and has the form τ ∝ m × (m × σ). A second type of torque can also arise from the accumulation of spins at the interface between layers, and results in a field-like (FL) torque with the form τ ∝ m × σ, where σ is the spin polarisation vector. This effective magnetic field due to these torques can be quantified using the Harmonic Hall method [2], where the ratio between the gradient of the second harmonic and the curvature of the first harmonic is proportional to the effective magnetic field.

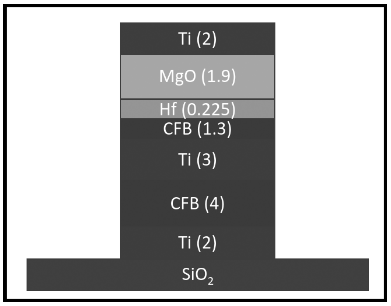

Figure 1: Schematic of the thin-film heterostructure deposited using magnetron sputtering. The two cobalt iron boron (CoFeB) layers are separated by a titanium spacer to minimise exchange coupling. A hafnium (Hf) dusting layer and a layer of magnesium oxide (MgO) was deposited on the top CoFeB layer to promote perpendicular magnetoanistropy (PMA) in the top magnet. Ti layers were used as capping layers below and on top of the heterostructure to prevent oxidation during the litho process.

To separate the AD torque from the FL torque, we apply an external magnetic field to tilt the out-of-plane magnetization of the readout magnet parallel and perpendicular to the current, such that only the AD torque and FL torques are non-zero respectively [3].

We compared the effective fields generated from the torques on the top magnetic layer with and without the bottom magnetic layer and found that there was a small but non-negligible effective field generated by the bottom CoFeB layer. Plots showing the variation of effective fields with the applied voltage are shown in Figures 2 and 3. Both the AD and FL torques increase with applied voltage and while the AD torque changes sign with mz, the FL torque remains the same sign, as expected from the formulae above.

Conclusion and Future Steps:

We have measured effective fields induced when a longitudinal current is applied through the ferromagnet CoFeB, supporting the theory that AHE in ferromagnets could lead to spin torque transfer via a spin polarized current. However, we have yet to confirm that this spin transfer torque does indeed have the same spin polarisation as the source magnet. This can be verified by sweeping the external field within the x-y plane and measuring the corresponding angular dependence of the spin torque driven oscillation of the upper readout magnet. In addition, other spin torque measurement techniques such as Spin torque ferromagnetic resonance, may be used to remove some of the thermal artifacts in the second harmonic measurement that may give an inaccurate effective field calculation.

References:

[1] Seung Heon C. Baek, Vivek P. Amin, Young Wan Oh, Gyungchoon Go, Seung Jae Lee, Geun Hee Lee, Kab Jin Kim, M.D. Stiles, Byong Guk Park, and Kyung Jin Lee. Spin currents and spin-orbit torques in ferromagnetic trilayers. Nature Materials, 17(6):509-513, June 2018.

[2] Masamitsu Hayashi, Junyeon Kim, Michihiko Yamanouchi, and Hideo Ohno. Quantitative characterization of the spin-orbit torque using harmonic Hall voltage measurements. Physical Review B-Condensed Matter and Materials Physics, 89(14), April 2014.

[3] Kevin Garello, Ioan Mihai Miron, Can Onur Avci, Frank Freimuth, Yuriy Mokrousov, Stefan Blugel, Stephane Auffret, Olivier Boulle, Gilles Gaudin, and Pietro Gambardella. Symmetry and magnitude of spin-orbit torques in ferromagnetic heterostructures. Nature Nanotechnology, 8(8):587-593, 2013.

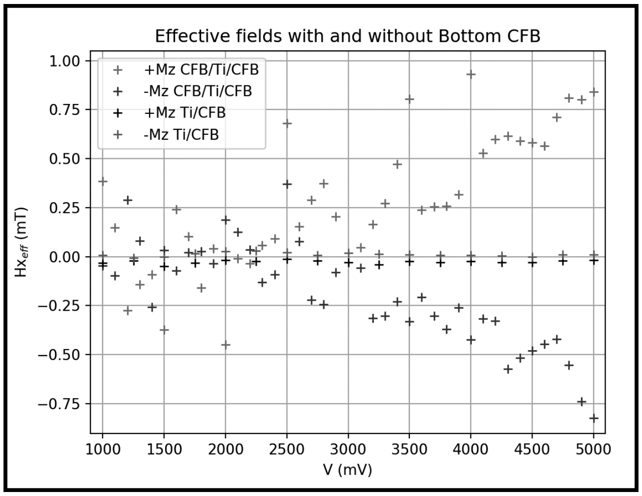

Figure 2: Anti-damping effective fields comparison with and without the CoFeB spin source layer. The effective field changes sign with the magnetization ofthe readout magnet (blue and red points), with both plots showing some voltage dependence, in contrast with the sample without the bottom CoFeB layer (black and green points). (See pages vi-vii for full color version.)

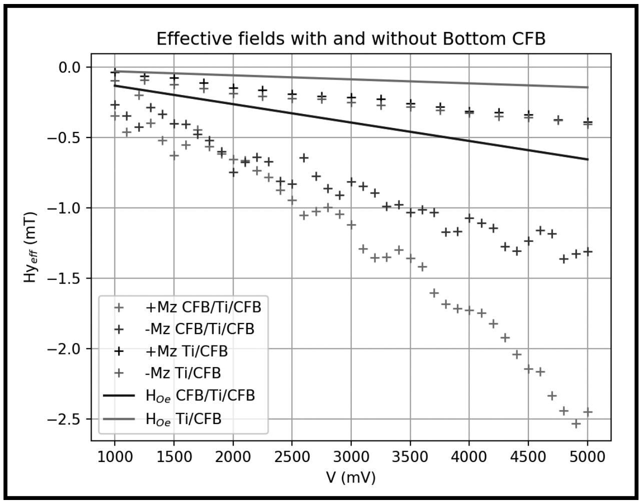

Figure 3: Field-like effective fields comparison with and without the CoFeB spin source layer. The effective field do not change sign with the magnetization of the readout magnet (blue and red points), with both plots showing some voltage dependence, in contrast with the sample without the bottom CoFeB layer (black and green points). The expected Oersted fields are plotted (blue and grey lines) to show that the measured effective fields are not solely a result of current induced Oersted fields. (See pages vi-vii for full color version.)

Microscopic Optically Powered Bubble Rockets

CNF Project Number: 900-00

Principal Investigator(s): Paul L. McEuen[1,2]

User(s): Samantha L. Norris[1], Michael F. Reynolds[1]

Affiliation(s): 1. Laboratory of Atomic and Solid State Physics, 2. Kavli Institute at Cornell for Nanoscale Science; Cornell University, Ithaca NY, USA

Primary Source(s) of Research Funding: Cornell Center for Materials Research with funding from the NSF MRSEC program (DMR-1719875), Air Force Office of Scientific Research (AFSOR) multidisciplinary research program of the university research initiative Grant FA2386-13-1-4118

Contact: plm23@cornell.edu, sn588@cornell.edu, mfr74@cornell.edu

Primary CNF Tools Used: Heidelberg DWL2000 mask writer, ABM contact aligner, Oxford 81/82/100/Cobra etchers, Xactix XeF_2 vapor etcher, AJA sputter deposition tool, Oxford PECVD, Arradiance ALD

Abstract:

We present artificial microswimmer devices that can be released from the substrate and propel themselves in fluid using bubble production and ejection. Unlike many other bubble-propelled microswimmers, ours operate in a range of fluids, including deionized water. These devices can be fabricated and released from the substrate in massive parallel using traditional photolithographic techniques. In this report, we discuss fabrication and characterization of these devices, and discuss initial results.

Summary of Research:

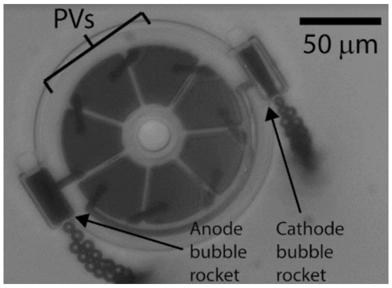

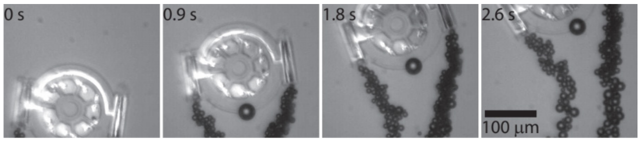

Figure 1, left: A bubble rocket in deionized water producing hydrogen at the cathode (left) and oxygen at the anode (right). Figure 2, above: A time lapse of a bubble rocket device swimming at an air-water interface, powered by a mercury lamp. The torque on the device is due to the inequality of hydrogen and oxygen production.

The ability to wirelessly power an artificial microswimmer lends itself well to a variety of applications, including *in vivo* cargo delivery [1]. Our technique for device fabrication and release from the substrate is fully scalable, allowing hundreds of thousands of devices to be studied simultaneously. In addition, the devices can be integrated with CMOS circuitry from commercial foundries, laying the foundation for additional complexity in the future.

For bubble propulsion, we create devices consisting of silicon photodiodes that provide enough voltage to perform electrolysis at two protruding electrodes, producing hydrogen and oxygen gas at the cathode and anode respectively (Figure 1). Inspired by previous works on bubble rockets [2], the electrodes are tapered to eject the produced bubbles preferentially in one direction, causing the device to be propelled forward. Under an illumination intensity of about 100 nW/μm^2 at 532 nm, a 100 μm diameter device consisting of seven photodiodes can produce about 20 μA and 4.5V. A device using bubble ejection for self-propulsion in deionized water is depicted in Figure 2.

To create the silicon photodiode devices, we begin by selectively doping the top of the device layer with phosphosilicate glass to create a vertical PN junction. We then electrically isolate the photodiodes by dry etching to the buried oxide layer in the Oxford Cobra inductively coupled plasma (ICP) etcher. At this point, we also define the shape of our tapered electrodes in the silicon.

We then connect the photodiodes in series to each other and the electrodes, also conformally coating the silicon defining the electrodes in metal at this step. The metal electrodes and interconnects are platinum with a titanium adhesion layer deposited in the AJA sputter deposition tool. We encapsulate the photodiodes with silicon dioxide using the Oxford plasma enhanced chemical vapor deposition tool, leaving the metal electrodes protruding.

Finally, we connect aluminum supports to the devices and undercut the silicon underneath them with the Xactix XeF_2 etcher — this also etches the silicon of the rockets, leaving a hollow tapered oxide cylinder with a metal undercoating. Our devices can then be released from the substrate after immersion in any aluminum etchant.

Because the operation of these devices isn't dependent on a fuel source on the electrodes or in the solution, our bubble rockets operate in a range of solutions, even deionized water. The fabrication is entirely CMOS-compatible, allowing for the future integration with more complex circuitry to enable steering and phototaxis.

References:

[1] Gao, W., Dong, R., Thamphiwatana, S., Li, J., Gao, W., Zhang, L., and Wang, J. (2015). Artificial Micromotors in the Mouse's Stomach: A Step toward *in vivo* use of Synthetic Motors. ACS Nano.

[2] Gallino, G., Gallaire, F., Lauga, E., and Michelin, S. (2018). Physics of Bubble-Propelled Microrockets. Advanced Functional Materials.

Nanofabricated Superconducting Devices for Vortex Dynamics and Qubits

CNF Project Number: 1314-05
Principal Investigator(s): Britton L.T. Plourde
User(s): Kenneth Dodge, Jaseung Ku, Yebin Liu, Michael Senatore

Affiliation(s): Department of Physics, Syracuse University
Primary Source(s) of Research Funding: Army Research Office
Contact: bplourde@syr.edu, krdodgej@syr.edu, jku102@syr.edu, yliu166@syr.edu, masenato@syr.edu
Website: https://bplourde.expressions.syr.edu/
Primary CNF Tools Used: ASML Autostepper, JEOL 9500, Plasma-Therm 770

Abstract:

We fabricate superconducting microwave devices for studying the dynamics of vortices at low temperatures and for forming novel qubits. Vortices are quantized bundles of magnetic flux that thread many different superconductors over a particular range of applied magnetic field. By using disordered superconducting thin films to form high kinetic inductance wires combined with novel arrays of Josephson junctions, we are able to build structures that can lead to qubits that are protected against decoherence.

Summary of Research:

Superconducting microwave circuits play an important role in quantum information processing. Circuits composed of Josephson junctions and capacitors with superconducting electrodes can serve as qubits, the fundamental element of a quantum computing architecture. Various loss mechanisms limit the ultimate performance of these devices, including trapped magnetic flux vortices. Vortices can be trapped in the superconducting electrodes when background magnetic fields are present and contribute dissipation when driven with microwave currents [1]. Thus, techniques for controlling the trapping of vortices are critical to the development of large-scale quantum information processors with superconducting circuits. In addition, highly disordered superconducting films, including granular Al, can be used to form wires with a compact high kinetic inductance. When combined with novel arrays of Al-AlO$_x$-Al Josephson junctions, it is possible to implement new qubit designs that are protected against decoherence [2,3].

We fabricate our microwave resonators from various superconducting films, including aluminum, deposited onto silicon wafers in vacuum systems at Syracuse University. We define the patterns at CNF on the ASML stepper and transfer them into the films with a combination of reactive ion etching and liftoff processing. For defining Josephson junctions, we use the JEOL 9500 along with a dedicated deposition system at Syracuse University. We measure these circuits at temperatures of 100 mK and below in our lab at Syracuse University.

References:

[1] Song, C., Heitmann, T.W., DeFeo, M.P., Yu, K., McDermott, R., Neeley, M., Martinis, John M., Plourde, B.L.T.; "Microwave response of vortices in superconducting thin films of Re and Al"; Physical Review B 79, 174512 (2009).

[2] Doucot, B., Ioffe, L.; "Physical implementation of protected qubits"; Reports on Progress in Physics 75, 072001 (2012).

[3] Liu, Y., Dodge, K., Senatore, M., Zhu, S., Naveen, Shearrow, A., Schlenker, F., Klots, A., Faoro, L., Ioffe, L., McDermott, R., Plourde, B.; "Implementation of pi-periodic Josephson Elements for Topologically Protected Charge-Parity Qubits"; Bull. Am. Phys. Soc. 2019, http://meetings.aps.org/Meeting/MAR19/Session/S26.11.

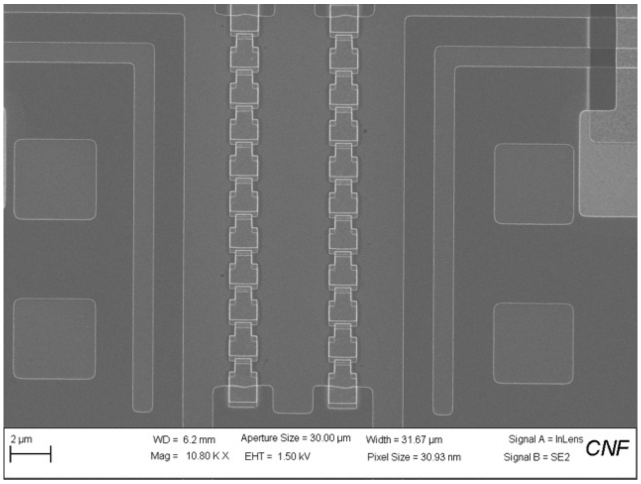

Figure 1: Scanning electron micrograph of inductors formed from arrays of Al-AlO$_x$-Al Josephson junctions for protected qubit design.

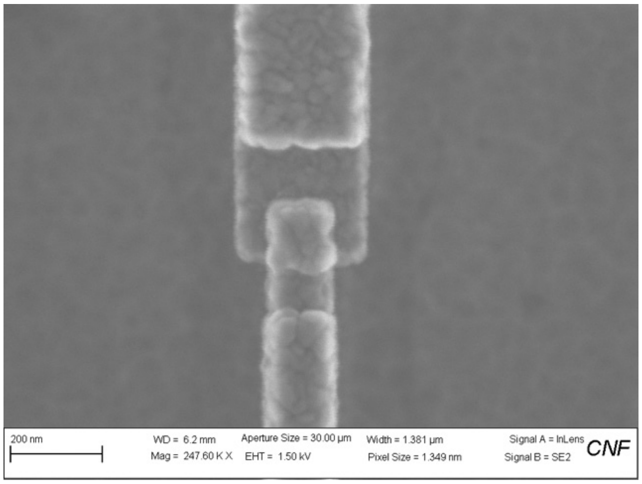

Figure 2: Scanning electron micrograph image of small-area Al-AlO$_x$-Al Josephson junction on protected qubit element.

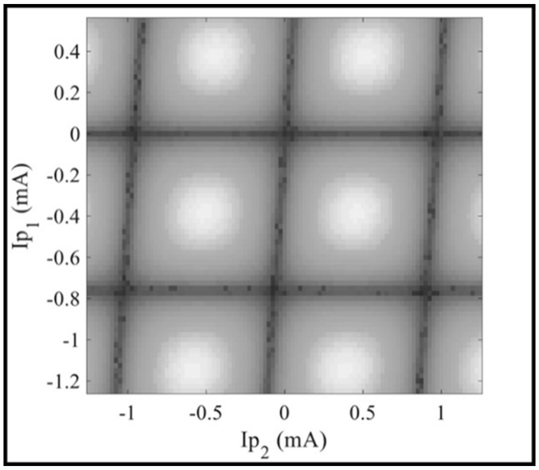

Figure 3: Two-dimensional flux bias current modulation of resonant frequency for readout microwave resonator coupled to qubit.

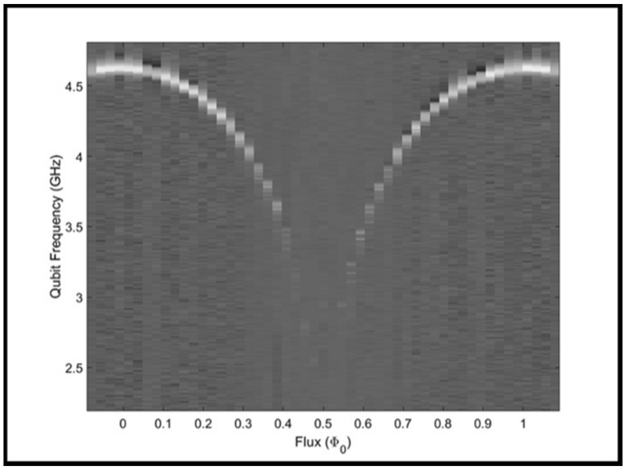

Figure 4: Flux modulation of qubit transition frequency.

Fabrication of Nanoscale Josephson Junctions for Quantum Coherent Superconducting Circuits

CNF Project Number: 1735-08

Principal Investigator(s): Britton L.T. Plourde

User(s): Andrew Ballard, Caleb Howington, Vito Iaia, Indrajeet

Affiliation(s): Department of Physics, Syracuse University

Primary Source(s) of Research Funding: Army Research Office, National Science Foundation

Contact: bplourde@syr.edu, alballar@syr.edu, cjhowing@syr.edu, vmiaia@syr.edu, indraje@syr.edu

Website: https://bplourde.expressions.syr.edu/

Primary CNF Tools Used: ASML Stepper, JEOL 9500, Plasma-Therm 770

Abstract:

We fabricate nanoscale superconductor tunnel junctions and other structures for experiments involving quantum coherent circuits. Such circuits have shown great promise in recent years for explorations of quantum mechanics at the scale of circuits on a chip and for forming qubits, the foundational elements of a quantum computer. The quantum state of these superconducting qubits can be manipulated with microwave radiation at low temperatures. In addition, we are developing alternative techniques for probing the state of these qubits and controlling their quantum state using superconducting digital circuitry, as well as superconducting metamaterial structures with novel microwave mode spectra for coupling to superconducting qubits.

Summary of Research:

The unique properties of nanoscale Josephson junctions enable a wide range of novel superconducting circuits for investigations in many diverse areas. In recent years, circuits composed of such junctions have emerged as promising candidates for the element of a quantum computer, due to the low intrinsic dissipation from the superconducting electrodes and the possibility of scaling to many such qubits on a chip [1]. The quantum coherent properties of the circuits are measured at temperatures below 50 mK with manipulation of the qubit state through microwave excitation.

We are currently working on a variety of experiments involving these nanoscale Josephson junctions and other superconducting structures that allow us to probe novel quantum effects in our microwave circuits. We are fabricating superconducting circuits for forming low-temperature detectors of single microwave photons and for implementing a new scheme for the efficient readout of the quantum state of superconducting qubits [2,3]. We are also working with collaborators at the University of Wisconsin, Madison to develop hybrid quantum/classical superconducting chips that allow us to perform coherent quantum control of a superconducting qubit based on digital pulses from a Single Flux Quantum (SFQ) circuit [4,5].

In another effort, we are using particular combinations of superconducting lumped-circuit elements to engineer metamaterial transmission lines that exhibit novel mode structures characteristic of left-handed materials. We are fabricating such metamaterial transmission lines from Al and Nb films on Si and characterizing these at low temperatures [6]. We are working on experiments to couple these left-handed lines to superconducting qubits for experiments involving the exchange of microwave photons [7].

We pattern these circuits at the CNF with nanoscale structures defined with electron-beam lithography on the JEOL 9500 integrated with photolithographically defined large-scale features. The junctions are fabricated using the standard double-angle shadow evaporation technique, in which a resist bilayer of copolymer and PMMA is used to produce a narrow PMMA airbridge suspended above the substrate. Evaporation of aluminum from two different angles with an oxidation step in between forms a small Al-AlO$_x$-Al tunnel junction from the deposition shadow of the airbridge. We have developed a process for defining these junctions with electron-beam lithography and we perform the aluminum evaporations in a dedicated chamber at Syracuse. We pattern large-scale features using the ASML stepper, with electron-beam evaporation of Al and sputter-deposition of Nb. Measurements of these circuits are performed in cryogenic systems at Syracuse University, including dilution refrigerators for achieving temperatures below 30 mK.

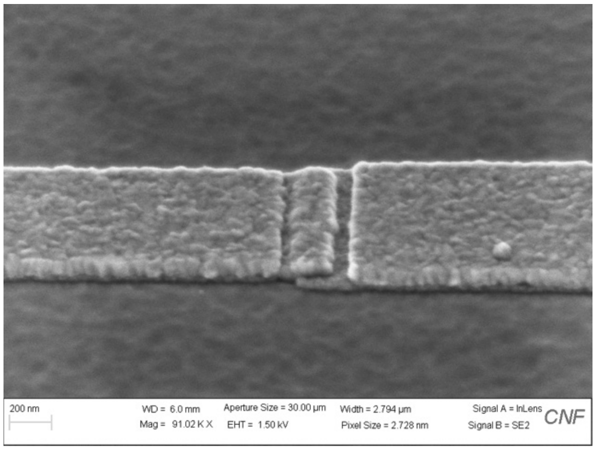

Figure 1: Scanning electron micrograph of Al-AlO$_x$-Al Josephson junction for superconducting qubit.

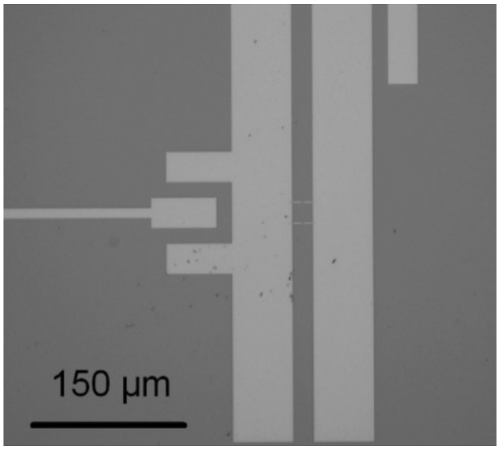

Figure 2: Optical micrograph of superconducting qubit coupled to metamaterial transmission line resonator.

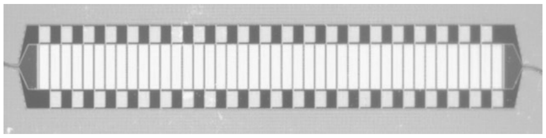

Figure 3: Optical micrograph of superconducting metamaterial transmission line resonator fabricated from Nb thin film on Si.

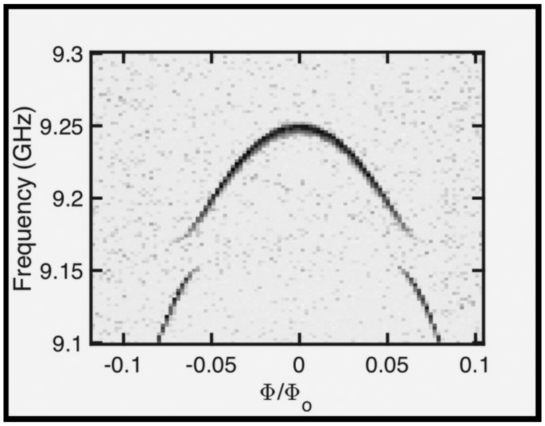

Figure 4: Spectroscopic measurement of flux modulation of qubit transition frequency for qubit coupled to metamaterial transmission line resonator.

References:

[1] Clarke, J. and Wilhelm, F.K.; "Superconducting quantum bits"; Nature, 453, 1031 (2008).

[2] Govia, L.C.G., Pritchett, Emily J., Xu, Canran, Plourde, B. L. T., Vavilov, Maxim G., Wilhelm, Frank K., McDermott, R.; "High-fidelity qubit measurement with a microwave-photon counter"; Physical Review A 90, 062307 (2014).

[3] Opremcak, A, Pechenezhskiy, I., Howington, C.,. Christensen, B.G., Beck, M.A., Leonard Jr, E., Suttle, J., Wilen, C., Nesterov, K.N., Ribeill, G.J., Thorbeck, T., Schlenker, F., Vavilov, M.G., Plourde, B.L.T., McDermott, R.; "Measurement of a Superconducting Qubit with a Microwave Photon Counter"; Science 361, 1239 (2018).

[4] McDermott, R., Vavilov, M.; "Accurate Qubit Control with Single Flux Quantum Pulses"; Physical Review Applied 2, 014007 (2014).

[5] Leonard, E., Beck, M., Nelson, JJ, Christensen, B., Thorbeck, T., Howington, C., Opremcak, A.,Pechenezhskiy, I., Dodge, K., Dupuis, N., Ku, J., Schlenker, F., Suttle, J. Wilen, C., Zhu, S., Vavilov, M., Plourde, B, McDermott, R.. "Digital coherent control of a superconducting qubit"; Phys.Rev.Applied 11, 014009 (2019).

[6] Wang, H., Zhuravel, A., Indrajeet, S., Taketani, B., Hutchings, M., Hao, Y., Rouxinol, F., Wilhelm,F., LaHaye, M.D., Ustinov, A., Plourde, B.; "Mode Structure in Superconducting Metamaterial Transmission Line Resonators"; Physical Review Applied 11, 054062 (2019).

[7] Indrajeet, S., Wang, H., Hutchings, M., LaHaye, M., Taketani, Bruno, Wilhelm, F., Plourde, B.; "Qubit Dynamics in a Multi-mode Environment with a Superconducting Metamaterial Resonator"; Bull. Am. Phys. Soc. 2019, http://meetings.aps.org/Meeting/MAR19/Session/P26.4.

Local Photothermal Control of Phase Transitions for On-Demand Room-Temperature Rewritable Magnetic Patterning

CNF Project Number: 2091-11

Principal Investigator(s): Gregory D. Fuchs[1], Darrell G. Schlom[2]

User(s): Isaiah Gray[1]

Affiliation(s): 1. School of Applied and Engineering Physics, 2. Materials Science and Engineering; Cornell University

Primary Source(s) of Research Funding: Cornell Center for Materials Research from the National Science Foundation MRSEC Program, Grant No. DMR-1719875

Contact: gdf9@cornell.edu, ig246@cornell.edu

Primary CNF Tools Used: GCA 5x stepper

Abstract:

The ability to make controlled patterns of magnetic structures within a nonmagnetic background provides the foundation of magnetic memory and logic devices, allows the creation of artificial spin-ice lattices, and enables the study of magnon propagation. Here, we report a novel approach for magnetic patterning that allows repeated creation and erasure of arbitrary shapes of thin-film ferromagnetic structures. This strategy is enabled by epitaxial $Fe_{0.52}Rh_{0.48}$ thin films designed so that both ferromagnetic and antiferromagnetic phases are stable at room temperature. Starting with the film in a uniform antiferromagnetic state, we demonstrate the ability to write arbitrary patterns of the ferromagnetic phase with submicron spatial resolution by local heating with a focused pulsed laser. The ferromagnetic patterns can be erased by cooling below room temperature and the material repeatedly re-patterned.

Summary of Research:

Local patterning of ferromagnetic regions forms the basis of magnetic logic and memory devices [1] as well as spin-wave devices such as magnon waveguides [2] and magnonic crystals [3]. Magnetic nanostructures are typically patterned with lithography and etching, which cannot be easily erased and repatterned. In this work [4] we present a platform for rewritable magnetic patterning, which is based on the 1st-order phase transition from antiferromagnet (AF) to ferromagnet (FM) in near 50/50 stoichiometric iron-rhodium (FeRh) [5].

Epitaxial FeRh films are grown on MgO(001) via molecular-beam epitaxy. Lower Rh concentration decreases the transition temperature T_C [6]; we therefore tune the stoichiometry to $Fe_{0.52}Rh_{0.48}$ during growth, which sets $T_C \approx 430$ K such that both AF and FM phases are stable at room temperature.

In Figure 1 we show radial plots of magnetization M as a function of magnetic field H (clockwise) and temperature T (radial). We plot $M(H,T)$ in both the cooling branch (Figure 1(a)) and the heating branch (1(b)) of the transition, which highlights the dissimilar T_C in heating (AF to FM) and cooling (FM to AF).

Plots of $M(T)$ and resistance $R(T)$ at constant field in Figure 1(c) and 1(d) show that both AF and FM phases are stable at 293 K.

Having established room-temperature phase bistability, we pattern local FM regions using a laser focused to ~ 650 nm spot size at 10.8 mJ/cm^2 fluence, which locally heats the FeRh by 90K. This temperature increase induces the FM phase, which remains after the laser is turned off. We image the resulting patterns with the same laser at low (0.6 mJ/cm^2) fluence, using anomalous Nernst microscopy [7].

In this technique, the focused laser generates a local thermal gradient ∇T, which induces an electric field $\boldsymbol{E}_{ANE}$ proportional to the moment: $\boldsymbol{E}_{ANE} = -N\mu_0 \nabla T \times \boldsymbol{M}$.

We raster scan the laser and measure the $\boldsymbol{E}_{ANE}$-induced voltage drop across the entire sample, which builds up a map of in-plane $\boldsymbol{M}$. By using low fluence, we image magnetic contrast without perturbing it.

Two examples of patterning and imaging are shown in Figure 2. In Figure 2(a) we show three anomalous Nernst effect (ANE) images at room temperature: one in the uniform AF phase before patterning, one after laser-writing FM patterns spelling out the authors' affiliation, and one after cooling the film below room temperature and warming back to room temperature. To subtract out artifacts from varying thermal conductivity and isolate the magnetic signal, each image presented is the

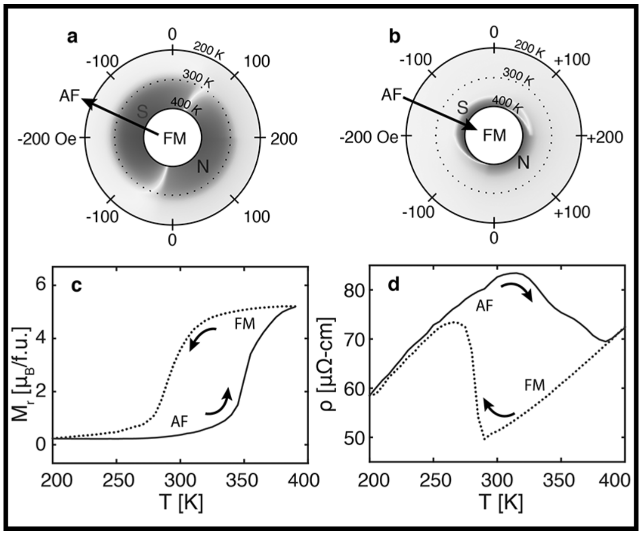

Figure 1: (a,b) Magnetization M *as a function of temperature* T *and magnetic field* H *in epitaxial* $Fe_{0.52}Rh_{0.48}$ *grown on MgO(001). The phase transition is observed in (a) the cooling branch and (b) the heating branch, showing the dissimilar transition temperatures between antiferromagnet to ferromagnet and vice versa. (c)* M(T) *and* R(T) *at fixed field show that both AF and FM phases are stable at room temperature.*

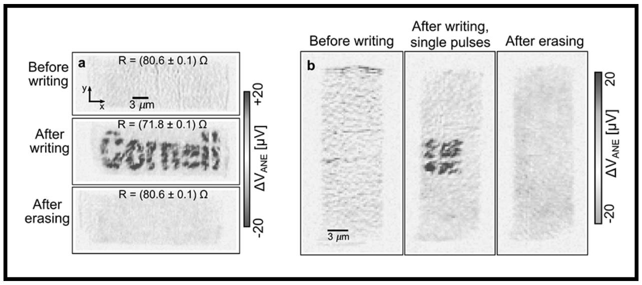

Figure 2: Laser-writing ferromagnetic regions within an antiferromagnetic background and imaging the written regions using anomalous Nernst microscopy. (a) Imaging at room temperature in the AF phase, after laser-writing, and after erasing by cooling and warming back to room temperature. (b) Demonstrating ultrafast patterning by imaging a 5 µm square written using a single 3 ps laser pulse per pixel. (See pages vi-vii for full color version.)

half-difference between raw ANE images acquired at 1 kOe magnetic field applied along opposite directions. Light red contrast represents uncompensated moments in the AF phase [8], while dark red represents FM moments. The images show that ferromagnetic regions can be patterned with submicron resolution, and that they are erased by cooling the sample below room temperature. Finally, in Figure 2(b) we demonstrate ultrafast magnetic patterning by writing a 5 × 5 µm square using a single 3 ps-wide laser pulse per pixel.

In summary, we demonstrate a platform for room-temperature rewritable magnetic patterning in bistable FeRh. Laser-written FM regions can be erased by cooling, and the film can be erased and rewritten many times with no measurable damage to the crystal structure. Our results could enable rapid prototyping of a variety of magnetic devices, including magnonic crystals and logic devices.

References:

[1] S. N. Piramanayagam, T. C. Chong, Developments in Data Storage: Materials Perspective, Wiley, 2011.

[2] A. V. Chumak, et al., Nat. Phys. 11, 453 (2015).

[3] B. Lenk, H. Ulrichs, F. Garbs, and M. Müzenberg, Phys. Rep. 507, 107-136 (2011).

[4] A. B. Mei*, I. Gray*, et al., Adv. Mater. (accepted), arXiv:1906.07239 (2019).

[5] J. B. McKinnon, D. Melville, and E. W. Lee, J. Phys. C 3, S46 (1970).

[6] A. B. Mei, et al., Appl. Phys. Lett. 113, 082403 (2018).

[7] J. M. Bartell*, D. H. Ngai*, et al., Nat. Comm. 6, 8460 (2015).

[8] I. Gray, et al., Phys. Rev. Mater. 3, 124407 (2019).

Topological Hall Effect in MnFeGe/FeGe Bilayer Thin Films

CNF Project Number: 2091-11
Principal Investigator(s): Gregory Fuchs
User(s): Varshith Kandula

Affiliation(s): Applied and Engineering Physics, Cornell University
Primary Source(s) of Research Funding: Cornell Center for Materials Research (DMR-1719875)
Contact: gdf9@cornell.edu, vk332@cornell.edu
Website: http://fuchs.research.engineering.cornell.edu/
Primary CNF Tools Used: GCA 5x stepper, AJA ion mill, SC4500 even-hour evaporator

Abstract:

We investigate the topological Hall effect (THE) in MnFeGe/FeGe and MnFeGe/FeGe/Pt thin films using Hall measurements. These materials host nanometer-sized quasiparticles called skyrmions in a range of temperature and magnetic field. Skyrmions are promising candidates for future applications in high density magnetic storage devices, for example, as bits to store information, and in racetrack type computing devices owing the low current densities required to move them. The presence of skyrmions results in an effective magnetic field acting on transport electrons that appears as an extra term to the Hall resistance. We compare the THE resistance of MnFeGe/FeGe and MnFeGe/FeGe/Pt and find that it is extended in the Pt-capped film.

Summary of Research:

MnFeGe and FeGe have a chiral B20 structure that induces antisymmetric exchange called the Dzyaloshinski-Moriya Interaction (DMI) that favors canting of magnetic spins. In conjunction with the Zeeman, exchange, magnetostatic, magnetocrystalline anisotropy and dipole-dipole interaction terms it stabilizes exotic spin structures called skyrmions [1] in a region of the temperature and external magnetic field. These quasiparticles are topologically stabilized once formed, and a finite energy is required to collapse a skyrmion into a trivial ferromagnetic (antiferromagnetic) state. A major direction of current research is stabilizing skyrmions at room temperature and zero magnetic fields in thin films for potential applications. Skyrmions can also be stabilized at ferromagnet (FM)/heavy metal (HM) interfaces [2] at room temperature due to interfacial DMI from large spin-orbit coupling (SOC) originating in the HM layer.

Skyrmions can be imaged directly by Lorentz transmission electron microscopy (LTEM), electron holography (EH), and magnetic force microscopy (MFM), and the skyrmion lattice can be detected in reciprocal space by small angle neutron scattering (SANS) and resonant elastic X-ray scattering (REXS) [3]. Indirect methods of detecting the skyrmion phase boundary include AC magnetic susceptibility (ACMS), microwave absorption spectroscopy (MAS), magnetoresistance vs. field and topological Hall effect measurements.

The presence of topologically non-trivial spin textures such as magnetic skyrmions can be modelled by an emergent magnetic field, which contributes an additional term to the Hall effect signal (the topological Hall resistance). The Hall resistance has three contributions; 1) an ordinary Hall resistance (OHR) due to the Lorentz force on electrons proportional to the external magnetic field, 2) an anomalous Hall resistance (AHR) in ferromagnets arising from SOC and/or spin dependent scattering that is approximately proportional to the magnetization, and 3) topological Hall resistance (THR). By subtracting the calculated OHR and AHR contributions from the measured Hall resistance the THR can be estimated in a sample.

Figure 1 shows the fabricated Hall device of two samples, MnFeGe(20nm)/FeGe(7nm) and MnFeGe(20nm)/FeGe(4nm)/Pt(1.5nm). The Heidelberg mask writer DWL2000 was used to make photomasks and photolithography was performed on a GCA 5x Stepper. An AJA ion mill was used to etch the material into a Hall geometry. An SC4500 even-hour evaporator was used to make gold contact pads for electrical measurements. Hall resistance as a function of the magnetic field at temperatures between 40 Kelvin (K) - 240 K was measured in a Quantum Design physical property measurement system (PPMS).

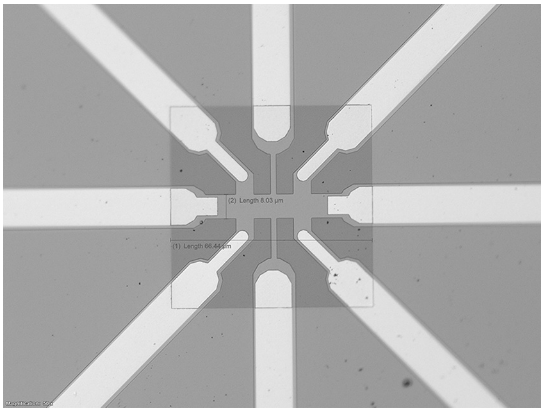

Figure 1: Patterned Hall bar device.

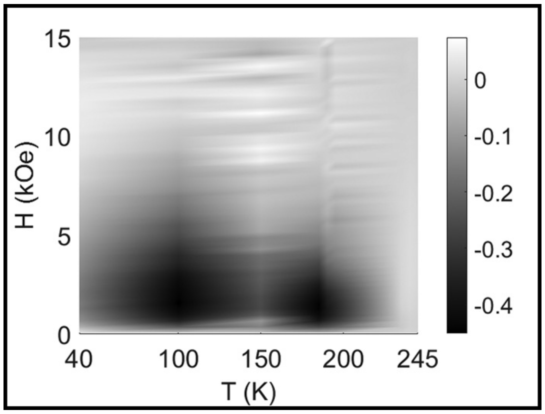

Figure 2: THR of MnFeGe(20nm)/FeGe(7nm).

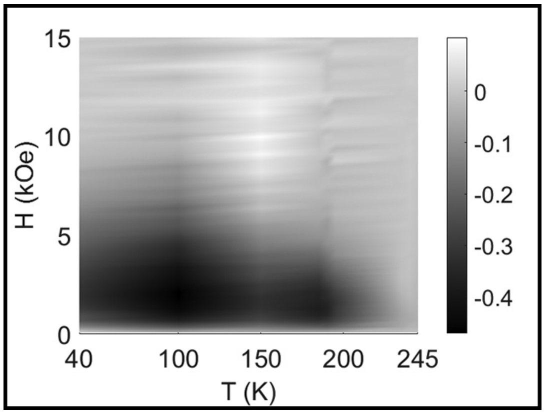

Figure 3: THR of MnFeGe(20nm)/FeGe (4nm)/Pt(1.5nm).

Figure 2 shows the THR (resistance given in ohms) as a function of temperature and external field for MnFeGe/FeGe and Figure 3 shows the THR for MnFeGe/FeGe/Pt. MnFeGe is known to host skyrmions below a critical temperature (T_c) ~ 180K and FeGe hosts skyrmions below T_c ~ 270K.

We observe a broadened phase space of the THR in the Pt-capped sample compared the MnFeGe/FeGe bilayer, which could be due to an increase in skyrmion stability from the interplay between interfacial DMI from Pt and bulk DMI from MnFeGe and FeGe. The THR could also arise due to other non-trivial magnetic textures and further experiments are needed to identify its origin.

Conclusions and Future Steps:

We have measured the THR of skyrmion-hosting B20 thin films and report a broadened phase space in the heavy metal capped sample. To further study the magnetic phases in our thin films we have fabricated spin-transfer ferromagnetic resonance (ST-FMR) [4] devices, which could shed light on resonant dynamics of the skyrmion phase.

References:

[1] Nagaosa, N., and Tokura, Y. (2013). Topological properties and dynamics of magnetic skyrmions. Nature Nanotechnology, 8(12), 899-911.

[2] Moreau-Luchaire, C., et al. (2016). Additive interfacial chiral interaction in multilayers for stabilization of small individual skyrmions at room temperature. Nature Nanotechnology, 11(5), 444-448.

[3] Mathur, N., Stolt, M. J., and Jin, S. (2019). Magnetic skyrmions in nanostructures of non-centrosymmetric materials. APL Materials, 7(12).

[4] Liu, L., Moriyama, T., Ralph, D. C., and Buhrman, R. A. (2011). Spin-torque ferromagnetic resonance induced by the spin Hall effect. Physical Review Letters, 106(3), 1-4.

Development of Operando Magnetic Device for Lorentz Transmission Electron Microscopy

CNF Project Number: 2091-11

Principal Investigator(s): Gregory D. Fuchs, David A. Muller

User(s): Albert M. Park

Affiliation(s): Applied Physics, Cornell University

Primary Source(s) of Research Funding: Defense Advanced Research Projects Agency (DARPA)

Contact: gdf9@cornell.edu, amp356@cornell.edu

Primary CNF Tools Used: GCA 5X stepper, wet stations, CVC evaporators, Heidelberg mask writer, dicing saw

Abstract:

We develop a magnetic device for operando Lorentz transmission electron microscope (LTEM) studies of magnetic skyrmions under the application of electric current pulses. We study the creation and annihilation of skyrmions in the presence of a strong pinning defect within a ferromagnetic multilayer with interfacial Dzyaloshinskii-Moriya interaction (DMI). We also show that Joule heating plays a primary role in this process. By controlling the magnetic field and total injected thermal energy, we can control the skyrmion density. Additionally, we study the relationship between skyrmion density and skyrmion stability to variations in the magnetic field. Our results show that the higher density skyrmions resist annihilation over a wider range of magnetic field.

Summary of Research:

Magnetic skyrmions are promising for potential high-performance memory and neuromorphic computing devices, however, to understand their behavior and dynamics at the smallest scales, a method of nanoscale imaging is essential [1,2]. To date, the study of chiral magnetic features in LTEM has been limited to operando changes of the magnetic field and temperature, with a few exceptions of single-crystalline samples, which were thinned and micropatterned by focus ion beam (FIB) for application of DC current [3-5]. To enable the study of skyrmion behavior with the application of electric current pulses, we develop a skyrmion device platform that is compatible with operando electrical biasing inside an electron microscope.

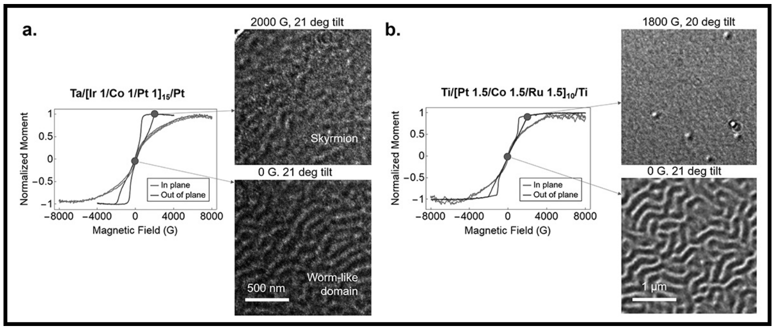

Figure 1: Magnetic hysteresis determined by vibrating sample magnetometry (VSM) and the LTEM image of spin textures for (a) Ta(2)/[Ir (1 nm)/Co (1 nm)/Pt (1 nm)]15 and (b) Ti(3)/[Pt (1.5 nm)/Co (1.5 nm)/Ru (1.5 nm)]10.

We start by optimizing the skyrmion materials. Two important micromagnetic interactions for stabilization of skyrmions in a thin-film multilayer structure are interfacial Dzyaloshinskii Moriya Interaction (DMI) and perpendicular magnetic anisotropy (PMA). We use platinum/cobalt (Pt/Co) bilayers to ensure PMA in our films. Iridium (Ir) or ruthenium (Ru) is used for the third layer because the interface on the opposite side of Pt in Pt/Co/Ir or Pt/Co/Ru trilayer is known to have an additive effect on effective DMI [6]. While we observe nucleation of skyrmions from both Pt/Co/Ir and Pt/Co/Ru stacks, we find that samples seeded from Ti/Pt or Ta/Pt on the membrane shows better LTEM contrast (Figure 1).

To enable an LTEM study of the chiral magnetic materials, we need to fabricate our device on an electron transparent material such as SiN_x membrane with a thickness of less than 100 nm. We use a Protochip™ fusion e-cell, which is composed of a 50 nm thick SiN_x

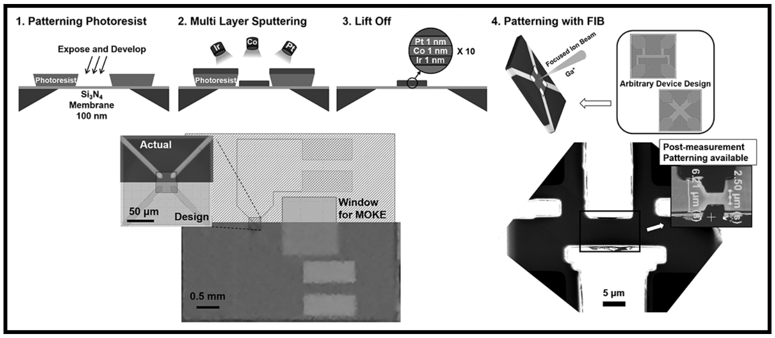

Figure 2: Fabrication process flow for the operando device. Optical image of Protochip™ fusion e-cell template overlaid with mask pattern for photolithography (left below) and a scanning electron micrograph of the device after patterning with FIB (right below). (See pages vi-vii for full color version.)

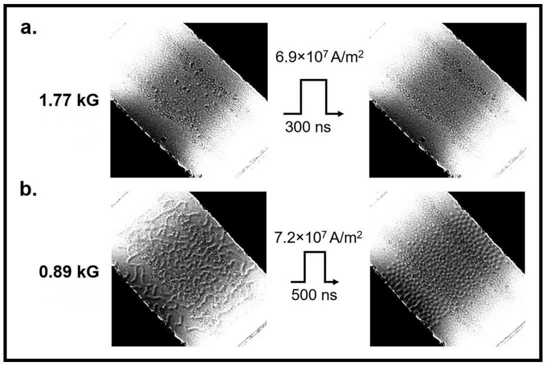

Figure 3: Current induced thermal annihilation (a) and nucleation (b) of skyrmions in the device.

membrane window with gold electrodes that extend toward the center of the membrane as a template to build our device. Multiple repeats of heavy metal/ferromagnet/heavy metal trilayer are deposited using an AJA sputter system (Figure 2). While micrometer-scale devices can be fabricated by lift-off alone, focused ion beam (FIB) can also be used as a post-processing method to define smaller features. We confirm that a versatile approach of defining a larger area of the film first and then direct writing a specific shape using FIB is possible.

Using the device, we observe thermal nucleation and annihilation of skyrmions induced by current-induced Joule heating (Figure 3) and quantify the energetics of the magnetic states with micromagnetic simulations. We find that the skyrmions are strongly bound to point-like pinning sites created by defects that are inherently present on the SiNx membrane provided by Protochip™. The thermal nucleation process enables the control of the skyrmion density choosing the magnetic field and the current pulse energy. Next, we investigate the stability of skyrmions as a function of their density. After systematically initializing a particular skyrmion density, we vary the magnetic field to find the magnetic field range that the skyrmions are stable. We find that while all skyrmions annihilate at high field regardless of the initial density, the lower bound of skyrmion stability is proportional to the initial skyrmion density.

Conclusions and Future Steps:

In conclusion, we have optimized a chiral material heterostructure and established a fabrication process for operando electron microscope studies of skyrmion creation and annihilation using electric current in the presence of strong magnetic pinning sites. We find that a thermal mechanism dominates these processes and that the resulting skyrmions have density-dependent stability. Understanding this mechanism has implications for controlling the density of skyrmions in devices. Additionally, operando transport properties such as the topological Hall effect and its relation to the nature of the chirality and the pinning effects can be investigated in the future based on this platform.

References:

[1] X. Zhang, Y. Zhou, K. Mee Song, T. Park, J. Xia, M. Ezawa, X. Liu, W. Zhao, G. Zhao, and S. Woo, J. Phys. Condens. Matter 32, 143001 (2020).

[2] N. Nagaosa and Y. Tokura, Nat. Nanotechnol. 8, 899 (2013).

[3] X. Z. Yu, N. Kanazawa, W. Z. Zhang, T. Nagai, T. Hara, K. Kimoto, Y. Matsui, Y. Onose, and Y. Tokura, Nat. Commun. 3, (2012).

[4] X. Z. Yu, Y. Tokunaga, Y. Kaneko, W. Z. Zhang, K. Kimoto, Y. Matsui, Y. Taguchi, and Y. Tokura, Nat. Commun. 5, (2014).

[5] L. Peng, Y. Zhang, M. He, B. Ding, W. Wang, H. Tian, J. Li, S. Wang, J. Cai, G. Wu, J. P. Liu, M. J. Kramer, and B. G. Shen, Npj Quantum Mater. 2, 1 (2017).

[6] D. Khadka, S. Karayev, and S. X. Huang, J. Appl. Phys. 123, 123905 (2018).

Frequency Domain Measurements of Arrays of Constriction-Based Spin-Hall Nano-Oscillators in Weak In-Plane Fields

CNF Project Number: 2091-11

Principal Investigator(s): Gregory D. Fuchs

User(s): Yanyou Xie

Affiliation(s): Applied and Engineering Physics, Cornell University

Primary Source of Research Funding: National Science Foundation

Contact: gdf9@cornell.edu, yx322@cornell.edu

Primary CNF Tools Used: JEOL 9500, MA6 contact aligner

Abstract:

Spin-Hall nano-oscillators (SHNOs) convert D.C. charge current to microwave frequency magnetic oscillations — enabling applications as highly agile microwave sources. The use of SHNOs for applications is still limited by low output microwave power and large linewidth. Mutual synchronization of arrays of constriction-based SHNOs under out-of-plane magnetic fields close to 1 T [1] have been studied as a route to improve these characteristics. However, such high magnetic fields are impractical for device applications. Therefore, we study mutual synchronization in devices under in-plane magnetic fields of tens of mT. We fabricated arrays of four constriction-based SHNOs with different geometries, and performed frequency domain measurements under varied bias current and magnitude of magnetic field.

Summary of Research:

The spin Hall effect (SHE) is the generation of transverse spin currents by electric currents; in a non- magnetic material (NM), this leads to the accumulation of spins with opposite polarization at opposite edges of the NM [2,3]. By placing a nonmagnetic film on top of a ferromagnetic film, the spin current generated in the NM can diffuse into the ferromagnet (FM), providing spin transfer torque (STT) to the FM [2]. Under suitable conditions, the STT is able to compensate the damping of magnetic precession, leading to steady precession of magnetization [4]. With this principle, spin-Hall nano-oscillators (SHNOs) are developed as a bilayer system consisting of NM and FM, patterned as nanowires or nanoconstrictions.

In our study, we fabricated arrays of four $Ni_{81}Fe_{19}$ (5 nm)/$Au_{0.25}Pt_{0.75}$ (5 nm) constriction-based SHNOs on 20.5 µm × 4 µm wires, with different constriction width, separation and lateral shift. We used JEOL 9500 for the e-beam patterning of the SHNOs, and MA6 contact aligner and evaporator for depositing contact pads for electrical measurements. We measured the auto-oscillations of two devices. Each has a constriction width w = 100 nm, constriction separation a = 550 nm, however, one has in-line constrictions (Figure 1a), and the other with a lateral shift of the constrictions corresponding to a 30° angle (Figure 1b).

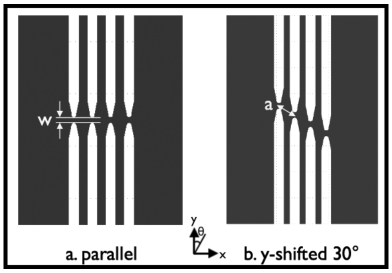

Figure 1: Central areas of SHNOs studied: (a) in-line constrictions (b) constrictions with a lateral shift.

To measure the auto-oscillations, we apply a D.C. charge current to the device under a static in-plane magnetic field. Magnetic precession is induced in the FM ($Ni_{81}Fe_{19}$) due to SHE, leading to the oscillation of the FM layer's resistance due to anisotropic magnetoresistance. The oscillation signals are then measured using a spectrum analyzer with a pre-amplifier.

For the device with a lateral shift, we observed a single dominant peak over a range of currents at external

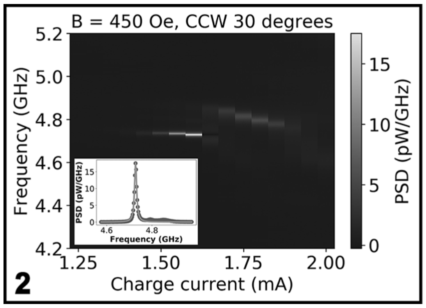

2

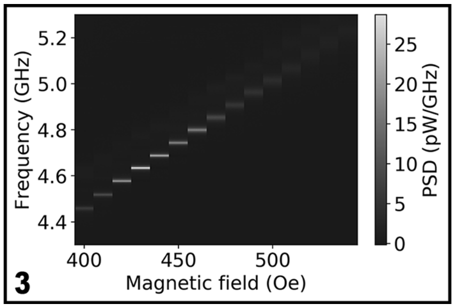

3

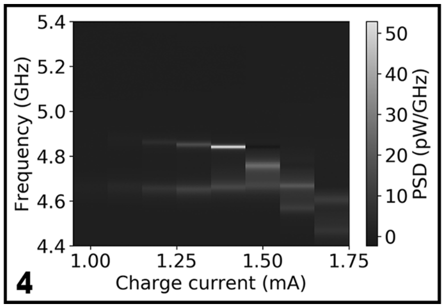

4

Figure 2, left: *Power spectral density (PSD) of device with lateral shift under* H *= 450 Oe with* θ *= 30°. Inset: the peak profile at 1.6 mA (dots) with Lorentzian fit (line).* ***Figure 3, middle:*** *PSD of device with lateral shift under a magnetic field with* θ *= 30° and charge currents of 1.6 mA.* ***Figure 4, right:*** *PSD of device with in-line constrictions under* H *= 450 Oe with* θ *= 30°. (See pages vi-vii for full color versions.)*

magnetic field H = 450 Oe applied θ = 30° with respect to the y axis (Figure 2). The angle of magnetic field accounts for the directionality of the spin wave emission perpendicular to the magnetic field [5]. By fitting the peak with a Lorentzian (Figure 2 inset), we extrapolate the linewidth of the optimal peak to be 10.8 MHz and the total power to be 0.2 pW, which is comparable to a prior report [6] in devices with similar resistance. We also observe a jump in the oscillation frequency, which is possibly due to the switching of dynamic modes [7]. At 1.6 mA bias current, the auto-oscillation frequency increases linearly with H; only one dominant peak occurs (Figure 3), suggesting that there may be some synchronization [1]. However, to verify whether the SHNOs are actually mutually synchronized, a study of the phase difference between them is required.

We also measured the auto-oscillation on the device with in-line constrictions under the same external magnetic field (Figure 4). In this case, two modes are observed at the same bias current, suggesting that the SHNOs are not synchronized.

Conclusions and Future Steps:

We performed frequency domain measurements on two of the fabricated devices, however, we have not yet experimentally confirmed mutual synchronization. Future studies using optical imaging techniques may reveal the phase information of the individual SHNOs. We also plan to study devices with smaller separation between constrictions, which we expect to synchronize robustly.

References:

[1] A. Awad, et al., "Long-range mutual synchronization of spin hall nano-oscillators," Nature Physics, vol. 13, no. 3, pp. 292-299, 2017.

[2] J. Sinova, et al., "Spin hall effects," Reviews of Modern Physics, vol. 87, no. 4, p. 1213, 2015.

[3] M. D'yakonov and V. Perel, "Possibility of orienting electron spins with current," Soviet Journal of Experimental and Theoretical Physics Letters, vol. 13, p. 467, 1971.

[4] D. C. Ralph and M. D. Stiles, "Spin transfer torques," Journal of Magnetism and Magnetic Materials, vol. 320, no. 7, pp. 1190-1216, 2008.

[5] T. Kendziorczyk and T. Kuhn, "Mutual synchronization of nanoconstriction-based spin Hall nano-oscillators through evanescent and propagating spin waves," Physical Review B, vol. 93, no. 13, p.134413, 2016.

[6] H. Mazraati, et al., "Low operational current spin Hall nano-oscillators based on NiFe/W bilayers," Applied Physics Letters, vol. 109, no. 24, p. 242402, 2016.

[7] J. Sankey, et al., "Mechanisms limiting the coherence time of spontaneous magnetic oscillations driven by dc spin-polarized currents," Physical review B, vol. 72, no. 22, p. 224427, 2005.

Imaging Nanoscale Magnetization Using Scanning-Probe Magneto-Thermal Microscopy

CNF Project Number: 2091-11

Principal Investigator(s): Gregory D. Fuchs

User(s): Chi Zhang

Affiliation(s): Applied and Engineering Physics, Cornell University

Primary Source(s) of Research Funding: Air Force Office of Scientific Research (FA9550-14-1-0243)

Contact: gdf9@cornell.edu, cz435@cornell.edu

Primary CNF Tools Used: JEOL 9500, GCA 5x stepper

Abstract:

High resolution, time-resolved magnetic microscopy is crucial for understanding novel magnetic phenomenon such as skyrmions, spinwaves, and domain walls. Currently, achieving 10-100 nanometer spatial resolution with 10-100 picosecond temporal resolution is beyond the reach of table-top techniques. We have developed a time-resolved near field magnetic microscope based on magneto-thermal interactions, which achieved spatial resolution of sub-100 nm. Our results suggest a new approach to nanoscale spatiotemporal magnetic microscopy in an accessible, table-top form to aid in the development of high-speed magnetic devices.

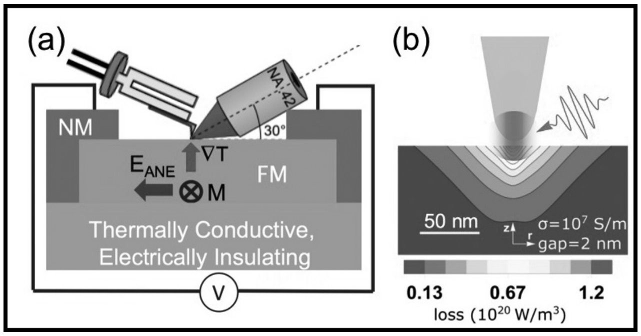

Figure 1: Schematics of (a) our scanning near field magneto-thermal microscopy setup, illustrating laser, sample and scan probe, and (b) near-field interaction. The sample figure in (b) is from Ref. [5].

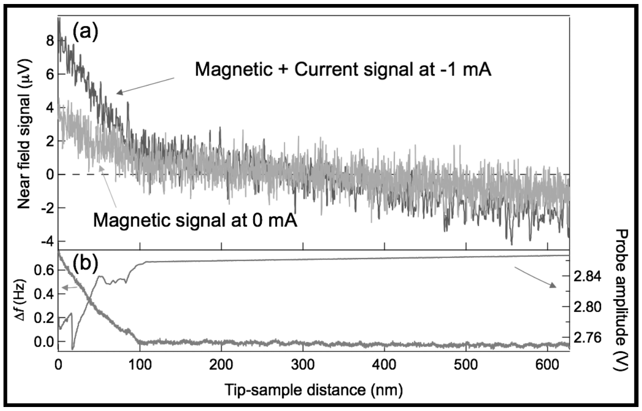

Figure 2: Near-field characteristic. Tip-sample distance dependence of (a) near-field signals and (b) probe parameters.

Summary of Research:

Our group has previously developed a time-resolved magneto-thermal microscopy [1-3]. We apply a pulsed laser to create thermal gradient ∇T. The local magnetization M subjected to ∇T generates an electric field E_{ANE} through anomalous Nernst effect [Figure 1(a)]. This enables us to do magnetic imaging, with a spatial resolution of 650 nm and a temporal resolution of 10 ps. This technique can be used to image both local static and dynamic magnetization, as well as an applied current density [4]. In this work, we extend the magneto-thermal microscopy to nanoscale resolution with near-field light. We use a gold-coated cantilever glued on tuning fork as our probe, controlled by atomic force microscopy.

We shine a laser on the tip apex, and the near field enhancement of the electric field at the tip [5-6] heats the sample as a nanoscale heat source [Figure 1(b)]. The heating length scale is comparable to the tip radius; below 100 nm.

We first study a 5 µm × 15 µm CoFeB/Hf/Pt sample fabricated using photolithography with the GCA 5x stepper. We confirm the near-field characteristic of the signal by measuring as a function of tip-sample distance. We record the near-field signal as well as other probe parameters as the tapping probe approaches the sample [Figure 2]. The near-field signal increases when the tip

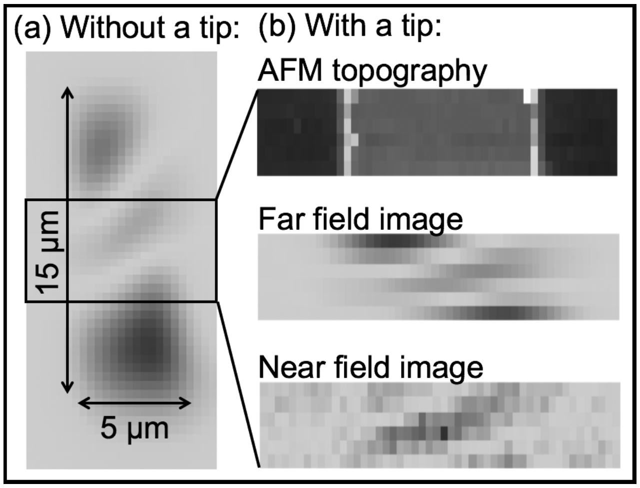

Figure 3: Magnetic multi-domain imaging. (a) Magnetic far-field images of a multi-domain state. (b) With a scanning probe tip, topography, far-field and near-field images acquired simultaneously.

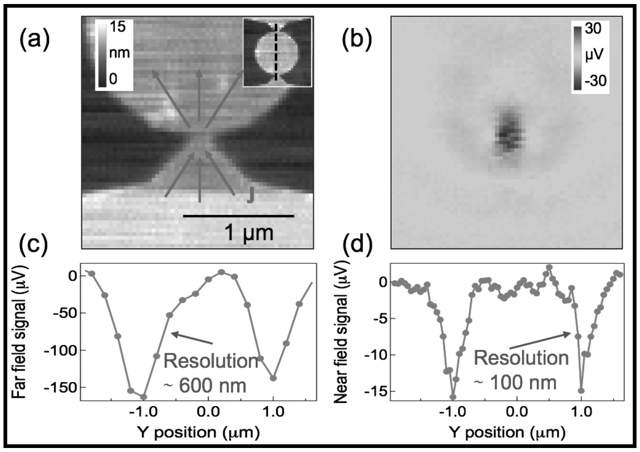

Figure 4: Current imaging and spatial resolution. (a) Topography and (b) current density images acquired by a near field tip. Line cuts through two necks (as illustrated in the inset of (a)) of (c) far field and (d) near field signals for resolution comparison.

is in first contact with the sample, indicated by an initial increase of the frequency and decrease of the amplitude. The short-range nature of the signal is consistent with a near-field interaction.

We next demonstrate magnetic imaging of near field scanning probe with a multi-domain state. Figure 3(a) shows a far-field image taken by a focused light to confirm the magnetic state. Figure 3(b) shows topography, far-field and near-field images, acquired simultaneously with the scanning probe. The near-field image resembles the far-field image, but with higher resolution. We note that the near-field image has a smallest feature of ~ 300 nm in this sample, which is below the optical diffraction limit of the set-up. That feature is likely the actual domain wall width rather than being limited by the instrument resolution.

To probe instrument resolution further, we measure in current imaging mode and use a new sample designed with a sharp current density feature. The sample is a thin-film heterostructure composed of 5 nm $Ni_{81}Fe_{19}$/2 nm Ru, then patterned into a 2-μm-diameter disk with two 130 nm necks using JEOL 9500 e-beam lithography. Figure 4 shows topography and near-field current density images taken with the near-field scanning probe. By taking linecuts through two necks, as shown in Figure4(a) inset, we compare signals between focused light far field and scanning probe near field. The scanning near-field image has higher resolution than far field image, and based on sharp features, demonstrates an upper bound of spatial resolution of 100 nm.

Conclusions and Future Steps:

We have developed a time-resolved scanning near field magneto-thermal microscopy for magnetic and current imaging. We confirmed near field nature of the signal, and characterized the spatial resolution to be sub-100 nm. In the future, we will apply this instrument to study the dynamics of nanoscale spin textures.

References:

[1] J. M. Bartell, D.H. Ngai, et al., Nat. Commun. 6, 8460 (2015).

[2] J. M. Bartell, et al., Phys. Rev. Appl. 7, 044004 (2017).

[3] I. Gray, et al., Phys. Rev. Mater. 3, 124407 (2019).

[4] F. Guo, et al., Phys. Rev. Appl. 4, 044004 (2015).

[5] J. C. Karsch, et al., APL Photonics 2, 086103 (2017).

[6] L. Meng, et al., Optics Express, 11, 13804, (2015).

Magnetic Resonance Force Detection and Imaging of Electron Spins in a Laminate Thin Film

CNF Project Number: 2125-12

Principal Investigator(s): John Marohn

User(s): Michael Boucher

Affiliation(s): Department of Chemistry and Chemical Biology, Cornell University

Primary Source(s) of Research Funding: Army Research Office

Contact: john.marohn@cornell.edu, mcb344@cornell.edu

Website: marohn.chem.cornell.edu

Primary CNF Tools Used: SC 4500 Combination Thermal/E-gun Evaporation System, Zeiss Supra SEM

Abstract:

Magnetic resonance force microscopy (MRFM) is a nanoscale imaging technique that uses a force sensor such as a cantilever, nanowire, or membrane, along with a field gradient to detect magnetic resonance and spatially resolve spins. The Marohn group is interested in using MRFM to image soft materials such as membrane proteins and other biomolecules. Detection of a few hundred nuclear spins or one electron and resolution of less than a nanometer have been demonstrated [1-3]. The Marohn group uses equipment at the Cornell NanoScale Facility (CNF) and the Cornell Center for Materials Research (CCMR) to produce cantilevers with nanomagnet tips as well as waveguides to deliver radio- and microwave frequency radiation to manipulate sample spins. In a previous report we detailed sample preparation methods we had developed to reduce noise due to sample charge fluctuations while avoiding sample damage. In this report we provide an update on measurement experiments performed on the sample prepared using our newly developed techniques.

Summary of Research:

Using a protocol developed at the CNF, the Marohn group fabricated attonewton-sensitivity cantilevers and nanomagnets that were affixed to the leading edge using a STEM-FIB system at the CCMR. An experiment on a 40 nm thin film demonstrated 500 proton-sensitivity in a mHz bandwidth [1], a sensitivity equivalent to that required for single electron radical imaging.

In our report for the 2017-2018 CNF Research Accomplishments, we described experiments performed on a 200 nm thick polystyrene thin film doped to 40 mM with 4-amino-TEMPO, a nitroxide radical. Our detection scheme modulates the sample electron spin polarization and detects the change in magnetization as a modulated shift in the cantilever frequency. To minimize cantilever frequency noise from fluctuating sample charges, we used e-beam evaporation to apply a 10 nm layer of gold to the polystyrene sample surface (SC 4500 Combination Thermal/E-gun Evaporation System). Based on our experimental measurements and later conventional ESR of test films, however, we believe that a 20 nm thick layer of the sample is destroyed by the gold deposition. This "dead layer" increases the standoff distance between the magnet tip and sample spins being measured, making it difficult to do single electron detection in a practical measurement time. In our previous report we presented a new "laminate" sample preparation technique that protects the cantilever from sample charge fluctuations without exposing sample nitroxide radicals to direct exposure from physical vapor deposition of metals (Figure 1).

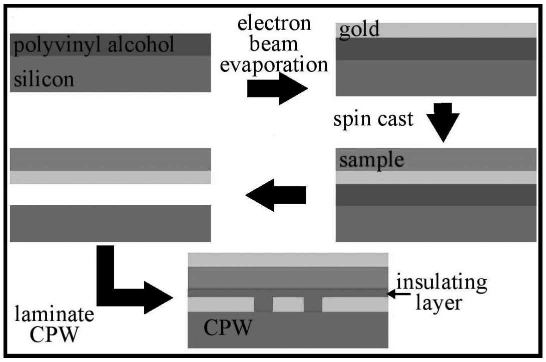

Figure 1: An outline of the sample/top contact transfer process which allows samples to be produced without exposing sensitive nitroxide electron radicals to physical deposition of the gold top contact.

In May-June 2019 we performed experiments on one of these laminate samples using a magnet-tipped cantilever prepared by epoxying a 4-micron-diameter spherical nickel magnet to one of our CNF-fabricated cantilevers. This larger tip reduces per-spin sensitivity of our system but puts more spins in resonance at a given microwave frequency, allowing us to more easily test and calibrate our system.

Our first measurement was to scan the irradiation frequency at a variety of tip-sample separations. This provides us with the tip-field at each separation, tells us about the field-gradient, and lets us fit the result to an analytical model of a spherical magnet (Figure 2).

We also used MRFM to detect the spin-lattice relaxation time T1 of sample spins using a "phase-kick" protocol described by Moore, et al. [4]. Our measured values match Moore's and provide evidence that the laminate sample preparation does not degrade the sample (Fig.3).

Another test of our setup was to perform a proof-of-concept imaging experiment. In theory our sample should not be interesting to image, being a uniform thin film with a constant dopant concentration. However, we found a protuberance in the sample that we could measure. We scan laterally over the sample in small steps to form a 12 × 12 grid. We also vary the irradiation frequency to change the shape of the resonant slice. As the resonant slice scans over the protuberance, it adds to the signal observed at that grid point. By changing the irradiation frequency, we change the radius of the resonant slice and therefore the size of the rings of increased signal (Figure 4). We expect imaging of smaller scale objects to behave in a similar manner.

Future work will involve using a smaller magnet tip to continue imaging experiments on samples with nanoscale features of interest for imaging.

References:

[1] Longenecker, et al. ACS Nano 2012, 6 (11), 9637-9645.

[2] Rugar, et al. Nature 2004, 430 (6997), 329-332.

[3] Grob, et al. Nano Letters 2019, 19 (11), 7935-7940.

[4] Moore, et al. PNAS 2009, 106 (52), 22251-22256.

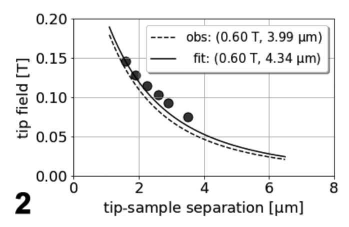

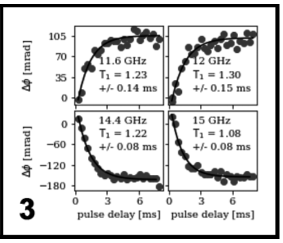

Figure 2, left: *Tip field versus tip-sample separation along with a fit to an analytical magnet field for a spherical model.* ***Figure 3, right:*** *Cantilever phase shift versus pulse delay measured at different irradiation frequencies. Inset shows best fit spin-lattice relaxation time.*

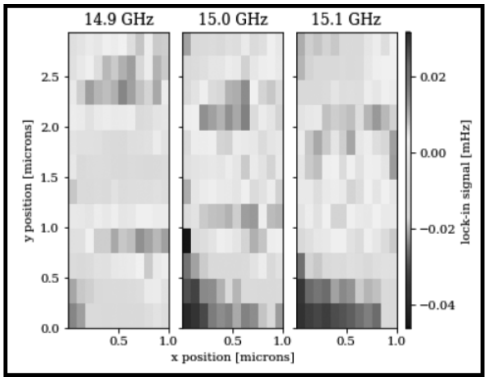

Figure 4: Map of spin-induced cantilever frequency shift at various irradiation frequencies. Step size: Δx = 91 nm, Δy = 258 nm. (See pages vi-vii for full color version of figure.)

Acoustically Driving the Single Quantum Spin Transition of Diamond Nitrogen-Vacancy Centers

CNF Project Number: 2126-12

Principal Investigator(s): Gregory D. Fuchs[1]

User(s): Huiyao Chen[2], Johnathan Kuan[2]

Affiliation(s): 1. School of Applied and Engineering Physics, 2. Department of Physics; Cornell University

Primary Source(s) of Research Funding: DARPA DRINQS program (Cooperative Agreement #D18AC00024); Office of Naval Research (Grants No. N000141712290)

Contact: gdf9@cornell.edu, hc846@cornell.edu, jk2788@cornell.edu

Website: http://fuchs.research.engineering.cornell.edu

Primary CNF Tools Used: PT770 etcher, GCA 5x stepper, Heidelberg mask writer DWL2000, AJA sputtering deposition System, odd/even evaporator, YES asher, P10 profilometer, Westbond 7400A ultrasonic wire bonder

Abstract:

Using a high quality factor 3 GHz bulk acoustic wave resonator device, we demonstrate the acoustically driven single quantum (SQ) spin transition ($|m_s = 0\rangle \leftrightarrow |\pm1\rangle$) for diamond nitrogen-vacancy (NV) centers and characterize the corresponding stress susceptibility. We find that the SQ spin-stress coupling is comparable to that for double quantum (DQ) transition, about an order of magnitude larger than a theoretical prediction. This work further completes our understanding of the NV spin-stress Hamiltonian and enables all-acoustic spin control of NV center spins.

Summary of Research:

Acoustic control of diamond nitrogen-vacancy (NV) center spins provides additional resources for quantum control and coherence protection that are unavailable in conventional magnetic resonance approaches. While acoustically-driven double quantum spin transition has been widely studied, acoustically-driven single quantum spin transition is yet unexplored.

Here we report our experimental study of acoustically-driven SQ spin transitions of NV centers using a 3 GHz diamond bulk acoustic resonator device [1]. The device converts a microwave driving voltage into an acoustic wave through a piezoelectric transducer, thus mechanically addressing the NV centers in the bulk diamond substrate (Figure 1). Because a microwave current flows through the device transducer, an oscillating magnetic field of the same frequency coexists with the stress field that couples to SQ spin transitions.

To identify and quantify the mechanical contribution to the SQ spin transition, we use Rabi spectroscopy to separately quantify the magnetic and stress fields present in our device as a function of driving frequency. The results are shown in Figure 2. Based on these results, we construct a theoretical model and simulate the SQ spin transition Rabi spectroscopy to compare to the experimental results. From a systematically identified closest match (Figure 3), we quantify the mechanical driving field contribution and extract the effective spin-stress susceptibility, b'. We perform measurements on both the $|0\rangle \leftrightarrow |+1\rangle$ and $|0\rangle \leftrightarrow |{-1}$. SQ spin transitions and obtain $b'/b = \sqrt{2}(0.5 \pm 0.2)$, where b is the spin-stress susceptibility of DQ transition.

The fact that b' is comparable to b, about an order of magnitude larger than expected theoretically [2], has important implications for applications. It raises the possibility of all-acoustic spin control of NV centers within their full spin manifold without the need for a magnetic antenna. For sensing applications, a diamond bulk acoustic device can be practical and outperform a microwave antenna in several aspects: 1) Acoustics waves provide direct access to all three qubit transitions, and the DQ qubit enables better sensitivity in magnetic metrology applications; 2) The micron-scale phonon wavelength is ideal for local selective spin control of NV centers; 3) Bulk acoustic waves contain a uniform stress mode profile and thus allows uniform field control of a large planar spin ensemble, for example, from a delta-doped diamond growth process.

This study [3], combined with previously demonstrated phonon-driven DQ quantum control and improvements in diamond mechanical resonator engineering, shows that diamond acoustic devices are a powerful tool for full quantum state control of NV center spins.

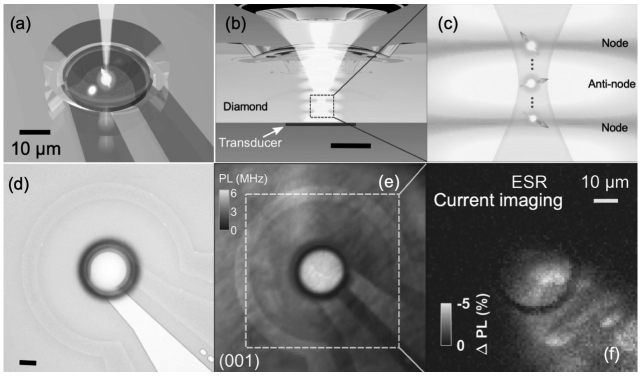

Figure 1: (a) and (b) are concept images of the device side view and cross-sectional view. An NA = 0.8 objective focuses the 532 nm laser down into diamond at a depth close to the transducer (around 3 μm in distance). The orange standing wave field illustrates the acoustic wave mode. (c) Closeup of the area under study. (d) and (e) are optical image and photoluminescence scan of the device, consisting of a semi-confocal diamond bulk acoustic resonator (center bright region) and a 50 μm radius microwave loop antenna. (f) Electron spin resonance signal mapping of the device current field around the resonator, showing current flow primarily along the electrodes.

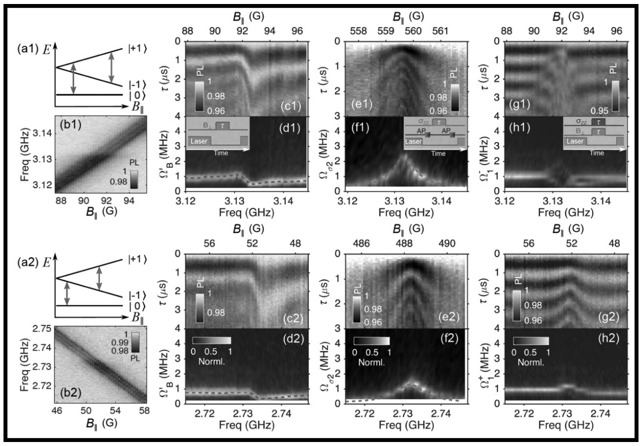

Figure 2: Spectroscopy study of NV center spin under driving fields at frequencies near two acoustic modes at (1) 3.132 GHz and (2) 2.732 GHz. Ground-state spin level diagrams in (a1-a2) show the targeted DQ (orange arrow, |-1⟩ ↔ |+1⟩) and SQ (blue arrow |0⟩ ↔ |±1⟩) transitions within nuclear spin |m_I = +1⟩ hyperfine manifold. Transducer driving creates both magnetic, $B_\perp$, and acoustic fields, σ_{ZZ}, in the device, which can be measured independently by (c) SQ Rabi spectroscopy near the leads and (e) DQ Rabi spectroscopy in the center of the resonator. In the resonator, the two vector fields add coherently and drive the SQ transition together. Measurements of the resulting total field probed by SQ ESR and Rabi spectroscopy are shown in (b) and (g), respectively. (d, f, h) are Fourier transforms of (c, e, g). The insets in (d1, f1, h1) show the corresponding measurement sequences.

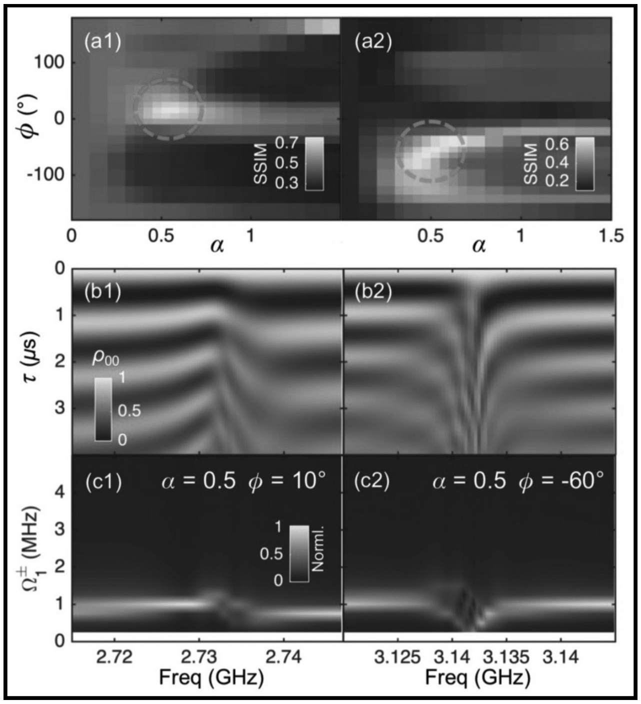

Figure 3: Quantum master simulation of SQ spin transition under dual field driving. (a1-a2) are heatmaps of structural similarity index measure between experimental data and simulation in {φ,α} parameter space for 2.732 GHz and 3.132 GHz mode, respectively. The dashed circles mark the locations of peak SSIM values. (b1-b2) The corresponding simulated Rabi spectroscopy results using the peak SSIM associated {φ,α} values match the experimental data in Figure 2g. (c1-c2) are Fourier transforms of (b1-b2).

References:

[1] H. Chen, N. F. Opondo, B. Jiang, E. R. MacQuarrie, R. S. Daveau, S. A. Bhave, and G. D. Fuchs, Nano letters 19, 7021 (2019).

[2] P. Udvarhelyi, V. O. Shkolnikov, A. Gali, G. Burkard, and A. Palyi, Physical Review B 98, 075201 (2018).

[3] H. Chen, S. Bhave, and G. Fuchs, arXiv preprint arXiv:2003.03418 (2020).

(See pages vi-vii for full color versions of all three figures.)

Shallow Diamond Silicon Vacancy Centers for Coherent Spin-Magnon Coupling

CNF Project Number: 2126-12

Principal Investigator(s): Gregory D. Fuchs[1]

User(s): Hil Fung Harry Cheung[2]

Affiliation(s): 1. School of Applied and Engineering Physics, 2. Department of Physics; Cornell University

Primary Source(s) of Research Funding: Department of Energy (Grants No. DE-SC0019250)

Contact: gdf9@cornell.edu, hc663@cornell.edu

Website: http://fuchs.research.engineering.cornell.edu

Primary CNF Tools Used: GCA 5x stepper, AJA sputtering deposition system, P10 profilometer, Westbond 7400A ultrasonic wire bonder, Veeco Icon atomic force microscope, PT770 etcher

Abstract:

We aim to develop a platform for coupling isolated silicon-vacancy (SiV) electron spins to magnetic spin waves, potentially enabling a magnon mode to act as a quantum bus. To enhance the dipolar coupling, SiV centers need to be placed near the magnetic material, and thus near the surface of the diamond. Here we report on our study of the optical properties of shallow diamond SiV centers.

Summary of Research:

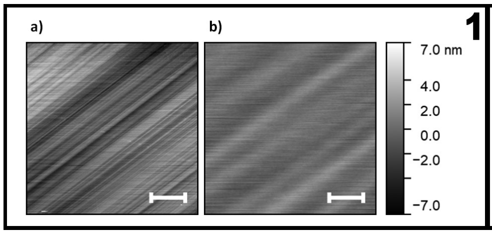

Figure 1, left: Diamond surface atomic force microscope (AFM) image before (a) and after (b) Ar/Cl2 and O2 reactive ion etch. Scale bar is 1 µm.

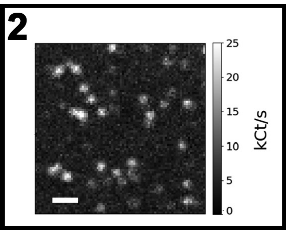

Figure 2, right: Photoluminescence image of SiV centers. Scale bar is 1 µm.

Diamond SiV centers can have long spin coherence times and narrow optical transitions, enabling the realization of spin-photon entanglement [1]. These good properties make SiV a good candidate for engineering a quantum bus. We aim to develop a spin-magnon interface by coupling SiV centers to a high-quality magnon mode. A key parameter, the spin-magnon coupling rate, is maximized when the SiV spins are close to the magnetic material [2]. However, shallow defects are more susceptible to surface states that reduce coherence times and broaden optical transitions [3,4]. Here we fabricate near surface diamond SiV centers and study their properties relevant to spin-magnon transduction.

We start from a single crystal diamond substrate (nitrogen concentration < 5 ppb). A polished diamond sample has a highly strained surface layer. We remove the top 5 µm using reactive ion etch (RIE) with Ar/Cl_2 and O_2 plasma [5,6] using the PT 770 etcher. This process reduces surface roughness and polishing streaks (Figure 1). The diamond sample is then implanted with 45 keV ^{28}Si ion at a fluence 10^{10} ions/cm^2, resulting in an estimated implanted depth of 32 ± 9 nm [7]. The sample is vacuum annealed to mobilize vacancies enabling the formation of SiV centers. Vacuum annealing also leaves behind graphite on the diamond surface, which we remove by cleaning the diamond in through a tri-acid boil (equal volume of sulfuric, nitric and perchloric acid).

We study the optical properties of the SiV centers in a home-built confocal microscope setup. SiV centers are excited with a continuous wave green laser (532 nm) with a power density of about 50 mW/µm^2. We observed a SiV density of 0.5 SiV/µm^2, corresponds to a conversion efficiency of 0.5% (Figure 2), comparable to conversion efficiency at a higher implant energy (150 keV) [8].

SiV centers emit about 70% of light into the zero-phonon line (ZPL) near 737 nm [9], which is advantageous for single photon generation. At room temperature, this line is a few nm broad due to electron-phonon processes [10]. At low temperature (10 K), the line narrows and a four-line fine structure emerges (Figure 3a). The fluorescence wavelength distribution is shown in Figure 3b. About half of the SiV centers transition emission lines have linewidths at the spectrometer resolution limit.

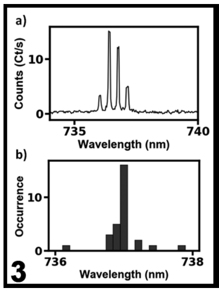

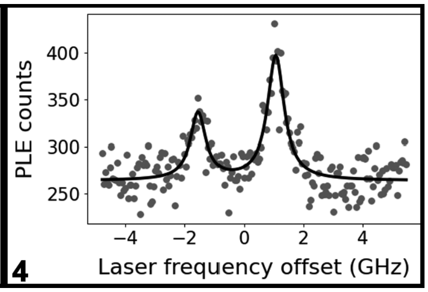

Figure 3, left: (a) Emission spectrum of a SiV center. (b) Wavelength distribution of 29 SiV centers. Figure 4, right: PLE scan of a SiV center under 400 nW/µm^2 resonant laser excitation. Full width half maximum (FWHM) are 630 ± 220 MHz and 680 ± 240 MHz.

To more accurately probe the linewidth, we use photoluminescence excitation (PLE) spectroscopy. We excite SiV centers with a frequency-tunable laser that we tune over the resonant optical transition while collecting emission from the phonon sidebands with wavelength larger than 750 nm. We observe narrow transition linewidths of 630 ± 220 MHz (Figure 4), which is only a few times larger than the lifetime limited linewidth (93 MHz) [8].

Conclusions and Future Steps:

We fabricated shallow diamond SiV centers with narrow optical transitions. In the future we plan to study the spin of shallow SiV centers as we work towards integration of SiV centers with magnetic material.

References:

[1] C. T. Nguyen, et al., "An integrated nanophotonic quantum register based on silicon-vacancy spins in diamond", Phys. Rev. B 100, 165428 (2019).

[2] D. R. Candido, et al., "Predicted strong coupling of solid-state spins via a single magnon mode", arXiv:2003.04341 (2020).

[3] B. A. Myers, et al., "Probing Surface Noise with Depth-Calibrated Spins in Diamond", Phys. Rev. Lett. 113, 027602 (2014).

[4] S. B. van Dam, et al., "Optical coherence of diamond nitrogen-vacancy centers formed by ion implantation and annealing", Physical Review B 99, 161203(R) (2019).

[5] Y. Chu, et al., "Coherent optical transitions in implanted nitrogen vacancy centers", Nano Lett. 14, 982 (2014).

[6] S. Sangtawesin, et al., "Origins of Diamond Surface Noise Probed by Correlating Single-Spin Measurements with Surface Spectroscopy", Phys. Rev. X 9, 031052 (2019).

[7] J. F. Ziegler, et al., "SRIM - The stopping and range of ions in matter (2010)", Nucl. Instrum. Methods Phys. Res., Sect. B 268, 1818 (2010).

[8] R. E. Evans, et al., "Narrow-Linewidth Homogeneous Optical Emitters in Diamond Nanostructures via Silicon Ion Implantation", Phys. Rev. Applied. 5, 044010 (2016).

[9] A. Dietrich, et al., "Isotopically varying spectral features of silicon vacancy in diamond", New J. Phys. 16, 113019 (2014).

[10] K. D. Jahnke, et al., "Electron-phonon processes of the silicon-vacancy centre in diamond", New J. Phys. 17, 043011(2015).

Quantum Emitters Activation in WSe_2 Monolayers via Hexagonal Boron Nitride Wrinkle Engineering

CNF Project Number: 2126-12

Principal Investigator(s): Gregory D. Fuchs

User(s): Raphael Sura Daveau, Tom Arno F. Vandekerckhove

Affiliation(s): Applied and Engineering Physics, Cornell University

Primary Source(s) of Research Funding: Air Force Office of Scientific Research (FA9550-18-1-0480)

Contact: gdf9@cornell.edu, rsd228@cornell.edu

Website: http://fuchs.research.engineering.cornell.edu

Primary CNF Tools Used: JEOL 6300 electron-beam writer, GCA 5x stepper, Oxford 81 etcher

Abstract:

Strain has been shown to be a key parameter to create quantum emitters in tungsten diselenide (WSe_2) monolayers. We report experimental observations of spatially and spectrally isolated single quantum emitters (QEs) in WSe_2 monolayers. We use hexagonal boron nitride (hBN) wrinkles nucleated from a nanostructured substrate to create strain at a size scale suitable to host single QEs, while avoiding other residual emission. In comparison, QEs stemming from direct strain points from the substrate yield multiple QEs per site and increased unwanted background emission.

Summary of Research:

Monolayer transition metal dichalcogenides are direct bandgap semiconductors with a strong light-matter interaction and possessing a new electronic degree of freedom, known as valley, that locks excitons to a given photon helicity [1]. Tungsten diselenide (WSe_2) has been shown to host bright and stable QEs [2]. While most reported emitters in WSe_2 monolayers are located at random, few reports show deterministic activation of QEs via local strain by placing the WSe_2 monolayer over a patterned substrate, in the form of nanopillars [3]. Strain engineering of WSe_2 monolayers is key to create QEs on demand and with position control [4].

Our approach uses a nano-patterned substrate as an indirect means to communicate strain to WSe_2 via a thin hBN layer, which appears to be suitable to create single QEs. In this work, we use a substrate patterned with nanopillars [3,4] and make a comparative study of emitters forming directly on the pillars versus along hBN wrinkles that propagate between pillars.

The nanopillars are fabricated from a SiO_2 substrate via electron-beam lithography (JEOL 6300) using M-aN 2403 negative resist. The nanopillars are etched into SiO_2 and are cylindrical with a diameter of 200 nm and height of 300 nm. Exfoliated WSe_2 monolayers and hBN are transferred using a polycarbonate (PC) on polydimethylsiloxane (PDMS) stamp technique. We study the samples using a homebuilt confocal microscopy setup with a 637 nm continuous wave laser at 10 K.

Figure 1 shows an atomic force micrograph (AFM) of a sample consisting of a hBN/WSe_2 heterostructure on a SiO_2 nanopillar substrate. The photoluminescence map from this sample shows that WSe_2 on the nanopillar (indicated with a large circle in Figure 1) emits most intensity because of the high strain while a less intense spot is visible along a hBN wrinkle (small circle in Fig.1).

The spectrum collected from the center of the nanopillar is shown in Figure 2 and shows two sharp features along with a broad emission from 755 nm to 775 nm.

Figure 3 on the other hand shows a spectrum taken on the wrinkle (see small circle in Fig.1). This spectrum features a single sharp peak at 765.8 nm with minimal background emission surrounding the peak. The AFM image reveals a kink in the wrinkle, i.e., increased strain, which can explain the creation of a quantum emitter at this specific site. At this location, the wrinkle is 90 nm high and has a full-width at half-maximum (FWHM) of 160 nm. The collected light from this spot is filtered through a 3 nm bandpass filter and sent to a Hanbury-Brown-Twiss interferometer for auto-correlation measurement. The time correlation between the two APD signals for the wrinkle QD is plotted as $g^{(2)}(t)$ in the

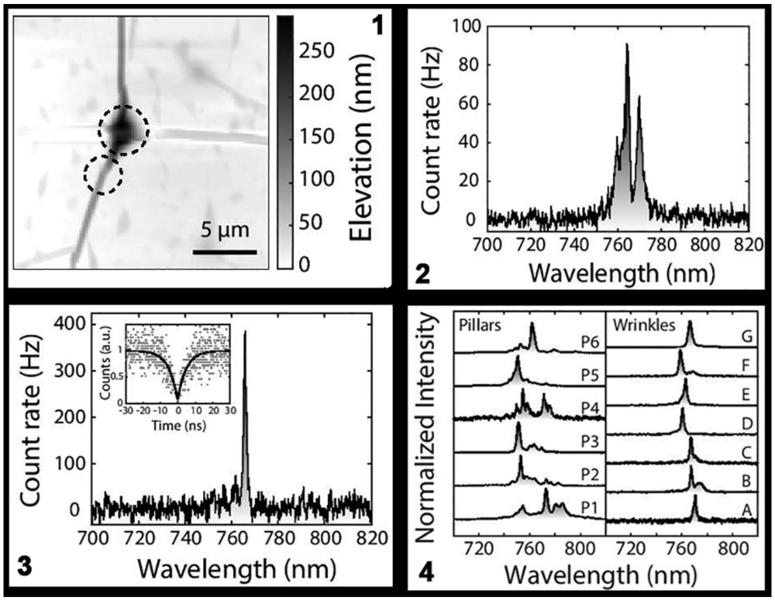

Figure 1: *Atomic force micrograph of the sample consisting of a WSe_2/hBN heterostructure on top of SiO_2 nanopillar substrate. Pillars bring most strain to WSe_2, however, hBN wrinkles bring more subtle strain suitable for creating cleaner single quantum emitters.* ***Figure 2:*** *Spectrum of light collected from the top of the nanopillar. Several peaks on top of a broad background are visible.* ***Figure 3:*** *Spectrum of light collected from the wrinkle, as circled in Fig.1. One clean peak is visible, meaning a single quantum emitter is created at this spot. Inset: second-order correlation function demonstrating the single-photon nature of the emission.* ***Figure 4:*** *(left) Spectra collected from the top of 300-nm high nanopillars. (right) Spectra collected from emission centers located along hBN wrinkles. The spectra systematically display a single peak and lower background level.*

inset of Figure 3. From the fit we extract $g^{(2)}(0) = 0.087$, demonstrating the single-photon nature of the emission.

The spectrum of Figure 2 does not allow us to quantify $g^{(2)}(0)$ for the signal coming from the top of the nanopillar.

In another sample, we have studied six nanopillar-based QEs and seven wrinkle-based QEs. The spectra collected from the top of the pillars are shown in Figure 4 (left panel) and display one or several lines attributed to QEs and a broad emission background. In contrast, spectra that are collected along hBN wrinkles away from the pillars, shown in Figure 4 (right panel), consistently display a single peak, i.e., a single quantum emitter probed at a time, while the background level is significantly reduced.

We study the amount of background light emitted at the same frequency of the emitters on a 3~nm spectral window to quantify the effect on single-photon purity. We find that 25% of the signal is composed of unwanted background light for nanopillar-based emitters whereas this number is 15% for wrinkle-based emitters in comparison. This latter result intrinsically increases single-photon purity of wrinkle-based QEs.

Conclusions and Future Steps:

The use of a nano-patterned substrate to indirectly induce hBN wrinkles, may be a good choice to create single WSe_2 QEs with low background. Emitters created with hBN wrinkles are spectrally isolated from other emitters and have an increased single-photon purity, which is an advantage for application purposes. Future work should address the deterministic positioning of QEs along hBN wrinkles.

References:

[1] K. F. Mak and J. Shan, Nat. Photonics 10, 216 (2016).

[2] A. Srivastava, M. Sidler, A. V. Allain, D. S. Lembke, A. Kis and A. Imamo.lu, Nat. Nanotechnology 10, 1038 (2015).

[3] C. Palacios-Berraquero, D. M. Kara, A. R.-P. Montblanch, M. Barbone, P. Latawiec, D. Yoon, A. K. Ott, M. Loncar, A. C. Ferrari and M. Atature, Nat. Comm. 8, 15093 (2017).

[4] A. Branny, S. Kumar, R. Proux, and B. D. Gerardot, Nat. Comm. 8, 1-7 (2017).

Fabrication of Nanophotonic Optical Cavity Device from Inverse Design

CNF Project Number: 2126-12
Principal Investigator(s): Gregory D. Fuchs[1]
User(s): Jialun Luo[2]

Affiliation(s): 1. School of Applied and Engineering Physics, 2. Department of Physics; Cornell University
Primary Source(s) of Research Funding: National Science Foundation (ECCS-1839196)
Contact: gdf9@cornell.edu, JL3562@cornell.edu
Website: http://fuchs.research.engineering.cornell.edu
Primary CNF Tools Used: AJA sputtering system, OEM Endeavor AlN sputtering system, JEOL 9500, PT770 etcher, P10 profilometer, GCA 5x stepper

Abstract:

On-demand polarized single-photons are essential in realizing many photon-based quantum communication protocols. We are developing and fabricating a nanophotonic cavity device from aluminum nitride (AlN) to serve as a platform for enhancing single-photon emission from isolated defects hosted in hexagonal boron nitride. The target structure is designed via numerical optimization known as the inverse design. We present an update on our work-in-progress on the fabrication of the device.

Summary of Research:

Hexagonal boron nitride (hBN) has drawn a lot of attention recently because of its bright emission of single photons [1]. The defect emission is stable at room temperature and appears in the visible spectrum [2]. Researchers have been able to find or create isolated defects, making these defects promising candidates for implementing single-photon emitters that are important for quantum communication protocols [3]. In this project, we aim to develop bright, on-demand single-photon emitters using hBN defects. To enhance the emissions we fabricate a nanophotonic cavity device based on inverse design techniques [4]. The structure is designed such that it resonates at frequencies of the emission of the single emitters with a small mode volume.

We take advantage of the similarity in the index of refraction of hBN and aluminum nitride (AlN). Starting from a fused silica wafer, we sputter a 300 nm thick AlN layer using the OEM Endeaver M1 AlN sputter system. In particular, the nanophotonic cavity design has a 600 nm mode that is strongly confined in the center of the structure, thus aiming to enhance the emission rate of isolated defects at that frequency.

The process flow is outlined as follows (Figure. 1). We use the AJA sputter system to deposit a thin layer (of 20 to 30 nm) of chromium (Cr) on top of AlN. The Cr layer serves as a hard mask for the etching AlN. The patterning is done with electron beam lithography (EBL) with the JEOL 9500 and reactive ion etching (RIE) with the PT770 etcher. We choose hydrogen silsesquioxane (HSQ) diluted into 3% solution as the EBL resist due to its sub-10 nm resolution. HSQ is spun on the wafer with a thickness of 10 to 15 nm, which implies an aspect ratio of 1:2 for the subsequent etching of Cr. To avoid charging artifacts on the HSQ resist during exposure, we spin a layer of water-soluble discharge polymer on top of the HSQ. We write the device structure with JEOL 9500. Next, we develop the exposed HSQ in MIF 300 for one minute, rinse with DI water, and then blow dry. The subsequent etching steps are carried out in the PT770 etcher. We etch the Cr layer with Cl_2/O_2 plasma and then the AlN layer with Cl_2 plasma. Lastly, the Cr layer is removed by wet chemical etch.

This project is a work-in-progress as we are debugging the etching step of the AlN layer. The SEM image of the Cr mask of the pattern is shown in Figure 2. The smallest feature size is of 10 nm.

Future Steps:

We will complete and refine the process parameters to fabricate the nanophotonic cavity devices. We will study the optical properties of the devices and characterize the Purcell enhancement of single emitters coupled to the devices.

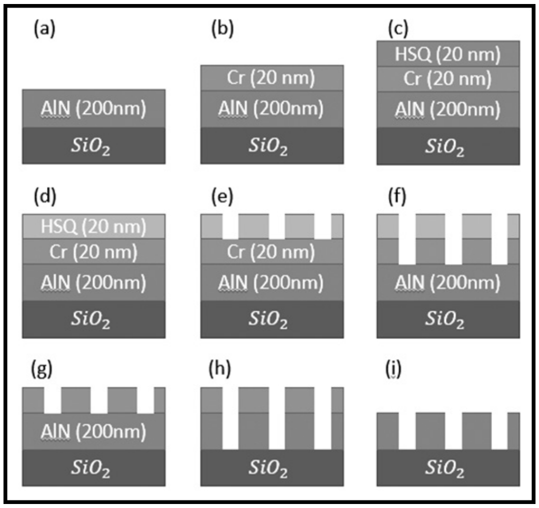

Figure 1: Outline of the process flow. (a-b) Sputtering of AlN and Cr on fused silica wafer, (c) deposition of HSQ, (d-e) EBL patterning on HSQ and development, (f) etching of Cr hard mask, (g) removal of HSQ, (h) etching of AlN, (i) removal of Cr mask.

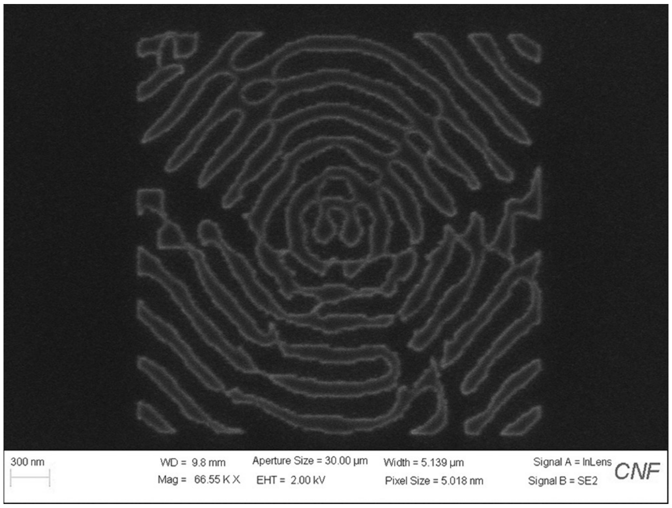

Figure 2: SEM image of the pattern after Cr etch.

Acknowledgements:

We would like to thank the Prof. Alejandro Rodriguez's group for the discussion on and their design of the nanophotonic cavity structure.

References:

[1] Aharonovich, I., Englund, D., and Toth, M. Solid-state single-photon emitters. Nature Photonics 10, 631-641 (2016).

[2] Jungwirth, N. R., and Fuchs, G. D. Optical Absorption and Emission Mechanisms of Single Defects in Hexagonal Boron Nitride. Phys. Rev. Lett. 119, 057401 (2017).

[3] Bennett, C. H., and Brassard, G. Quantum cryptography: Public key distribution and coin tossing. Theoretical Computer Science 560, 7-11 (2014).

[4] Molesky, S., et al. Inverse design in nanophotonics. Nature Photonics 12, 659-670 (2018).

Ultrafast Energy-Efficient Spin-Torque Magnetic Random Access Memories

CNF Project Number: 2444-16

Principal Investigator(s): Robert A. Buhrman

User(s): Lijun Zhu

Affiliation(s): School of Applied and Engineering Physics, Cornell University
Primary Source(s) of Research Funding: Office of Naval Research
Contact: rab8@cornell.edu, lz442@cornell.edu
Primary CNF Tools Used: ASML stepper, Veeco Icon AFM, JEOL JBX-6300FS, AJA sputter

Abstract:

Spin-orbit torques [1-5] have been a hot topic in the research and technology communities due to their great promise for magnetic memories, oscillators and logic of post-Moore era. Here we demonstrate ultrafast energy-efficient magnetic random access memories (MRAMs) [6,7] fabricated at the Cornell NanoScale Science and Technology Facility.

Summary of Research:

We fabricated the spin-torque MRAM devices shown in Figure 1(a). The magnetic multilayer samples are patterned into three-terminal MRAM devices with a three-step procedure. First, we defined the spin Hall channel using DUV lithography (ASML stepper) and ion beam etching and measured the channel size by atomic force microscopy (Veeco Icon). We then defined the elliptical magnetic tunnel junction nanopillars with different aspect ratios and micron-size "via" pillars (as vertical connector between the bottom channel to top contact) onto the spin Hall channel with e-beam lithography (JEOL JBX-6300FS) and ion beam etching, and isolated the pillars with 80 nm thick SiO_2 deposited by an e-beam evaporator. Finally, contacts of Ti/Pt were deposited on the top of the magnetic tunnel junction pillars and "via" pillars for electrical measurements by combining the DUV lithography (ASML stepper), AJA sputtering, and liftoff processes.

Figure 1(b) shows ultrafast, reliable, and efficient current switching of our spin-torque MRAMs.

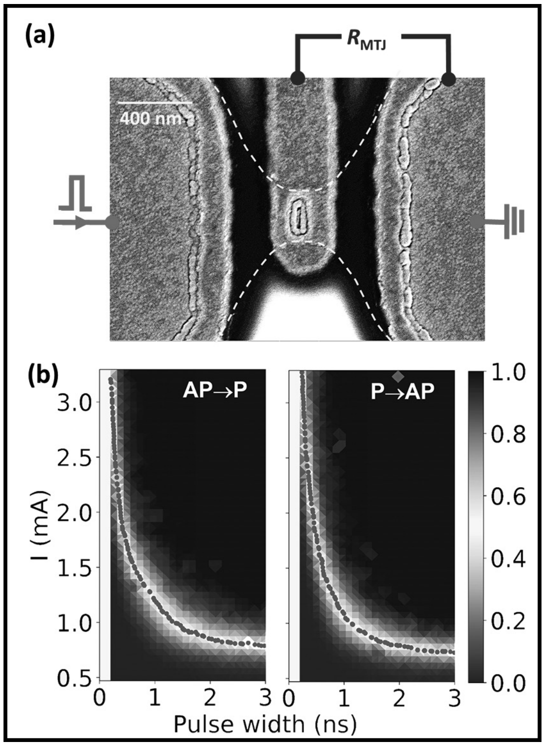

Figure 1: (a) Top-view scanning electron microscopy image of a spin-torque MRAM device; (b) Current-induced switching of the MRAMs. (See pages vi-vii for full color version.)

References:

[1] L. Zhu, D.C. Ralph, R.A. Buhrman, Phys. Rev. Lett. 122, 077201 (2019).

[2] L. Zhu, K Sobotkiewich, X. Ma, X. Li, D.C. Ralph, R.A. Buhrman, Adv. Funct. Mater. 29, 1805822 (2019).

[3] L. Zhu, D.C. Ralph, R.A. Buhrman, Phys. Rev. B 99, 180404 (R)(2019).

[4] L. J. Zhu, D.C. Ralph, R.A. Buhrman, Phys. Rev. B 98, 134406 (2018).

[5] L. Zhu, D.C. Ralph, R.A. Buhrman, Phys. Rev. Appl. 10, 031001 (2018).

[6] L. Zhu, L. Zhu, S. Shi, M. Sui, D. C. Ralph, R. A. Buhrman, Phys. Rev. Appl. 11, 061004 (2019).

[7] L. Zhu, L. Zhu, S. Shi, D. C. Ralph, R. A. Buhrman, Adv. Electron. Mater. 6, 1901131 (2020).

Magnetic Imaging of Ionic Liquid Gated Transition Metal Dichalcogenides

CNF Project Number: 2514-16
Principal Investigator(s): Katja Nowack
User(s): Alexander Jarjour

Affiliation(s): LASSP, Cornell University
Primary Source(s) of Research Funding: Cornell Center for Materials Research (NSF MRSEC, DMR-1719875)
Contact: kcn34@cornell.edu, abj46@cornell.edu
Primary CNF Tools Used: SC4500 evaporators, JEOL 6300, Oxford PlasmaLab 80+ RIE

Abstract:

We report fabrication of superconducting ionic-liquid (IL) gated MoS_2 devices compatible with scanned probe microscopy (SPM). Using a spin-coated IL gate, the thickness of the ionic layer is reduced to less than 0.5 micron, enabling local magnetic measurements of the superconducting state.

Summary of Research:

Atomically thin exfoliated MoS_2 devices have been reported to superconduct at an n-type charge carrier density of $\sim 10^{14}$ cm^{-2} [1] with a critical temperature of approximately $\sim$ 2 K in a monolayer [2]. To achieve the high charge carrier density ionic gating has been employed in the literature, however, this prevents scanned probe measurements due to the macroscopic thickness of the ionic gate on top of the device. Our group is interested in imaging the magnetic response of the superconducting state, using scanning Superconducting QUantum Interference Device (SQUID) microscopy. This technique can be used to measure the superfluid density of a superconductor as a function of temperature, which can reveal information about the order parameter [3].

Our device fabrication is performed in the CNF. First, optical contact lithography is used to pattern liftoff resist for bond pads, long leads from the device area to the bond pads, and a large gate for biasing the ionic liquid. A completed device is shown in Figure 1, which includes these features. The SC4500 electron beam evaporator is then used to deposit a Ti/Pt/Au trilayer. The gold is wet etched in the gate region, exposing the platinum. Thus, the device side of the electrolytic capacitor is gold, and the gate side is platinum, with the aim of minimizing electrochemistry during gating. Using the polymer stamp transfer techniques developed for graphene heterostructures [4], MoS_2 flakes are transferred onto these prepatterned substrates, and any polymer residue is removed by a chloroform dip. Then, contacts are patterned to the flake using the JEOL 6300 electron-beam lithography system, connecting it to the long leads and bond pads. These contacts are then metalized in the SC4500 with Ti/Au. Next, a hall bar geometry is defined with the JEOL 6300, and the Oxford 80 is used to etch the MoS_2. Finally, a vacuum bake is used to remove any residue from the devices. A completed MoS_2 device before liquid gating is shown in the left in Figure 2.

In our lab, an ionic gel is prepared from diethylmethyl(2-methoxyethyl)ammonium bis(trifluoromethylsulfonyl) imide (DEME-TFSI) and polystyrene-poly(methyl methacrylate)-polystyrene (PS-PMMA-PS). In an inert atmosphere, this gel is spin-coated onto the devices, covering the MoS_2 flake and the platinum gate. The device is then transferred into a scanning SQUID microscope and is dessicated under high vacuum for 24 hours before cooldown. Upon cooling to < 10 Kelvin, a superconducting transition is observed. We have measured both DC magnetization and AC magnetic susceptibility of these devices, a first in a van der Waals superconductor. On the right in Figure 2, the AC susceptibility of a device is shown. Positive signals correspond to diamagnetism. The white dashed outline is the device geometry.

Magnetic measurements of the superconducting state are still a work in progress. Magnetic features suggestive of vortex-vortex interactions, including a Berezinskii-Kosterlitz-Thouless transition, are observed but not shown. We continue to improve and refine these measurements and their analysis.

References:

[1] J. T. Ye, et al., Science 338, 1193 (2012).

[2] D. Costanzo, et al., Nature Nanotechnology 11, 339 (2016).

[3] J.A. Bert, et al., PRB Vol 86 (2012).

[4] P. J. Zomer, et al., Appl. Phys. Lett. 105, 013101 (2014).

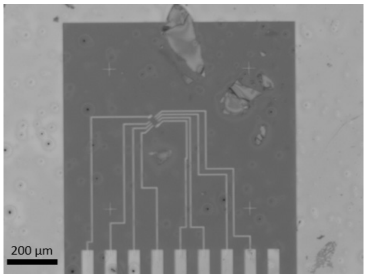

Figure 1: Spin-coated 380 nm ionic gel on MoS_2 few-layer device. Large surrounding metallic region is Pt gate, bars at bottom of image are optically patterned leads to bond pads.

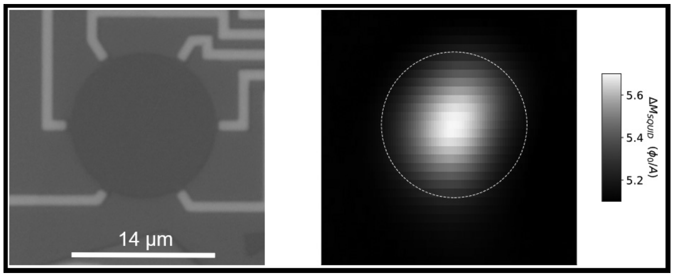

Figure 2: Left, optical image of few layer MoS_2 device fabricated by the authors. Right, magnetic susceptibility map of the same device, as acquired by scanning SQUID microscope.

Two-Dimensional Magnetic Nanoelectromechanical Resonators

CNF Project Number: 2633-18

Principal Investigator(s): Jie Shan, Kin Fai Mak

User(s): Shengwei Jiang

Affiliation(s): Laboratory of Atomic and Solid State Physics, School of Applied and Engineering Physics; Cornell University

Primary Source(s) of Research Funding: Air Force Office of Scientific Research

Contact: jie.shan@cornell.edu, kinfai.mak@cornell.edu, sj538@cornell.edu

Primary CNF Tools Used: Autostep i-line stepper, Hamatech wafer processor develop, Heidelberg mask writer - DWL2000, photolithography spinners, SC4500 odd/even-hour evaporator, DISCO dicing saw

Abstract:

Two-dimensional (2D) layered materials possess out-standing mechanical, electronic and optical properties, making them ideal materials for nanoelectromechanical applications. The recent discovery of 2D magnetic materials has promised a new class of magnetically active nanoelectromechanical systems. In this project, we demonstrate resonators made of 2D magnet CrI_3, whose mechanical resonances depend on the magnetic state of the material.

Summary of Research:

Two-dimensional (2D) layered magnetic materials are attractive building blocks for nanoelectromechanical systems (NEMS): while they share high stiffness and strength and low mass with other 2D materials, they are magnetically active [1-3]. In this project, we develop magnetic NEMS resonators made of 2D chromium triiodide (CrI_3) and investigate the magnetostriction effects in the material.

Figure 1 shows the schematics of the drumhead device structure and the measurement system. The device is made of a bilayer CrI_3 membrane (an antiferromagnet) encapsulated by few-layer graphene and monolayer tungsten diselenide (WSe_2). The few-layer graphene acts as a conducting electrode, and monolayer WSe_2, as a strain gauge [4]. The heterostructure is suspended over a microtrench to form a mechanical resonator.

Figure 2 is an optical image of a typical device. The circular microtrenches of 2-3 µm in radius and 600 nm in depth are patterned on Si/SiO_2 substrates by the combined UV photolithography and plasma etching of the SiO_2 layer. The Ti/Au electrodes are patterned on the Si/SiO_2 substrates by photolithography and metal evaporation. Atomically thin samples of CrI_3, WSe_2, and graphene are first exfoliated from their bulk crystals onto silicon substrates covered with a 300 nm thermal oxide layer. Selected thin flakes of appropriate thickness and geometry are then picked up one-by-one by a stamp consisting of a thin layer of polycarbonate on polydimethylsiloxane (PDMS). The complete heterostructure is first released onto a new PDMS substrate so that the residual PC film on the sample can be

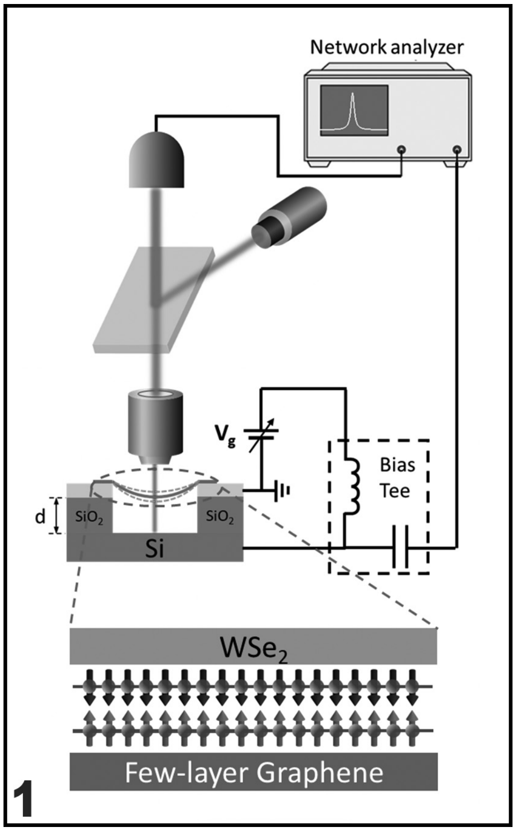

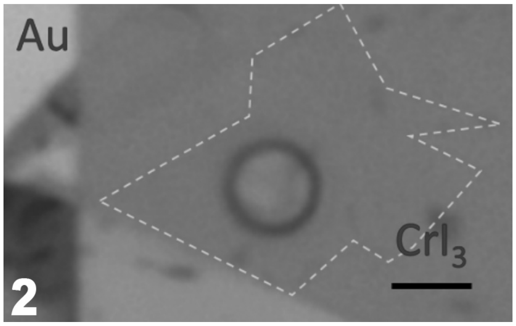

Figure 1, top: *Schematic of the device structure and the measurement system. Filled spheres and arrows denote Cr atoms and spins in the top and bottom CrI_3 layer.*
Figure 2, bottom: *Optical microscope image of a bilayer CrI_3 device suspended over a circular trench. Dashed line shows the boundary of the CrI_3 flake. Scale bar is 4 µm.*

removed. The sample is then deposited onto the substrates with pre-patterned microtrench and Au electrodes.

The resonator is actuated by an R.F. voltage from a vector network analyzer (VNA) through a bias tee (Figure 1). A DC voltage V_g can be superimposed to apply static tension to the membrane. The motion is detected interferometrically by a HeNe laser, which is focused onto the center of the resonator. Figure 3 shows the fundamental resonance mode of a bilayer CrI_3 membrane at V_g = 0. It has a Lorentzian lineshape (solid line) with a peak frequency f around 25.5 MHz and a width around 10 kHz, corresponding to a quality factor of about 2500. The resonance frequency is well described by the continuum model (assuming zero bending stiffness) with fully clamped boundary [5]. It is inversely proportional to the drumhead radius, and is determined by the initial stress on the membrane and the 2D mass density of the membrane.

We investigate the effect of magnetic field on CrI_3 resonators. The nanomechanical resonance of the bilayer CrI_3 device is measured while the out-of-plane field is swept from 1 T to -1 T back to 1 T. The resonance frequency *f* is independent of field except an abrupt redshift of ~ 0.06% when the field magnitude exceeds ~ 0.5 T. We correlate the field dependence of *f* with the sample's magnetic circular dichroism. The latter shows that bilayer CrI_3 is antiferromagnetic (AF) under small fields and undergoes a first-order spin-flip transition around ± 0.5 T to become ferromagnetic (FM) [6]. The mechanical resonance frequency is thus correlated with the sample's magnetic state with the resonance frequency in the AF state larger than in the FM state. This phenomenon can be understood as exchange magnetostriction. We extract the intrinsic saturation magnetostriction in bilayer CrI_3 (10^{-5}), which is comparable to that of elemental ferromagnetic metals.

In conclusion, we have demonstrated a new type of magnetostrictive NEMS based on 2D CrI_3. Our results also establish the basis for mechanical detection of the magnetic states and magnetic phase transitions in 2D layered magnetic materials.

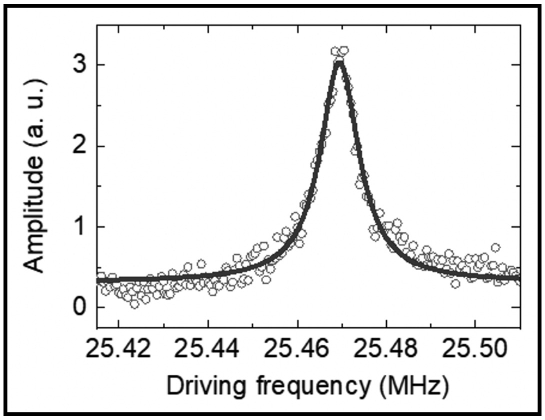

Figure 3: Fundamental mechanical resonance (symbols) of a bilayer CrI_3 resonator (radius 2 µm) and a Lorentzian fit of the resonance spectrum (solid line).

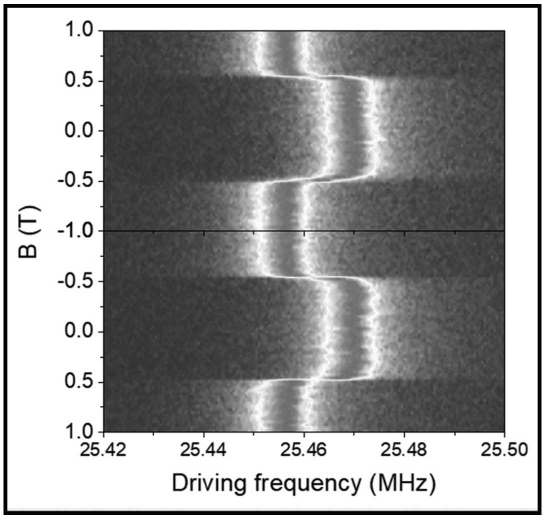

Figure 4: Normalized vibration amplitude of a bilayer CrI_3 resonator vs. driving frequency under an out of-plane magnetic field that sweeps from 1 T to -1 T to 1 T.

References:

[1] Craighead, H. G. Nanoelectromechanical Systems. Science 290, 1532-1535 (2000).

[2] Huang, B., et al. Nature 546, 270 (2017).

[3] Gong, C., et al. Nature 546, 265-269 (2017).

[4] Frisenda, R., et al. Biaxial strain tuning of the optical properties of single-layer transition metal dichalcogenides. npj 2D Mater. Appl. 1, 10 (2017).

[5] Bunch, J. S., et al. Electromechanical Resonators from Graphene Sheets. Science 315, 490-493 (2007).

[6] Jiang, S., Shan, J., and Mak, K. F. Nature Materials 17, 406 (2018).

Mass Transport on Graphene

CNF Project Number: 2767-19
Principal Investigator(s): Scott Schiffres
User(s): Yingchun Jiang, Morteza Bagheri

Affiliation(s): Mechanical Engineering, Binghamton University
Primary Source(s) of Research Funding: Startup funding
Contact: sschiffr@binghamton.edu, yjiang89@binghamton.edu, mortezahb@binghamton.edu
Primary CNF Tools Used: Heidelberg DWL2000, ABM, MA6 contact aligner, Oxford 81 etcher, YES Asher, SC4500 evaporator, Zeiss Ultra SEM

Abstract:

A graphene channel with various widths for atomic mass transportation was fabricated photolithographically. Transportation of aluminum nanoparticles on graphene ribbon under ambient condition was demonstrated.

Summary of Research:

The development of nanotechnology requires versatile manipulation tools for atomic scale assembly and controlled material delivery. Scanning tunneling microscope (STM), atomic force microscope (AFM) have been demonstrated as powerful tools for manipulation of atoms and molecules on clean surfaces. However, these tools suffer from low delivery efficiency: they are not capable to deliver nanometer scale features containing large amounts of atoms, and they cannot deliver atom efficiently to the desired work area (sticky). Carbon nanotubes and graphene have been suggested as possible nanoscale mass conveyors with an electric field as the source of applied force. Controllable and reversible atomic metal transportation along carbon nanotubes (CNTs) and transport of more than 10^7 atoms have been demonstrated [1-3]. Graphene is mechanically robust and chemically inert; it can sustain large current density similar to CNTs. It has the advantage over CNTs that more complicated mass transport circuits can be designed with lithographic techniques [4-7].

We fabricated graphene ribbon with traditional photolithography process as shown in Figure 1. Pt/Au contact pads were patterned on top of the graphene channel or the graphene electrodes. Thin Al pads (around 2 µm wide and 7 nm thick) were evaporated on the graphene circuits (as shown in Figure 2 (a)) for demonstration of atomic mass transportation on graphene. After deposition of the Al pads, it was annealed under vacuum to reflow the Al, the topography of the Al after annealing is shown in Figure 3 (b). The Al atoms are manipulated by applying large electric field along the graphene circuit. Mass loss of Al and mass increase near the electrode were observed after applying large electric field, as shown in Figure 3.

Conclusions and Future Steps:

The motion of thin Al pads along graphene circuit under ambient condition was demonstrated. The characterization of the actuation should be studied further, especially the contribution of the thermal effect to the motion. We should also find the electric field that is large enough for continuous manipulation of the atoms without damaging the graphene device.

References:

[1] B.C. Regan, S. Aloni, R.O. Ritchie, U. Dahmen, A. Zetti, Carbon nanotubes as nanoscale mass conveyors, Nature. 428 (2004) 924-927. doi:10.1038/nature02496.

[2] Z. Ren, Y. Lan, Y. Wang, Subnanometer motion of cargoes driven by thermal gradients along carbon nanotubes, Science (80-.). (2012) 7-43. doi:10.1007/978-3-642-30490-3_2.

[3] N. Mingo, L. Yang, J. Han, Current-induced forces upon atoms adsorbed on conducting carbon nanotubes, J. Phys. Chem. B. 105 (2001) 11142-11147. doi:10.1021/jp011491s.

[4] S. Hertel, F. Kisslinger, J. Jobst, D. Waldmann, M. Krieger, H.B. Weber, Current annealing and electrical breakdown of epitaxial graphene, Appl. Phys. Lett. 98 (2011) 2009-2012. doi:10.1063/1.3592841.

[5] A. Barreiro, R. Rurali, E.R. Hernández, A. Bachtold, Structured graphene devices for mass transport, Small. 7 (2011) 775-780. doi:10.1002/smll.201001916.

[6] J. Moser, A. Barreiro, A. Bachtold, Current-induced cleaning of graphene, Appl. Phys. Lett. 91 (2007) 1-4. doi:10.1063/1.2789673.

[7] D. Solenov, K.A. Velizhanin, Adsorbate transport on graphene by electromigration, Phys. Rev. Lett. 109 (2012) 1-5. doi:10.1103/PhysRevLett.109.095504.

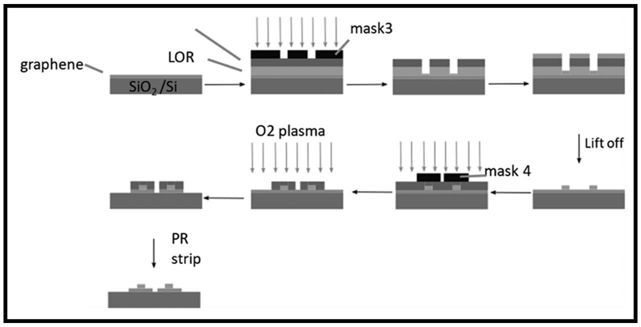

Figure 1: Process flow for making Al pads on graphene ribbon by lift off.

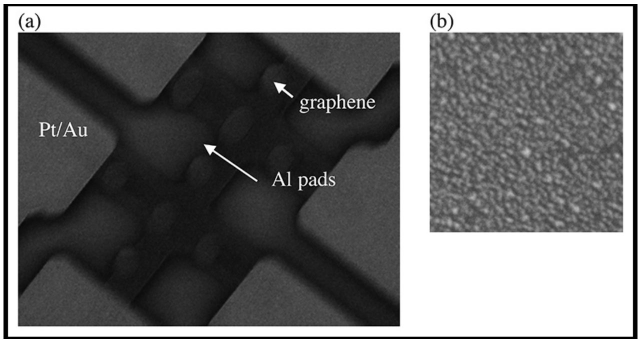

Figure 2: (a) SEM image of the graphene circuit with Al pads.
(b) Topography of thin aluminum film after annealing.

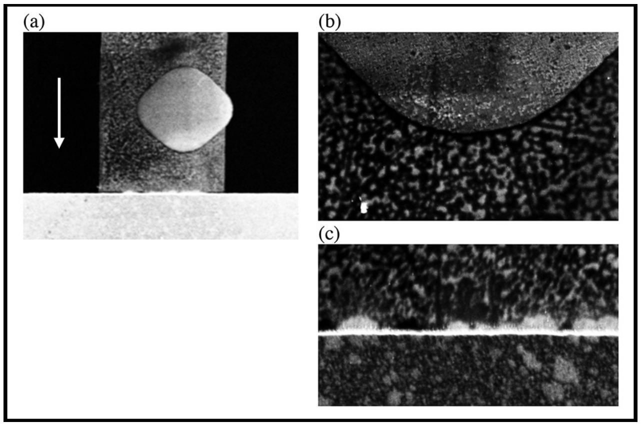

Figure 3: (a) SEM image of an Al pad after applying electric field in air.
(b) Edge of the Al showing mass loss after applying electric field.
(c) edge of the electrodes showing mass increase.

Superconducting Thin Film Growth, Post-Treatments, and Defects Investigation

CNF Project Number: 2779-19

Principal Investigator(s): Matthias Liepe

User(s): Zeming Sun

Affiliation(s): Cornell Laboratory for Accelerator-based Sciences and Education, Cornell University

Primary Source(s) of Research Funding: National Science Foundation under Grant No. PHY-1549132

Contact: MUL2@cornell.edu, zs253@cornell.edu

Website: https://physics.cornell.edu/matthias-liepe

Primary CNF Tools Used: Chemical vapor deposition system, Oxford FlexAL ALD, Arradiance Gemstar-6 atomic layer deposition system, Thermal/ E-gun evaporation system, Woollam spectroscopic ellipsometer, Zygo optical profilometer, P10 profilometer

Abstract:

Superconducting radio frequency (SRF) cavities are important in accelerating charged particle beams that have broad applications such as colliders, neutron sources, and light sources. Niobium tin (Nb_3Sn), vanadium silicate (V_3Si), and magnesium diboride (MgB_2) are the most promising superconductor candidates for the next generation SRF cavities. However, their thin film growth is still challenging due to surface roughness, defect generation, grain boundaries, and surface oxidation. Thus, this project investigates the growth mechanisms of superconducting films deposited via electroplating, sputtering, chemical vapor deposition approaches, and explores post-processing techniques, such as electropolishing, surface passivation, and laser annealing, to mitigate the crystal defects, surface roughness, and oxidation. Moreover, this project studies the impact of defects on the SRF performance through studying the performance of artificial structures that are fabricated at the Cornell NanoScale Science and Technology Facility (CNF).

Summary of Research:

(1) We demonstrated ultra-low surface roughness Nb_3Sn superconductors (detailed in Reference [1]). This is achieved by thermal conversion of a pre-deposited Sn film that is uniform, smooth, dendrite-free, and has strong adhesion. Electroplating, as an excellent method for coating intricate SRF cavity surface, is used to enable the deposition process of a high-quality Sn film. The resultant Nb_3Sn shows an extremely low surface roughness of 65 nm as shown in the atomic force microscopy image (Figure 1).

(2) Alternative deposition approaches such as sputtering, chemical vapor deposition, and chemical methods are explored to deposit Nb_3Sn and V_3Si. For example, a fast-ion transport reaction is demonstrated for generating Nb_xSn (detailed in Reference [2]). X-ray photoelectron spectroscopy (XPS) depth profiling provides direct evidence of film stoichiometry (Figure 2). Another success is sputtering of Nb_3Sn and V_3Si have been enabled on Nb and Cu substrates (Figure 3). The optimization of film quality is ongoing.

(3) Post treatments such as electropolishing and laser annealing are explored to improve the superconductor film quality. For example, the chemical vapor deposited Nb film is greatly smoothed via electropolishing with the surface roughness reduced by half (detailed in Reference [3]). Moreover, the laser annealing technique has been studied to reduce film surface roughness. A titanium nitride film was deposited via atomic layer deposition to improve the laser light absorption. The deposition condition is optimized for desired film thickness and refractive index (Figure 4). With this critical absorption layer, the laser is able to melt the Nb_3Sn surface and remove the sharp surface pits.

(4) MgB_2 superconducting thin film is easily oxidized in air which hinders its wider application. An aluminum nitride film is deposited on the film using plasma-enhanced atomic layer deposition to passivate the surface. The interface is being analyzed using XPS.

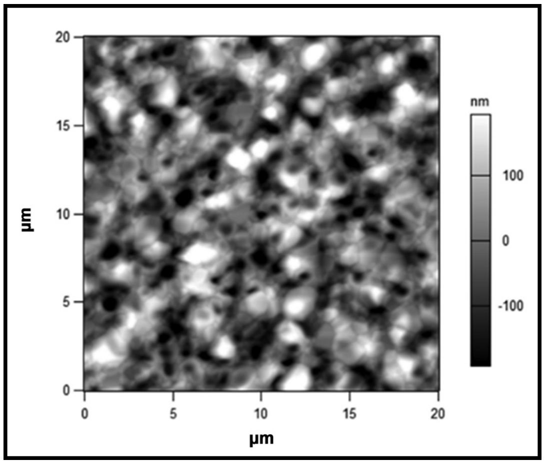

Figure 1: Atomic force microscopy of thermally converted Nb_3Sn from electroplated Sn films, showing an extreme low surface roughness.

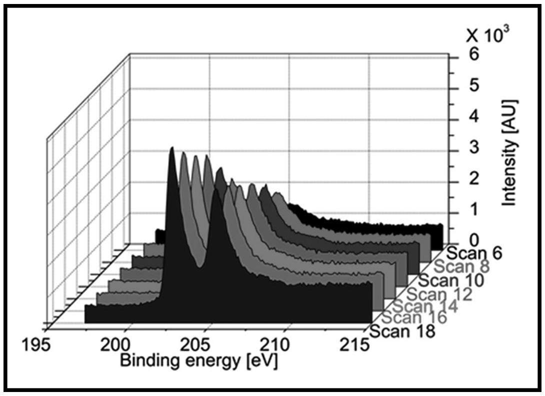

Figure 2: X-ray photoelectron spectroscopy depth profiling of fast-transported Nb_xSn film showing Nb 3d intensity approaching stoichiometry of Nb_3Sn.

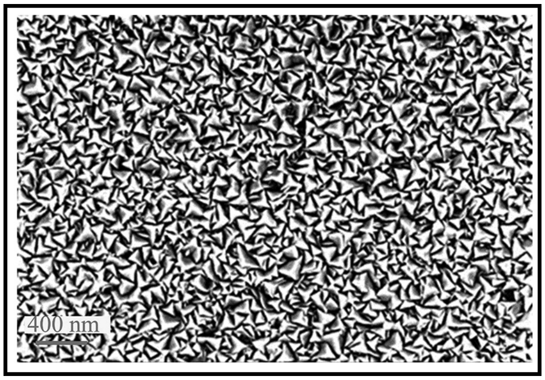

Figure 3: SEM of the sputtered Nb_3Sn films.

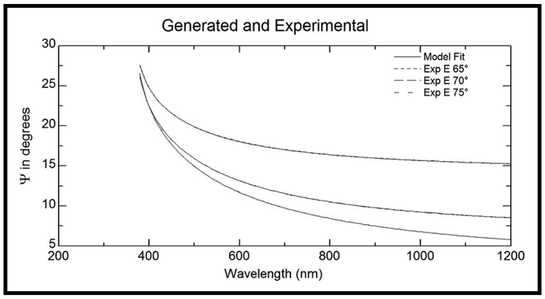

Figure 4: Ellipsometry modeling for optimizing titanium nitride deposition by thermal atomic layer deposition.

References:

[1] Z. Sun, M. Liepe, T. Oseroff, R.D. Porter, T. Arias, N. Sitaraman, A. Connolly, J. Scholtz, M.O. Thompson, Electroplating of Sn film on Nb substrate for generating Nb-Sn thin films and post laser annealing, Proceeding of SRF'19, Dresden, Germany, 2019.

[2] Z. Sun, M. Liepe, J.T. Maniscalco, T. Oseroff, R.D. Porter, D. Zhang, X. Deng, Fast Sn-ion transport on Nb surface for generating NbxSn, Proceeding of NAPAC'19, Michigan, 2019.

[3] Z. Sun, M. Ge, K. Howard, M. Liepe, J. Maniscalco, T. Oseroff, R. Porter, V. Arrieta, S. McNeal, TESLA Technology Collaboration workshop, Geneva, Switzerland, February, 2020.

Development of Strain-Tunable Bilayer Graphene Devices

CNF Project Number: 2790-19
Principal Investigator(s): Katja C. Nowack
User(s): Brian T. Schaefer, Justin Oh

Affiliation(s): Laboratory of Atomic and Solid-State Physics, Department of Physics; Cornell University

Primary Source(s) of Research Funding: Cornell Center for Materials Research with funding from the NSF MRSEC program (DMR-1719875), National Science Foundation Graduate Research Fellowship under Grant No. DGE-1650441

Contact: kcn34@cornell.edu, bts72@cornell.edu
Website: http://nowack.lassp.cornell.edu/

Primary CNF Tools Used: Zeiss Supra SEM/Nabity, Trion Minilock III ICP etcher, 5x stepper

Abstract:

The direct application of uniaxial strain is a versatile and low-disorder technique to tune the electronic properties of materials [1]. Specifically, in two-dimensional materials with a hexagonal lattice, strain can result in a net magnetization with a purely orbital origin [2]. Dual-gated bilayer graphene is a versatile platform for studying this magnetization because the electronic bandgap and charge carrier density can be tuned widely and independently [3]. Here, we describe our efforts towards fabricating strainable multi-terminal bilayer graphene devices on flexible polyimide substrates. We continuously apply strain up to ~ 1.4% confirmed using Raman spectroscopy.

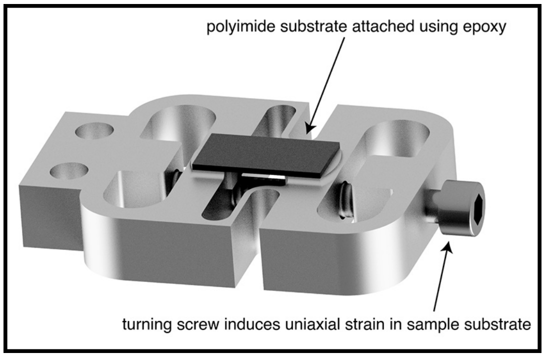

Figure 1: Custom titanium-based strain apparatus4 with polyimide substrate attached using Stycast 2850FT epoxy.

Summary of Research:

We use the custom titanium-based apparatus [4] illustrated in Figure 1 to apply strain to a polyimide substrate upon which our bilayer graphene devices are fabricated. Turning the screw displaces the two halves of the apparatus and enables continuous application of uniaxial tensile strain to a sample mounted to the split central platform. The maximum strain depends on the elastic modulus and geometry of the sample along with the yield strength of the epoxy used to attach the sample. Optical images of lithographically defined features on the surface of the substrate suggest a typical maximum strain of ~ 2% for polyimide substrates limited by failure of the epoxy.

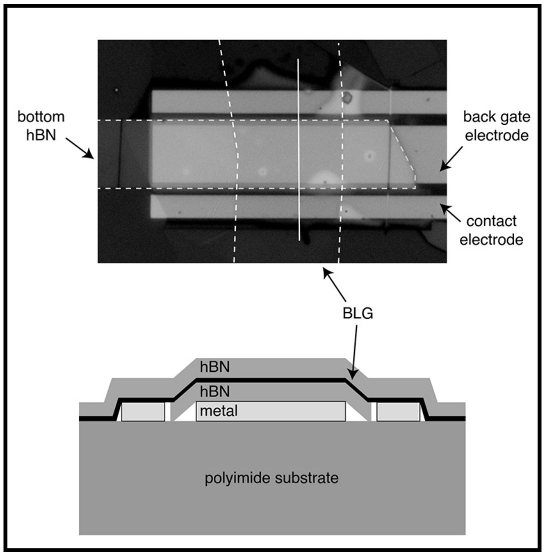

Figure 2: Top: optical image of a bilayer graphene device fabricated upon a polyimide substrate. Bottom: cross-sectional schematic along the solid line in the optical image.

Figure 2 shows an optical image and cross-sectional schematic of a strainable bilayer graphene device. We initially pattern metal electrodes for the device back gate and contacts onto a bare polyimide substrate. Next, we use a polymer-stamp-based dry-transfer technique [5] to sequentially pick up and transfer exfoliated flakes of bilayer graphene (BLG) and hexagonal boron nitride (hBN) onto the pre-patterned metal features.

We first transfer a single hBN flake onto the patterned electrodes and use reactive-ion etching (Trion Minilock III ICP Etcher) to uncover the metal contact electrodes. On top of this, we transfer a stack of hBN/BLG to complete the device. The top hBN flake facilitates the transfer of BLG, while the bottom hBN flake is a dielectric for the back gate. Encapsulation with hBN on both top and bottom improves the electronic quality of graphene devices [5]. Previous iterations of the fabrication process suggest that the direct areal contact between the BLG flake and polyimide substrate in our current design is essential for effective strain transfer from the substrate to the BLG flake.

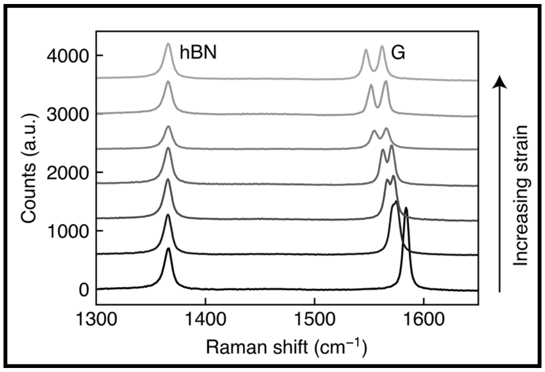

Figure 3: Strain evolution of the in-plane Raman peaks for BLG (labeled "G") and hBN.

We use Raman spectroscopy to monitor changes in the vibrational modes of the lattice under application of strain, and use the position of the BLG "G" peak to estimate the amount of strain transfer. Figure 3 shows the evolution of the in-plane Raman peaks for hBN ("hBN", ~ 1366 cm^{-1} at zero strain) and BLG ("G", ~ 1583 cm^{-1} at zero strain) upon straining the substrate. The G peak shifts to lower wavenumber and splits into two distinct peaks, as expected for a hexagonal lattice with rotational symmetry broken by in-plane uniaxial strain [6]. The hBN peak is also expected to shift under uniaxial strain, so the unchanging peak position suggests that strain is not transferred to hBN. The hBN-graphene interface exhibits notably low friction [7], so the lack of strain in the hBN layer is not surprising. Comparing the peak positions to those reported in the literature [6], we estimate that we induced at most ~ 1.4% uniaxial strain into this BLG device.

Conclusions and Future Steps:

We demonstrate application of uniaxial strain in a two-terminal bilayer graphene device fabricated on a metallic back gate and polyimide substrate. Moving forward, we aim to add a top gate electrode and identify improvements to the process that increase the yield of devices that strain reliably. This motivates investigation of the mechanism of strain transfer from the substrate into BLG. We then will study the effects of strain on the magnetic properties of our devices and extend this technique to other two-dimensional material systems.

References:

[1] Wang, L. et al. Mobility Enhancement in Graphene by *in situ* Reduction of Random Strain Fluctuations. Phys. Rev. Lett. 124, 157701 (2020).

[2] Lee, J., Wang, Z., Xie, H., Mak, K. F., and Shan, J. Valley magnetoelectricity in single-layer MoS_2. Nat. Mater. 16, 887-891 (2017).

[3] Zhang, Y., et al. Direct observation of a widely tunable bandgap in bilayer graphene. Nature 459, 820-823 (2009).

[4] Sunko, V., et al. Direct Observation of a Uniaxial Stress-driven Lifshitz Transition in Sr_2RuO_4. npj Quantum Materials 4 (2019).

[5] Wang, L., et al. One-dimensional electrical contact to a two-dimensional material. Science 342, 614-617 (2013).

[6] Tsoukleri, G., Parthenios, J., Galiotis, C., and Papagelis, K. Embedded trilayer graphene flakes under tensile and compressive loading. 2D Mater. 2, 024009 (2015).

[7] Song, Y., et al. Robust microscale superlubricity in graphite/hexagonal boron nitride layered heterojunctions. Nat. Mater. 17, 894-899 (2018).

Inkjet-Printed Colloidal Quantum Dot Superlattices

CNF Project Number: 1645-08

Principal Investigator(s): Tobias Hanrath

User(s): Daniel M. Balazs, N. Deniz Erkan, Michelle Quien

Affiliation(s): School of Chemical and Biomolecular Engineering, Cornell University

Primary Source(s) of Research Funding: Department of Energy - Basic Energy Sciences (DE-SC0018026), National Science Foundation (DMR-1719875) for the use of Cornell Center for Materials Research tools

Contact: tobias.hanrath@cornell.edu, daniel.balazs@cornell.edu, nde26@cornell.edu, mq65@cornell.edu

Primary CNF Tools Used: Dimatix printer

Abstract:

In this work, we investigated whether inkjet printing is a suitable method to form nanocrystal superlattices on top of (sub-)mm sized droplets or not. We identified the choice of solvent as a bottleneck in the process. We reviewed and adapted the common and system-specific constraints and found a suitable candidate. We successfully prepared highly ordered superlattices using dodecane, and explored the limitations of the approach.

Summary of Research:

Colloidal quantum dot (CQD) superlattices with epitaxial connections between the constituents are exciting bottom-up fabricated metamaterials with properties adjustable between zero and three dimensions. Assemblies can be achieved on solid substrates, but the shrinkage and consequent mechanical strain following the fabrication leads to cracks and low domain sizes. Liquid "substrates" offer the necessary translational and rotational freedom for highly ordered systems.

In this approach, a thin film of a liquid is layered onto an immiscible second liquid, with CQDs dissolved in the top phase and not soluble in the bottom phase [1]. The method works well on the centimeter scale when a microliter scale volume of the top liquid is manually injected using a pipette. Automation and scaling down to the sub-mm level require a different approach to liquid handling.

In this work, the CNF Dimatix Materials printer was used to jet picoliter sized droplets of a CQD solution onto an immiscible glycol droplet (see Figure 1a). The glycol droplets were created using patterned Si substrates; the two approaches used to contain the glycol are geometric contrast (created by etching wells of the desired shape into the wafer) and wetting contrast (created by lithographic definition of wetting and nonwetting regions, as shown in Figure 1b). While the former approach provided better glycol droplet stability, the latter allows the samples to be picked up by stamping for TEM characterization, and is more suitable for prospective integration into device fabrication processes.

The approach is a modified, more complex version of that developed for the creation of ordered polymer thin films [2]. The key problem we had to solve was the choice of solvent, as any common printing additives affect the superlattice assembly. Multiple thermodynamic and kinetic constraints need to be fulfilled for the formation of high-quality films. The constrains related to the inkjet printing stem from fluid dynamics: (a) the kinetic energy has to be higher than the surface free energy so that a droplet forms, (b) the droplet acceleration, the viscous and surface forces have to be in balance so that a droplet forms and does not fall apart and (c) the same forces need to allow the droplet to break off from the jetter [3].

These constraints are expressed in terms of the dimensionless Reynolds number ($Re = \rho vd/\gamma$) and Weber-number ($We = \rho v^2 d/\mu$) as $We < 1/16\ Re^2$, $We > 1/200\ Re^2$ and $We > 4$. The numerical relations are only approximate and strongly depend on the details of the instrument. However, the general idea applies: low enough surface tension and viscosity are required for droplets to form, but the droplets have to be stabilized by high enough viscosity and surface tension.

A fourth constraint is set by the aim that the jetted droplet does not splatter the subphase droplet [4]. This is described by $We' = \rho v^2 d^3/\gamma_s h_s^2 < 1$, where the subscript "s" indicates subphase property. Using EG, this can be converted into $We < 40$, suggesting that high viscosity and low jetting velocity are required. The constraint for spreading of the CQD solution on glycol is expressed as coefficient $S = \gamma_{02} - (\gamma_{01} + \gamma_{12})$, where 0 is air, 1 is top and 2 is bottom liquid; only a system with

S > 0 fully spreads into a flat film. This constraint requires a solvent with low surface tension, in contrast with the high surface tension requirement of the jetting process. The final, and most important set of constraints is the immiscibility with glycol and high solubility of the CQDs. From all common solvents, alkanes with more than 10 carbon are the only suitable ones.

We performed a set of experiments with pure alkanes and their mixtures with polar solvents, and we found that dodecane is the only suitable candidate. Shorter alkanes, such as decane are not viscous enough for the jetting process (even dodecane requires a low velocity to form stable droplets), and longer alkanes do not spread well on glycol due to a high surface tension. However, we managed to optimize the jetting parameters for dodecane and the derived CQD solution without the use of additives. Example superlattices are shown in Figure 2. Good homogeneity and local order are observed in line with previous reports on large-scale samples [5].

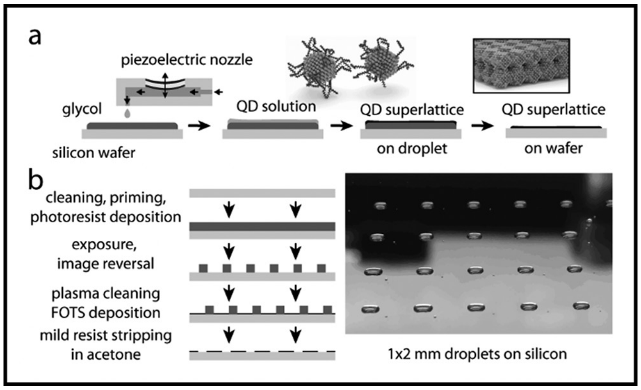

Figure 1: a) Scheme for the interfacial assembly of CQD superlattices using inkjet printing; b) scheme for creating droplets on substrates using wetting contrast and example droplets.

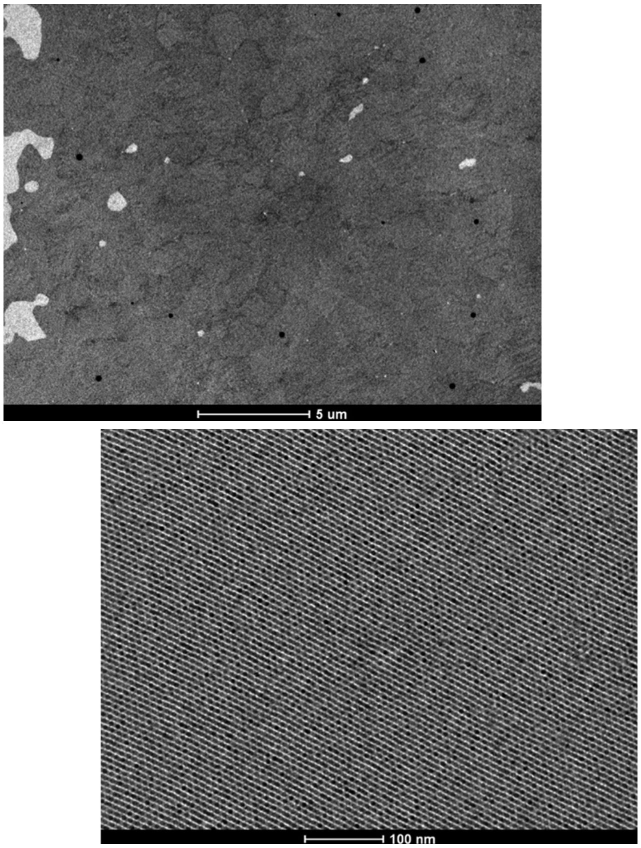

Figure 2: Two TEM images of CQD superlattices formed on glycol droplets via inkjet printing.

References:

[1] Dong, A.; Chen, J.; Vora, P. M.; Kikkawa, J. M.; Murray, C. B. Binary Nanocrystal Superlattice Membranes Self-Assembled at the Liquid-Air Interface. Nature 2010, 466 (7305), 474-477.

[2] Minemawari, H.; Yamada, T.; Matsui, H.; Tsutsumi, J.; Haas, S.; Chiba, R.; Kumai, R.; Hasegawa, T. Inkjet Printing of Single-Crystal Films. Nature 2011, 475 (7356), 364-367.

[3] Derby, B. Inkjet Printing of Functional and Structural Materials: Fluid Property Requirements, Feature Stability, and Resolution. Annu. Rev. Mater. Res. 2010, 40 (1), 395-414.

[4] Noda, Y.; Minemawari, H.; Matsui, H.; Yamada, T.; Arai, S.; Kajiya, T.; Doi, M.; Hasegawa, T. Underlying Mechanism of Inkjet Printing of Uniform Organic Semiconductor Films Through Antisolvent Crystallization. Advanced Functional Materials 2015, 25 (26), 4022-4031.

[5] Balazs, D. M.; Dunbar, T. A.; Smilgies, D.-M.; Hanrath, T. Coupled Dynamics of Colloidal Nanoparticle Spreading and Self-Assembly at a Fluid-Fluid Interface. Langmuir 2020. in press.

Nanoscale Periodic Pillar Feature Process Survival

CNF Project Number: 2217-13

Principal Investigator(s): Ioannis (John) Kymissis

User(s): Tanya Cruz Garza

Affiliation(s): Department of Electrical Engineering, Columbia University, New York, NY

Primary Source(s) of Research Funding: National Science Foundation

Contact: johnkym@ee.columbia.edu, tanyacruzgarza@gmail.com

Website: http://kymissis.columbia.edu

Primary CNF Tools Used: ASML 300C DUV, GCA 5x Autostep i-line stepper

Abstract:

The ASML 300C DUV and GCA 5x Autostep i-line stepper have been used in previous years to produce pillar and hole features with diameters ranging from 232 nm to 816 nm on fused silica and silicon wafers. Hole features are favored over pillar features because pillars are more susceptible to destruction during further wafer processing. It has been found that pillar features give optical performance up to 3.5 times higher than the hole features in spectral applications. For this reason, pillar feature fabrication with further front and backside wafer processing as well as diced die polishing was explored. For wafers that had additional metal layers patterned on the front and back side of the wafer yields of 71-79% was found with hole features and a wafer yield of 50% was found for pillar features. For wafers that had additional metal layers patterned on the front and back side of the wafer that also had an edge polished on each die after singulation had yields of 53-89% for hole features and 8% for pillar features. This reduction in wafer yield for wafers with pillars versus holes was consistent with the initial results reported last year.

Summary of Research:

In previous years a process for patterning nanophotonic pillar and hole structures was developed at CNF that used the ASML 300C DUV stepper as well as the GCA 5x Autostep i-line stepper. These features were etched into the substrate material using the patterned resist as an etch mask. The ASML 300C DUV stepper process has been used to pattern 4-inch borosilicate float glass wafers ("borofloat"), 4-inch fused silica wafers, and 4-inch silicon wafers. Pillar features like those shown in Figure 1 were fabricated with diameters ranging from 232 nm to 816 nm. Hole features were fabricated with design diameters ranging from 306 nm to 446 nm. Optimal depth of focus (DOF), exposure dose, and etch time were determined for nanophotonic patterns in fused silica by varying these parameters incrementally and examining the resultant features. Photonic crystal geometry was examined in the SEM and photonic crystal performance was assessed optically via extraction of waveguided light.

For recent applications, nanophotonic patterning was mainly focused on holes versus pillars because pillars are more likely to become damaged in a way which renders them useless for our spectral application during further processing and wafer handling. In recent years, processing steps have been added to the wafer after nanophotonic crystal pattering to include both front and back side aluminum reflector layers. These added layers can be combined with single edge polishing after die singulation as shown in Figure 2. These added steps make the pillars more exposed to handing that could damage them. It has been found that pillars designed to the same diameter of corresponding holes give spectral responsively between 50% -350% higher over a range of inputs between 400-1000 nm for designs with a diameter of 446 nm. It is because pillars give such a greater spectral responsively, that they have again been investigated for the fabrication of monolithic optical bench die design which include the light-scattering nanophotonic pattern, reflectors, and polished angular light input.

In the previous reporting period, nanophotonic pillar structures with diameters of 612 nm and 816 nm were made in fused silica wafers with the intent of seeing how they would survive further processing to produce the monolithic optical bench die design. These pillars were patterned on fused silica wafers with the ASML 300C DUV and etched into the substrate using the resist as an etch mask. The 612 nm diameter pillar wafers then had aluminum sputtered onto the front and backside which was patterned via contact lithography plus liftoff. The wafer was then coated with a protective ion beam assisted physical vapor deposited SiO_2 coating layer,

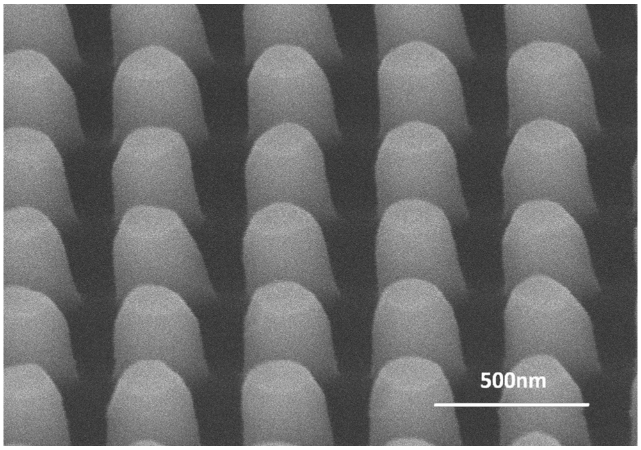

Figure 1: SEM image of photonic crystal pattern, nominally with 270 nm pillar features, fabricated fused silica with process developed with ASML 300C DUV stepper.

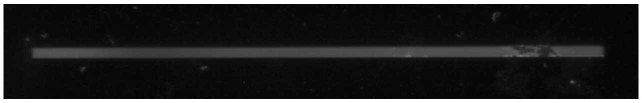

Figure 3: Green light (gray) being scattered through a 306 nm diameter nanophotonic pattern illuminating pillar damage.

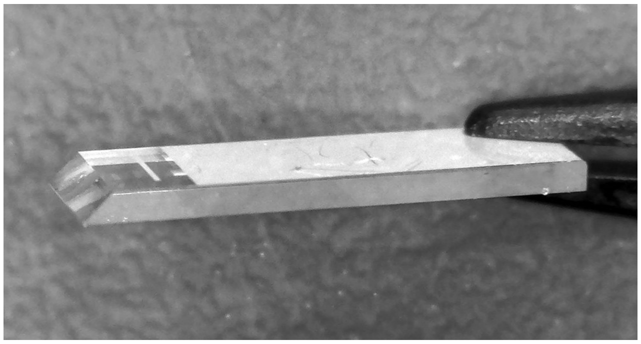

Figure 2: Diced and polished fused silica die with pattered Al reflectors on both sides in addition to the nanophotonic pattern and 45° edge polish.

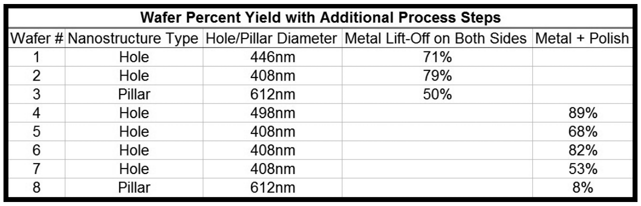

Wafer Percent Yield with Additional Process Steps

Wafer #	Nanostructure Type	Hole/Pillar Diameter	Metal Lift-Off on Both Sides	Metal + Polish
1	Hole	446nm	71%	
2	Hole	408nm	79%	
3	Pillar	612nm	50%	
4	Hole	498nm		89%
5	Hole	408nm		68%
6	Hole	408nm		82%
7	Hole	408nm		53%
8	Pillar	612nm		8%

Figure 4: Wafer percent yield with additional process steps and a variety of nanophotonic pattern diameters.

diced, optionally polished and cleaned. The resulting dies were inspected by waveguiding green light into the edge of the die and inspecting the nanophotonic crystal pattern in a microscope to check for defects. Pillar damage seen in this kind of inspection is apparent in the example given in Figure 3. Nanophotonic patterns may also be rejected for other kinds of defects.

A significant drop in photonic crystal yield was found for wafers with pillar nanophotonic patterns versus holes. Yield results are listed in the Figure 4 table. Wafers that only had metal patterning on the front and back had about 25% higher yield with holes versus pillar. Wafers that had edge polishing in addition to the front and back side metal patterning had an order of magnitude higher yield for wafers with holes versus pillars.

In summary, a process to fabricate nanophotonic pillar structures with a diameter of 612 nm has been used to make dies to with further processing including front and backside aluminum patterns and singulated die polishing. Although pillar features tend to be more fragile when it comes to further wafer processing, these features tend to give higher optical throughput in spectral scattering applications in spectrometer systems.

For wafers that had additional metal layers patterned on the front and backside of the wafer yields of 71-79% was found with hole features and 50% for pillar features. For wafers that had additional metal layers patterned on the front and backside of the wafer and also had an edge polished on each die after singulation yields of 53-89% was found with hole features and 8% for pillar features.

Size Characterization of Plasma Membrane Vesicles, Virus Particles, and Synthetic Vesicles

CNF Project Number: 2575-17

Principal Investigator(s): Susan Daniel

User(s): Tiffany Tang, Miya Bidon

Affiliation(s): Chemical and Biomolecular Engineering, Cornell University

Primary Source(s) of Research Funding: National Science Foundation, National Institute of Health

Contact: sd386@cornell.edu, tt528@cornell.edu, mrb346@cornell.edu

Primary CNF Tools Used: Malvern NS300 NanoSight

Abstract:

The CNF's Malvern NS300 NanoSight was used to determine the concentration and size distribution of various biologically relevant particles, including viruses and plasma membrane vesicles.

Summary of Research:

Our research investigates interactions of biologically relevant particles (viruses, microvesicles, plasma membrane vesicles) on a supported lipid bilayer and with synthetic vesicles. Most of the particles used are generated in-house and as such, it is important to characterize them (diameter, size distribution, concentration of particles) to ensure that we are using the similar quality and concentration of particles across various experiments for consistency. The concentration is especially important as too much or too little of the plasma membrane vesicles used to form the supported lipid bilayer will influence the bilayer's diffusivity and patchiness and varying concentration of viral particles may impact fluorescent dye incorporation.

Typical sizes of viruses, plasma membranes vesicles, and synthetic vesicles that we use range from 100-200 nm and typical values of concentration are on the order of 10^8 particles/mL for plasma membrane particles, 10^{10} particles/mL for viruses and 10^{12} particles/mL for synthetic vesicles.

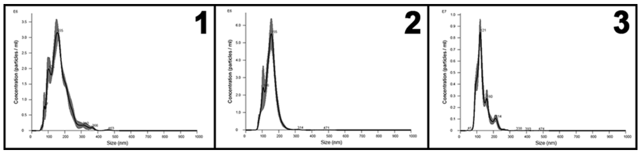

Figure 1, left: *Concentration vs. size (nm) distribution plot for virus like particles.* ***Figure 2, center:*** *Concentration vs. size (nm) distribution plot for pseudotyped virus particles.* ***Figure 3, right:*** *Concentration vs. size (nm) distribution plot for synthetic vesicles.*

Wet Etching of N-Polar AlN on NbN for Novel III-N Device Applications

CNF Project Number: 2800-19

Principal Investigator(s): Debdeep Jena, Huili Grace Xing

User(s): Jeffrey Miller

Affiliation(s): Electrical and Computer Engineering, Cornell University

Primary Source(s) of Research Funding: Semiconductor Research Corporation

Contact: grace.xing@cornell.edu, jpm433@cornell.edu

Primary CNF Tools Used: ABM contact aligner, PT770 etcher, Oxford 81 etcher, odd hour e-beam evaporator, Oxford PECVD, AJA sputter deposition, Zeiss Ultra and Supra SEM, P7 and P10 profilometers, Veeco Icon

Abstract:

Typically, the highest quality thin film heterostructures achieved via epitaxial growth techniques prefer a blanket growth condition, covering the entire substrate. For device applications that demand a buried metallic layer, one must use subtractive fabrication techniques to access the buried metallic layer. In this report, we show that a KOH-based wet etch can be used to selectively etch N-polar AlN thin films with selectivity to a buried, metallic, NbN.

Summary of Research:

Over the past few decades, the III-N material system has developed into a particularly rich family of materials, playing key roles in the photonics [1], electronics [2], MEMs [3] device families — and more recently, the development of ferroelectric, magnetic, and metallic materials [4]. For III-N devices grown via epitaxial techniques, often it is preferred to grow a heterostructure or segments of a heterostructure in a blanket fashion, spanning the entire substrate. In this growth condition, one must define individual device mesas in a subtractive fashion. Recent growth efforts have shown that single crystalline wurtzite AlN can be grown on metallic, superconducting, NBN on 6H-SiC substrate by molecular beam epitaxy (MBE) [5,6]. For high frequency device applications looking to access this buried metallic NbN, but utilize a semi-insulating (SI) SiC substrate, one must etch a via through the top nitride heterostructure or through the entire SiC substrate.

Initial attempts to access the buried NbN layer via ICP-RIE etching revealed poor etch selectivity of AlN to NbN. For instance, a typical Cl- (BCl_3: 10 SCCM, Cl_2: 20 SCCM) and Ar-based (Ar72: 10 SCCM) etch in the PT 770 yielded an etch rate was ~ 1 nm/s, while the epitaxial NbN layer etched at ~ 2-4 nm/s under the same conditions. Over this past year, we have found one can access a buried NbN with relative ease using a two-step ICP-RIE and wet etch, overcoming the difficulty to etch 6H-SiC [7,8]. The process is shown schematically in Figure 1.

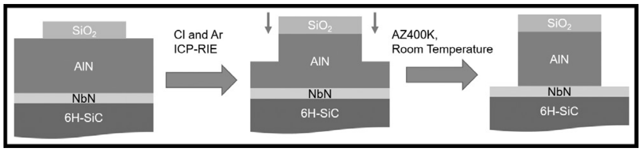

Figure 1: Schematic depiction of the two-step ICP-RIE and wet etch process. To overcome a lack of etch selectivity of AlN to NbN, etch through a small amount of remaining N-polar AlN (<200 nm) with room temperature AZ 400K.

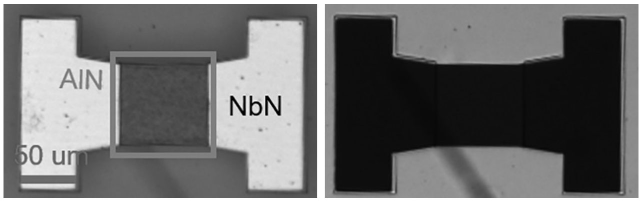

Figure 2: Optical microscope images of exposed NbN with a square AlN mesa (10,000 µm^2) post AZ 400K etch. The surrounding region is transparent 6H-SiC substrate. The thickness of the AlN mesa was 330 nm, and the height of the buried NbN was 24 nm. (a) Bright field illumination, and (b) dark field illumination. The NbN is thick enough such that it remains reflective under illumination, and the 6H-SiC substrate is optically transparent. Hence, the exposed NbN is reflective under bright-field illumination, and strongly blocks light under dark-field illumination, showing the buried NbN remains continuous under the AlN mesa.

First, the same ICP-RIE etch was applied to remove a majority of the AlN, with a PECVD SiO_2 etch mas. Then, using the same SiO_2 etch mask from the first step, the remaining (<200nm) AlN was then removed by using a dilute KOH wet etch, in the photolithographic developer AZ400K, at room temperature in under five minutes.

The exposed NbN remains conductive at room temperature, and is continuous underneath an AlN mesa.

Here, we show process results of a 330 nm thick AlN and 24 nm thick NbN heterostructure grown via MBE. Optical microscope images of the exposed NbN surface post-exposure to AZ400K are shown in Figure 2. No visible etching of the exposed NbN layer was detected, as verified by profilometry. Little lateral etching (<1µm) for AlN mesas with areas on order of 10,000 $µm^2$. The uniformity and speed of the etch in room temperature dilute KOH was attributed to an N-polar AlN surface (also observed by TEM in ref [6]), where KOH simultaneously serves as a catalyst in the oxidation of N-polar AlN and as a solvent for an Al_2O_3 product [8,9].

Conclusions and Future Steps:

Looking forward, we plan to see if the etch translates to N-polar GaN, and eventually more complicated III-N heterostructures. In principle, an etch selective to nitride semiconductors over metallic NbN would provide a potential pathway to dramatically scale various nitride electronics via epitaxial growth techniques. In the high frequency electronics arena, we are using the two-step etch to explore a novel bulk overtone acoustic wave resonator on 6H-SiC10 as well as a means to back-gate AlN-GaN-AlN "quantum well" high electron mobility transistors 11].

References:

[1] Akasaki, I. Nobel Lecture: Fascinated journeys into blue light. Reviews of Modern Physics 87, 1119-1131 (2015).

[2] Eastman, L. F. and Mishra, U. K. The toughest transistor yet [GaN transistors]. IEEE Spectrum 39, 28-33 (2002).

[3] Mahon, S. The 5G Effect on RF Filter Technologies. IEEE Transactions on Semiconductor Manufacturing 30, 494-499 (2017).

[4] Jena, D., et al. The new nitrides: layered, ferroelectric, magnetic, metallic and superconducting nitrides to boost the GaN photonics and electronics eco-system. Japanese Journal of Applied Physics 58, SC0801 (2019).

[5] Meyer, D. J., et al. Epitaxial Lift-Off and Transfer of III-N Materials and Devices from SiC Substrates. IEEE Transactions on Semiconductor Manufacturing 29, 384-389 (2016).

[6] Yan, R., et al. GaN/NbN epitaxial semiconductor/superconductor heterostructures. Nature 555, 183-189 (2018).

[7] Okamoto, N., et al. SiC Backside Via-hole Process for GaN HEMT MMICs Using High Etch Rate ICP Etching. 5 (2009).

[8] Zhuang, D. and Edgar, J. H. Wet etching of GaN, AlN, and SiC: a review. Materials Science and Engineering: R: Reports 48, 1-46 (2005).

[9] Guo, W., et al. KOH based selective wet chemical etching of AlN, Al x Ga 1-x N, and GaN crystals: A way towards substrate removal in deep ultraviolet-light emitting diode. Applied Physics Letters 106, 082110 (2015).

[10] Miller, J., Wright, J., Xing, H. G. and Jena, D. All-Epitaxial Bulk Acoustic Wave Resonators. physica status solidi (a) 217, 1900786 (2020).

[11] Hickman, A., et al. High Breakdown Voltage in RF AlN/GaN/AlN Quantum Well HEMTs. IEEE Electron Device Letters 40, 1293-1296 (2019).

Oxide Materials and Devices

CNF Project Number: 2802-19

Principal Investigator(s): Huili Grace Xing

User(s): Emma Long

Affiliation(s): Materials Science and Engineering, Cornell University

Primary Source(s) of Research Funding: Materials Science and Engineering, Cornell University

Contact: grace.xing@cornell.edu, yl3394@cornell.edu

Primary CNF Tools Used: Autostep i-line stepper, SC4500 odd-hour evaporator, PT770 etcher, P10 profilometer

Abstract:

In order to approach our research of gallium oxide lateral structure microdevices, we have worked at CNF for six months to get familiar with the gallium oxides metal oxide semiconductor field effect and fin field effect transistor processing.

Summary of Research:

In this past six months, we have been working on processing gallium oxide lateral structure microdevices, including metal oxide semiconductor field effect transistor (MOSFET), fin field effect transistor (FinFET).

MOSFET. To avoid the gallium oxide sample loss due to misoperation, an old gallium nitride (GaN) sample was used to be familiar with the standard processing. The GaN sample went through the mesa-isolation, drain and source metal deposition and metal contact annealing, shown in Figure 1a. The mesa-isolation involved photolithography and plasma etching. The metal deposition was completed by electron beam assistant physical vapor deposition. Metal contact annealing was done by the rapid thermal anneal. After the ohmic contact test, it appears that the resistance of the contact was much higher than expected. The reason could be unexpected oxidization of metal contact during the annealing shown in Figure 1b. In the rapid thermal anneal chamber, the temperature didn't reach the desired value and the ambiance didn't maintain as nitrogen along with the annealing.

With the previous experience in mind, a gallium oxide sample was processed with the same procedure. However, due to the brittle property of gallium oxides, the sample was broken during the sonication cleaning in glass beaker shown in Figure 2.

With the experience from the last two failures, the second gallium oxide sample (shown in Figure 3) was successfully processed. It was cleaned in a Teflon® beaker during sonication. We repeated the same procedure as the GaN sample. However, during the annealing process, the ambiance and temperature of the chamber were carefully controlled in a nitrogen atmosphere. This sample showed acceptable ohmic contact of drain and source metal. The sample has deposited a layer of the dielectric layer by atomic layer deposition. The gate metal was deposited with an electron beam assistant physical vapor deposition. The contact hole was done by the wet etching.

During this processing, it's vital to ensure the photolithography alignment of building each layer. In order to achieve good alignment, the manual operation on i-line stepper was practiced several times.

FinFET. In order to study the property of FinFET with gallium oxides, one gallium oxide sample was processed with a newly designed procedure. In order to identify the electron-beam dose of the electron-beam lithography, a control sample went through the same designed procedure as the official sample, mesa-isolation, and recess etching. The mesa-isolation involved photolithography, metal deposition, and plasma etching. Ion milling, metal deposition, and electron-beam lithography consisted of recess etching.

Due to the lab closing for COVID-19, the official sample needs to be completed in the future.

Conclusions and Future Steps:

During the six months of work in the CNF, we mastered the basic processing techniques of gallium oxide MOSFET and FinFET, including photolithography, plasma etching, metal deposition, dielectrics deposition and wet etching. In the future, in order to complete this research of gallium oxide FinFETs, we plan to master more characterization techniques (such as atomic force morphology, scanning electron microscopy), and electron-beam lithography.

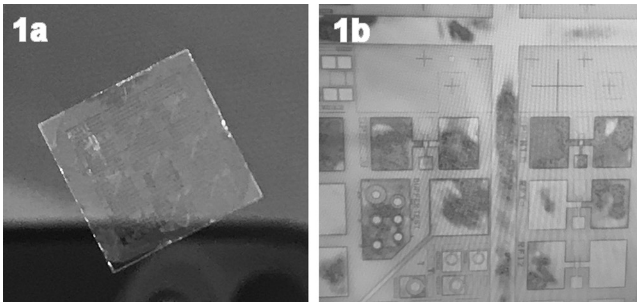

Figure 1: After mesa-isolation, drain and source metal deposition and metal contact annealing, a) contact metal turn to a greenish color, b) oxides under the microscope.

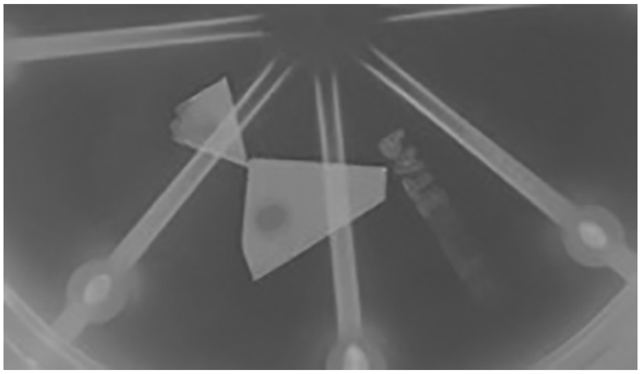

Figure 2: First gallium oxides sample after sonication clean.

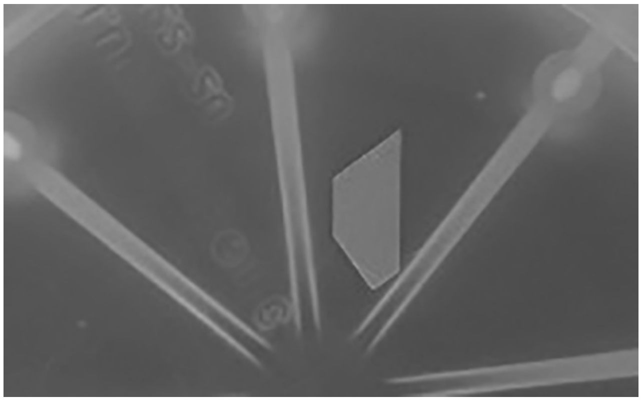

Figure 3: Second gallium oxide sample after sonication clean.

The Release of Thick SU-8 Films from Silicon Substrates

CNF Staff User: Aaron Windsor

Affiliation(s): Cornell NanoScale Facility, Cornell University
Primary Source(s) of Research Funding: Staff Funding/NSF
Contact: windsor@cnf.cornell.edu
Primary CNF Tools Used: ABM contact aligner, hot plates

Abstract:

For over three decades, SU-8 photoresist has been a vital tool for the fabrication of three-dimensional, high aspect ratio geometries. The resist's mechanical and chemical attributes have enabled its use throughout the many disciplines of MEMS and microfluidic research. Still, SU-8 does have a few drawbacks that have hindered its use, one being its difficulty to be removed from a substrate. There are currently many unique methods from the MEMS and electrodeposition industries for removing SU-8 off metal and silicon, but they all involve either hazardous chemicals or specialized equipment. It was discovered that thick SU-8 features could be lifted off or released from a silicon substrate after a few weeks submerged in a simple detergent bath. With proper cleaning and an overnight dehydration, a new layer of SU-8 could be reapplied on these stripped wafers. Applying different forms of mechanical force and increasing the bath temperature greatly reduced the time required to remove SU-8 and repeatedly release full SU-8 structures. This low-cost and environmentally friendly process may open new pathways for rescuing wafers, producing three-dimensional parts or devices independent of a substrate, flexible electronics and other applications.

Summary of Research:

A solution of room temperature Dawn Detergent™ and deionized water (DI) can slowly undercut the interface between thick SU-8 features and the silicon substrate wafer. Depending on the surface area, the removal of microfluidic-sized SU-8 features may require two to six weeks of soaking. The use of running water or a nitrogen/compressed air gun at an incident angle could assist with the removal of the soaked SU-8 features before they completely detach in the solution.

It was later found that increasing the temperature of the detergent solution to 95°C along with thermal cycling hastened the release process. Thermal cycling could also release SU-8 without the use of detergents.

Currently, 38 µm of SU-8 has been the thinnest SU-8 film removed using this method. It may be safe to assume that the film stress of the SU-8 combined with the surfactant undercutting action may instigate the delamination. Research is currently being done on how film stress and thickness affects this process.

In order to spin SU-8 on stripped wafers again, any traces of the detergent or residual SU-8 should be removed. Wafers were first soaked overnight in DI water and then rinsed three more times. A piranha etch was done afterwards to strip away any remaining organic residues off the substrate. The wafers were dehydrated overnight in an oven at 90°C before spinning a new layer of SU-8 on the wafer again. Some outlines of the detached SU-8 features may remain on the surface of the wafer. Repeated piranha etches may eventually remove these features, but these outlines have not affected SU-8 applications or PDMS molding.

This method was used to release large 3-D shapes from a silicon wafer. The first example was a release a complete 160 µm microfluidic device from a silicon substrate using a 200 ml DI bath with 1 ml of Triton-X at 95°C for three hours (Figure 1).

Next, an 89 µm thick, two-inch diameter spiral was fabricated with SU-8 100. Twenty-four hours after the post exposure bake, this wafer was placed in a room temperature DI water bath and was slowly heated 1.3°C a minute to 98°C. After one hour at the desired temperature, the wafer was removed from the bath and the SU-8 spiral was released from the wafer (Figure 2). This same wafer was again rinsed, piranha etched and dehydrated before repeating the experiment.

SU-8 was spun again, but at 1500 RPM with hopes of producing a 200 µm thick spiral (actual thickness was 178 µm). Again, the SU-8 structure was successfully removed after two total hours in the DI water bath.

In the short term, this method may be used to remove and reapply SU-8 after design changes, fabrication errors or replace essential features that are lost or broken by PDMS molding. SU-8 may be used as a quick way for fabricating prototype parts. Many ideas are currently being explored such as detachable SU-8 filters, gears and group of parts that could be released from a wafer and assembled later. Future work will focus on simulating a known UV-LIGA process of patterning SU-8 as electroplating molds and later removing the resist after depositing thick metallic films.

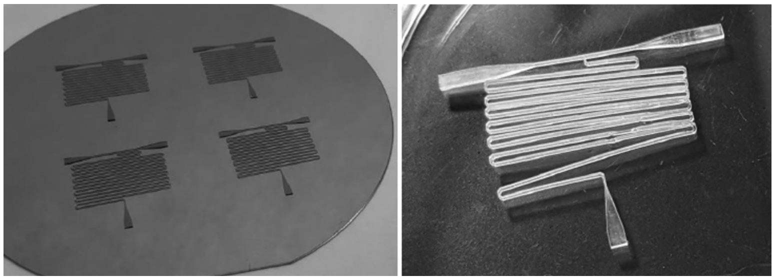

Figure 1: A complete SU-8 microfluidic device mold released from a silicon wafer. Left: Four 160 µm thick SU-8 devices patterned on a four-inch wafer. Right: Released device after submerged in heated Triton X-100 detergent solution for three hours.

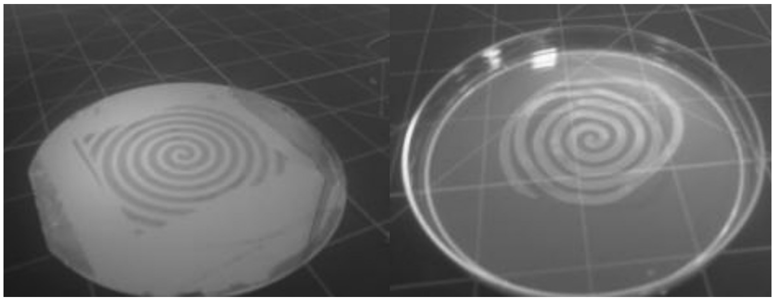

Figure 2: A complete 89 µm thick SU-8 spiral released from a silicon wafer after two hours in a DI water bath at 98°C.

CNF 2019-2020 Research Accomplishments

INDEX

Reports by CNF Project Number

CNF Principal Investigators & Users

The 2019-2020 Cornell NanoScale Facility
Research Accomplishments
are online in PDF,
http://cnf.cornell.edu/publications/research_accomplishments

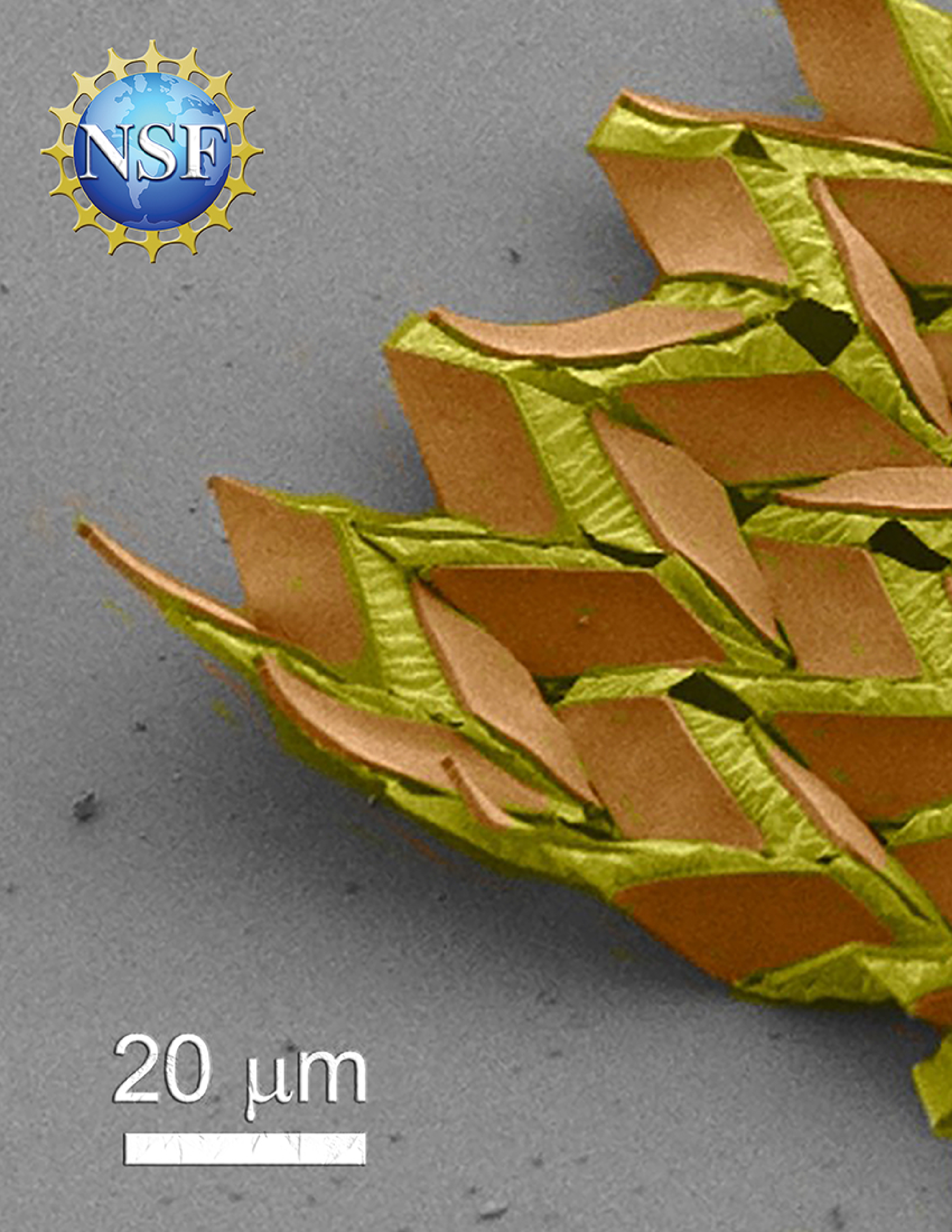
20 μm